


Spring 5-9-2020

Ocular, Neural, and Cellular Biodistribution of Multifunctional Antioxidants

Damian Daszynski
University of Nebraska Medical Center

Follow this and additional works at: <https://digitalcommons.unmc.edu/etd>

 Part of the [Medicinal and Pharmaceutical Chemistry Commons](#), [Other Pharmacy and Pharmaceutical Sciences Commons](#), and the [Pharmaceutics and Drug Design Commons](#)

Recommended Citation

Daszynski, Damian, "Ocular, Neural, and Cellular Biodistribution of Multifunctional Antioxidants" (2020). *Theses & Dissertations*. 446.
<https://digitalcommons.unmc.edu/etd/446>

This Dissertation is brought to you for free and open access by the Graduate Studies at DigitalCommons@UNMC. It has been accepted for inclusion in Theses & Dissertations by an authorized administrator of DigitalCommons@UNMC. For more information, please contact digitalcommons@unmc.edu.

**Ocular, Neural, and Cellular Biodistribution of
Multifunctional Antioxidants**

By

Damian Mark Daszynski

A DISSERTATION

Presented to the Faculty of
The Graduate College in the University of Nebraska
In Partial Fulfillment of the Requirements
For the Degree of Doctor of Philosophy

Pharmaceutical Sciences Graduate Program

Under the Supervision of Professor Peter F. Kador

University of Nebraska Medical Center
Omaha, NE

April, 2020

Supervisory Committee:

Dong Wang, Ph.D.

Wallace B. Thoreson, Ph.D.

Haizhen A. Zhong, Ph.D.

Steven J. Fliesler, Ph.D.

ACKNOWLEDGEMENTS

No words can express how grateful I am to my advisor, Dr. Peter F. Kador, for providing me the opportunity to learn and grow in his laboratory as a graduate student. Under Dr. Kador's guidance, I was transformed from a physical chemist into a biomedical research scientist. He instilled in me the necessary critical thinking skills to approaching and solving problems, aided in my mastery of basic research techniques, and honed my skill set for analyzing, discussing and communicating data. For this, I am forever grateful.

I would also like to express my sincerest gratitude to my graduate supervisory committee who include Dr. Dong Wang, Dr. Wallace B. Thoreson, Dr. Haizhen A. Zhong, and Dr. Steven J. Fliesler. Their input and support throughout my studies have given me to confidence to "look outside the box" and consider how my research may be applicable to other scientific disciplines. I cannot thank them enough for all their time and effort, which helped me grow as a scientist.

Most of the work presented in this thesis would not have been possible without the support of my colleagues in the laboratory, Mr. Theodor Woolman and Ms. Karen Blessing, who both played critical roles in my graduate training. Over the course of my studies, Mr. Woolman taught and refine my hands-on synthetic chemistry skills, while Ms. Blessing taught and refined my cell culture skills. I would also like to thank the former graduate students of the lab, Dr. James Randazzo and Dr. Hiroyoshi Kawada, for setting the foundation upon which my research was built. Finally, a heartiest thank you to Mr. Ed Ezell of the NMR Core Facility for all of his assistance with the NMR.

I would like to also thank all whom I have befriended through the University of Nebraska Medical Center and the Department of Pharmaceutical Sciences, especially Dr. Constance Mietus, Dr. Karen Zagorski, Dr. Mohtadin Hashemi, Dr. Laura Weber, Dr. R. Lee Sleightholm, Dr. Carolyn Carr, Dr. Calliste Reiling, Catherine Orzechowska, Derek Leas, Swagat Sharma, Kirsten Antonio-Tolentino, Angelica Carmona, Yaqing Wang, Michelle Pham, Sridhar Vemulapalli, Shaun Filliaux, and Tommy Stormberg. A special thank you to the current and past faculty and staff of the Department of Pharmaceutical Sciences.

Finally, I would like to thank my family, especially my mother (Teresa Daszynski) and my sister (Camille Daszynski), my father no longer with us (Mark Daszynski), my best friend and better half (Caitlin Vera), and her parents (Carlos and Rita Vera) for their unconditional love, support, and encouragement during my pursuit of the highest degree of education.

Contributors: The author would like to thank Dr. Hongxia Jin and Dr. Hiroyoshi Kawada for designing the synthetic schemes for all compounds presented in Chapters 2 and 3, and Drs. Lynette Smith and Haizhen Zhong for their assistance with the biodistribution, hierarchical cluster analysis, and quantitative structure activity relationship analyses. The author would also like to thank Dr. Haizhen Zhong for his assistance with the computational chemistry in Chapter 4, our collaborators at University of Missouri, Columbia, under Dr. K Krishna Sharma for their work on the biological binding studies, and Dr. Marjorie Lou for her assistance with the manuscript. The author would also like to thank Mr. Theodor Woolman for his guidance with synthetic chemistry and Ms. Karen Blessing for her guidance with *in vitro* cell culture experiments presented in Chapter 5.

Ocular, Neural, and Cellular Biodistribution of Multifunctional Antioxidants

Damian Mark Daszynski, Ph.D.

University of Nebraska, 2020

Advisor: Peter F. Kador, Ph.D.

Aging is a complex biological process which stems from a growing imbalance between the regenerative capacity of an organism and endogenous as well as exogenous damaging factors. This imbalance leads to the slow deterioration of individual cells, organs, and eventually the entire organism. The free radical theory of aging combines the evolutionary and mechanistic aspects of aging, postulating that the innate process is caused by deleterious, irreversible, and inevitable changes in biological systems caused by oxidative damage that accumulates over the lifespan. Evidence of this phenomenon is supported by the pathogenesis of age-related diseases, such as age-related macular degeneration and Alzheimer's disease, which show that there is an age-related decrease of cellular antioxidant defenses. This results in the dyshomeostasis of redox-active metals, such as iron, copper, and zinc, and in turn exacerbates the oxidative stress induced by reactive oxygen species and free radicals such as superoxide, hydrogen peroxide, and the hydroxyl radical.

Our laboratory has developed two series of multifunctional antioxidants (MFAOs), the JHX and HK series, which can simultaneously chelate biologically active transition metals and scavenge free radicals. These orally-active compounds have demonstrated therapeutic effects against age-related eye diseases, such as cataract and macular degeneration. Despite their efficacy, little is known about the ocular biodistribution of these orally-administered molecules.

I have conducted a biodistribution study of 24 such molecules. These included the MFAOs, their monofunctional free radical scavenging (FRS) and biologically active transition metal chelating (CHL) analogs, as well as their nonfunctional (NF) analogs in Sprague Dawley rats. In Chapter Two, I demonstrate that all compounds can be detected unmetabolized in the cornea, iris with the ciliary body, lens, neural retina, retinal pigmented epithelium with the choroid, brain, sciatic nerve, kidney, and liver. In Chapter Three, I describe the predictive models of ocular, neural, and visceral tissue distribution, which I developed based on the biodistribution data from Chapter Two, using hierarchical cluster analysis (HCA) and quantitative structure activity relationship analysis (QSAR). The results indicated that both HCA and QSAR analysis yielded many predictive models which agree with other reported trends of drug delivery to ocular, neural, and visceral tissues. In Chapter Four, I present my investigation into the potential pharmacological chaperone activity of two oxysterols, lanosterol and 25-hydroxycholesterol, to three model α B-crystallin chaperone proteins *in silico* and compare their binding against the MFAOs. Our results confirm that the oxysterols fail to meet the predictive binding threshold, indicating weak binding affinity to the model α B-crystallin proteins. However, their predicted K_d values matched experimentally reported values. The MFAOs exceeded the threshold for predictive binding and support previous *in vivo* studies which suggest our molecules may have some chaperone activity. Finally, in Chapter Five, I will present several synthetic approaches for the preparation of various novel triphenylphosphonium-linked (TPP) JHX-series compounds. I will also discuss their *in vitro* evaluation in HEI-OC1 inner ear cells. Since mitochondrial dysfunction is linked to neurodegeneration, we hypothesized that directly linking a mitochondria-targeting moiety to our compounds would increase their potency by quenching free radicals at their main generation source. Our results indicate that the TPP compounds do not adversely affect mitochondria as shown using a viability assay and Rhodamine-123 fluorescence stain.

TABLE OF CONTENTS

ACKNOWLEDGEMENTS	i
ABSTRACT	iii
TABLE OF CONTENTS	v
LIST OF TABLES	x
LIST OF FIGURES	xiii
LIST OF SCHEMES	xviii
CHAPTER 1: INTRODUCTION	
1.1 Oxidative Stress in Aging	1
1.2 Multifunctional Antioxidant: A New Generation of Antioxidant Compounds	3
1.3 Multifunctional Antioxidants are Protective <i>In Vitro</i> and <i>In Vivo</i> After Oral Administration	10
1.4 Mitochondrial Targeting of Multifunctional Antioxidants as a Potential Therapeutic Avenue for Ocular and Neural Diseases	13
1.4.1 Targeting of Mitochondria through Linkage to Triphenylphosphonium Lipophilic Cations	16
1.5 Overview	19
1.6 References	20
CHAPTER 2: Biodistribution of Multifunctional Antioxidants, Their Monofunctional Free Radical Scavenging and Chelating Analogs, and Nonfunctional Parents After Oral Administration	

2.1	Summary	32
2.2	Introduction	33
2.3	Methods	35
2.4	Results	39
2.4.1	Distribution of Parent Compounds	41
2.4.2	Distribution of Free Radical Scavenging Compounds	43
2.4.3	Distribution of Metal Binding Compounds	46
2.4.4	Distribution of Multifunctional Compounds	49
2.5	Discussion	52
2.6	Conclusions	59
2.7	References	61
CHAPTER 3:	Developing Predictive Models of Multifunctional Antioxidant Compound Distribution and Their Analogs using Hierarchical Cluster Analysis and Quantitative Structure Activity Relationship Methods	
3.1	Summary	68
3.2	Introduction	69
3.2.1	Physicochemical Parameters	69
3.2.2	Hierarchical Cluster Analysis	69
3.2.3	Quantitative Structure Activity Relationships	71
3.3	Programs and Methods	72
3.4	Results	74
3.4.1	Calculation of Molecular Descriptors	74
3.4.2	Preliminary Linear Regression Analysis	76

3.4.3	Full and Standardized Data Set Linear Regression	79
3.4.4	Clustered Correlations	81
3.4.5	Confirmation of HCA Clusters using QSAR Algorithms	109
3.4.6	Extended QSAR Analysis using Validated Clustered Correlations	110
3.5	Discussion	123
3.5.1	Preliminary Linear Regression Analysis	123
3.5.2	Clustered Correlations and Cluster Confirmations using QSAR Algorithms	124
3.5.2a	Blood-Aqueous Barrier Penetration	127
3.5.2b	Blood-Retinal Barrier Penetration	130
3.5.2c	Blood-Brain and Blood-Nerve Barrier Penetration	132
3.5.2d	Peripheral Tissue Distribution	134
3.5.2e	Verification of HCA Clustered Correlations	135
3.5.3	Expanded Linear Regression Using QSAR-Derived Clustered Correlations	136
3.6	Conclusion	139
3.7	References	140
CHAPTER 4:	Failure of Oxysterols such as Lanosterol to Restore Lens Clarity from Cataract	
4.1	Summary	149
4.2	Introduction	150
4.3	Materials and Methods	153

4.4	Results	160
4.5	Discussion	171
4.6	Conclusion	189
4.7	References	190
CHAPTER 5:	Approaches to the Synthesis of Mitochondrial-Targeted JHX-4 and their Preliminary <i>In Vitro</i> Evaluation in the HEI- OC1 Cell Line	
5.1	Summary	199
5.2	Introduction	200
5.3	Results and Discussion	203
5.3.1	Chemistry	203
5.3.1a	Synthesis of the Parent TPP Compound	203
5.3.1b	Synthesis of the Metal Chelating TPP Compound	207
5.3.1c	Progress towards the Free Radical Scavenging TPP Compound	209
5.3.1d	Progress towards the Multifunctional Antioxidant TPP Compound	210
5.3.2	A New Approach to the TPP Compounds using an Ester Linkage	216
5.3.2a	Development of the JHX-1-TPP-Ester	216
5.3.2b	Progress towards the JHX-2-TPP-Ester	217
5.3.2c	Development of the JHX-3-TPP-Ester	218
5.3.2d	Progress towards the JHX-4-TPP-Ester	219
5.3.3	Preliminary Evaluation of HEI-OC1 Cells	222

5.4	Conclusion	230
5.5	Materials and Methods	231
5.5.1	Chemistry Procedures	231
5.5.2	<i>In Vitro</i> Materials and Methods	247
5.6	References	251
CHAPTER 6:	CONCLUSIONS AND FUTURE DIRECTIONS	258
6.1	Biodistribution Study	258
6.2	Predictive Modeling Study	259
6.3	Oxysterol Study	260
6.4	Mitochondria-Targeted TPP Synthesis and <i>In Vitro</i> Study	261

LIST OF TABLES

Chapter 2:

Table 2.1	Biodistribution summary of all compounds in the ocular, neural, and visceral tissues	40
-----------	--	----

Chapter 3:

Table 3.1	Definitions of select calculated physicochemical descriptors, which were chosen based on literature precedence	75
Table 3.2	Correlation results between the NFs JHX-1 and HK-13, the FRS JHX-6, the CHLs JHX-3 and HK-1, and the MFAOs HK-2 and HK-8	77
Table 3.3	Correlation results between the functional antioxidants including the FRS JHX-6, the CHLs JHX-3 and HK-1, and the MFAOs HK-2 and HK-8	77
Table 3.4	Expanded correlations examining more calculated physicochemical parameters continued from Table 3.2	78
Table 3.5	Expanded correlations examining more calculated physicochemical parameters continued from Table 3.3	79
Table 3.6	Linear regression analysis of the full data set (all 24 drugs) summarizing the resulting Pearson's correlation coefficients (r-values)	80
Table 3.7	Linear regression analysis of the mathematically standardized data sets summarizing the resulting Pearson's correlation coefficients (r-values)	81
Table 3.8	Cluster correlations for the structural parameters of the full data set for each tissue using the average-linkage algorithms	84
Table 3.9	Cluster correlations for the structural parameters of the full data set for each tissue using the complete-linkage algorithms	85
Table 3.10	Cluster correlations for the structural parameters of the standardized data set for each tissue using the average-linkage algorithms	86
Table 3.11	Cluster correlations for the structural parameters of the standardized data set for each tissue using the complete-linkage algorithms	87
Table 3.12	Cluster correlations for the hydrophilic parameters of the full data set for each tissue using the average-linkage algorithms	88

Table 3.13	Cluster correlations for the hydrophilic parameters of the full data set for each tissue using the complete-linkage algorithms	90
Table 3.14	Cluster correlations for the hydrophilic parameters of the standardized data set for each tissue using the average-linkage algorithms	92
Table 3.15	Cluster correlations for the hydrophilic parameters of the standardized data set for each tissue using the complete-linkage algorithms	94
Table 3.16	Cluster correlations for the hydrophobic parameters of the full data set for each tissue using the average-linkage algorithms	96
Table 3.17	Cluster correlations for the hydrophobic parameters of the full data set for each tissue using the complete-linkage algorithms	97
Table 3.18	Cluster correlations for the hydrophobic parameters of the standardized data set for each tissue using the average-linkage algorithms	98
Table 3.19	Cluster correlations for the hydrophobic parameters of the standardized data set for each tissue using the complete-linkage algorithms	99
Table 3.20	Cross-validated linear regression models obtained with the MOE™ QuaSAR algorithm, many of which are the same as those obtained using OriginPro™ HCA algorithm and subsequent linear regression analysis (indicated with *)	110
Table 3.21	Extended and cross-validated QSAR models relating to the measured parameters with clustered drug tissue levels in the cornea	112
Table 3.22	Extended and cross-validated QSAR models relating to the measured parameters with clustered drug tissue levels in the iris/CB	113
Table 3.23	Extended and cross-validated QSAR model relating to the measured parameters with clustered drug tissue levels in the lens	115
Table 3.24	Extended and cross-validated QSAR models relating to the measured parameters with clustered drug tissue levels in the NR	116
Table 3.25	Extended and cross-validated QSAR models relating to the measured parameters with clustered drug tissue levels in the RPE/C	118
Table 3.26	Extended and cross-validated QSAR models relating to the measured parameters with clustered drug tissue levels in the SN	120
Table 3.27	Extended and cross-validated QSAR models relating to the measured parameters with clustered drug tissue levels in the kidney	122

Table 3.28	Extended and cross-validated QSAR model relating to the measured parameter vsurf_Cp with clustered drug tissue levels in the liver	122
------------	--	-----

Chapter 4:

Table 4.1	MOE™ docking scores of all compounds (Figure 4.1) to the dimer interface on PHE 55 of wildtypes, 2WJ7 and 2KLR , and the R120G mutant, 2Y1Z	167
Table 4.2	Maestro docking scores of all compounds (Figure 4.1) to the dimer interface on PHE 55 of wildtypes, 2WJ7 and 2KLR , and the R120G mutant, 2Y1Z	168
Table 4.3	Maestro docking scores and predicted K _d values of ATP, oxysterols, and MFAOs to wildtypes 2WJ7 and 2KLR , and mutant 2Y1Z	171

LIST OF FIGURES

Chapter 1:

Figure 1.1	General schematic diagram of the redox cascade	3
Figure 1.2	Common small molecule antioxidants	4
Figure 1.3	MFAO compound scaffolds and their monofunctional and nonfunctional analog derivatives	9
Figure 1.4	The JHX and HK series MFAOs	11
Figure 1.5	The structure of Elamipretide (also known as SS-31 or MT-131)	16
Figure 1.6	Common TPP-derived mitochondrial antioxidants	17

Chapter 2:

Figure 2.1	The 24 orally-active analogs of N,N-dimethyl-4-(pyrimidin-2-yl)piperazine-1-sulfonamide, 2-(pyrrolidine-1-yl)pyrimidine, and 2-(piperidine-1-yl)pyrimidine)	36
Figure 2.2	Summary of the NF drug levels to ocular, neural, and visceral tissues	42
Figure 2.3	Summary of the FRS drug levels to ocular, neural, and visceral tissues	44
Figure 2.4	Summary of the CHL drug levels to ocular, neural, and visceral tissues	47
Figure 2.5	Summary of the MFAO drug levels to ocular, neural, and visceral Tissues	50

Chapter 3:

Figure 3.1	Examples of the resulting dendrograms after applying the HCA algorithm	83
Figure 3.2	Linear regression models between physicochemical descriptors and drug levels in the cornea where (A) corresponds to Cluster 1 between cornea and CASA+ in Table 3.12 , (B) corresponds to the Cluster 2 between cornea and ASA_P in Table 3.14 , (C) corresponds to Cluster 2 between cornea and SMR in Table 3.9 , and (D) corresponds to Cluster 3 between cornea and LogS in Table 3.14	101
Figure 3.3	Linear regression models between physicochemical descriptors and drug levels in the iris/CB where (A) corresponds to Cluster 2 between iris/CB and FASA_H in Table 3.19 , (B) corresponds to Cluster 2	102

between iris/CB and FASA_P in **Table 3.15**, (C) corresponds to Cluster 1 between iris/CB and LogP in both **Table 3.16** and **Table 3.18**, and (D) corresponds to Cluster 2 between iris/CB and vsurf_G in **Table 3.11**

- Figure 3.4 Linear regression models between physicochemical descriptors and drug levels in the lens where (A) corresponds to Cluster 3 between lens and FASA_H in **Tables 3.18** and **3.19**, (B) corresponds to Cluster 2 between lens and FASA_P in **Tables 3.14** and **3.15**, (C) corresponds to Cluster 1 between lens and LogP in **Tables 3.16** and **3.18**, and (D) corresponds to Cluster 3 between lens and LogS in **Tables 3.13** and **3.14** 103
- Figure 3.5 Linear regression models between physicochemical descriptors and drug levels in the NR where (A) corresponds to Cluster 2 between NR and SLogP in **Tables 3.16** and **3.17**, (B) corresponds to Cluster 2 between NR and SLogP in **Table 3.18**, and (C) corresponds to Cluster 2 between NR and Kier1 in **Tables 3.8, 3.9, 3.10**, and **3.11** 104
- Figure 3.6 Linear regression models between physicochemical descriptors and drug levels in the RPE/C where (A) corresponds to Cluster 1 between RPE/C and Apol in **Tables 3.14** and **3.15**, (B) corresponds to Cluster 1 between RPE/C and ASA in **Tables 3.14** and **3.15**, (C) corresponds to Cluster 3 between RPE/C and LogS in **Table 3.14**, and (D) corresponds to Cluster 1 between RPE/C and vsurf_W1 in **Table 3.15** 105
- Figure 3.7 Linear regression model between physicochemical descriptors and drug levels in the brain where (A) corresponds to Cluster 1 between brain and vsurf_Cp in **Table 3.11** 106
- Figure 3.8 Linear regression models between physicochemical descriptors and drug levels in the SN where (A) corresponds to Cluster 2 between SN and ASA_P in **Table 3.12**, (B) corresponds to Cluster 2 between SN and SLogP in **Table 3.19**, (C) corresponds to Cluster 2 between SN and vsurf_Cp in **Tables 3.8, 3.9**, and **3.10**, as well as Cluster 3 between SN and vsurf_Cp in **Table 3.11**, and (D) corresponds to Cluster 1 between SN and vsurf_W1 in **Table 3.12** 107
- Figure 3.9 Linear regression models between physicochemical descriptors and drug levels in the kidney where (A) corresponds to Cluster 1 between kidney and CASA+ in **Table 3.12**, and (B) corresponds to Cluster 2 between kidney and SMR in **Table 3.9** 108
- Figure 3.10 Linear regression models between physicochemical descriptors and drug levels in the Liver where (A) corresponds to Cluster 2 between liver and PM3_Dipole in **Tables 3.12, 3.13, 3.14**, and **3.15**, and (B) corresponds to Cluster 2 between liver and LogP in **Tables 3.16, 3.17, 3.18**, and **3.19** 109

Figure 3.11	Cross-validated linear regression models between physicochemical descriptors and drug levels in the cornea where (A) and (B) correspond to the new FASA_H and vsurf_Cp cluster correlations identified from Cluster 1 between cornea and CASA+ in Table 3.14 , (C) corresponds to the new FASA_P cluster correlation identified from Cluster 1 between cornea and CASA+ in Table 3.14 , and (D) corresponds to the validated Cluster 3 between cornea and LogS in Table 3.14	112
Figure 3.12	Cross-validated linear regression models between physicochemical descriptors and drug levels in the iris/CB where (A) corresponds to a newly identified vsurf_Cp cluster correlation between iris/CB and CASA+, (B) through (G) correspond to the new calculated ASA, ASA_P, CASA-, ASA_H, FASA_P, and Kier1 clusters from iris/CB and FASA_H in Table 3.19 or FASA_P in Table 3.15 , and (H) corresponds to the validated Cluster 1 between iris/CB and LogP in Table 3.18	114
Figure 3.13	Cross-validated linear regression models between physicochemical descriptors and drug levels in the NR where (A) corresponds to the newly calculated CASA- clusters from Cluster 2 between NR and SLogP in Tables 3.16 and 3.17 , and (B) corresponds to the newly calculated cluster from Cluster 2 between NR and SLogP in Table 3.18	117
Figure 3.14	Cross-validated linear regression models between physicochemical descriptors and drug levels in the RPE/C where (A) through (C) corresponds to the newly calculated Dipole, PM3_Dipole, and SMR clusters from Cluster 1 between RPE/C and Apol in Tables 3.14 and 3.15	118
Figure 3.15	Cross-validated linear regression models between physicochemical descriptors and drug levels in the SN where (A) and (B) correspond to the newly calculated ASA_P and vsurf_W1 clusters from Cluster 2 between SN and ASA_P in Tables 3.12 , (C) through (E) correspond to the validated SLogP cluster and new calculated ASA_H and vsurf_P clusters from Cluster 2 between SN and SLogP in Table 3.19 , and (F) corresponds to the validated vsurf_W1 cluster from Cluster 1 between SN and vsurf_W1 in Table 3.12	121
Figure 3.16	Cross-validated linear regression model between physicochemical descriptor Kier1 and drug levels in the Kidney where (A) corresponds to the newly calculated Kier1 cluster from Cluster 2 between kidney and SMR in Table 3.9	122
Chapter 4:		
Figure 4.1	Structures of molecules used in the docking studies with the human cryAB wildtypes, 2WJ7 and 2KLR , and the R120G mutant, 2Y1Z	157

Figure 4.2	Appearance of rat lenses after 48-hour incubation following the induction of cataract and subsequent additional incubation with 15 mM of lanosterol liposomes	162
Figure 4.3	Change in protein levels from 47-year-old human lens fragments after 3 days incubation at 37 °C in media containing 0.20 mM lanosterol	163
Figure 4.4	Change in soluble/insoluble protein levels of 60-year-old human lens homogenate after 3 days incubation at 37 °C in media containing either 0.0, 0.25, or 0.50 mM of 25-hydroxycholesterol	164
Figure 4.5	The solubility of human lens proteins in the presence of (A) lanosterol and (B) 25-hydroxycholesterol	165
Figure 4.6	Comparison of the surface and charge differences (sphere structure), along with the location of key amino acid residues (ribbon structure) between the α B-crystallin wildtypes 2WJ7 and 2KLR and the ARG120GLY mutant 2Y1Z	178
Figure 4.7	MOE ribbon structures depicting the best docked complexes for lanosterol and 25-hydroxycholesterol with the wildtype and mutant α B-crystallins	181
Figure 4.8	MOE ribbon structures depicting the best docked complexes for all MFAOs to the dimer interface of the wildtype α B-crystallin, 2WJ7	182
Figure 4.9	MOE ribbon structures depicting the best docked complexes for all MFAOs with the dimer interface of the wildtype α B-crystallin, 2KLR	184
Figure 4.10	MOE ribbon structures depicting the best docked complexes for all MFAOs to the dimer interface of the R120G mutant α B-crystallin, 2Y1Z	186
Figure 4.11	Appearance of 25-hydroxycholesterol dissolved in PBS solution with or without the presence of α B-crystallin	187
Chapter 5:		
Figure 5.1	Proposed structures of the novel JHX-TPP class of compounds	203
Figure 5.2	Proposed structures of the novel JHX-TPP-Ester class of compounds	216
Figure 5.3	HEI-OC1 cytotoxicity with the non-conjugated JHX compounds	223
Figure 5.4	HEI-OC1 mitochondriotoxicity study with the non-conjugated JHX compounds	224

Figure 5.5	Cell viability of the HEI-OC1 cells after 24 hours of culture with or without the JHX-1-TPP or the HK-2-Benzyl-TPP	226
Figure 5.6	Mitochondria membrane potential of HEI-OC1 cells after 8 hours of culture with or without the JHX-1-TPP or HK-2-Benzyl-TPP	227
Chapter 6:		
Figure 6.1	The new proposed JHX-based compound series	262

LIST OF SCHEMES**Chapter 5:**

Scheme 5.1	Progress towards the C3-linked JHX-1-TPP (1)	204
Scheme 5.2	Progress towards the C4-linked JHX-1-TPP (17)	206
Scheme 5.3	Synthesis of the first C4-linked JHX-1-TPP (17)	206
Scheme 5.4	Synthesis of the first C3-linked JHX-1-TPP (1)	207
Scheme 5.5	Progress towards the C3-linked JHX-3-TPP (3)	208
Scheme 5.6	Progress towards the C3-linked JHX-2-TPP (2)	210
Scheme 5.7	Progress towards the C3-linked JHX-4-TPP (4)	212
Scheme 5.8	Alternate MFAO-TPP synthesis using the TBDMS protecting group	213
Scheme 5.9	Synthesis of the bottom ring intermediates for the MFAO synthesis	214
Scheme 5.10	Progress towards the MFAO-TPP (4) with the TBDPS protecting group	215
Scheme 5.11	Synthesis of the JHX-1-TPP-Ester (51)	217
Scheme 5.12	Progress towards the JHX-2-TPP-Ester (52)	218
Scheme 5.13	Synthesis of the JHX-3-TPP-Ester (53)	219
Scheme 5.14	Progress towards the JHX-4-TPP-Ester (54)	222

CHAPTER 1

INTRODUCTION

1.1 Oxidative Stress in Aging

Aging is a complex biological process which results in senescence and eventually death. Many theories have been proposed to explain the phenomenon of aging such as the Wear-and-Tear theory by Weismann [1] and the Mutation Accumulation theory by Medawar [2]. These two hallmark theories postulate that natural selection eliminates older members of a population so that they no longer compete with younger generations for resources, and that aging results from the accumulation of cellular damage and damage to genes coding for repair function, respectively [3]. While the theories of aging continue to be refined, researchers have identified that many aging theories may not be mutually exclusive. However, one aging theory has remained at the forefront of aging research: The Free Radical Theory of Aging proposed by Harnam [4].

The free radical theory of aging combines evolutionary and mechanistic aspects of the aging process, suggesting that the innate process is caused by deleterious, irreversible changes to biological systems that increase in frequency over the lifespan [4]. Moreover, it also postulates that aging is the cumulative result of oxidative damage to cells and tissues that arise primarily as due to aerobic metabolism. Several lines of evidence support this hypothesis, such as that variations in species lifespan are correlated with metabolic rate and protective antioxidant activity [5], enhanced expression of antioxidant enzymes in experimental animals can produce a significant increase in longevity [6-8], cellular levels of free radical damage increase with age [9, 10], and reduced caloric intake

leads to a decline in the production of reactive oxygen species and an increased lifespan [11, 12]. Additionally, anti-aging research has demonstrated that persistent oxidative stress by reactive oxygen species (ROS) and reactive nitrogen species (RNS) contributes to the development of many disease pathologies such as cancer [13], diabetes [14], cardiovascular diseases [15], neurodegenerative diseases [16], and eye diseases [17, 18], all of which contribute to decreases in quality of life [19].

A general diagram of the redox pathways in biological systems is summarized in **Figure 1.1**. Starting with molecular oxygen (O_2), its single electron reduction generates superoxide ($O_2^{\cdot-}$) which may then undergo one of three reaction paths. First, it may react with nitric oxide ($\cdot NO$) to form peroxynitrite ($ONOO^{\cdot-}$), a biomarker for oxidative stress that in high concentrations leads to apoptotic or necrotic cell death [20]. It is also in equilibrium with the hydroperoxyl radical (HOO^{\cdot}), which is an initiator of lipid peroxidation [21]. Finally, it may auto-dismutate or be catalytically dismutated by superoxide dismutase into hydrogen peroxide (H_2O_2). Hydrogen peroxide may also undergo one of three reaction paths. First, it may react with a biologically active redox metal such as Fe^{2+}/Fe^{3+} through the Fenton reaction to yield either the hydroxyl radical (HO^{\cdot}) or the hydroperoxyl radical (HOO^{\cdot}). Second, it can be generated and used by neutrophils to produce hypochlorous acid ($HOCl$) during the antimicrobial respiratory burst [22]. Finally, it can be dissociated by catalase to form water and oxygen. The reactive species $ONOO^{\cdot-}$, HOO^{\cdot} , and HO^{\cdot} have been reported to damage DNA, oxidize proteins, and cause the peroxidation of lipids, all of which lead to tissue damage.

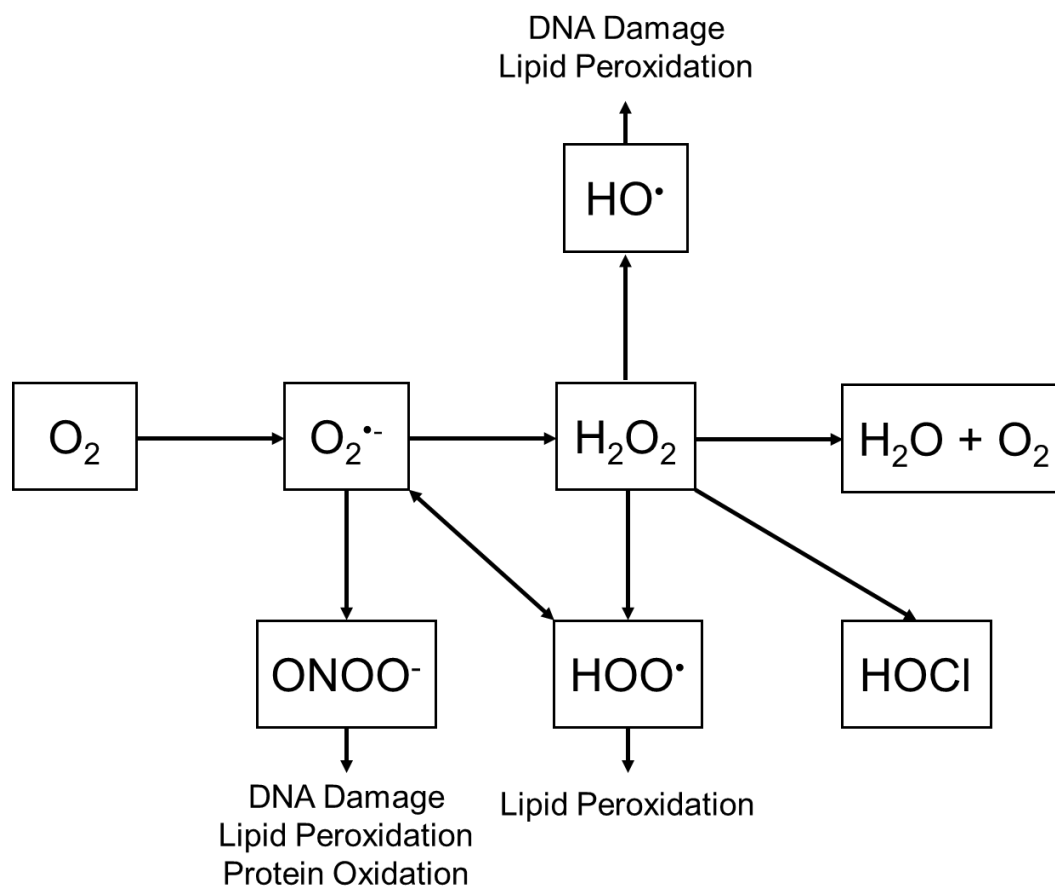


Figure 1.1. General schematic diagram of the redox cascade. Molecular oxygen (O_2) undergoes a variety of biochemical reactions to form different reactive oxygen species which can damage DNA, oxidize proteins, and cause lipid peroxidation, ultimately leading to tissue damage.

1.2 Multifunctional Antioxidants: A New Generation of Antioxidant Compounds

The frontline defense against ROS and RNS in the biological system are the endogenous antioxidants which range from small molecules to large proteins. Common small molecule antioxidants are shown in **Figure 1.2** which include glutathione [23], lipoic acid [24], α -tocopherol (Vitamin E) [25], ubiquinone (Coenzyme Q10) [26], and ascorbic acid (Vitamin C) [27]. Additionally, proteins such as superoxide dismutase [28],

glutathione peroxidase [28], catalase [28], thioredoxin [29], transferrin [30], and metallothionein [31] also participate in redox pathways.

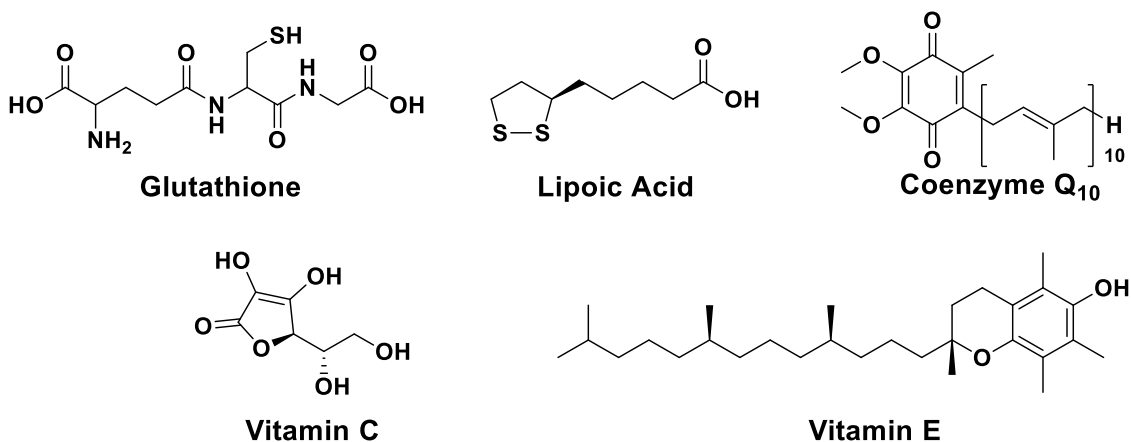


Figure 1.2. Common small molecule antioxidants. Glutathione, lipoic acid, and Coenzyme Q₁₀ are both biosynthesized endogenous antioxidants. Both vitamin C and vitamin E are essential antioxidants that support the biological antioxidant defense cycle.

The endogenous antioxidant defense systems have been found to decrease in efficacy with age [32], which is due to the age-related decreased expression of endogenous antioxidant proteins [33-35] as well as decreased biosynthesis of endogenous antioxidants [36]. Hence, exogenous anti-oxidants are a critical necessity to synergistically assist the endogenous defense system to manage and prevent cumulative age-related oxidative damage [37]. These include a wide array of compounds such as the carotenoids β -carotene and astaxanthin, the polyphenols resveratrol and quercetin, vitamin E, and vitamin C.

Antioxidants protect against oxidative damage mainly by scavenging and quenching free radicals and sequestering redox-active metals by chelation. These mechanisms ensure the disruption of the redox cascade caused by free radicals and can

lead to the repair of molecules damaged by free radicals if administered early enough. Commercially available antioxidants generally work under the mechanism of free radical scavenging, and many research formulations have included chelators or protein mimetics that can decrease specific ROS interactions with bio-active transition metals [38, 39].

In order to be effective, these antioxidants must be administered at high enough concentrations to deliver to the appropriate site of action. However, the delivery of these antioxidants should not exceed maximum therapeutic concentrations or minimum toxic concentrations which varies depending on the antioxidant [40]. Surpassing the antioxidant therapeutic threshold shifts the beneficial anti-oxidative properties to detrimental pro-oxidative ones, which consequently exacerbates oxidative stress and propagates the pathological processes that were intended to be mitigated. This phenomenon has been documented to occur with Vitamin C [41, 42], quercetin [43], beta-carotene [44], and Vitamin E [45].

Despite the reported protective effects on antioxidant supplementation in basic research, the clinical use of antioxidants has unfortunately had limited success [46]. The lack of clinical benefit is likely due to critical components of drug delivery: absorption, distribution, metabolism, and excretion (ADME). Antioxidants used in clinical trials were not chosen based on potency, but rather on ease of accessibility and administration (*i.e.*, oral agents) [47]. A meta-analysis of seven randomized trials of vitamin E treatment and of eight trials of beta-carotene treatment indicated there were no cardiovascular or mortality benefits of supplementation [48]. Moreover, supplementation with beta-carotene led to a small, but significant increase in cardiovascular deaths, suggesting its long-term supplementation may be harmful [49, 50]. Similarly, although ROS-mediated cardiac injury is implicated in the development of heart failure, antioxidant supplement trials in

heart failure patients have been disappointing and a meta-analysis concluded that vitamin E may contribute to the development or aggravation of heart failure [51]. Furthermore, daily ingestion of vitamin C and E abrogated exercise-related enhancement of insulin sensitivity [52], and the HDL-raising effects of nicotinic acid was blunted with high-dose vitamin E [53].

Mounting evidence suggests that diets rich in fruits and vegetables are associated with a lower incidence of various disease pathologies [54, 55], such as cardiovascular disease [56] and neurodegenerative disease [57]. Studies have also examined whether dietary antioxidants could mitigate the damaging effects of ROS [58, 59], and a recent meta-analysis reported that adherence to diets rich in fruits and vegetables reduce the risk of all-cause mortality [60]. Moreover, there is evidence that consumption of whole foods is better than isolated food components such as dietary supplements and nutraceuticals. For instance, increased consumption of carotenoid-rich fruits and vegetables offered better protective effects than carotenoid dietary supplements by increasing LDL-oxidation resistance, lowering DNA damage, and inducing higher DNA repair activity [61, 62].

Studies indicate that antioxidant supplements as oral agents do not result in significant protective effects, but antioxidant-rich diets with fruits and vegetables can reduce overall mortality and improve health [55, 63]. This suggests that the delivery platform (*i.e.*, food versus pill) affects the ADME properties of antioxidants [64]. Importantly, antioxidant efficacy is not just a delivery platform problem. If the antioxidant reacts before it can reach its target tissue, it can no longer quench free radicals causing oxidative damage. Therefore, antioxidant efficacy is also a distribution problem. Topical skin formulations highlight the importance of both delivery route and appropriate distribution/tissue targeting. When delivered to the appropriate site of action, significant

therapeutic effects have been observed, both by patients and their dermatologists, with topical skin formulations containing 5% Vitamin C against photo-aging [65, 66]. None of the systemically administered antioxidants tested in clinical trials have been site-specific (*i.e.*, targeted), which supports that both the poor delivery to, and un-targeted distribution of, antioxidants may account for the lack of clinical efficacy. If these barriers to delivery can be overcome, antioxidants have the potential to become potent therapeutic modalities against age-related diseases such as cardiovascular disease, cancer, cataract, and Alzheimer's [67]. Therapeutic potential can be maximized if a molecule is site-specific, stable in-transit, potent, and contains multiple antioxidant mechanisms to combat the overproduction of ROS or RNS.

Our laboratory has developed a novel class of compounds called the multifunctional antioxidants (MFAOs). These MFAOs use the innovative therapeutic strategy of integrating two independent functional motifs, a free radical scavenging moiety (FRS) and a transition metal chelating moiety (CHL), into one molecule to maximize their therapeutic efficacy against oxidative stress. Because the MFAOs both scavenge free radicals and independently sequester and re-distribute free bio-active transition metals, they are superior to compounds which only scavenge free radicals or only bind to bio-active transition metals. The scaffolds of these compounds (**Figure 1.3**, top row) possess a similar central amine-based skeleton with varying "top ring" modifications which include either a piperazine, pyrrolidine, or piperidine system. Each of the top ring moieties are conjugated to the 1,3-pyrimidine "bottom ring" at its 2-position.

The first JHX-series of MFAOs were developed based on an *in vivo* study which demonstrated that oral administration of the nonfunctional parent (NF), JHX-1, delayed the progression of diabetic cataracts without reducing the levels of hyperglycemia or lens

polyols [68]. The second series of MFAOs, known as the HK-series, replaced the piperazine “top-ring” with either a pyrrolidine or piperidine to increase compound lipophilicity, thereby increasing the likelihood of compound delivery into the brain. Moreover, these modifications also decreased compound susceptibility to the acid- or base-catalyzed decomposition of their respective imide derivatives (**Figure 1.3**, second row). Compared to the piperazine-2,6-dione of the JHX-series, both the pyrrolidine-2,5-dione (succinimide) and piperidine-2,6-dione (glutarimide) of the HK-series are less likely to be hydrolyzed in acidic or basic conditions due to their increased lipophilic profiles [69].

Unlike other small molecule antioxidants which contain phenolic moieties that scavenge ROS, the MFAOs contain the 2-amino-5-hydroxypyrimidine moiety. The incorporation of nitrogen atoms into the aromatic ring of the phenolic compounds was found to significantly increase antioxidant potency [70]. Compared to phenols, 5-hydroxypyrimidine possesses a greater O-H bond dissociation energy and oxidation potential while maintaining similar or higher reactivity towards ROS [70-72]. This means they are less susceptible to auto-oxidation while maintaining their specific mechanism of ROS-scavenging action. This specific system increases the inherent stability of the antioxidant and the probability that the antioxidant will be delivered to the desired site of action. Additionally, many compounds containing the 5-hydroxypyrimidine moiety have been reported as anti-inflammatory and cytoprotective, with targets including lipoxygenases and cyclooxygenases [73]. This suggests that these compounds may also have a targeted mechanism of action. These two ring systems were combined, and the scaffolds were modified to create four functional derivatives (**Figure 1.3**, last row) which include a nonfunctional parent (NF), a monofunctional free radical scavenger (FRS), a monofunctional bio-active transition metal chelator (CHL), and a multifunctional antioxidant (MFAO). Mechanistically, the NF derivative contains no known antioxidative

properties. The para-hydroxyl group on the pyrimidine bottom ring of the monofunctional FRS derivative allows for the quenching of radical-propagated reactions, and the CHL derivative includes an imide functionality on the top ring that can sequester bio-active transition metals and prevent the Fenton reaction. The MFAO combines both the FRS and CHL functionalities into one molecule.

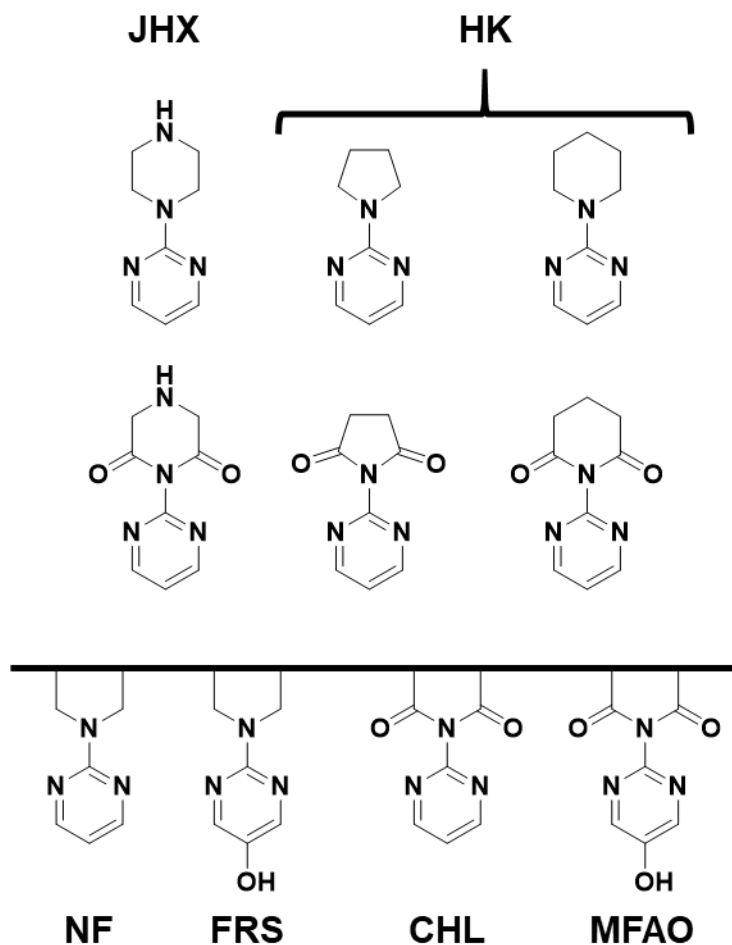


Figure 1.3. MFAO compound scaffolds and their monofunctional and nonfunctional analog derivatives. The first row of compounds shows the scaffolds for the nonfunctional parent (NF) and the free radical scavenging (FRS) derivatives, while the second row of compounds shows the scaffold for the transition metal chelating (CHL) and multifunctional (MFAO) derivatives. These scaffolds are further elaborated in the last row. Compared to the NF, the monofunctional FRS contains a para-hydroxyl group on the pyrimidine bottom ring and the monofunctional CHL contains the two carbonyl groups adjacent to the central amine. The MFAO combines both FRS and CHL functionalities into one molecule.

1.3 Multifunctional Antioxidants are Protective *In Vitro* and *In Vivo* After Oral Administration

The JHX-series demonstrated protective effects *in vitro* against ROS in SRA-1 lens epithelial cells and ARPE-19 retinal pigmented epithelial cells, both of which are believed to be instrumental in the development of cataract and age-related macular degeneration, respectively [74]. Furthermore, the oral administration of the JHX MFAOs to Sprague Dawley and Long-Evans rats significantly delayed the progression of diabetic cataracts and cataracts induced by gamma-irradiation, respectively [75]. Moreover, these compounds also protected the retina of dark-adapted Wistar rats against light-induced retinal injury, further suggesting that the MFAOs may be effective candidates for preventative therapy of age-related macular degeneration [76].

The HK-series also demonstrated protective effects against ROS in various human neural cell lines such as the SH-SY5Y neuroblastoma and the ARPE-19 retinal pigmented epithelial cells [69]. These compounds prevented manganese-induced mitochondrial dysfunction *in vitro* in the same cell lines and removed zinc from amyloid β :zinc complexes, allowing for the degradation of plaques by matrix metalloproteinase-2 [77]. Furthermore, in stoichiometric studies *via* Job plot (method of continuous variation), the HK-series were found to selectively bind redox-active iron, copper, zinc, and manganese, but not calcium or magnesium [69]. These results are similar to reported results for the JHX-series [74].

Little is known of the molecular characteristics required to cross the various physiological barriers in the eye. Dr. Hiroyoshi Kawada conducted preliminary biodistribution studies in mice which compared MFAO drug distributions into the lens, neural retina, and brain (the specific MFAOs examined are shown in **Figure 1.4**). These

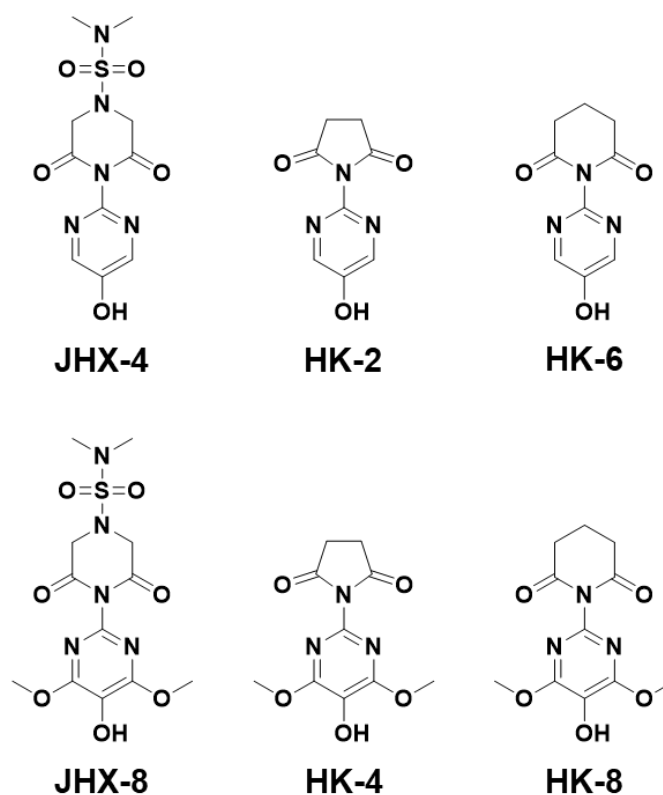


Figure 1.4. The JHX and HK series MFAOs. These compounds combine the mechanisms of the free radical scavenging moiety (5-hydroxyl on the bottom ring) and metal binding (imide moiety on the top ring) monofunctional analogs into one molecule.

compounds were orally administered and, after whole body perfusion, their levels were analyzed to investigate drug permeability across the blood-aqueous barrier (BAB), blood-retinal barrier (BRB), and blood-brain barrier (BBB). It has been generally assumed that drug accumulation in the lens requires a certain level of lipophilicity that also allowed for passage into the brain. However, the results from this study observed the opposite effects where lipophilicity was directly proportional with brain levels but inversely proportional with lens levels. The HK-series was found in greater level in the brain than the JHX-series, but the JHX-series was found in greater levels in the lens than the HK-series. Both MFAO classes were found in similar levels in the neural retina. These results confirmed that lipophilicity is required for drugs to penetrate the BBB for entry into the brain. Contrary to

previous assumptions, these results also showed that lipophilicity decreases the likelihood of a compound to penetrate the BAB and enter the lens. Finally, these results suggested that the mechanisms required for BRB passage extended past simple hydrophilic/lipophilic properties of the small molecules.

Drug delivery to specific ocular tissues is a major challenge because the factors required for the uptake and ocular distributions of drugs remain largely undefined, and our preliminary work demonstrated that brain accumulation was not related to lens accumulation. Previous studies investigated drug permeability through these physiological barriers as well, however these drugs were administered intravenously [78] which presents a significant barrier to their clinical feasibility. Oral administration is the preferred route as it represents the most convenient and non-invasive route of ocular drug delivery, while concurrently holding high potential for patient compliance. Our preliminary study was, to our knowledge, the first conducted in examining drug levels in both ocular and neural tissues after oral administration of a drug [69]. We have expanded on Dr. Kawada's preliminary results with more detailed studies in rats, whose eyes are larger than mice. In Chapter 2, we demonstrate the distribution of all 24 MFAOs, their monofunctional FRS and CHL analogs, and NF parents, to various ocular, neural, and visceral tissues including the cornea, iris with the ciliary body (iris/CB), lens, neural retina (NR), retinal pigmented epithelium with the choroid (RPE/C), brain, sciatic nerve (SN), kidney, and liver.

The MFAOs have also been tested in other neurodegenerative pathologies such as blast-induced retinal injury and noise-induced hearing loss. Both pathologies are strongly linked to oxidative stress where inflammation, mitochondrial dysfunction, and cellular apoptosis are common [79, 80]. Studies using an acoustic blast overpressure

(ABO) model for retinal injury in rats pre-fed with the MFAO JHX-4, or an enriched diet containing 2% cholesterol, vitamins C & E, and sodium selenite, found varying degrees of protection between the antioxidants. This study suggests that protective mechanisms are dependent on the antioxidant type (JHX-4 as a MFAO or an enriched diet), as well as the number of blast exposures (single or double). Both diets protected against loss of spatial frequency and contrast sensitivity to varying extents. The JHX-4 diet group exhibited significant spatial frequency protection in the post-4-month single-blast group (compared to control), whereas both diet groups exhibited significant spatial frequency protection compared to control in the double-blast group. Additionally, both diet groups were protective of contrast sensitivity for the single-blast group but provided no contrast sensitivity protection in the double-blast group [81]. Similarly, studies using a high-intensity noise exposure system simulating workday noise exposure was employed as a model for noise-induced hearing loss (NIHL). The oral administration of the MFAO HK-2 prevented the decline of summing potential amplitude, compound action potential amplitude, and cochlear hair cell loss of rodents, suggesting neuroprotective effects presumably due to ROS quenching [82].

1.4 Mitochondrial Targeting of Multifunctional Antioxidants as a Potential Therapeutic Avenue for Ocular and Neural Diseases

Neural tissues depend on mitochondrial function to establish membrane excitability and execute the complex processes of neurotransmission and neuroplasticity. The retina has one of the highest metabolic demands, and thus, the highest mitochondrial density of any tissue in the body [83]. The mitochondria play central roles in ATP production, intracellular calcium signaling, and the generation of ROS, all of which are increased in the retina. The majority of intracellular ROS is generated in the mitochondria

by the electron transport chain [84]. This generates not only superoxide, but also hydrogen peroxide, peroxy radicals, and hydroxyl radicals (**Figure 1.1**). Additionally, the mitochondria are a source of iron-sulfur clusters that are used by proteins throughout the cell in various critical processes [85]. The post-transcriptional system that mammalian cells use to regulate gene expression depends on iron-sulfur cluster-containing proteins and environmental signals such as oxygen, free iron levels, and ROS levels [86]. Hence, proper mitochondrial function is crucial for neuronal cell homeostasis [87].

Mitochondria-generated ROS are major mediators of age-associated cellular damage. With age, the antioxidant enzyme activity in the mitochondria decreases [88, 89]. The subsequent increased levels of ROS can damage aging mitochondria which may induce mutations and decrease mitochondrial DNA integrity and functionality. Mitochondrial dysfunction has been linked to multiple neurodegenerative pathologies, including retinal degenerations. Mitochondrial dysfunction may also initiate and/or contribute to iron dysregulation, which is seen as an increase in free iron concentration during the neurodegenerative processes [87, 90]. Because mitochondria are vital intracellular organelles for neuronal cell function and survival, many investigators have advocated for mitochondrial dysfunction as a target for ocular neurodegenerative diseases which include glaucoma and age-related macular degeneration [91-93]. Targeting the mitochondria with pharmacological agents that protect against oxidative stress or promote the repair of mitochondrial DNA damage offers new therapeutic avenues for the treatment of retinal degeneration [94]. Moreover, targeting mitochondria in ocular tissues is not limited to neural cells. Experimental evidence also supports targeting mitochondrial dysfunction in retinal pigmented epithelial cells as a strategy for combating age-related macular degeneration [92].

To combat mitochondrial dysfunction, two main classes of mitochondria-targeted compounds have shown promise. The first class of compounds are called *mitochondria-targeted peptides* and contain both natural and synthetic amino acid-based mitochondria targeting sequences which carry hydrophobic and positively-charged residues. An example of such a peptide includes a group known as the Szeto-Schiller (SS) series which were designed to deliver dimethyl-tyrosine as an antioxidant motif to the mitochondria [95]. These SS peptides can accumulate at the inner mitochondrial membrane (IMM) and readily cross cell membranes in an energy-independent manner, thereby increasing their potency as antioxidants [96]. The SS peptides have been reported to protect the mitochondria from oxidative damage, suggesting they can scavenge ROS and RNS, and inhibit lipid peroxidation due to their aromatic tyrosine residues [97].

To protect these peptides from enzymatic cleavage, the D-isomer of arginine was incorporated. Furthermore, the peptide amino acid sequence, hydrophobicity, and overall charge for efficient mitochondrial penetration were extensively investigated [98]. Based on positive pre-clinical results, an SS peptide successfully made its way into clinical trials. Elamipretide, also known as SS-31 (**Figure 1.5**), is a small mitochondrially-targeted tetrapeptide with the sequence (*D*-Arg-dimethylTyr-Lys-Phe-NH₂) that has been shown to reduce the production of ROS in the IMM and stabilize cardiolipin, a diphosphatidyl-glycerol lipid which participates in a variety of mitochondrial survival pathway mechanisms [99]. Though Elamipretide has obtained orphan drug designation for use in mitochondrial myopathy, it did not meet primary end-goals in a Phase III clinical trial.

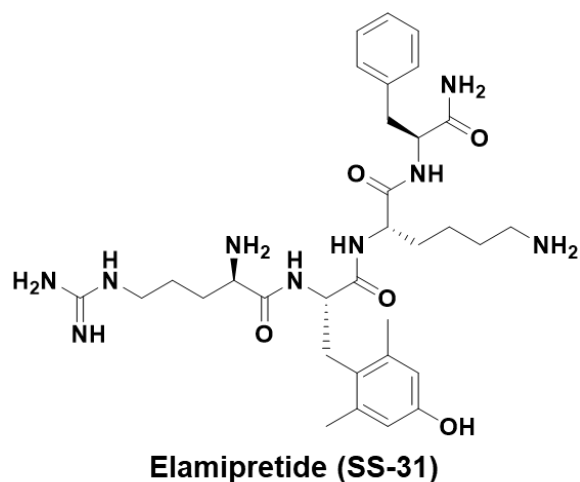


Figure 1.5. The structure of Elamipretide (also known as SS-31 or MT-131). It is a small mitochondrially-targeted tetrapeptide that has been reported to reduce mitochondrial ROS and stabilize cardiolipin.

1.4.1 Targeting of Mitochondria through Linkage to Triphenylphosphonium Lipophilic

Cations

Triphenylphosphonium-based (TPP-based) modifications of molecules for targeting mitochondria is not a novel concept. Abundant literature exists documenting the potent biological effects exhibited by small molecules containing TPP [100]. TPP cations conjugated to alkyl chain linkers were initially used as probes to study and determine mechanisms of coupling the mitochondrial membrane potential and oxidative phosphorylation. The use of TPP-conjugated bio-active molecules was refined by M. Murphy when his group delivered TPP-based probes and antioxidants to mitochondria [101]. Since Murphy, many groups have synthesized novel mitochondria-targeted cationic compounds to traffic into the mitochondrial matrix and/or membranes. Typically, the molecules with active moieties (*i.e.*, free radical scavenging system) are conjugated to a linker sequence, generally an alkyl chain, which is conjugated to the lipophilic, charge-delocalized TPP moiety. Depending on the length of the linker alkyl chain, the compound's

lipophilicity, cellular uptake, and site of mitochondrial sequestration can be modulated [102, 103]. Examples of these molecules are shown in **Figure 1.6**.

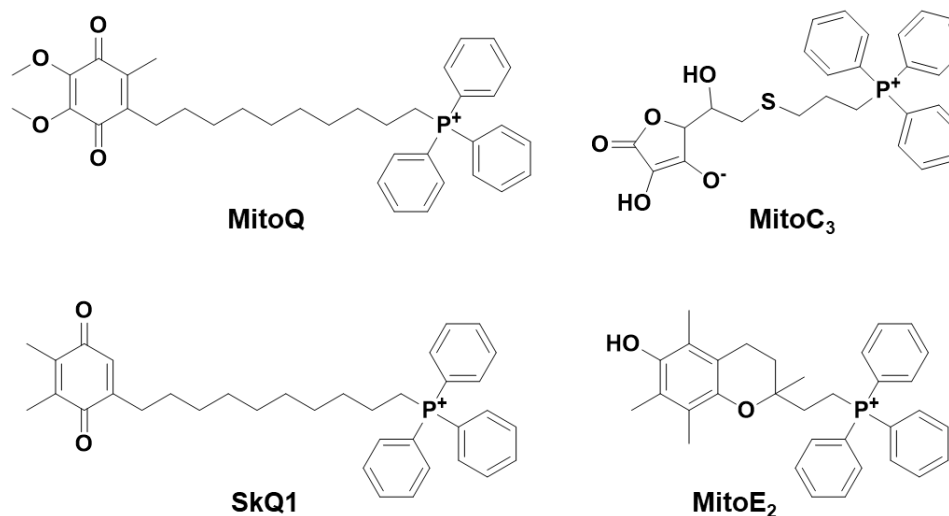


Figure 1.6. Common TPP-derived mitochondrial antioxidants. Depending on the antioxidant, different alkyl chain lengths were found to optimize activity while minimizing toxicity. MitoQ, the mammalian-based ubiquinone derivative, and SkQ1, the plant-based plastoquinone derivative, are derivatives of molecules found in the electron transport chain and currently in clinical trials. MitoC₃, a vitamin C derivative, and MitoE₂, a vitamin E derivative, have also been developed but have not progressed past animal studies.

Two TPP compounds have shown promise in clinical trials: MitoQ and SkQ1. *MitoQ*, developed by R. Smith and M. Murphy in the 1990s, is the most extensively studied and best understood TPP-derived compound. It is an ubiquinone derivative with a C10-linker that has been investigated because of its known endogenous antioxidant activity in the electron transport chain. Not only is MitoQ taken up rapidly by mitochondria, which is driven by the membrane potential, but nearly all of it is adsorbed to the matrix surface of the inner membrane [104-106]. The ubiquinol form of MitoQ is the active antioxidant, which is oxidized to the ubiquinone form and then rapidly re-reduced by complex II, restoring its antioxidant efficacy [105]. As MitoQ is largely found adsorbed to the mitochondrial inner membrane, and its linker chain has been reported to enable its active

ubiquinol antioxidant component to penetrate deeply into the membrane core, it was anticipated that it may be an effective antioxidant against lipid peroxidation which has been confirmed in isolated mitochondria [104]. Clinical trials on MitoQ have demonstrated that it can be formulated into an effective pharmaceutical that can be successfully delivered orally to humans, including a safety profile of up to a year of use in patients [107]. These findings also suggest that orally administered MitoQ and related mitochondria-targeted antioxidants may also be applicable to the wide range of human pathologies that involve mitochondrial oxidative damage.

SkQ1, developed by V. Skulachev in the 2000s, is a novel compound comprising of a plant-derived plastoquinone moiety with a C10-linked TPP head group. It was synthesized for a multi-national collaboration project to study and prevent cellular senescence [108]. Studies of *SkQ1* showed that it protected the mitochondria from a wide array of stressors in various human-derived cells and was able to act as a “rechargeable” antioxidant in the mitochondria like MitoQ [109-114]. Clinical trials of *SkQ1* indicated that it was safe and efficacious in treating dry eye by increasing corneal tear film stability, reducing corneal damage, and alleviating symptoms of dryness, burning, grittiness, and blurred vision, in addition to its anti-inflammatory effects [115-117].

The results from both mechanistic research and clinical trials for MitoQ and *SkQ1* suggest a viable avenue for developing mitochondrially-targeted antioxidants. Though ubiquinone and plastoquinone showed therapeutic merit, they are mono-functional antioxidants which only quench ROS through the mechanism of free radical scavenging activity. Furthermore, the phenol moiety, which is present on both MitoQ and *SkQ1*, is prone to auto-oxidation. Therefore, we investigated the possibility of targeting our MFAOs to the mitochondria through conjugation of the TPP lipophilic cation. We hypothesized

that the activity of our MFAOs can be enhanced by directly targeting mitochondrial dysfunction, thereby specifically delivering a drug to the greatest source of cellular ROS. The multifunctional compounds, especially JHX-4 and HK-2 (**Figure 1.4**), have shown the most therapeutic merit for neural disease pathologies affected by ROS. The addition of a TPP lipophilic cation is likely to increase their efficacy by improving their targeting capability directly to the mitochondria, thereby decreasing the necessary dose to achieve the same, or enhanced, therapeutic outcomes compared to the traditional, non-TPP MFAOs.

1.5 Overview

The following chapters of this dissertation investigate various aspects of the drug development process with the MFAOs. Investigations into the biodistribution of the pre-existing MFAOs, their monofunctional FRS and CHL analogs, and their NF parents in various ocular, neural, and visceral tissues are reported in Chapter 2. Multiple predictive models investigating the biological activity of the 24 compounds (*i.e.*, experimentally determined tissue levels) against several calculated physicochemical descriptors were developed using both hierarchical cluster analysis (HCA) and quantitative structure activity relationship (QSAR) methods, resulting in the first ever published predictive models of ocular tissue deliver of orally-administered drugs in Chapter 3. Molecular modeling studies, *in vitro* lens cultures, and *in vitro* binding studies in Chapter 4 examine the feasibility of oxysterol and MFAO binding against the lens protein α B-crystallin, which is reported to play a major role in cataractogenesis. Finally, progress towards the synthesis of the JHX-series triphenylphosphonium (TPP) derivatives and their preliminary *in vitro* investigations in HEI-OC1 cells are explored in Chapter 5.

1.6 References

1. Weismann, A., *Essays upon hereditary and kindred biological problems*. Oxford, Clarendon press, 1889.
2. Medawar, P., *An unsolved problem of Biology*. 1952: London: H.K Lewis.
3. Fabian, D.F., T., *The Evolution of Aging*. Nature Education Knowledge, 2011. **2**(11): p. 9.
4. Harman, D., *Aging: a theory based on free radical and radiation chemistry*. J Gerontol, 1956. **11**(3): p. 298-300.
5. Sacher, G.A., *Evaluation of the Entropy and Information Terms Governing Mammalian Longevity*. Cellular Ageing: Concepts and Mechanisms. Part I: General Concepts. Mechanisms I: Fidelity of Information Flow., ed. R.G. Cutler. Vol. 9. 1976, Basel: Karger.
6. Tolmasoff, J.M., T. Ono, and R.G. Cutler, *Superoxide dismutase: correlation with life-span and specific metabolic rate in primate species*. Proc Natl Acad Sci U S A, 1980. **77**(5): p. 2777-81.
7. Munkres, K.D. and C.A. Furtek, *Linkage of conidial longevity determinant genes in Neurospora crassa*. Mechanisms of Ageing and Development, 1984. **25**(1): p. 63-77.
8. Sohal, R.S., P.L. Toy, and R.G. Allen, *Relationship between life expectancy, endogenous antioxidants and products of oxygen free radical reactions in the housefly, Musca domestica*. Mechanisms of Ageing and Development, 1986. **36**(1): p. 71-77.
9. Matsuo, M., *Age-related alterations in antioxidant defense*. Free Radicals in Aging, ed. B.P. Yu. 1993: CRC Press, Boca Raton.

10. Sohal, R.S.O., W.C., *Is oxidative stress a causal factor in aging?* Molecular Aspects of Aging, ed. K.M. Esser, G.M. 1995, Chichester: Wiley. 107-127.
11. McCay, C.M., M.F. Crowell, and L.A. Maynard, *The effect of retarded growth upon the length of life span and upon the ultimate body size.* 1935. Nutrition, 1989. **5**(3): p. 155-71; discussion 172.
12. Anderson, R.M. and R. Weindruch, *The caloric restriction paradigm: implications for healthy human aging.* American journal of human biology : the official journal of the Human Biology Council, 2012. **24**(2): p. 101-106.
13. Sosa, V., et al., *Oxidative stress and cancer: an overview.* Ageing Res Rev, 2013. **12**(1): p. 376-90.
14. Asmat, U., K. Abad, and K. Ismail, *Diabetes mellitus and oxidative stress—A concise review.* Saudi Pharmaceutical Journal, 2016. **24**(5): p. 547-553.
15. Moris, D., et al., *The role of reactive oxygen species in the pathophysiology of cardiovascular diseases and the clinical significance of myocardial redox.* Annals of translational medicine, 2017. **5**(16): p. 326-326.
16. Andersen, J.K., *Oxidative stress in neurodegeneration: cause or consequence?* Nature Medicine, 2004. **10**(7): p. S18-S25.
17. Ohira, A., et al., *[Oxidative stress in ocular disease].* Nippon Ganka Gakkai Zasshi, 2008. **112**(1): p. 22-9.
18. Kruk, J., K. Kubasik-Kladna, and H.Y. Aboul-Enein, *The Role Oxidative Stress in the Pathogenesis of Eye Diseases: Current Status and a Dual Role of Physical Activity.* Mini Rev Med Chem, 2015. **16**(3): p. 241-57.
19. Belenguer-Varea, A., et al., *Oxidative stress and exceptional human longevity: Systematic review.* Free Radic Biol Med, 2020. **149**: p. 51-63.

20. Ahmad, R., Z. Rasheed, and H. Ahsan, *Biochemical and cellular toxicology of peroxynitrite: implications in cell death and autoimmune phenomenon*. Immunopharmacol Immunotoxicol, 2009. **31**(3): p. 388-96.
21. Pratt, D.A., K.A. Tallman, and N.A. Porter, *Free radical oxidation of polyunsaturated lipids: New mechanistic insights and the development of peroxy radical clocks*. Acc Chem Res, 2011. **44**(6): p. 458-67.
22. Klebanoff, S.J., et al., *Myeloperoxidase: a front-line defender against phagocytosed microorganisms*. J Leukoc Biol, 2013. **93**(2): p. 185-98.
23. Forman, H.J., H. Zhang, and A. Rinna, *Glutathione: overview of its protective roles, measurement, and biosynthesis*. Mol Aspects Med, 2009. **30**(1-2): p. 1-12.
24. Moini, H., L. Packer, and N.E. Saris, *Antioxidant and prooxidant activities of alpha-lipoic acid and dihydrolipoic acid*. Toxicol Appl Pharmacol, 2002. **182**(1): p. 84-90.
25. Traber, M.G. and J. Atkinson, *Vitamin E, antioxidant and nothing more*. Free Radic Biol Med, 2007. **43**(1): p. 4-15.
26. Liu, H.T., et al., *Effects of coenzyme Q10 supplementation on antioxidant capacity and inflammation in hepatocellular carcinoma patients after surgery: a randomized, placebo-controlled trial*. Nutr J, 2016. **15**(1): p. 85.
27. Padayatty, S.J., et al., *Vitamin C as an antioxidant: evaluation of its role in disease prevention*. J Am Coll Nutr, 2003. **22**(1): p. 18-35.
28. Ighodaro, O.M. and O.A. Akinloye, *First line defence antioxidants-superoxide dismutase (SOD), catalase (CAT) and glutathione peroxidase (GPX): Their fundamental role in the entire antioxidant defence grid*. Alexandria Journal of Medicine, 2018. **54**(4): p. 287-293.
29. Lu, J. and A. Holmgren, *The thioredoxin antioxidant system*. Free Radic Biol Med, 2014. **66**: p. 75-87.

30. Pacht, E.R. and W.B. Davis, *Role of transferrin and ceruloplasmin in antioxidant activity of lung epithelial lining fluid*. J Appl Physiol (1985), 1988. **64**(5): p. 2092-9.
31. Viarengo, A., et al., *Antioxidant role of metallothioneins: a comparative overview*. Cell Mol Biol (Noisy-le-grand), 2000. **46**(2): p. 407-17.
32. Cutler, R.G., *Antioxidants and aging*. Am J Clin Nutr, 1991. **53**(1 Suppl): p. 373s-379s.
33. Miao, L. and D.K. St Clair, *Regulation of superoxide dismutase genes: implications in disease*. Free Radic Biol Med, 2009. **47**(4): p. 344-56.
34. Kodydkova, J., et al., *Human catalase, its polymorphisms, regulation and changes of its activity in different diseases*. Folia Biol (Praha), 2014. **60**(4): p. 153-67.
35. Lubos, E., J. Loscalzo, and D.E. Handy, *Glutathione peroxidase-1 in health and disease: from molecular mechanisms to therapeutic opportunities*. Antioxid Redox Signal, 2011. **15**(7): p. 1957-97.
36. Ballatori, N., et al., *Glutathione dysregulation and the etiology and progression of human diseases*. Biol Chem, 2009. **390**(3): p. 191-214.
37. Fusco, D., et al., *Effects of antioxidant supplementation on the aging process*. Clin Interv Aging, 2007. **2**(3): p. 377-87.
38. Vrailas-Mortimer, A., et al., *A survey of the protective effects of some commercially available antioxidant supplements in genetically and chemically induced models of oxidative stress in Drosophila melanogaster*. Exp Gerontol, 2012. **47**(9): p. 712-22.
39. Villegas, L.R., et al., *Superoxide dismutase mimetic, MnTE-2-PyP, attenuates chronic hypoxia-induced pulmonary hypertension, pulmonary vascular*

- remodeling, and activation of the NALP3 inflammasome. Antioxid Redox Signal*, 2013. **18**(14): p. 1753-64.
40. Bouayed, J. and T. Bohn, *Exogenous antioxidants--Double-edged swords in cellular redox state: Health beneficial effects at physiologic doses versus deleterious effects at high doses. Oxid Med Cell Longev*, 2010. **3**(4): p. 228-37.
 41. Nadežda, B., et al., *Concentration-Dependent Antioxidant/Pro-Oxidant Activity of Ascorbic Acid in Chickens. Proceedings of the Latvian Academy of Sciences. Section B. Natural, Exact, and Applied Sciences.*, 2012. **66**(6): p. 256-260.
 42. Seo, M.Y. and S.M. Lee, *Protective effect of low dose of ascorbic acid on hepatobiliary function in hepatic ischemia/reperfusion in rats. J Hepatol*, 2002. **36**(1): p. 72-7.
 43. Zhang, F.F., et al., *[Effects of kaempferol and quercetin on cytochrome 450 activities in primarily cultured rat hepatocytes]. Zhejiang Da Xue Xue Bao Yi Xue Ban*, 2006. **35**(1): p. 18-22.
 44. Young, A.J. and G.M. Lowe, *Antioxidant and prooxidant properties of carotenoids. Arch Biochem Biophys*, 2001. **385**(1): p. 20-7.
 45. Kontush, A., et al., *Antioxidant and prooxidant activity of alpha-tocopherol in human plasma and low density lipoprotein. J Lipid Res*, 1996. **37**(7): p. 1436-48.
 46. A, M.D. and G.H. A, *Why antioxidant therapies have failed in clinical trials. J Theor Biol*, 2018. **457**: p. 1-5.
 47. Steinhubl, S.R., *Why have antioxidants failed in clinical trials? Am J Cardiol*, 2008. **101**(10a): p. 14d-19d.
 48. Vivekananthan, D.P., et al., *Use of antioxidant vitamins for the prevention of cardiovascular disease: meta-analysis of randomised trials. Lancet*, 2003. **361**(9374): p. 2017-23.

49. Omenn, G.S., et al., *Risk factors for lung cancer and for intervention effects in CARET, the Beta-Carotene and Retinol Efficacy Trial*. J Natl Cancer Inst, 1996. **88**(21): p. 1550-9.
50. *The effect of vitamin E and beta carotene on the incidence of lung cancer and other cancers in male smokers*. N Engl J Med, 1994. **330**(15): p. 1029-35.
51. Thomson, M.J., M.P. Frenneaux, and J.C. Kaski, *Antioxidant treatment for heart failure: friend or foe?* Qjm, 2009. **102**(5): p. 305-10.
52. Ristow, M., et al., *Antioxidants prevent health-promoting effects of physical exercise in humans*. Proc Natl Acad Sci U S A, 2009. **106**(21): p. 8665-70.
53. Cheung, M.C., et al., *Antioxidant supplements block the response of HDL to simvastatin-niacin therapy in patients with coronary artery disease and low HDL*. Arterioscler Thromb Vasc Biol, 2001. **21**(8): p. 1320-6.
54. Boeing, H., et al., *Critical review: vegetables and fruit in the prevention of chronic diseases*. European journal of nutrition, 2012. **51**(6): p. 637-663.
55. Slavin, J.L. and B. Lloyd, *Health benefits of fruits and vegetables*. Advances in nutrition (Bethesda, Md.), 2012. **3**(4): p. 506-516.
56. Joshipura, K.J., et al., *The effect of fruit and vegetable intake on risk for coronary heart disease*. Ann Intern Med, 2001. **134**(12): p. 1106-14.
57. Martin, A., et al., *Roles of vitamins E and C on neurodegenerative diseases and cognitive performance*. Nutr Rev, 2002. **60**(10 Pt 1): p. 308-26.
58. Huang, D., *Dietary Antioxidants and Health Promotion*. Antioxidants (Basel), 2018. **7**(1).
59. Yashin, A., et al., *Antioxidant Activity of Spices and Their Impact on Human Health: A Review*. Antioxidants (Basel), 2017. **6**(3).
60. Jayedi, A., et al., *Dietary Antioxidants, Circulating Antioxidant Concentrations, Total Antioxidant Capacity, and Risk of All-Cause Mortality: A Systematic Review*

- and Dose-Response Meta-Analysis of Prospective Observational Studies.* Advances in Nutrition, 2018. **9**(6): p. 701-716.
61. Southon, S., *Increased fruit and vegetable consumption: potential health benefits.* Nutr Metab Cardiovasc Dis, 2001. **11**(4 Suppl): p. 78-81.
 62. Seifried, H.E., et al., *The antioxidant conundrum in cancer.* Cancer Res, 2003. **63**(15): p. 4295-8.
 63. Pem, D. and R. Jeewon, *Fruit and Vegetable Intake: Benefits and Progress of Nutrition Education Interventions- Narrative Review Article.* Iranian journal of public health, 2015. **44**(10): p. 1309-1321.
 64. Holecek, V., R. Rokyta, and R. Vlasak, *[Antioxidants and their gastrointestinal absorption and interferences of their effects].* Cesk Fysiol, 2008. **57**(1): p. 24-32.
 65. Humbert, P.G., et al., *Topical ascorbic acid on photoaged skin. Clinical, topographical and ultrastructural evaluation: double-blind study vs. placebo.* Exp Dermatol, 2003. **12**(3): p. 237-44.
 66. Oresajo, C., et al., *Antioxidants and the skin: understanding formulation and efficacy.* Dermatol Ther, 2012. **25**(3): p. 252-9.
 67. Belikov, A.V., *Age-related diseases as vicious cycles.* Ageing Res Rev, 2019. **49**: p. 11-26.
 68. Kador, P.F., J. Inoue, and K. Blessing, *Anticataract activity of analogs of a sorbitol dehydrogenase inhibitor.* J Ocul Pharmacol Ther, 2004. **20**(4): p. 333-44.
 69. Kawada, H. and P.F. Kador, *Orally Bioavailable Metal Chelators and Radical Scavengers: Multifunctional Antioxidants for the Coadjutant Treatment of Neurodegenerative Diseases.* J Med Chem, 2015. **58**(22): p. 8796-805.
 70. Pratt, D.A., et al., *5-Pyrimidinols: novel chain-breaking antioxidants more effective than phenols.* J Am Chem Soc, 2001. **123**(19): p. 4625-6.

71. Valgimigli, L., et al., *3-Pyridinols and 5-pyrimidinols: Tailor-made for use in synergistic radical-trapping co-antioxidant systems*. Beilstein J Org Chem, 2013. **9**: p. 2781-92.
72. Valgimigli, L., et al., *The effect of ring nitrogen atoms on the homolytic reactivity of phenolic compounds: understanding the radical-scavenging ability of 5-pyrimidinols*. Chemistry, 2003. **9**(20): p. 4997-5010.
73. Walker, F.J., U.P.a.T. Office, Editor. 1991: USA.
74. Jin, H., et al., *Multifunctional antioxidants for the treatment of age-related diseases*. J Med Chem, 2010. **53**(3): p. 1117-27.
75. Randazzo, J., et al., *Orally active multi-functional antioxidants delay cataract formation in streptozotocin (type 1) diabetic and gamma-irradiated rats*. PLoS One, 2011. **6**(4): p. e18980.
76. Randazzo, J., et al., *Orally active multi-functional antioxidants are neuroprotective in a rat model of light-induced retinal damage*. PLoS One, 2011. **6**(7): p. e21926.
77. Kawada, H., et al., *Effects of multifunctional antioxidants on mitochondrial dysfunction and amyloid-beta metal dyshomeostasis*. J Alzheimers Dis, 2015. **44**(1): p. 297-307.
78. Toda, R., et al., *Comparison of drug permeabilities across the blood-retinal barrier, blood-aqueous humor barrier, and blood-brain barrier*. J Pharm Sci, 2011. **100**(9): p. 3904-11.
79. Khatri, N., et al., *Oxidative Stress: Major Threat in Traumatic Brain Injury*. CNS Neurol Disord Drug Targets, 2018. **17**(9): p. 689-695.
80. Henderson, D., et al., *The role of oxidative stress in noise-induced hearing loss*. Ear Hear, 2006. **27**(1): p. 1-19.

81. al., M.e., *The Effect of Antioxidant- and Vitamin-Enriched Diets on Vision in Rats Exposed to Primary Blast Injury*. 2018: Biomedical Engineering Society.
82. Chen, G.D., et al., *Novel oral multifunctional antioxidant prevents noise-induced hearing loss and hair cell loss*. *Hear Res*, 2020. **388**: p. 107880.
83. Wong-Riley, M.T., *Energy metabolism of the visual system*. *Eye Brain*, 2010. **2**: p. 99-116.
84. Balaban, R.S., S. Nemoto, and T. Finkel, *Mitochondria, oxidants, and aging*. *Cell*, 2005. **120**(4): p. 483-95.
85. Rouault, T.A., *Biogenesis of iron-sulfur clusters in mammalian cells: new insights and relevance to human disease*. *Dis Model Mech*, 2012. **5**(2): p. 155-64.
86. Mettert, E.L. and P.J. Kiley, *Fe-S proteins that regulate gene expression*. *Biochim Biophys Acta*, 2015. **1853**(6): p. 1284-93.
87. Horowitz, M.P. and J.T. Greenamyre, *Mitochondrial iron metabolism and its role in neurodegeneration*. *J Alzheimers Dis*, 2010. **20 Suppl 2**: p. S551-68.
88. Barja, G., *Updating the mitochondrial free radical theory of aging: an integrated view, key aspects, and confounding concepts*. *Antioxid Redox Signal*, 2013. **19**(12): p. 1420-45.
89. Indo, H.P., et al., *A mitochondrial superoxide theory for oxidative stress diseases and aging*. *J Clin Biochem Nutr*, 2015. **56**(1): p. 1-7.
90. Barot, M., M.R. Gokulgandhi, and A.K. Mitra, *Mitochondrial dysfunction in retinal diseases*. *Curr Eye Res*, 2011. **36**(12): p. 1069-77.
91. Osborne, N.N., C.N. Alvarez, and S. del Olmo Aguado, *Targeting mitochondrial dysfunction as in aging and glaucoma*. *Drug Discov Today*, 2014. **19**(10): p. 1613-22.
92. Terluk, M.R., et al., *Investigating mitochondria as a target for treating age-related macular degeneration*. *J Neurosci*, 2015. **35**(18): p. 7304-11.

93. Chhetri, J. and N. Gueven, *Targeting mitochondrial function to protect against vision loss*. *Expert Opin Ther Targets*, 2016. **20**(6): p. 721-36.
94. Jarrett, S.G., et al., *Mitochondrial DNA damage and its potential role in retinal degeneration*. *Prog Retin Eye Res*, 2008. **27**(6): p. 596-607.
95. Szeto, H.H., *Mitochondria-targeted peptide antioxidants: novel neuroprotective agents*. *Aaps j*, 2006. **8**(3): p. E521-31.
96. Szeto, H.H., *Cell-permeable, mitochondrial-targeted, peptide antioxidants*. *Aaps j*, 2006. **8**(2): p. E277-83.
97. Pang, Y., C. Wang, and L. Yu, *Mitochondria-Targeted Antioxidant SS-31 is a Potential Novel Ophthalmic Medication for Neuroprotection in Glaucoma*. *Med Hypothesis Discov Innov Ophthalmol*, 2015. **4**(3): p. 120-6.
98. Szeto, H.H., *First-in-class cardiolipin-protective compound as a therapeutic agent to restore mitochondrial bioenergetics*. *Br J Pharmacol*, 2014. **171**(8): p. 2029-50.
99. Ren, M., C.K. Phoon, and M. Schlame, *Metabolism and function of mitochondrial cardiolipin*. *Prog Lipid Res*, 2014. **55**: p. 1-16.
100. Zielonka, J., et al., *Mitochondria-Targeted Triphenylphosphonium-Based Compounds: Syntheses, Mechanisms of Action, and Therapeutic and Diagnostic Applications*. *Chemical reviews*, 2017. **117**(15): p. 10043-10120.
101. Murphy, M.P., *Targeting lipophilic cations to mitochondria*. *Biochim Biophys Acta*, 2008. **1777**(7-8): p. 1028-31.
102. Khailova, L.S., et al., *Uncoupling and Toxic Action of Alkyltriphenylphosphonium Cations on Mitochondria and the Bacterium *Bacillus subtilis* as a Function of Alkyl Chain Length*. *Biochemistry (Mosc)*, 2015. **80**(12): p. 1589-97.
103. Reily, C., et al., *Mitochondrially targeted compounds and their impact on cellular bioenergetics*. *Redox Biol*, 2013. **1**(1): p. 86-93.

104. Kelso, G.F., et al., *Selective targeting of a redox-active ubiquinone to mitochondria within cells: antioxidant and antiapoptotic properties*. J Biol Chem, 2001. **276**(7): p. 4588-96.
105. James, A.M., et al., *Interaction of the mitochondria-targeted antioxidant MitoQ with phospholipid bilayers and ubiquinone oxidoreductases*. J Biol Chem, 2007. **282**(20): p. 14708-18.
106. Ross, M.F., et al., *Rapid and extensive uptake and activation of hydrophobic triphenylphosphonium cations within cells*. Biochem J, 2008. **411**(3): p. 633-45.
107. Rossman, M.J., et al., *Chronic Supplementation With a Mitochondrial Antioxidant (MitoQ) Improves Vascular Function in Healthy Older Adults*. Hypertension (Dallas, Tex. : 1979), 2018. **71**(6): p. 1056-1063.
108. Skulachev, V.P., et al., *An attempt to prevent senescence: a mitochondrial approach*. Biochim Biophys Acta, 2009. **1787**(5): p. 437-61.
109. Skulachev, M.V. and V.P. Skulachev, *Programmed Aging of Mammals: Proof of Concept and Prospects of Biochemical Approaches for Anti-aging Therapy*. Biochemistry (Mosc), 2017. **82**(12): p. 1403-1422.
110. Skulachev, V.P., *A biochemical approach to the problem of aging: "megaproject" on membrane-penetrating ions. The first results and prospects*. Biochemistry (Mosc), 2007. **72**(12): p. 1385-96.
111. Skulachev, V.P., et al., *Prevention of cardiolipin oxidation and fatty acid cycling as two antioxidant mechanisms of cationic derivatives of plastoquinone (SkQs)*. Biochim Biophys Acta, 2010. **1797**(6-7): p. 878-89.
112. Neroev, V.V., et al., *Mitochondria-targeted plastoquinone derivatives as tools to interrupt execution of the aging program. 4. Age-related eye disease. SkQ1 returns vision to blind animals*. Biochemistry (Mosc), 2008. **73**(12): p. 1317-28.

113. Adlam, V.J., et al., *Targeting an antioxidant to mitochondria decreases cardiac ischemia-reperfusion injury*. *Faseb j*, 2005. **19**(9): p. 1088-95.
114. Agapova, L.S., et al., *Mitochondria-targeted plastoquinone derivatives as tools to interrupt execution of the aging program. 3. Inhibitory effect of SkQ1 on tumor development from p53-deficient cells*. *Biochemistry (Mosc)*, 2008. **73**(12): p. 1300-16.
115. Brzheskiy, V.V., et al., *Results of a Multicenter, Randomized, Double-Masked, Placebo-Controlled Clinical Study of the Efficacy and Safety of Visomitin Eye Drops in Patients with Dry Eye Syndrome*. *Adv Ther*, 2015. **32**(12): p. 1263-79.
116. Lemp, M.A., *Advances in understanding and managing dry eye disease*. *Am J Ophthalmol*, 2008. **146**(3): p. 350-356.
117. Zinovkin, R.A., et al., *Role of mitochondrial reactive oxygen species in age-related inflammatory activation of endothelium*. *Aging (Albany NY)*, 2014. **6**(8): p. 661-74.

CHAPTER 2

Biodistribution of Multifunctional Antioxidants, Their Monofunctional Free Radical Scavenging and Chelating Analogs, and Nonfunctional Parents After Oral Administration

2.1 Summary

The tissue distribution of N,N-dimethyl-4-(pyrimidin-2-yl)piperazine-1-sulfonamide, 2-(pyrrolidin-1-yl)pyrimidine, 2-(piperidin-1-yl)pyrimidine, and their respective analogs possessing either free radical scavenger groups (FRS), chelating groups (CHL), or both as a multifunctional antioxidant (MFAO) were administered to 200-gram Sprague Dawley rats by mixing 0.05% of each compound into rodent chow. After 7 days of feeding, the rats (n = 8 per group) were terminally perfused with phosphate-buffered saline and the biodistribution of these compounds were determined in ocular tissues including the cornea, iris with the ciliary body (iris/CB), lens, neural retina (NR), retinal pigmented epithelium with the choroid (RPE/C), brain, sciatic nerve (SN), kidney, and liver. Each tissue was extracted, their protein concentration determined using the Bradford assay, and drug levels analyzed by HPLC-MS. Oral administration showed that the unmetabolized levels of these compounds were present in all tissues examined. While no obvious trends in the biodistribution data was evident, separating compounds by functional group indicated that the highest quantity of monofunctional CHL analogs were present in the cornea while the MFAOs, which possesses both CHL and FRS activity, distributed in highest quantity to the neural retina.

2.2 Introduction

Ocular drug delivery continues to be a major challenge for pharmacologists and drug delivery scientists because the main mechanisms for drug distribution and uptake into the eye remain largely undefined [1]. The access of drugs to ocular structures through the route of systemic administration is greatly hindered by the presence of two physiological barriers, the blood-aqueous barrier (BAB) and the blood-retinal barrier (BRB), that separate the eye from general circulation. Successful oral ocular drug delivery depends on the ability of the drug to pass through these barriers [2-4]. Unfortunately, this often requires high doses of systemically administered drugs in order to reach therapeutic concentrations in the internal structures of the eye which can increase potential side effects due to systemic toxicity [5].

Topical administration is considered the most suitable route of administration to the anterior chamber of the eye. This is because the ocular surface is easily accessible, especially regarding pathologies affecting the anterior segment [6, 7]. However, conventional topical ophthalmic formulations have low ocular bioavailability because of dilution caused by constant physiologic lacrimal secretion and losses due to rapid drainage away from the ocular surface [8]. To improve topical administration in the anterior segment, several methods for sustained drug release have been studied such as nanoparticles [9-11], nanosuspensions [12-14], liposomes [15-17], dendrimers [18-20], hydrogels [21-23], and contact lenses [24-26]. Even with the rise in novel ophthalmic drug delivery systems, the basic understanding of major factors associated with drug targeting to specific intraocular tissues remain unknown.

Other common routes of drug delivery to the eye include intravitreal, periocular, subretinal, and suprachoroidal injections [27]. However, the invasiveness and risks associated with injectable administrations, as well as the diversity of factors affecting biodistribution, limit clinical ocular pharmacokinetic research [28]. Appropriate and effective patient-compliant treatments are still an unmet medical need. This is especially evident with the aging population through which an increase of irreversible visual impairments has been documented such as cataract, glaucoma, and macular degeneration [29].

Little is known about the ocular biodistribution of orally-administered drugs. Our laboratory previously developed three orally-active MFAOs and experimentally demonstrated that these MFAOs were able to independently scavenge reactive oxygen species (ROS) and chelate bio-active transition metals [30, 31], protect the lens against ROS generated by gamma irradiation, UV light, and ER stress [32], protect the retina and photoreceptor layer against light-induced retinal degeneration in an age-related macular degeneration (AMD) rat model [33], and prevent the formation of neurotoxic amyloid β :zinc complexes in the lens, retina, and brain of transgenic Alzheimer's mice [34]. Recently, two of these MFAOs were also shown to protect against blast-induced retinal function loss [35] and against noise-induced hearing loss [36]. A preliminary biodistribution study of all six MFAOs was conducted in mice to examine levels of drug in the lens, retina, and brain. In this study, it was found that the hydrophilic JHX-series of MFAOs distributed in greater levels to the lens, while the lipophilic HK-series of MFAOs distributed in greater levels to the brain. Both JHX and HK compounds were observed in similar levels in the retina[37].

This chapter extends these preliminary investigations from mice to Sprague Dawley rats. Not only are the eyes of the rats larger compared to mice, but various tissues

of the eye can be more easily dissected and extracted. In this study, all 24 compounds (**Figure 2.1**) which included the MFAOs, their monofunctional free radical scavengers (FRS) and transition metal chelators (CHL), as well as their nonfunctional parents (NF) were orally administered at 0.05 wt% in rat chow for seven days. The unmetabolized levels of these compounds were measured in various ocular, neural, and visceral tissues including the cornea, iris with the ciliary body (iris/CB), lens, neural retina (NR), retinal pigmented epithelium with the choroid (RPE/C), brain, sciatic nerve (SN), kidney, and liver. Because the JHX and HK drugs have similar structures and functions, it was hypothesized that similar trends would be observed between the drug classes to tissues requiring penetration through the blood-aqueous barrier (BAB), blood-retinal barrier (BRB), blood-brain barrier (BBB), and blood-nerve barrier (BNB). Our results indicated that various trends can be identified depending on distribution data division.

2.3 Methods

Animal Care. All procedures were performed according to the ARVO Statement for the Use of Animals in Ophthalmic and Vision Research, as well as the University of Nebraska Medical Center Guidelines for Animals in Research.

Bioavailability in Rats. The bioavailability study was conducted using Sprague Dawley rats (male, 200-gram, n = 8 per group, 24 groups) with rat chow containing 0.05 wt% of one of the 24 MFAO or analog compounds (**Figure 2.1**). The compounds, dissolved in either acetone or ethanol, were sprayed onto rat chow and mixed, followed by removal of solvent at 50 °C for 1 hour in an oven. The compounds were stable under these conditions.

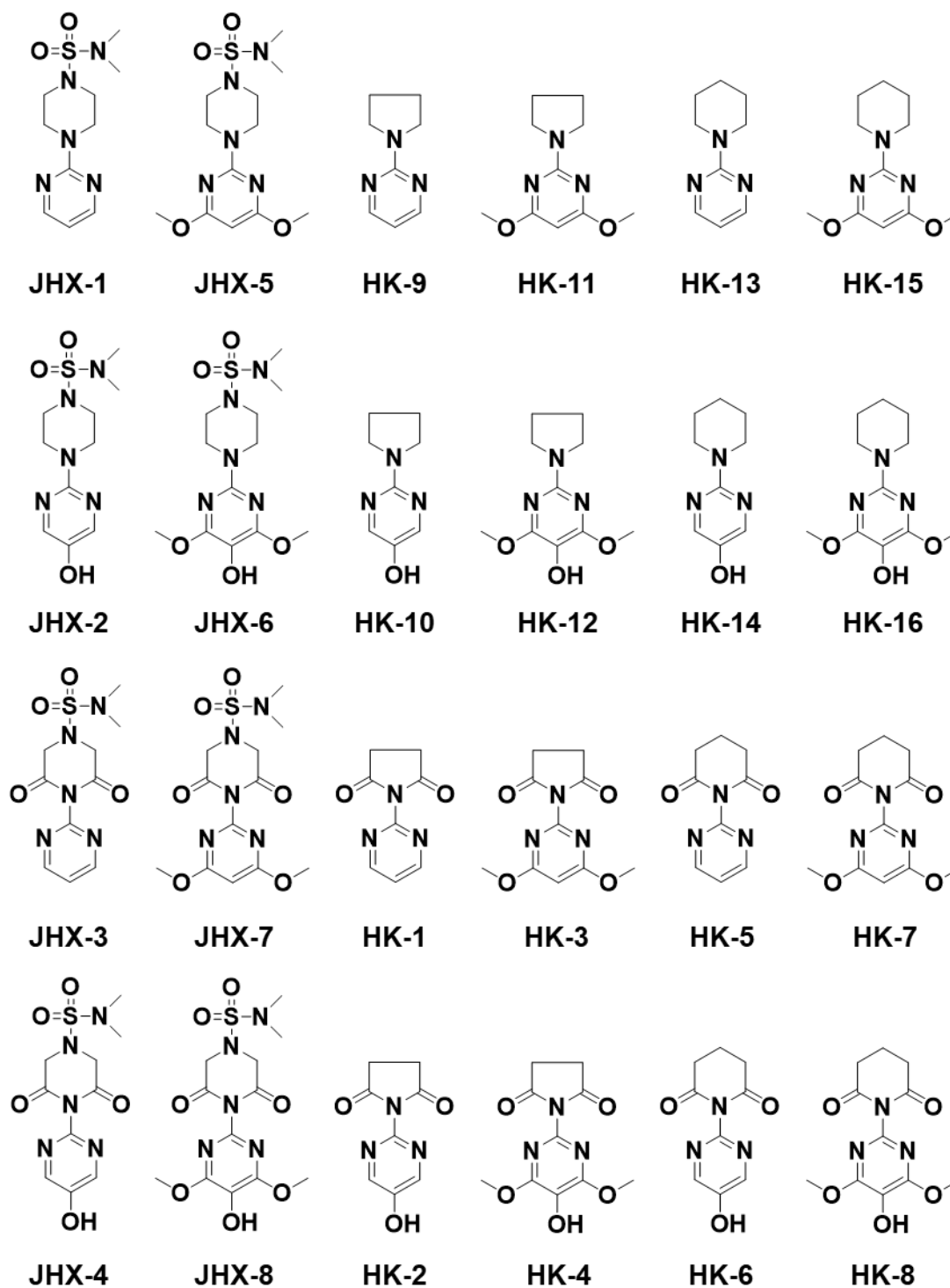


Figure 2.1. The 24 orally-active analogs of N,N-dimethyl-4-(pyrimidin-2-yl)piperazine-1-sulfonamide, 2-(pyrrolidine-1-yl)pyrimidine, and 2-(piperidine-1-yl)pyrimidine. The compounds are separated into their nonfunctional parent (first row), free radical scavenging (FRS) analog (second row), chelating analog (third row), and multifunctional analog (bottom row).

Rats were housed as follows: either groups of 2 or 3 per cage. Rats had free access to food and water and were kept on a 12-hour day/night cycle. Food consumption studies, measured at the beginning and end of the 7-day feeding period, indicated that each rat received an average daily dose of 46.2 ± 2.2 mg drug/kg body weight.

After 7 days, each rat was placed under isoflurane anesthesia followed by a terminal trans-cardial perfusion. The chest wall was opened, and the rib cage was cracked open to expose the heart. The hepatic portal vein was sliced (terminal site of perfusion), and a 60-mL syringe filled with 1X phosphate-buffered saline with a 22-gauge needle was inserted into the left ventricle and slowly injected. Upon completion of perfusion, which was monitored by bloodless, clear liquid flowing out of the hepatic portal vein, both eyes were enucleated followed by removal of the top lobe of the liver, one kidney (randomly), and one sciatic nerve (randomly). The head was then decapitated via guillotine and the whole brain was removed. The brain, kidney, liver, and sciatic nerve were placed in labeled 15 mL polypropylene centrifuge tubes and stored at -80 °C until homogenization. The eyes of the rats were immediately dissected at the ora serrata to separate the anterior and posterior segments. From the anterior segment, the cornea, iris and ciliary body (Iris/CB), and lens were carefully removed. From the posterior segment, the neural retina (NR) and the posterior globe containing the retinal pigmented epithelium with the choroid (RPE/C) were carefully removed. All ocular tissues were placed in labeled 1.5 mL Eppendorf tubes and stored at -80 °C until homogenization.

Determination of Drug Levels in the Ocular, Neural, and Visceral Tissues.

The left and right cornea, iris/CB, NR, RPE/C, and SN of four rats were combined. These combined organs, as well as the left and right lenses, half brain, and segments of the kidney and liver were homogenized using ground glass homogenizers in 10 mM acetate

buffer, pH 4, and 10 μ L of 10 mM JHX-5 or JHX-1 in acetonitrile as an internal standard. Total sample volumes were as follows: 1 mL for cornea, iris/CB, and NR; 2 mL for RPE/C, SN, and lens; 3 mL for brain, kidney, and liver. Following centrifugation at 5,000 \times g for 15 minutes (Sorvall RC-5B PLUS, Thermo Fisher Scientific, Waltham, MA) at 25 $^{\circ}$ C, the supernatant was transferred to a clean test tube. The protein concentrations were determined according to Bradford [38] from a 10 μ L aliquot directly from the supernatant for the cornea, iris/CB, NR, RPE/C, and SN, a 10 μ L aliquot to 290 μ L dilution of liver supernatant, a 10 μ L aliquot to 200 μ L dilution of lens and kidney supernatant, and a 10 μ L aliquot to 75 μ L dilution of brain supernatant. Dilutions were conducted using double distilled water. The remaining supernatants were then de-proteinized with 1 mL of 20% trichloroacetic acid (TCA). Following additional centrifugation at 15,000 \times g for 30 minutes at 25 $^{\circ}$ C, each supernatant was transferred by pipette to a clean conical vial and dried *in vacuo* on Speedvac (Savant Speed Vac Plus SC210A, Thermo Fisher Scientific, Waltham, MA) for 5 hours at 25 $^{\circ}$ C. Each remaining residue containing both the extracted compound and internal standard was dissolved in 200 μ L of HPLC-grade acetonitrile, analyzed in triplicate by reverse-phase HPLC (HP Agilent Technologies, Series 1100, Santa Clara, CA) column (Luna 5 μ m, C18, 250 mm \times 4 mm, Phenomenex Inc., Torrance, CA), and eluted with 75% HPLC-grade aqueous methanol. The eluent was monitored by UV at 220, 254, and 280 nm and quantified by ESI-MS in either positive or negative mode on a Thermo Finnigan LCQ (Thermo Fisher Scientific, Waltham, MA).

Data Analysis. The HPLC/MS data was analyzed using the XCalibur QualBrowser program (Thermo Fisher Scientific, Waltham, MA) to determine the area under the curve. Samples were quantified against standard curves of the analyzed compounds and all analyses were conducted in triplicate. Final compound concentrations were reported in nanograms of drug per milligram of protein (ng drug/mg protein) \pm SEM.

Linear regression analysis and bar graphs were generated with OriginPro Software (OriginPro 2016, OriginLab Co., Northampton, MA).

2.4 Results

Distribution values for these compounds ranged from 0 nanograms of drug per milligram of protein (ng drug/mg protein) to nearly 3.7 milligrams of drug per milligram of protein (mg drug/mg protein). The parent HK-15 was undetectable in any ocular tissue or the brain, and both parents JHX-1 and JHX-5 were undetectable in the sciatic nerve. The levels FRS JHX-6 were found to approach 3.7 mg drug/mg protein in the cornea, while the levels of HK-2 exceeded 3.5 mg drug/mg protein in the NR and RPE/C. The feeding data revealed that consumption of HK-15 was 49 mg/kg/day, both JHX-1 and JHX-5 were 50 mg/kg/day, JHX-6 was 46 mg/kg/day, and HK-2 was 44 mg/kg/day. The results of undetectable HK-15, JHX-1, and JHX-5 were confirmed by colleagues in the Fletcher laboratory using reverse-phase HPLC-MS.

The quantified results of the biodistribution for all 24 compounds are summarized in **Table 2.1**. The data is grouped according to the physiological barriers (blood-aqueous barrier [BAB], blood-retinal barrier [BRB], blood-brain barrier [BBB], blood-nerve barrier [BNB]) that the compounds were required to traverse in order to accumulate in the tissues examined. While it was expected that similar tissue levels would be seen between the JHX and HK compounds, none were observed. However, it is evident that tissue uptake of JHX-6 and HK-2 appear to be much greater than the other compounds. To investigate whether any trends could be identified within each functional family, the compounds separated by their functional groups (*e.g.*, parent vs. FRS vs. CHL vs. MFAO).

Compound Structure	Compound	Classification	BAB		BRB		BBB	BNB		Visceral	
			Cornea	Iris/CB	Lens	Neural Retina		RPE/C	Brain	Sciatic Nerve	Kidney
	JHX-1	Parent	5067.7 ± 4675.3	2502.6 ± 1651.0	128.7 ± 58.1	5098.6 ± 4794.2	15303.0 ± 14160.0	3786.6 ± 139.0	0	26.8 ± 4.0	5.9 ± 2.0
	JHX-2	FRS	229582.6 ± 59775.9	31260.9 ± 12980.8	491.0 ± 163.2	454803.0 ± 55755.8	57874.9 ± 1607.4	23370.1 ± 1671.7	28.3 ± 5.6	174.3 ± 28.6	56.3 ± 5.4
	JHX-3	CHL	276810.9 ± 266294.2	63539.0 ± 59481.2	5734.0 ± 2747.1	113422.4 ± 108249.8	110259.4 ± 107743.9	18421.0 ± 7343.0	193.9 ± 73.3	19.0 ± 1.5	2048.9 ± 460.5
	JHX-4	MFAO	54960.5 ± 7253.3	60382.0 ± 6589.2	842.9 ± 152.1	63156.8 ± 6394.7	20728.4 ± 7975.0	21.2 ± 5.1	712.0 ± 169.4	6.6 ± 0.9	1309.3 ± 149.0
	JHX-5	Parent-OMe	62.2 ± 47.3	366.5 ± 278.3	12.3 ± 3.5	2200.9 ± 1986.2	737.7 ± 50.8	48.2 ± 14.0	0	4.8 ± 1.1	3.4 ± 0.8
	JHX-6	FRS-OMe	3675384.9 ± 2275193.8	290537.4 ± 37652.7	7481.3 ± 3768.7	526247.7 ± 386001.8	282432.7 ± 222233.1	121128.5 ± 23572.9	13830.5 ± 4799.6	2544.5 ± 344.5	1563.9 ± 264.0
	JHX-7	CHL-OMe	141893.4 ± 35657.5	99954.0 ± 10413.0	35.4 ± 9.4	56271.5 ± 26969.8	19336.5 ± 7430.4	849.3 ± 117.6	12125.9 ± 1312.7	1081.3 ± 184.8	1819.3 ± 291.4
	JHX-8	MFAO-OMe	3710.7 ± 1772.0	1882.9 ± 1408.9	15.0 ± 6.7	2938.1 ± 351.8	722.7 ± 219.7	169.3 ± 42.0	7215.6 ± 1077.1	18.1 ± 1.3	320.2 ± 43.3
	HK-9	Parent	160.0 ± 15.1	178.9 ± 134.3	48.8 ± 10.8	1221.6 ± 474.4	829.4 ± 391.2	457.8 ± 93.4	2300.7 ± 153.5	15.1 ± 6.1	34.6 ± 8.6
	HK-10	FRS	1916.7 ± 374.1	1234.9 ± 319.1	10.7 ± 1.6	323.7 ± 51.1	193.4 ± 6.7	268.4 ± 44.4	532.4 ± 60.0	2230.8 ± 505.8	904.4 ± 200.0
	HK-11	CHL	66899.5 ± 10797.3	130611.2 ± 26486.2	2324.2 ± 462.0	1644007.0 ± 409261.4	236231.7 ± 16270.0	10344.0 ± 1470.9	597.4 ± 232.4	162.7 ± 15.4	47.8 ± 4.0
	HK-12	MFAO	310281.6 ± 59428.2	200437.3 ± 1768.0	3599.2 ± 1196.4	3542362.6 ± 1086805.0	3580173.1 ± 566837.9	8535.7 ± 1960.2	25634.4 ± 3880.2	2303.4 ± 407.4	2314.1 ± 904.4
	HK-13	Parent-OMe	1038.8 ± 427.8	990.7 ± 320.2	33.5 ± 14.4	133.5 ± 35.0	478.6 ± 384.2	730.2 ± 311.9	3115.3 ± 805.9	20.9 ± 1.7	37.2 ± 12.2
	HK-14	FRS-OMe	2462.4 ± 1529.5	9580.5 ± 816.3	90.7 ± 25.8	32493.4 ± 1459.3	2818.2 ± 1392.9	560.2 ± 114.9	20291.1 ± 9365.4	1096.3 ± 243.9	135.3 ± 27.6
	HK-15	CHL-OMe	12781.5 ± 2081.1	1343.9 ± 132.7	2.9 ± 1.4	903.8 ± 497.4	180.7 ± 83.2	344.4 ± 67.9	404.0 ± 177.1	50.4 ± 16.1	1438.7 ± 461.6
	HK-16	MFAO-OMe	54.5 ± 13.8	84.3 ± 27.7	69.4 ± 34.9	3055.8 ± 955.4	712.2 ± 521.8	205.0 ± 116.8	102.3 ± 18.6	43.3 ± 14.6	28.6 ± 1.0
	HK-13	Parent	79123.4 ± 23689.5	136546.9 ± 51508.9	60.2 ± 5.7	1488.7 ± 802.0	1387.5 ± 216.6	1913.1 ± 795.0	46988.8 ± 20136.4	406.6 ± 57.8	317.0 ± 114.0
	HK-14	FRS	34938.2 ± 30793.5	8930.0 ± 5059.6	323.1 ± 190.2	44199.0 ± 33864.2	10731.5 ± 6565.1	1455.2 ± 257.2	1865.1 ± 487.1	67.0 ± 6.3	47.9 ± 6.7
	HK-5	CHL	24305.6 ± 9948.0	10917.2 ± 8743.5	123.6 ± 40.8	23310.2 ± 12589.6	4469.0 ± 815.5	2215.1 ± 591.3	10002.8 ± 1749.7	191.2 ± 6.0	107.8 ± 16.2
	HK-6	MFAO	165.1 ± 20.7	150.8 ± 23.4	2.9 ± 0.8	508.9 ± 194.5	238.9 ± 70.6	14.8 ± 1.4	244.8 ± 62.8	137.9 ± 26.0	93.5 ± 16.9
	HK-15	Parent-OMe	0	0	0	0	0	0	350.9 ± 127.4	26.2 ± 3.2	53.7 ± 14.2
	HK-16	FRS-OMe	15.2 ± 1.5	57.8 ± 3.3	1989.9 ± 1332.6	302.4 ± 73.8	632.2 ± 182.2	8209.9 ± 3081.2	30825.5 ± 10755.3	88.3 ± 10.1	375.9 ± 73.1
	HK-7	CHL-OMe	15767.7 ± 956.5	4273.2 ± 412.5	16.5 ± 4.3	11421.8 ± 2169.5	6341.0 ± 1650.7	6621.5 ± 570.0	12301.8 ± 6976.0	176.7 ± 22.5	544.4 ± 94.8
	HK-8	MFAO-OMe	65781.4 ± 13270.2	249700.1 ± 29795.0	18932.9 ± 8397.5	350382.5 ± 112067.5	90863.7 ± 36430.0	11346.3 ± 4945.6	78.2 ± 6.8	164.0 ± 30.0	563.1 ± 72.9

Table 2.1. Biodistribution summary of all compounds in the ocular, neural, and visceral tissues. All quantities are expressed in nanograms of drug per milligram of protein (ng drug/mg protein) ± SEM.

Parent: R₁, R₂, R₃ = H

Parent-OMe: R₁ and R₂ = H, R₃ = OMe

FRS: R₁ = OH, R₂ and R₃ = H

FRS-OMe: R₁ = OH, R₂ = H, R₃ = OMe

CHL: R₁ and R₃ = H, R₂ = O

CHL-OMe: R₁ = H, R₂ = O, R₃ = OMe

MFAO: R₁ = OH, R₂ = O, R₃ = H

MFAO-OMe: R₁ = OH, R₂ = O; R₃ = OMe

2.4.1 Distribution of the Nonfunctional Parent (NF) Compounds

The uptake of the parent compounds possessing no antioxidant functional groups (NF) in the eye, brain, sciatic nerve, kidney, and liver are shown in **Figure 2.2**. Tissue uptake was separated according to drug penetration through physiological barriers (BAB, BRB, BBB, BNB) or normal tissue circulation (kidney and liver). While no trends between the NFs were apparent, it was clear that the parent compounds JHX-1 and HK-13 were found in greatest levels across most tissues.

Across the tissues requiring BAB passage, the following trends were observed. The methoxy JHX-5 and HK-11 showed an overall decrease in tissue levels compared to their non-methoxy derivatives JHX-1 and HK-9, while HK-15 was absent in both the eye and brain. However, the non-methoxy HK-9 was found in higher levels in the lens compared to its methoxy derivative HK-11. Furthermore, the non-methoxy HK-13 was observed to distribute in greatest quantities to the cornea and iris/CB, followed by non-methoxy compounds JHX-1 and HK-9. In the lens, JHX-1 was found in highest concentrations followed by HK-13 and HK-9. This data suggests that the HK-13 parent scaffold may be superior for developing drugs targeted to the cornea and iris/CB, and the JHX-1 scaffold may be superior for developing drugs targeted to the lens.

A similar trend was observed among all methoxy-containing NF compounds penetrating the BRB to reach the NR and the RPE/C. Compared to the non-methoxy-containing compounds, decreased distribution concentrations was observed with the methoxy derivatives. JHX-1 was found in highest concentration in both the NR and RPE/C, while HK-11 was found in lowest concentration. HK-15 was undetectable in both

the NR and RPE/C. This suggests that JHX-1 may be the superior scaffold for developing drugs targeting the NR and RPE/C.

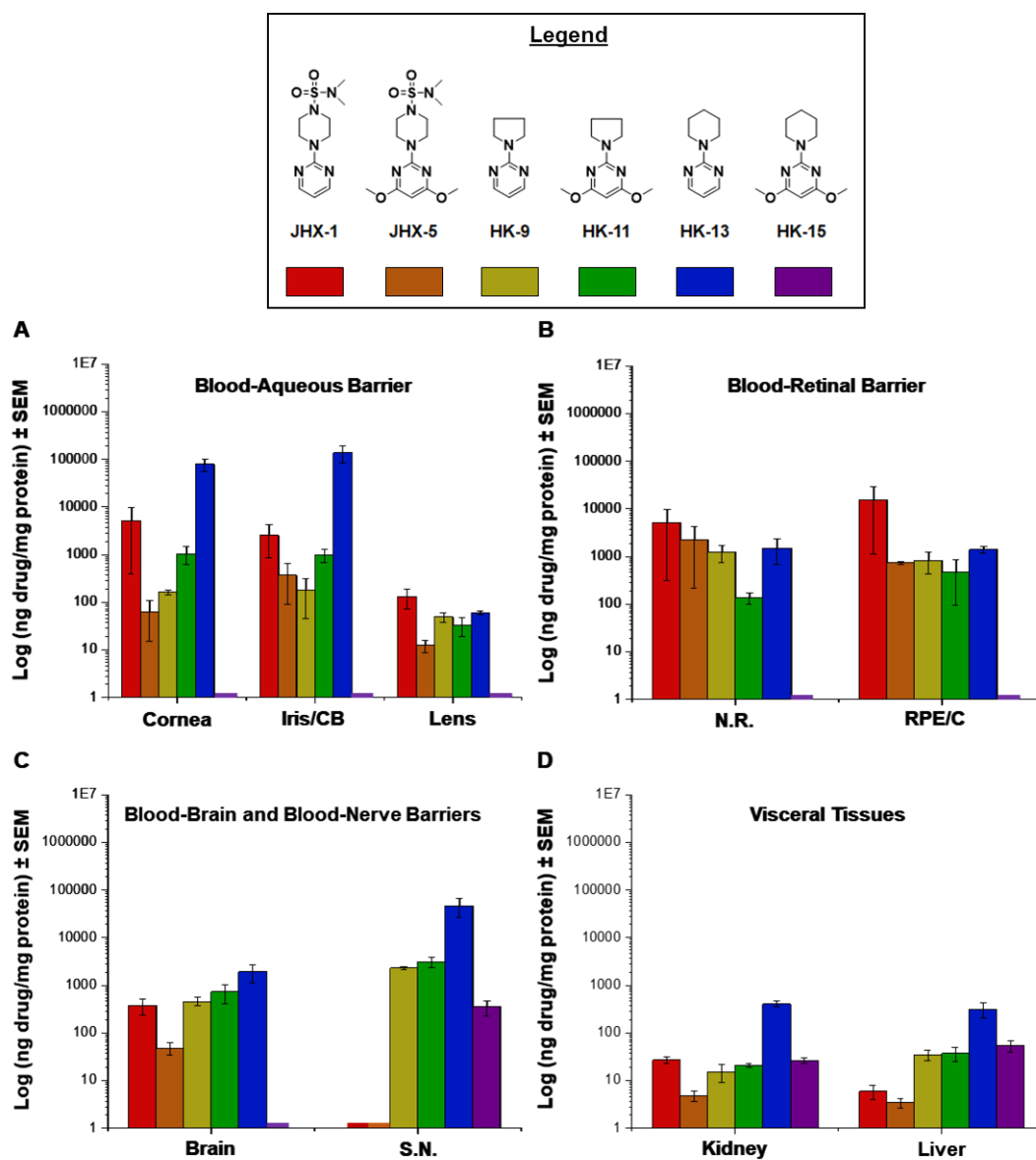


Figure 2.2. Summary of the NF drug levels to ocular, neural, and visceral tissues. The distribution of NF drugs to tissues traversing through the (A) blood-aqueous barrier, (B) blood-retinal barrier, or (C) blood-brain and blood-nerve barriers, and (D) directly into visceral tissues to reach target tissues. Drug levels are presented as the log of drug concentration in nanograms of drug per milligram of protein (\pm SEM).

For neural tissue penetration through the BBB and the BNB, a similar trend was again observed for the parent compounds. In the brain, the uptake methoxy JHX-5 was lower than the non-methoxy JHX-1, and neither JHX-1 or JHX-5 were detected in the SN. The methoxy HK-11 had slightly enhanced uptake into both the brain and sciatic nerve over the non-methoxy HK-9, and the non-methoxy HK-13 was found in highest levels in both the brain and SN. Again, HK-15 was undetectable in the brain, but present in lowest levels in the SN compared to the other NF HK compounds. This data suggests that the HK-13 parent scaffold may be superior for developing small molecules penetrating both the central and peripheral nervous system barriers.

For visceral tissues, the uptake of methoxy compounds JHX-5 and HK-15 were lower than the non-methoxy compounds JHX-1 and HK-13. The opposite trend was observed between the methoxy HK-11 and the non-methoxy HK-9. HK-13 is again found in highest levels in both the kidney and liver compared to the other NF compounds. However, compared to drug levels quantified in the ocular and neural tissues, the NF drug concentrations in both the kidney and liver are at least 1 order of magnitude lower. This is not surprising as the main roles of both the kidney and liver are to eliminate and/or metabolize drugs. More polar and hydrophilic drugs are excreted by kidneys, and those which are more lipophilic can be metabolized and/or excreted by the liver into the gastrointestinal tract through bile [39].

2.4.2 Distribution of Free Radical Scavenging Compounds

The structures and tissue levels of the free radical scavenging compounds (FRS) are shown in **Figure 2.3**. The difference between the parent (NF) compounds and the FRS compounds is the 5-hydroxyl group on the pyrimidine bottom ring.

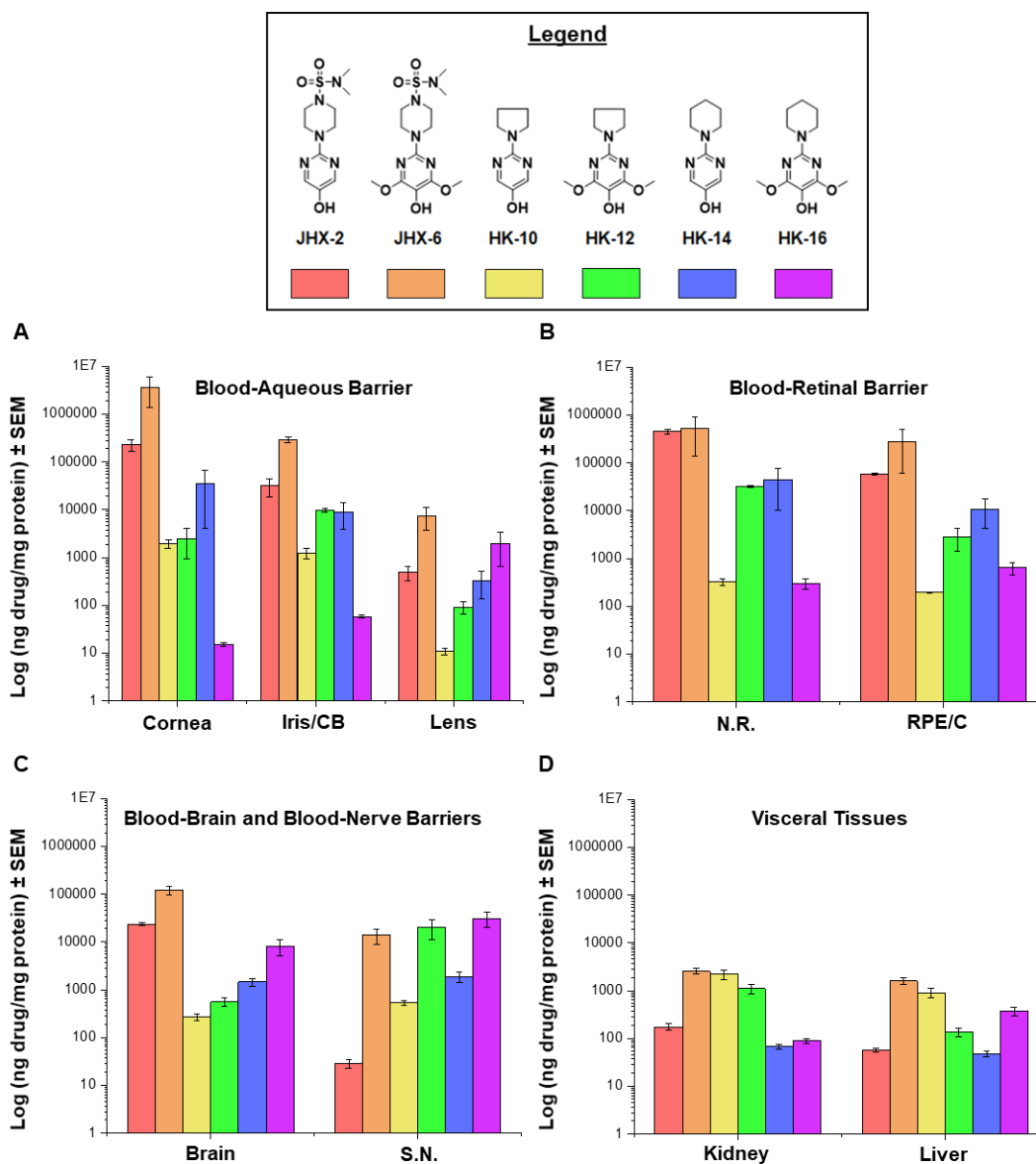


Figure 2.3. Summary of the FRS drug levels to ocular, neural, and visceral tissues. The distribution of FRS drugs to tissues traversing through the (A) blood-aqueous barrier, (B) blood-retinal barrier, or (C) blood-brain and blood-nerve barriers, and (D) directly into visceral tissues to reach target tissues. Drug levels are presented as the log of drug concentration in nanograms of drug per milligram of protein (\pm SEM).

Distribution to tissues requiring BAB penetration showed similar trends between the cornea and iris/CB. The methoxy compounds JHX-6 and HK-12 attained high tissue levels compared to their non-methoxy derivatives, and the same trend was observed between the methoxy HK-16 and non-methoxy HK-14 in the lens. Increased tissue levels

were observed by all FRS methoxy derivatives compared to their non-methoxy counterparts except between methoxy HK-16 and non-methoxy HK-14 in the cornea and iris/CB. Overall, JHX-6 was found in the highest levels among all BAB-related tissues. This contrasts with the BAB trend observed by the NFs where the greatest levels observed in the cornea and iris/CB were by the non-methoxy HK-13, and in the lens by non-methoxy JHX-1.

For drugs crossing the BRB, a similar trend was observed among all FRS compounds. Higher levels of the methoxy compounds JHX-6 and HK-12 were found compared to their non-methoxy derivatives JHX-2 and HK-10, and the opposite trend was observed between the methoxy HK-16 and the non-methoxy HK-14. Once again, JHX-6 demonstrated highest levels among all tissues with the non-methoxy JHX-2 also observed in higher levels compared to the HK compounds. This trend is similar to the observation with the NFs. While the NF non-methoxy JHX-1 was found in greatest levels in both the NR and RPE/C, both the FRS non-methoxy JHX-2 and FRS methoxy JHX-6 compounds achieved greater tissue levels than the HK compounds.

With respect to BBB and BNB penetration, the methoxy derivatives of all FRS compounds achieved higher tissue concentrations in both in the brain and sciatic nerve. The methoxy JHX-6 achieved the highest brain levels, while the methoxy HK-16 achieved the highest SN levels. This is surprising since the parent NF scaffolds for these compounds, the methoxy compounds JHX-5 and HK-15, respectively, achieved the lowest levels in the brain and SN. This observation suggests that the addition of the para-hydroxy moiety may play an important role in BBB and BNB penetration. These trends may also be due to the differences in compound lipophilicity, as it is generally assumed that drugs with greater lipophilic characteristics are more permeable through the BBB and BNB [40].

In the visceral tissues, similar trends were observed for the FRS compounds. Again, the methoxy compounds JHX-6 and HK-16 achieved higher levels compared to their non-methoxy counterparts, but the methoxy HK-12 was observed in lower levels compared to the non-methoxy HK-10. The visceral tissue levels of the NF non-methoxy HK-13 were found to be greatest, while the FRS methoxy JHX-6 was observed in greatest levels. Overall FRS levels in visceral tissues were higher than for the NF compounds. Interestingly, the non-methoxy HK-10 was observed to distribute in similar levels to certain groups of tissues. Its distribution was observed to not only be similar between the cornea, iris/CB, kidney, and liver, but also between the NR, RPE/C, brain, and SN, suggesting that HK-10 may have a good balance of both hydrophilic and lipophilic properties.

2.4.3 Distribution of Metal Binding Compounds

The structures of the transition metal binding compounds (CHL) and their tissue levels are shown in **Figure 2.4**. The difference between the CHL compound and their parent analogs are the presence of two carbonyl groups adjacent to the nitrogen conjugated to the pyrimidine bottom ring (*i.e.*, an imide functionality). For the JHX-series, this is called a piperazine-2,6-dione moiety; for the five-membered HK-series, a succinimide moiety; for the six-membered HK-series, a glutarimide moiety.

In tissues requiring transport through the BAB, the trends appear to be similar for the HK compounds. Lower tissue concentrations are observed for the methoxy derivatives compared to their non-methoxy analogs. For the JHX compounds, this trend was observed in the cornea and the lens, but not in the iris/CB. These trends differed from those observed for the NF compounds except in the lens. The non-methoxy JHX-3

achieved the highest levels in the cornea and lens, while the non-methoxy HK-1 achieved highest concentrations in the iris/CB.

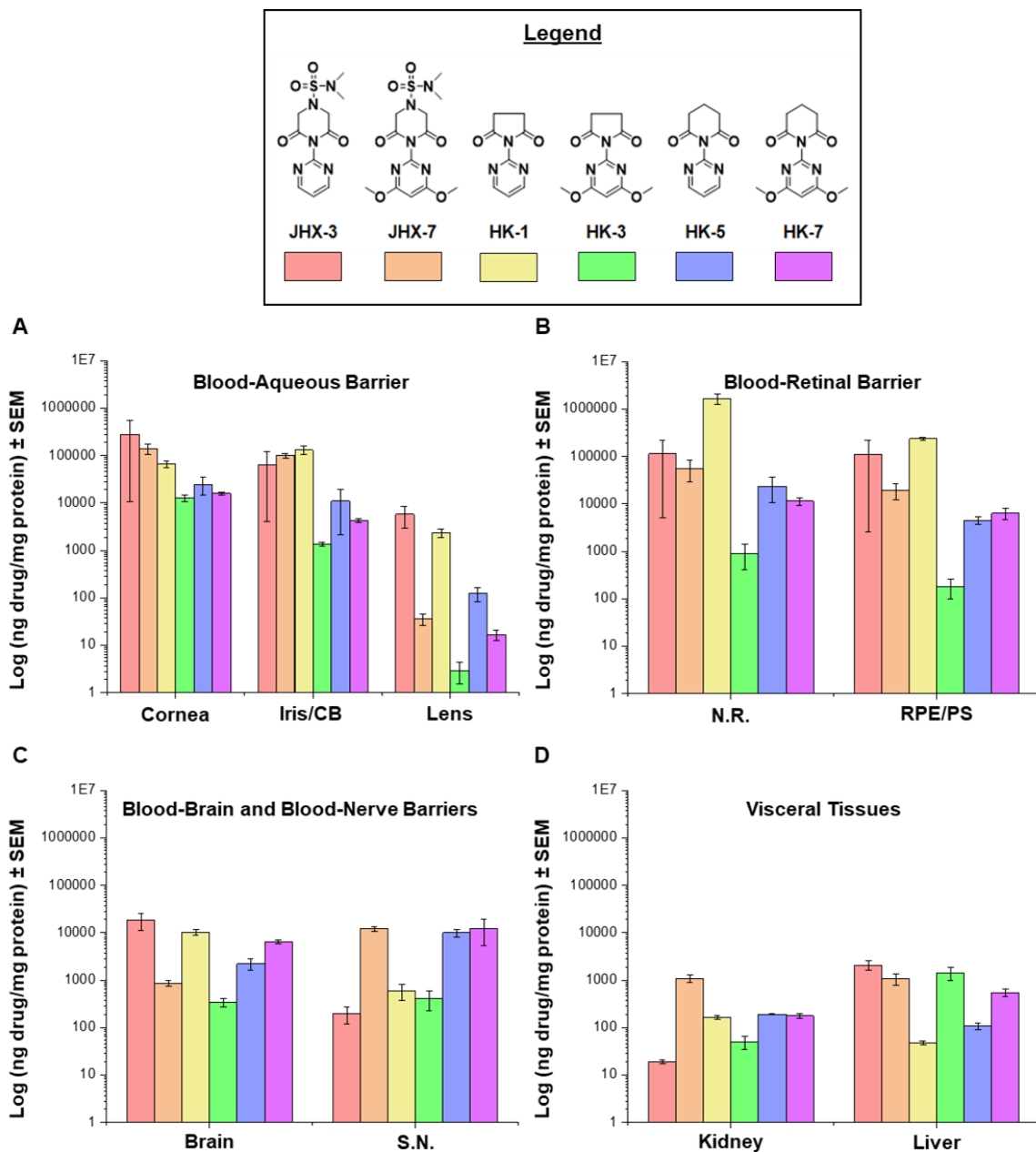


Figure 2.4. Summary of the CHL drug levels to ocular, neural, and visceral. The distribution of CHL drugs to tissues traversing through the (A) blood-aqueous barrier, (B) blood-retinal barrier, or (C) blood-brain and blood-nerve barriers, and (D) directly into visceral tissues to reach target tissues. Drug levels are presented as the log of drug concentration in nanograms of drug per milligram of protein (\pm SEM).

In tissues penetrating the BRB, similar trends were observed for the CHLs between the NR and RPE/C. The methoxy compounds JHX-7 and HK-3 were found in lower levels than their non-methoxy derivatives JHX-3 and HK-1, while the methoxy HK-7 was found in lower levels in the NR, but in higher levels in the RPE/C, compared to its non-methoxy HK-5. These trends were also observed in the NF compounds, though HK-15 was undetectable in both the NR and RPE/C. Compared to the NF compounds which demonstrated highest levels of the non-methoxy JHX-1 in the NR and RPE/C, the non-methoxy HK-1 was observed in highest levels in both the NR and RPE/C.

The observed trends for BBB and BNB passage were similar among HK compounds but opposite for JHX compounds. The non-methoxy HK-1 achieved higher levels compared to its methoxy HK-3 in both the brain and SN, and the methoxy HK-7 achieved higher levels than its non-methoxy HK-5 in both the brain and SN. The non-methoxy JHX-3 was found in higher levels in the brain, but in lower levels in the SN, compared to the methoxy JHX-7. The non-methoxy JHX-3 was also observed in highest levels in the brain, while the methoxy HK-7 was observed in highest levels in the SN. Apart from the observation between the non-methoxy JHX-3 and methoxy JHX-7 in the brain, none of the CHL compounds shared the trends observed with their NF parent analogs.

In the visceral tissues, kidney levels of the methoxy JHX-7 were markedly higher compared to all other CHLs, and both methoxy compounds HK-3 and HK-7 were observed in lower levels compared to their non-methoxy derivatives HK-1 and HK-5. In the liver, opposite trends were observed where the level of the methoxy JHX-7 was lower compared to the non-methoxy JHX-3, but the levels for both methoxy compounds HK-3 and HK-7 were higher compared to their non-methoxy derivatives HK-1 and HK-5. The JHX CHLs

followed a similar trend compared to their NF analogs in the liver, but not in the kidney. The methoxy derivatives of both HK compounds showed decreased kidney levels but increased liver levels compared to their NF analogs. Compared to their NF analogs, HK-1 and HK-3 showed similar levels in the liver and HK-5 showed similar levels in the kidney. Finally, the NF non-methoxy HK-13 was found in the greatest levels in both the kidney and liver, while the methoxy JHX-7 and the non-methoxy JHX-3 were found in greatest levels in the kidney and liver, respectively.

2.4.4 Distribution of Multifunctional Compounds

The compounds of greatest interest are the MFAOs because they combine the effects of the FRS and CHL compounds into one molecule. Their structures and tissue levels are presented in **Figure 2.5**.

In tissues requiring BAB penetration, the methoxy compounds JHX-8 and HK-4, as well as the non-methoxy compound HK-6, were found in markedly lower levels compared to their analogs JHX-4, HK-2, and HK-8, respectively. Unlike the NF non-methoxy HK-13, found in greatest levels in the cornea and iris/CB, and NF non-methoxy JHX-1 which was found in greatest levels in the lens, the MFAO non-methoxy HK-2 was found in the greatest levels in the cornea, while the methoxy HK-8 was found in greatest levels in both the iris/CB and the lens. The same distribution trends were observed in tissues requiring BRB penetration to distribute into the NR and the RPE/C. Though the NF non-methoxy JHX-1 was observed in highest levels in both the NR and RPE/C, the non-methoxy HK-2 was found in greatest levels in both the NR and RPE/C. Though the trends in greatest tissue uptake between the NFs and the MFAOs are different, the MFAOs all appear to exhibit similar distribution trends to both the BAB and the BRB. This may

suggest that the MFAOs all share similar properties which allow for their comparable passage through both the BAB and BRB.

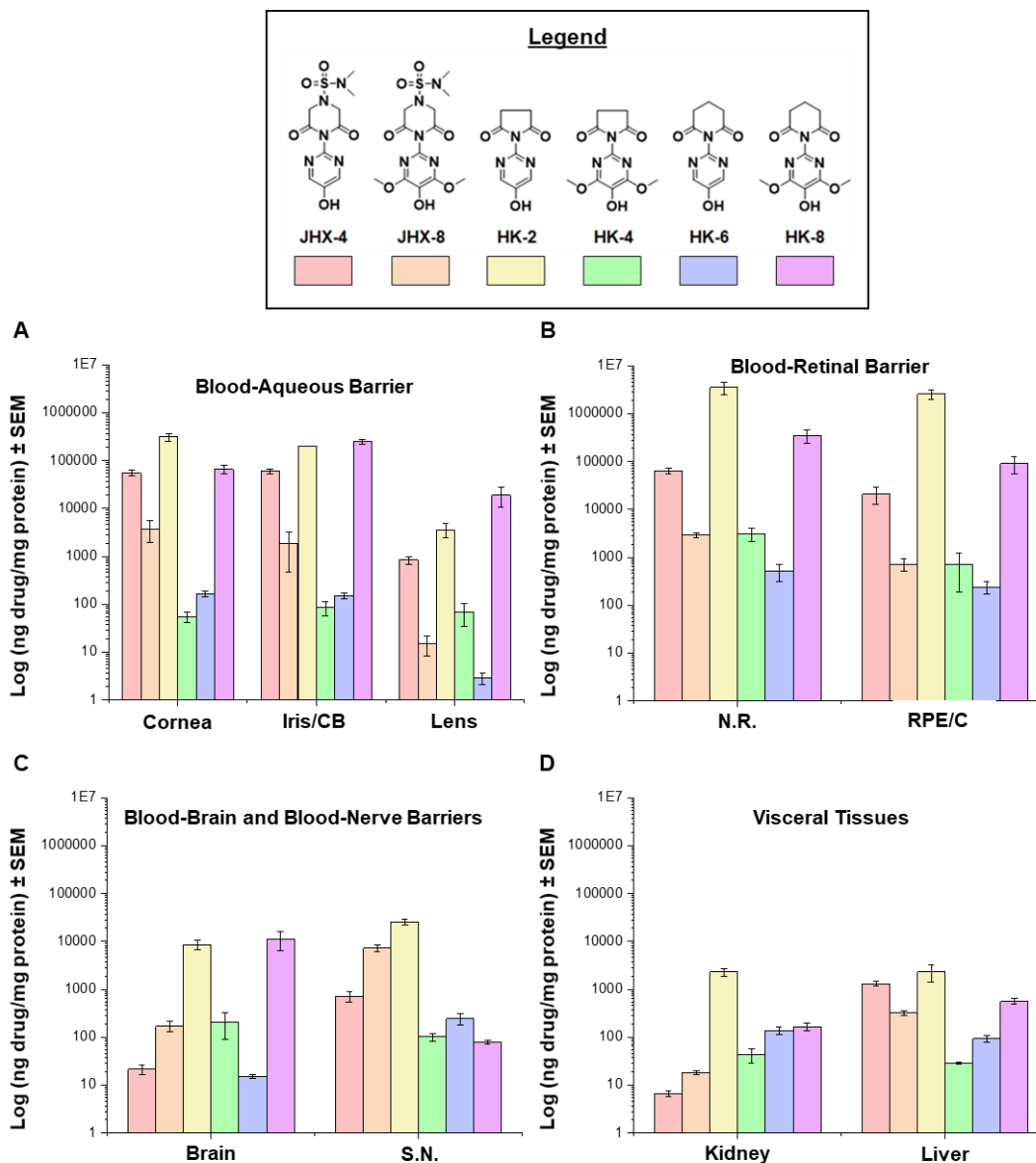


Figure 2.5. Summary of the MFAO drug levels to ocular, neural, and visceral tissues. The distribution of MFAO drugs to tissues traversing through the (A) blood-aqueous barrier, (B) blood-retinal barrier, or (C) blood-brain and blood-nerve barriers, and (D) directly into visceral tissues to reach target tissues. Drug levels are presented as the log of drug concentration in nanograms of drug per milligram of protein (\pm SEM).

In the brain, the non-methoxy HK-2 achieved higher levels than the methoxy HK-4. In contrast, both the methoxy compounds JHX-8 and HK-8 achieved higher levels compared to their non-methoxy derivatives JHX-4 and HK-6. In the SN, again the non-methoxy HK-2 achieved higher levels than the methoxy HK-4 and the methoxy JHX-8 achieved higher levels than its non-methoxy JHX-4. However, the methoxy HK-8 was found in lower levels than its non-methoxy HK-6. The methoxy compound HK-8 was found in greatest overall levels in the brain (though HK-2 was close), while the non-methoxy HK-2 was found in greatest overall levels in the SN. The MFAO distribution levels to the brain and SN are unexpected because it is thought that the properties of compounds requiring passage across the BBB are similar to those required for passage across the BNB due to anatomical similarities between these barriers [41]. With the exception of the non-methoxy HK-2 and its methoxy HK-4 which distribute in similar levels to both the brain and SN, the other MFAOs vary in multiple orders of magnitude.

Finally, in the visceral tissues examined, tissue uptake trends are opposite between the non-methoxy JHX-4 and methoxy JHX-8 where JHX-8 is observed in higher levels in the kidney but in lower levels in the liver. The non-methoxy HK-2 and methoxy HK-4 are observed in similar levels in both the kidney and liver where levels of HK-2 are markedly increased compared to HK-4. The trends between the non-methoxy HK-6 and methoxy HK-8 show that the presence of the methoxy group increase tissue levels to both the kidney and liver. Compared to the NF compounds, a similar trend was only observed with the JHX compounds in the liver.

2.5 Discussion

There are multiple routes of drug administration to the body such as subcutaneous, intramuscular, and intravenous injections, topical ointments or drops, inhaled aerosols, and oral agents. Each of these routes is known to have a specific purpose, certain advantages, and varying absorption, distribution, metabolism, and excretion (ADME) profiles [2, 42]. To increase patient compliance, topical and oral dosage forms are the major foci of ocular drug delivery even though these routes may suffer from slow and/or low drug absorption [43]. Unfortunately, no single route of administration is optimal for all drugs [44].

Though oral drug administration is the most preferred and common drug delivery route resulting in the highest patient compliance and decreased cost of care [45], little is known about the ocular drug distribution of orally available compounds. Upon oral administration, the efficacy of a small molecule depends on its stability and absorption in the gastrointestinal tract, rate of metabolism, and distribution. Disadvantages associated with general oral drug administration include low stability, poor solubility, and low membrane permeability which may prevent the uptake of drugs into the bloodstream and tissues [46].

This study investigated the levels of unmetabolized drugs distributed to various intraocular, neural, and visceral tissues, including the cornea, iris with the ciliary body (iris/CB), lens, neural retina (NR), retinal pigmented epithelium with the choroid (RPE/C), brain, sciatic nerve (SN), kidney, and liver, and provides a starting point for pharmaceutical scientists to identifying the necessary factors for penetrating the BAB, BRB, BBB, and BNB. 200-gram Sprague Dawley rats were fed with chow containing 0.05 wt% of one of

the 24 compounds (**Figure 2.1**) for seven days. The major assumption of this study was that after 7 days of oral treatment, steady-state levels of drug would be achieved. Using this method, the average daily dose of all drugs was calculated to be 46.2 ± 2.2 mg/kg/day and the unmetabolized drug levels were found to range from 0 ng drug/mg protein to 3.7 mg drug/mg protein among all tissues examined. The drug levels achieved in all examined tissues are summarized in **Table 2.1**. In this table, 17 out of 216 data points had high errors, which was defined as an SEM value greater than or equal to 60% of the mean value. All 17 samples with high error were re-analyzed to confirm tissue concentrations. This high error could be attributed to several factors including incomplete perfusion, low tissue protein concentrations (for example, the cornea), or the small sample size of the pooled tissues, and it appears that the high errors occurred primarily with the smaller pooled samples (cornea, iris/CB, neural retina, and RPE/C). Additionally, there were two high errors identified in the lens with the FRS JHX-6 and FRS HK-16 where these factors may not have a role because the lens is avascular and has a high protein concentration. It cannot be ruled out that these errors may be linked to the assumption that steady-state drug levels should have been achieved after 7 days without having conducted proper time-course studies.

Compounds were separated into their functional families (*i.e.*, NF, FRS, CHL, or MFAO) and their tissue levels were examined (**Figures 2.2 – 2.5**, respectively). In addition, the tissues were grouped according to required barrier passage through the BAB, BRB, BBB, or BNB, or directly to visceral tissues. Organs and tissues have layers of epithelial cells and endothelial cells which contain tight junctions, forming barriers between them and the circulating blood [47]. These tight junctions establish a barrier that directly regulates paracellular flux and indirectly regulates transcellular flux. While these structures were thought to be static and largely impermeable, they are dynamic and allow

for the transepithelial permeability to small ions, as well as larger molecular flux depending on the expression of the tight junction proteins such as occludin and claudins [48-51]. In general, small lipophilic molecules are passively diffused transcellularly if they are not substrates to any cellular transporter, and paracellular permeability can greatly differ between the various diverse tissue barriers, such as the BAB, BRB, BBB, and BNB, depending on the expression and composition of tight junction proteins [52].

The vasculature of the ciliary body is supplied by the anterior ciliary arteries and long posterior ciliary arteries, forming the major arterial circle near the root of the iris wherefrom branches supply the iris, ciliary body, and the anterior choroid. The ciliary body vasculature is also fenestrated to allow passage of plasma proteins and molecules into the stroma as part of aqueous humor production [53]. The BAB is believed to be composed of the non-pigmented cell layer of the ciliary epithelium and the endothelial cells of the iris blood vessels [54]. Tight junctions are present in the non-pigmented cell layer of the ciliary epithelium, suggesting its role as the physical barrier to drug movement across the ciliary body [55].

Passage through the BAB in our studies was measured by drug levels in the cornea, iris/CB, and lens. The NF compounds demonstrate that non-methoxy JHX-1 and HK-13 distribute in greater quantities to the cornea, iris/CB, and lens than their methoxy derivatives and that this same trend is observed in the lens between the non-methoxy HK-9 and its methoxy derivative HK-11 (**Figure 2.2A**). The non-methoxy NFs are inherently more lipophilic than their methoxy counterparts. The distribution of the FRS compounds indicate that, with the exception of the non-methoxy HK-14 and its methoxy derivative HK-16 in the cornea and the iris/CB, the methoxy derivatives achieve higher levels in the cornea, iris/CB, and lens compared to their non-methoxy counterparts (**Figure 2.3A**). The

CHL compounds show that, with the exception of non-methoxy JHX-3 and methoxy JHX-7 in the iris/CB, all non-methoxy compounds were found in greater concentrations than their methoxy derivatives in the cornea, iris/CB, and lens (**Figure 2.4A**). Finally, the MFAO results show the same trends across all tissues where the non-methoxy compounds JHX-4 and HK-2 are found in greater concentrations than their methoxy derivatives JHX-8 and HK-4, but the methoxy HK-8 was found in greater concentrations than its non-methoxy HK-6 (**Figure 2.5A**). Of these analogs, the NF non-methoxy HK-13, the FRS methoxy JHX-6, the CHL non-methoxy JHX-3, and the MFAO methoxy HK-8 were found to penetrate the BAB best as determined by their drug levels in the cornea, iris/CB, and lens. The FRS and MFAO results agree with previous reports that less lipophilic/more hydrophilic compounds better penetrate the BAB [56]. The investigations of a 400 mg oral dose of moxifloxacin and subsequent levels in the aqueous humor [57] comprise one of the few studies examining drug penetration across the BAB in humans. Moxifloxacin achieved therapeutic concentrations without any observed or reported patient side effects for up to 12 hours. Though this study confirms penetration of an orally-administered prescription antibiotic across the BAB, the factors required for BAB permeability have yet to be elucidated. Another study examining ocular distribution of intravenous-infused drugs in Sprague Dawley rats reports that more hydrophilic characteristics are required for BAB passage [56]. However, because limited evidence exists in understanding the factors required for BAB penetration, these results warrant further investigations.

In the posterior segment of the eye, the blood-retinal barrier (BRB) restricts the entry of therapeutic agents from the circulating blood into the retina. The BRB consists of two parts, the inner BRB (iBRB) formed by non-fenestrated retinal capillary endothelial cells, and the outer BRB (oBRB) formed by the tight junctions of the retinal pigmented epithelial cells with support from Bruch's membrane that prevent passage of large

molecules from the choriocapillaris [58, 59]. Drugs in the bloodstream rapidly equilibrate with the extravascular space of the choroid because the choriocapillaris is fenestrated, and the RPE limits the permeation of drugs from the choroid to the retina [60]. Unlike the BAB where drugs with more hydrophilic characteristics are required for passage, drugs penetrating both the inner and outer BRB are reported to exhibit more lipophilic characteristics [56, 61]. Unfortunately, few studies have investigated the factors required for orally-administered drugs to penetrate the BRB and distribute to the NR or the RPE/C. A study conducted in 10 human patients examined the vitreous permeability of an orally-administered antiviral prodrug, famciclovir (3 x 500 mg) through the BRB. It was reported that these patients were scheduled to undergo an elective pars plana vitrectomy and were overall healthy (*i.e.*, BRB was not compromised). This small lipophilic molecule was found to achieve therapeutic concentrations without any observed or reported patient side effects [62]. Though in a small patient population, this study provides evidence supporting the necessity of lipophilic properties of drugs for BRB passage.

Our BRB results show that, with the NF compounds, the non-methoxy derivatives are found in greater levels than methoxy derivatives in both the NR and RPE/C (**Figure 2.2B**). The FRS compounds indicate that the methoxy derivatives JHX-6 and HK-12, but not HK-16, are found in greater levels compared to their non-methoxy derivatives in both the NR and RPE/C (**Figure 2.3B**). The CHL compounds show that all non-methoxy derivatives are found in greater levels than the methoxy derivatives in the NR, and the same is seen in the RPE/C except between the non-methoxy HK-5 and methoxy HK-7 (**Figure 2.4B**). Finally, the MFAOs demonstrate that the non-methoxy JHX-4 and HK-2, and the methoxy HK-8, are found in greater levels than their derivatives in both the NR and RPE/C (**Figure 2.5B**). Of these analogs, the NF non-methoxy JHX-1, the FRS methoxy JHX-6, the CHL non-methoxy HK-1, and the MFAO non-methoxy HK-2 were

found to penetrate the BRB best as determined by drug levels in the NR and the RPE/C. With the exception of the methoxy FRS JHX-6, the compounds with greater lipophilic characteristics were found to penetrate the BRB better, providing further evidence that compounds with greater lipophilic properties can better penetrate the BRB [56].

Few studies exist investigating drug distribution through the BNB into peripheral nerves such as the SN. One recent study from GlaxoSmithKline examined the penetration of intravenous-infused small molecule drugs into various peripheral nerves, including the sciatic nerve and dorsal root ganglion, and compared their distribution to the CNS (brain and spinal cord). Unlike passage through the BNB which is not well studied, investigations of drug permeability through the BBB are well documented, though hampered due to lack of robust strategies to mimic the BBB *in vitro* [63]. It was observed that the sciatic nerve is permeable to small molecule drugs with large structural diversity and, in general, most small molecule drugs exhibited higher BNB than BBB penetration [40]. With a caveat, our study does support GlaxoSmithKline's study results. The NF HK-series distributed in higher levels to the SN, while the NF JHX-series achieved higher levels to the brain (**Figure 2.2C**). The FRS HK-series also distributed in higher levels to the SN, while the FRS JHX-series achieved higher levels in the brain. Moreover, all methoxy derivatives were found in higher concentrations than the non-methoxy derivatives in both the SN and the brain (**Figure 2.3C**). The methoxy CHLs JHX-7, HK-3, and HK7 and non-methoxy HK-5 achieved higher levels in the SN, while the non-methoxy CHLs JHX-3 and HK-1 were observed in higher levels in the brain (**Figure 2.4C**). Finally, the MFAO non-methoxy compounds JHX-4, HK-2, and HK-6, as well as the methoxy JHX-8, distributed in higher levels to the SN, while the methoxy compounds HK-4 and HK-8 achieved higher levels in the brain (**Figure 2.5C**). Of the 24 studied drugs, 16 achieved higher levels in the SN than the brain. These drugs included JHX-4, 5, 6, 7, and HK-2, 3, 5, 6, which inherently

possess more hydrophilic properties, and HK-9, 10, 11, 12, 13, 14, 15, 16, which inherently possess more lipophilic properties. This property characterization was based on calculated LogP values where a LogP of less than 0 denotes greater hydrophilic properties, and a LogP of greater than 0 denotes greater lipophilic properties. These results differ from the reported properties believed to maximize both BNB and BBB penetration (*i.e.*, lipophilicity is directly proportional to both BNB and BBB penetration) [40, 64, 65]. Additionally, the NF non-methoxy HK-13, the FRS methoxy HK-16, the CHL methoxy JHX-7, and the MFAO non-methoxy HK-2 achieved greatest levels in the SN and are observed to penetrate the BNB best, while the NF non-methoxy HK-13, the FRS methoxy JHX-6, the MB non-methoxy JHX-3, and the MFAO methoxy HK-8 achieved greatest levels in the brain and penetrate the BBB best. Further investigations are required to elucidate the required factors for penetration through these complex physiological barriers [40]. Moreover, though the BBB is one of the most studied physiological barrier with overwhelming evidence supporting the claims that lipophilic drugs more easily penetrate the BBB [64-66], computational algorithms are being employed to further improve BBB drug development and to confirm whether currently assumed drug properties for BBB permeation are crucial [67].

Both the kidney and liver are visceral tissues involved in drug ADME. The liver is responsible for selective uptake, metabolism, and excretion of the majority of drugs introduced to the body [68], while the kidney filters and excretes drugs and their metabolites [69]. Due to their role in drug elimination, it is no surprise that all drugs were found in much lower levels in both the kidney and the liver compared to other target tissues. The trends between the kidney and liver for the NF compounds were similar, where the non-methoxy compounds JHX-1 and HK-13, and the methoxy HK-11, were found in greater levels than their derivatives (**Figure 2.2D**). The opposite trends were

observed with the FRS compounds where the methoxy JHX-6 and HK-16, and the non-methoxy HK-10, were found in greater levels compared to their derivatives in both the kidney and liver (**Figure 2.3D**). The trends for the CHL compounds were opposite between the kidney and liver, where the methoxy JHX-7 and non-methoxy compounds HK-1 and HK-5 were found in greater levels than their derivatives in the kidney, but the non-methoxy JHX-3 and methoxy compounds HK-3 and HK-7 were found in greater levels than their derivatives in the liver (**Figure 2.4D**). The MFAO trends show that the non-methoxy HK-2 and methoxy HK-8 were both found in greater levels in the kidney and liver compared to their derivatives, while the methoxy JHX-8 was found in greater levels in the kidney and its non-methoxy JHX-4 was found in greater levels in the liver (**Figure 2.5D**). The compounds found in greatest overall concentrations to both the kidney and liver were the NF non-methoxy HK-13, the FRS methoxy JHX-6, and the MFAO non-methoxy HK-2. The CHL methoxy compound JHX-7 was found in greater levels in the kidney, while the non-methoxy JHX-3 was found in greater levels in the liver. It is well recognized that the lipophilicity and extent of metabolism of a drug contribute to liver accumulation [70]. Moreover, increased hydrophilic properties of a drug contributes to the increase of the probability of excretion through the kidneys [69]. Our results indicate that the drugs accumulate in the visceral tissues at much lower levels compared to the ocular or neural tissues, suggesting that they are effectively excreted and do not strongly target the kidney or the liver.

2.6. Conclusions

We have demonstrated that the unmetabolized compound levels of orally administered MFAOs and their analogs can be measured in various intraocular tissues. With the exception of HK-15 in ocular tissues and the brain, and JHX-1 and JHX-5 in the

SN, the remainder of the compounds were found in all tissues. Various trends in the distribution profiles were identified depending on how the drugs are parsed. While the trends reported here confirm previous findings in our laboratory, further investigations are required to understand the pertinent factors of drug passage across the physiological barriers required to deliver into target tissues. Because few attempts have been made to study the relationship between oral drug administration, physiological barrier penetration, and intraocular drug delivery, I have pursued and conducted modeling studies based on the data presented here to identify the physicochemical parameters necessary to predict the biological activity of these 24 compounds in ocular, neural, and visceral tissues. The modeling studies and their results are presented and discussed in Chapter 3.

2.7. References

1. Patel, A., et al., *Ocular drug delivery systems: An overview*. World J Pharmacol, 2013. **2**(2): p. 47-64.
2. Gaudana, R., et al., *Ocular drug delivery*. Aaps j, 2010. **12**(3): p. 348-60.
3. Kim, S.H., et al., *Transport barriers in transscleral drug delivery for retinal diseases*. Ophthalmic Res, 2007. **39**(5): p. 244-54.
4. Lee, S.J., et al., *Evaluation of clearance mechanisms with transscleral drug delivery*. Invest Ophthalmol Vis Sci, 2010. **51**(10): p. 5205-12.
5. Gower, N.J.D., et al., *Drug discovery in ophthalmology: past success, present challenges, and future opportunities*. BMC Ophthalmol, 2016. **16**: p. 11.
6. Bourlais, C.L., et al., *Ophthalmic drug delivery systems--recent advances*. Prog Retin Eye Res, 1998. **17**(1): p. 33-58.
7. Gulsen, D. and A. Chauhan, *Ophthalmic drug delivery through contact lenses*. Invest Ophthalmol Vis Sci, 2004. **45**(7): p. 2342-7.
8. Cholkar, K., et al., *Novel Nanomicellar Formulation Approaches for Anterior and Posterior Segment Ocular Drug Delivery*. Recent Pat Nanomed, 2012. **2**(2): p. 82-95.
9. Venkatraman, S. and T. Wong, *How can nanoparticles be used to overcome the challenges of glaucoma treatment?* Nanomedicine (Lond), 2014. **9**(9): p. 1281-3.
10. Nguyen, H., et al., *Delivery of therapeutics for deep-seated ocular conditions - status quo*. J Pharm Pharmacol, 2018. **70**(8): p. 994-1001.
11. Wang, Y., A. Rajala, and R.V.S. Rajala, *Nanoparticles as Delivery Vehicles for the Treatment of Retinal Degenerative Diseases*. Adv Exp Med Biol, 2018. **1074**: p. 117-123.

12. Bodoki, E., et al., *Topical nanodelivery system of lutein for the prevention of selenite-induced cataract*. *Nanomedicine*, 2019. **15**(1): p. 188-197.
13. Lai, F., et al., *Production of nanosuspensions as a tool to improve drug bioavailability: focus on topical delivery*. *Curr Pharm Des*, 2015. **21**(42): p. 6089-103.
14. Maged, A., A.A. Mahmoud, and M.M. Ghorab, *Nano Spray Drying Technique as a Novel Approach To Formulate Stable Econazole Nitrate Nanosuspension Formulations for Ocular Use*. *Mol Pharm*, 2016. **13**(9): p. 2951-65.
15. Agarwal, R., et al., *Liposomes in topical ophthalmic drug delivery: an update*. *Drug Deliv*, 2016. **23**(4): p. 1075-91.
16. Vicario-de-la-Torre, M., et al., *Design and characterization of an ocular topical liposomal preparation to replenish the lipids of the tear film*. *Invest Ophthalmol Vis Sci*, 2014. **55**(12): p. 7839-47.
17. Zhao, F., et al., *Comparison of response surface methodology and artificial neural network to optimize novel ophthalmic flexible nano-liposomes: Characterization, evaluation, in vivo pharmacokinetics and molecular dynamics simulation*. *Colloids Surf B Biointerfaces*, 2018. **172**: p. 288-297.
18. Rodriguez Villanueva, J., M.G. Navarro, and L. Rodriguez Villanueva, *Dendrimers as a promising tool in ocular therapeutics: Latest advances and perspectives*. *Int J Pharm*, 2016. **511**(1): p. 359-366.
19. Lancina, M.G., 3rd and H. Yang, *Dendrimers for Ocular Drug Delivery*. *Can J Chem*, 2017. **95**(9): p. 897-902.
20. Spataro, G., et al., *Designing dendrimers for ocular drug delivery*. *Eur J Med Chem*, 2010. **45**(1): p. 326-34.

21. Kang Derwent, J.J. and W.F. Mieler, *Thermoresponsive hydrogels as a new ocular drug delivery platform to the posterior segment of the eye*. *Trans Am Ophthalmol Soc*, 2008. **106**: p. 206-13; discussion 213-4.
22. Shikamura, Y., et al., *Hydrogel Ring for Topical Drug Delivery to the Ocular Posterior Segment*. *Curr Eye Res*, 2016. **41**(5): p. 653-61.
23. Bhamra, T.S., B.J. Tighe, and J. Li, *High modulus hydrogels for ophthalmic and related biomedical applications*. *J Biomed Mater Res B Appl Biomater*, 2019. **107**(5): p. 1645-1653.
24. Gulsen, D., C.C. Li, and A. Chauhan, *Dispersion of DMPC liposomes in contact lenses for ophthalmic drug delivery*. *Curr Eye Res*, 2005. **30**(12): p. 1071-80.
25. Tieppo, A., et al., *Sustained in vivo release from imprinted therapeutic contact lenses*. *J Control Release*, 2012. **157**(3): p. 391-7.
26. Gupta, H. and M. Aqil, *Contact lenses in ocular therapeutics*. *Drug Discov Today*, 2012. **17**(9-10): p. 522-7.
27. Hartman, R.R. and U.B. Kompella, *Intravitreal, Subretinal, and Suprachoroidal Injections: Evolution of Microneedles for Drug Delivery*. *J Ocul Pharmacol Ther*, 2018. **34**(1-2): p. 141-153.
28. Ghemtio, L., et al., *Predictive Modeling of Ocular Pharmacokinetics and Adverse Effects*. *Curr Pharm Des*, 2016. **22**(46): p. 6928-6934.
29. Lin, J.B., K. Tsubota, and R.S. Apte, *A glimpse at the aging eye*. *NPJ Aging Mech Dis*, 2016. **2**: p. 16003.
30. Jin, H., et al., *Multifunctional antioxidants for the treatment of age-related diseases*. *J Med Chem*, 2010. **53**(3): p. 1117-27.
31. Kawada, H. and P.F. Kador, *Orally Bioavailable Metal Chelators and Radical Scavengers: Multifunctional Antioxidants for the Coadjutant Treatment of Neurodegenerative Diseases*. *J Med Chem*, 2015. **58**(22): p. 8796-805.

32. Randazzo, J., et al., *Orally active multi-functional antioxidants delay cataract formation in streptozotocin (type 1) diabetic and gamma-irradiated rats*. PLoS One, 2011. **6**(4): p. e18980.
33. Randazzo, J., et al., *Orally active multi-functional antioxidants are neuroprotective in a rat model of light-induced retinal damage*. PLoS One, 2011. **6**(7): p. e21926.
34. Kawada, H., et al., *Effects of multifunctional antioxidants on mitochondrial dysfunction and amyloid-beta metal dyshomeostasis*. J Alzheimers Dis, 2015. **44**(1): p. 297-307.
35. al., M.e., *The Effect of Antioxidant- and Vitamin-Enriched Diets on Vision in Rats Exposed to Primary Blast Injury*. 2018: Biomedical Engineering Society.
36. Chen, G.D., et al., *Novel oral multifunctional antioxidant prevents noise-induced hearing loss and hair cell loss*. Hear Res, 2020. **388**: p. 107880.
37. Kawada, H., *Multi-Functional Antioxidants Targeting Neurodegenerative Diseases*. 2013.
38. Bradford, M.M., *A rapid and sensitive method for the quantitation of microgram quantities of protein utilizing the principle of protein-dye binding*. Anal Biochem, 1976. **72**: p. 248-54.
39. Kapusta, D., *Drug Excretion*, in *xPharm: The Comprehensive Pharmacology Reference*, S.J. Enna and D.B. Bylund, Editors. 2007, Elsevier: New York. p. 1-2.
40. Liu, H., et al., *Drug Distribution into Peripheral Nerve*. J Pharmacol Exp Ther, 2018. **365**(2): p. 336-345.
41. Richner, M., et al., *Functional and Structural Changes of the Blood-Nerve-Barrier in Diabetic Neuropathy*. Frontiers in Neuroscience, 2019. **12**(1038).
42. Doogue, M.P. and T.M. Polasek, *The ABCD of clinical pharmacokinetics*. Ther Adv Drug Saf, 2013. **4**(1): p. 5-7.

43. Fox, C.B., et al., *Micro/nanofabricated platforms for oral drug delivery*. J Control Release, 2015. **219**: p. 431-444.
44. Kantae, V., et al., *Integration of pharmacometabolomics with pharmacokinetics and pharmacodynamics: towards personalized drug therapy*. Metabolomics, 2017. **13**(1): p. 9.
45. Moeller, E.H. and L. Jorgensen, *Alternative routes of administration for systemic delivery of protein pharmaceuticals*. Drug Discov Today Technol, 2008. **5**(2-3): p. e89-94.
46. Agrawal, U., et al., *Is nanotechnology a boon for oral drug delivery?* Drug Discov Today, 2014. **19**(10): p. 1530-46.
47. Zihni, C., et al., *Tight junctions: from simple barriers to multifunctional molecular gates*. Nat Rev Mol Cell Biol, 2016. **17**(9): p. 564-80.
48. Greene, C. and M. Campbell, *Tight junction modulation of the blood brain barrier: CNS delivery of small molecules*. Tissue Barriers, 2016. **4**(1): p. e1138017.
49. Peltonen, S., M. Alanne, and J. Peltonen, *Barriers of the peripheral nerve*. Tissue barriers, 2013. **1**(3): p. e24956-e24956.
50. Coca-Prados, M., *The blood-aqueous barrier in health and disease*. J Glaucoma, 2014. **23**(8 Suppl 1): p. S36-8.
51. Díaz-Coránguez, M., C. Ramos, and D.A. Antonetti, *The inner blood-retinal barrier: Cellular basis and development*. Vision research, 2017. **139**: p. 123-137.
52. Tscheik, C., I.E. Blasig, and L. Winkler, *Trends in drug delivery through tissue barriers containing tight junctions*. Tissue barriers, 2013. **1**(2): p. e24565-e24565.
53. Stewart, P.A. and U.I. Tuor, *Blood-eye barriers in the rat: correlation of ultrastructure with function*. J Comp Neurol, 1994. **340**(4): p. 566-76.
54. Braakman, S.T., et al., *Transport across Schlemm's canal endothelium and the blood-aqueous barrier*. Exp Eye Res, 2016. **146**: p. 17-21.

55. Sonsino, J., et al., *Co-localization of junction-associated proteins of the human blood--aqueous barrier: occludin, ZO-1 and F-actin*. *Exp Eye Res*, 2002. **74**(1): p. 123-9.
56. Toda, R., et al., *Comparison of drug permeabilities across the blood-retinal barrier, blood-aqueous humor barrier, and blood-brain barrier*. *J Pharm Sci*, 2011. **100**(9): p. 3904-11.
57. Kampougeris, G., et al., *Penetration of moxifloxacin into the human aqueous humour after oral administration*. *Br J Ophthalmol*, 2005. **89**(5): p. 628-31.
58. Diaz-Coranguuez, M., C. Ramos, and D.A. Antonetti, *The inner blood-retinal barrier: Cellular basis and development*. *Vision Res*, 2017. **139**: p. 123-137.
59. Coburn, P.S., et al., *Bloodstream-To-Eye Infections Are Facilitated by Outer Blood-Retinal Barrier Dysfunction*. *PLoS One*, 2016. **11**(5): p. e0154560.
60. Liu, L. and X. Liu, *Roles of Drug Transporters in Blood-Retinal Barrier*. *Adv Exp Med Biol*, 2019. **1141**: p. 467-504.
61. Tyagi, A., Sharma, P.K., and Malviya, R., *Role of Blood Retinal Barrier in Drug Absorption*. *Pharmaceutica Analytica Acta*, 2018. **9**(5).
62. Chong, D.Y., et al., *Vitreous penetration of orally administered famciclovir*. *Am J Ophthalmol*, 2009. **148**(1): p. 38-42.e1.
63. Roux, G.L., et al., *Proof-of-Concept Study of Drug Brain Permeability Between in Vivo Human Brain and an in Vitro iPSCs-Human Blood-Brain Barrier Model*. *Scientific Reports*, 2019. **9**(1): p. 16310.
64. Pardridge, W.M., *Drug transport across the blood-brain barrier*. *Journal of cerebral blood flow and metabolism : official journal of the International Society of Cerebral Blood Flow and Metabolism*, 2012. **32**(11): p. 1959-1972.

65. Warren, K.E., *Beyond the Blood:Brain Barrier: The Importance of Central Nervous System (CNS) Pharmacokinetics for the Treatment of CNS Tumors, Including Diffuse Intrinsic Pontine Glioma*. *Frontiers in Oncology*, 2018. **8**(239).
66. Banks, W.A., *Characteristics of compounds that cross the blood-brain barrier*. *BMC neurology*, 2009. **9 Suppl 1**(Suppl 1): p. S3-S3.
67. Wager, T.T., et al., *Moving beyond rules: the development of a central nervous system multiparameter optimization (CNS MPO) approach to enable alignment of druglike properties*. *ACS Chem Neurosci*, 2010. **1**(6): p. 435-49.
68. Larrey, D., *Epidemiology and individual susceptibility to adverse drug reactions affecting the liver*. *Semin Liver Dis*, 2002. **22**(2): p. 145-55.
69. Naidoo, S. and A.M. Meyers, *Drugs and the kidney*. *S Afr Med J*, 2015. **105**(4): p. 2683.
70. McEuen, K., et al., *Associations of Drug Lipophilicity and Extent of Metabolism with Drug-Induced Liver Injury*. *International journal of molecular sciences*, 2017. **18**(7): p. 1335.

CHAPTER 3

Developing Predictive Models of Multifunctional Antioxidant Compound Distribution and Their Analogs using Hierarchical Cluster Analysis and Quantitative Structure Activity Relationship Methods

3.1 Summary

Drug delivery to the eye is a major challenge and distribution to ocular tissues includes passage through physiological barriers. There have been few attempts at studying the relationships between drug administration and intraocular drug delivery, but none have examined ocular tissue distribution of orally-administered drugs. Preliminary linear regression analysis was conducted on the most abundant compounds found in ocular, neural, and visceral tissues presented in Chapter 2 to determine whether their observed accumulation can be linked to their calculated physicochemical parameters. Several strong correlations were revealed when the whole data set was subjected to hierarchical cluster analysis (HCA) and quantitative structure activity relationship (QSAR) analysis, paired with linear regression analysis. The results from these methods have identified several previously unknown relationships among the examined compounds and identified several physiologically-relevant predictive models to various ocular, neural, and visceral tissues. This is the first published report for the development of predictive models for ocular tissue delivery of orally-administered compounds.

3.2 Introduction

Methods to effectively and efficiently handle and analyze the exponential increase of data have become increasingly important [1]. Conventionally, data research involves data sets with numerous variables that can be handled by multivariate regression modeling. In the area of drug development, various data mining techniques, such as hierarchical cluster analysis (HCA), quantitative structural activity relationship analysis (QSAR), and linear regression analysis have been applied to understand relationships between the intrinsic properties of drugs and how they relate to a drug's biological activity [2, 3].

3.2.1 *Physicochemical Parameters*

Physicochemical parameters, also known as molecular descriptors, describe various properties of a molecule that are obtained through theoretical calculations. These descriptors are fundamental in computational drug design and discovery because they relate the various intrinsic properties of chemicals to their determined biological profiles [4, 5]. Over time, molecular descriptors have been improved by various refined chemoinformatic methods, and the continuous development of computational tools further improves the accuracy of physicochemical descriptors and therefore, computational models. The physiochemical descriptors used in this chapter, and their definitions, are summarized in **Table 3.1**.

3.2.2 *Hierarchical Cluster Analysis*

Clustering is a fundamental task in data mining whose goal is to discover new relationships between data based on a geometric distance measure to determine the (dis)similarity between any pair of data points. It is an invaluable tool for the exploratory and unsupervised analysis of multi-dimensional or multivariate data sets which partition data into homogeneous subsets, or clusters, to uncover undetermined relationships within data sets. The two most common clustering techniques are “K-means clustering” (KCA) and “hierarchical clustering” (HCA). KCA involves pre-specifying a number of desired clusters while HCA allows for a single-nested hierarchy of clusters from which partitions can be post-specified. This allows the HCA algorithm to study relationships between clusters not possible with KCA as the HCA is able to test all possible hierarchical permutations of a given data set [6].

HCA has gained popularity in the biomedical sciences, specifically with analyzing healthcare and genomics data [7, 8]. HCA attempts to group subjects within proximity into clusters using one of two strategies. The first strategy is *agglomerative clustering*, or a “bottom-up” approach where each data point is treated as its own cluster. Based on the algorithm, data is combined into larger clusters until all data points are part of the same cluster. The second strategy is *divisive clustering*, or the “top-down” approach which is the exact opposite of agglomerative clustering, where all data points are part of one cluster and are gradually broken down to individual data points. The advantages of both methods are that no prior knowledge or information about the number of desired clusters is required and the methods are simply implemented through the application of mathematical algorithms. One major drawback to HCA, which is used advantageously here, is that this method is preferred with smaller data sets which minimizes computing time.

Within HCA are multiple distance metric algorithms that may alter the number and type of clusters. The three most common linkage metrics include single-linkage, complete-linkage, average-linkage, and the most common geometric distance is Euclidean [9]. For the purposes of this study, the linkage metrics *complete-linkage* and *average-linkage* were paired with Euclidean distance (*i.e.*, the distance of the straight line between two points) metric. The complete-linkage algorithm identifies the maximum distance between the furthest data points between two clusters. At each stage of the clustering process, the two clusters with the smallest complete-linkage distance are combined. This allows for the merging of most dissimilar clusters, thereby maximizing the probability that the final cluster groups are different and new relationships can be identified. Mathematically, the complete-linkage algorithm is optimally efficient due to its rigor [10]. In contrast, the average-linkage algorithm takes the average distance between central data points of two clusters (*i.e.*, the cluster centroids). Here, the two clusters with the smallest distance between their centroids are combined. This linkage metric combines the sensitivity of the single-linkage algorithm, which is prone to skewing from outliers, and the rigor of complete-linkage, resulting in clusters with average dissimilarity [11]. Both the complete-linkage and average-linkage algorithms are most commonly used in HCA.

3.2.3 Quantitative Structure Activity Relationships

Quantitative structure activity relationship (QSAR) models are mathematical classifications that relate a set of predictor variables to biological response variables. In QSAR modeling, the goal is to identify molecular properties (*i.e.*, physicochemical parameter(s)) important for biological activity (*i.e.*, tissue distribution) [12]. The data obtained from QSAR is two-fold: the QSAR model summarizes alleged relationships between chemical structures and biological activity in a data set of chemicals, and then it

predicts the activity of new chemicals based on the summarized relationship from the identified model [13]. Additionally, there are essential steps taken in QSAR to ensure maximal efficiency in developing representative models such as data preparation, data analysis, and model validation.

The objective of this study is to determine whether the compound levels observed in chapter 2 can be correlated with the molecular attributes of the compounds. From here, the most important relationships between compound properties and their tissue levels can be identified to develop predictive models for ocular drug delivery. Although developing these predictive models appears to be a relatively simple task, it has substantial applications in understanding how drugs exert different biological responses [14]. Using both HCA and QSAR confirms the validity of the models by comparing the similarity of the results between the use of two different algorithms.

3.3 Programs and Methods

Programs. Hierarchical cluster analysis was conducted using the intrinsic “Hierarchical Cluster Analysis” algorithm with OriginPro Software (OriginPro 2016, OriginLab Co., Northampton, MA). Quantitative structure activity relationship analysis was conducted using the intrinsic “QuaSAR” algorithm with Molecular Operating Environment Software (MOE v. 2016.08, Chemical Computing Group, Montreal, Canada).

Data. The distribution data for this chapter was obtained from Chapter 2 (**Table 2.1**). As is common practice in QSAR, all average drug concentrations (ng drug/mg protein \pm SEM) were transformed to a logarithm scale, base 10. A second data set was generated by mathematically standardizing the drug levels for each tissue and calculating a standardized Z-score. All values of zero, and Z-scores greater than two standard

deviations about the mean ($Z\text{-score} \geq 2$ or $Z\text{-score} \leq -2$), were excluded from the data set. These included HK-15 in the cornea, iris/CB, lens, and NR; HK-15 and HK-2 in the RPE/C; HK-15 and JHX-6 in the brain; JHX-1 and JHX-5 in the SN; and JHX-5 in the liver. This data was also transformed to a logarithm scale, base 10.

To calculate the physicochemical parameters, each of the 24 multifunctional antioxidants (MFAOs), their monofunctional free radical scavenging (FRS) and bio-active transition metal chelating (CHL) analogs, and their nonfunctional analogs (NF) were modeled using “Molecule Builder” in MOE™. After all 24 compounds were modelled, they were added to a molecular database where they were all energy-minimized using Merck’s Molecular Forcefield 94x with a gradient of 0.05. After the minimization procedure, the physicochemical parameters for each drug was calculated using the “Calculate Descriptors” algorithm in MOE™. The selected descriptors and their definitions are listed in **Table 3.1**.

Hierarchical Cluster Analysis. The logged drug distribution data and the calculated physicochemical descriptors of the drugs were isolated for each tissue. The data was subject to hierarchical cluster analysis (HCA) for both data sets (all data and standardized data) using the “average-linkage” and “complete-linkage” clustering algorithms paired with Euclidean distance metric. The resulting dendrograms, one generated per descriptor per tissue, were obtained and each identified group was manually separated into their respective clusters. The clusters chosen for further analysis were selected based on meeting Hansch analysis criteria, which requires a minimum of 5-6 drugs per cluster per calculated descriptor. The resulting clusters were analyzed by linear regression analysis, and all clusters with a Pearson’s correlation coefficient of greater than 0.5 ($r \geq 0.5$) were identified. To meet modeling criteria, clusters with a

coefficient of determination greater than 0.5 ($r^2 \geq 0.5$) and a calculated p-value ≤ 0.05 were identified and confirmed with quantitative structure activity relationship (QSAR) algorithms in MOE™.

Quantitative Structure Activity Relationship Analysis. Both data sets and their calculated physicochemical descriptors were also subject to the “QuaSAR” algorithm in MOE™, and the resulting clusters were compared to those from HCA. All correlations with an $r^2 \geq 0.5$ were validated using the “QuaSAR” intrinsic validation function. The clusters that matched those identified using HCA and passed validation were re-correlated against all calculated physicochemical parameters to investigate whether any other relationships could be identified between these clusters.

3.4 Results

3.4.1 Calculation of Molecular Descriptors

The physicochemical parameters for the 24 compounds consisting of multifunctional antioxidants (MFAOs), their monofunctional free radical scavenging (FRS) and bio-active transition metal chelating (CHL) analogs, and their nonfunctional parents (NF) were modeled using “Molecule Builder” in MOE™. After all compounds were constructed, they were added to a molecular database where they were all energy-minimized using Merck’s Molecular Forcefield 94x with a gradient of 0.05. After the minimization procedure, the physicochemical parameters for each compound was calculated using the “Calculate Descriptors” algorithm in MOE™. The selected descriptors and their definitions are listed in **Table 3.1**.

<u>Physicochemical Descriptor</u>	<u>Classification</u>	<u>Definition</u>
Apol	Hydrophilic	A measure of how easily a molecule's electron cloud is distorted by an electric field[15]
ASA	Hydrophilic	Water accessible surface area calculated using a radius of 1.4 Angstroms for the water molecule using a polyhedral atomic representation
ASA_H	Hydrophobic	Water accessible surface area of all hydrophobic ($ q_i \leq 0.2$) atoms where q_i denotes the partial charge of atom 'i'
ASA_P	Hydrophilic	Water accessible surface area of all polar ($ q_i \geq 0.2$) atoms where q_i denotes the partial charge of atom 'i'
CASA-	Hydrophilic	Water accessible surface area of all atoms with a negative partial charge multiplied by the maximum negative partial charge of the molecule
CASA+	Hydrophilic	Water accessible surface area of all atoms with positive partial charge multiplied by the maximum positive partial charge of the molecule
Dipole	Hydrophilic	Dipole moment calculated from the partial charges of the molecule
FASA_H	Hydrophobic	Fractional hydrophobic accessible surface area calculated as ASA_H / ASA
FASA_P	Hydrophilic	Fractional polar accessible surface area calculated as ASA_P / ASA
Kier1	Structural	First kappa shape index: $(n-1)^2 / m^2$ where n denotes the number of atoms and m is the number of bonds (excluding hydrogens)[16]
LogP	Hydrophobic	Log of the octanol/water partition coefficient. This property is calculated from a linear atom type model with $r^2 = 0.931$ and RMSE = 0.393 on 1,827 molecules[17]
LogS	Hydrophilic	Log of the aqueous solubility (mol/L). This property is calculated from an atom contribution linear atom type model with $r^2 = 0.90$ on ca. 1,200 molecules[18]
PM3_Dipole	Hydrophilic	The dipole moment calculated using the PM3 Hamiltonian[19]
SLogP	Hydrophobic	Log of the octanol/water partition coefficient (including implicit hydrogens). This property is an atomic contribution model that calculated logP from the given structure, i.e., the correct protonation state. Results may vary from the logP descriptor. The training set for SLogP was ca. 7,000 structures[20]
SMR	Structural	Molecular refractivity (including implicit hydrogens). This property is calculated from an 11 descriptor linear model with $r^2 = 0.997$ and RMSE = 0.168 on 1,947 small molecules[21]
vsurf_Cp	Structural	Critical packing parameter which measures the steric bulk of the molecule.
vsurf_D1	Hydrophobic	A measure of the hydrophobic surface area of a molecule.
vsurf_G	Structural	Globularity which measures how close the molecular shape resembles a perfect sphere.
vsurf_W1	Hydrophilic	A measure of the hydrophilic surface area of a molecule.

Table 3.1. Definitions of select calculated physicochemical descriptors, which were chosen based on literature precedence. Each of the 24 compounds were modeled and their descriptors calculated using Molecular Operating Environment (MOE, v.2016.08).

3.4.2 Initial Linear Regression Analysis

The biodistribution results from Chapter 2 revealed that there were no obvious trends with tissue accumulation. The compounds were then separated into their functional families and it was observed that various compounds in each functional family accumulated in highest tissue levels overall. These compounds included the NFs JHX-1 and HK-13, the FRS JHX-6, the CHLs JHX-3 and HK-1, and the MFAOs HK-2 and HK-8. The relationships between the common calculated physicochemical parameters of these compounds and compound tissue levels observed in the cornea, iris with the ciliary body (Iris/CB), lens, neural retina (NR), retinal pigmented epithelium with the choroid (RPE/C), brain, sciatic nerve (SN), kidney, and liver were investigated. Two linear correlations were conducted with these compounds: one including the NFs JHX-1 and HK-13, and those excluding the NFs. This was done to isolate a data set for only compounds with known antioxidant activity. Initial linear regression analysis was conducted using calculated physicochemical parameters that have been most commonly identified in literature, which include the partition coefficient (logP), dipole moment (Dipole), kappa shape index (Kier1), and the log of predicted aqueous solubility (logS). The definitions of these calculated physicochemical parameters are reported in **Table 3.1**. **Moderate correlations** were defined as having an “r” value between ± 0.5 and ± 0.7 , while **strong correlations** were defined as an “r” value between ± 0.7 and ± 1.0 .

When the NF parent compounds were included, initial correlations resulted in three moderate correlations between **iris/CB** and LogS (-0.513), **lens** and Kier1 (+0.519), and **brain** and Kier1 (+0.505). These correlations are highlighted in **Table 3.2**. However, when the parent compounds were excluded and the calculated correlations were focused only on compounds with known antioxidant function, six moderate correlations (r between

± 0.5 and ± 0.7) and seven strong correlations (r between ± 0.7 and ± 1.0) were observed. These correlations, reported in **Table 3.3**, include: **cornea** with dipole (+0.777) and Kier1 (+0.797); **lens** with dipole (+0.810), Kier1 (+0.655), and LogS (-0.653); **NR** with dipole (-0.664) and Kier1 (-0.733); **RPE/C** with LogS (+0.668); **brain** with dipole (+0.734) and Kier1 (+0.818); **SN** with LogS (+0.837); and **liver** with dipole (+0.542) and Kier1 (+0.535).

	Log P	Dipole	Kier1	LogS
Cornea	-0.043	0.315	0.464	-0.205
Iris/CB	0.386	-0.210	-0.073	-0.513
Lens	-0.283	0.396	0.519	-0.252
N.R.	-0.237	-0.014	0.125	0.018
RPE/C	-0.424	0.071	0.192	0.278
Brain	-0.179	0.313	0.505	-0.194
S.N.	0.440	-0.393	-0.294	-0.240
Kidney	0.371	-0.100	-0.086	-0.019
Liver	-0.007	0.125	0.257	-0.284

Table 3.2. Correlation results between the NFs JHX-1 and HK-13, the FRS JHX-6, the CHLs JHX-3 and HK-1, and the MFAOs HK-2 and HK-8. Three moderate correlations were observed between iris/CB and LogS, lens and Kier1, and brain and Kier1.

	Log P	Dipole	Kier1	LogS
Cornea	-0.309	0.777	0.797	0.419
Iris/CB	0.337	0.170	0.097	0.377
Lens	0.303	0.810	0.665	-0.653
N.R.	0.453	-0.664	-0.733	0.359
RPE/C	0.029	-0.462	-0.494	0.668
Brain	-0.376	0.734	0.818	0.351
S.N.	-0.158	-0.083	-0.060	0.837
Kidney	0.293	0.071	-0.010	0.469
Liver	-0.480	0.542	0.535	0.383

Table 3.3. Correlation results between the functional antioxidants including the FRS JHX-6, the CHLs JHX-3 and HK-1, and the MFAOs HK-2 and HK-8. Six moderate correlations and seven strong correlations were observed, which is more than the data set which included the parent NFs (**Table 3.2**). Excluding the parent NFs strengthened the correlations between lens and Kier1 and brain and Kier1 but did not yield a correlation between iris/CB and LogS.

Because these preliminary correlations showed promising results, the linear regression analysis was expanded to include additional calculated physicochemical parameters: atomic polarizability (Apol), water-accessible surface area (ASA), hydrophobic-accessible surface area (ASA_H), polar-accessible surface area (ASA_P), semi-empirical parameterized model 3 dipole (PM3_Dipole), atomic-contribution partition coefficient (SLogP), and molecular refractivity including correct molecular protonation states (SMR). These parameters are also defined in **Table 3.1**. Calculated correlations using the data set that included the NF parent compounds yielded 6 more moderate correlations and 4 new strong correlations, mainly between the ocular tissues and the brain and ASA_H/ASA_P (**Table 3.4**). Excluding the NF parent compounds yielded 16 more moderate correlations and 12 more strong correlations, and all parameters examined correlated to at least one tissue (**Table 3.5**). These results indicate that conducting linear regression analysis between the drug tissue levels and their calculated descriptors may lead to the development of predictive tissue uptake models.

	Apol	ASA	ASA_H	ASA_P	SLogP	PM3_Dipole	SMR
Cornea	0.330	0.391	-0.308	0.647	-0.240	0.142	0.350
Iris/CB	-0.206	-0.155	-0.524	0.197	0.228	-0.320	-0.197
Lens	0.217	0.317	-0.645	0.801	-0.472	0.401	0.275
N.R.	-0.173	-0.055	-0.874	0.552	-0.331	-0.075	-0.114
RPE/C	-0.091	0.025	-0.818	0.601	-0.483	0.019	-0.029
Brain	0.323	0.401	-0.377	0.706	-0.371	0.146	0.356
S.N.	-0.287	-0.274	-0.274	-0.110	0.380	-0.548	-0.303
Kidney	-0.098	-0.062	-0.349	0.176	0.300	-0.346	-0.114
Liver	0.091	0.142	-0.423	0.453	-0.181	0.120	0.118

Table 3.4. Expanded correlations examining more calculated physicochemical parameters continued from **Table 3.2**. Linear regression analysis with the parent NFs JHX-1 and HK-13, the monofunctional FRS JHX-6, the monofunctional CHLs JHX-3 and HK-13, and the MFAOs HK-2 and HK-8 yielded six more moderate correlations and four new strong correlations.

	Apol	ASA	ASA_H	ASA_P	SLogP	PM3_Dipole	SMR
Cornea	0.833	0.848	0.617	0.912	-0.465	0.479	0.825
Iris/CB	0.176	0.198	-0.047	0.353	0.319	-0.195	0.147
Lens	0.599	0.586	0.361	0.679	0.024	0.905	0.595
N.R.	-0.676	-0.658	-0.757	-0.504	0.640	-0.801	-0.696
RPE/C	-0.469	-0.445	-0.657	-0.233	0.194	-0.555	-0.474
Brain	0.882	0.892	0.840	0.819	-0.516	0.387	0.873
S.N.	0.007	0.036	-0.169	0.182	-0.064	-0.383	-0.004
Kidney	0.055	0.079	-0.208	0.282	0.305	-0.244	0.030
Liver	0.482	0.493	0.190	0.655	-0.589	0.570	0.497

Table 3.5. Expanded correlations examining more calculated physicochemical parameters continued from **Table 3.3**. Linear regression analysis with the monofunctional FRS JHX-6, the monofunctional CHLs JHX-3 and HK-13, and the MFAOs HK-2 and HK-8 yielded 12 more moderate correlations and 16 more strong correlations.

3.4.3 Full and Standardized Data Set Linear Regression Analyses

Linear regression analysis was then used to investigate any potential relationships between the 24 drug tissue levels and their calculated physicochemical descriptors. These results are shown in **Table 3.6**, where nine moderate correlations (“r” value between ± 0.5 and ± 0.7) were identified. Relationships included **cornea** vs. LogP and vsurf_Cp; **iris/CB** vs. vsurf_Cp; **NR** vs. LogP, LogS, and vsurf_Cp; and **RPE/C** vs. LogP, LogS, and vsurf_Cp. No strong correlations (“r” value between ± 0.7 and ± 1.0) were identified. Next, the data set was mathematically standardized to exclude any experimental concentration zero values or outliers determined by Z-score. This standardized data set was also subject to linear regression analysis against the calculated physicochemical descriptors and results are shown in **Table 3.7**. Interestingly, no correlations were identified.

All Drug Correlations	<u>Ocular and Visceral Tissues</u>								
	Cornea	Iris/CB	Lens	NR	RPE/C	Brain	SN	Kidney	Liver
Apol	0.093	0.059	0.050	0.048	0.043	-0.010	-0.229	-0.209	0.041
ASA	0.092	0.060	0.048	0.066	0.053	-0.020	-0.207	-0.198	0.085
ASA_H	-0.205	-0.214	-0.200	-0.396	-0.316	-0.084	-0.186	-0.234	-0.417
ASA_P	0.202	0.175	0.154	0.277	0.222	0.024	-0.114	-0.079	0.308
CASA+	0.383	0.346	0.242	0.392	0.377	0.080	-0.309	-0.186	0.179
CASA-	0.386	0.364	0.188	0.370	0.349	0.015	-0.186	-0.220	0.311
Dipole	0.259	0.212	0.353	0.303	0.297	0.186	-0.322	-0.112	0.123
FASA_H	-0.208	-0.184	-0.203	-0.353	-0.290	-0.041	0.104	0.005	-0.364
FASA_P	0.208	0.184	0.203	0.353	0.290	0.041	-0.104	-0.005	0.364
Kier1	0.199	0.163	0.112	0.197	0.165	0.018	-0.184	-0.179	0.203
LogP	-0.518	-0.486	-0.310	-0.565	-0.548	-0.141	0.345	0.127	-0.202
LogS	0.419	0.402	0.368	0.508	0.519	0.203	-0.369	0.084	-0.069
PM3	0.137	0.091	0.150	0.148	0.127	0.005	-0.326	-0.266	0.098
SLogP	-0.450	-0.422	-0.259	-0.489	-0.460	-0.092	0.265	0.151	-0.281
SMR	0.132	0.098	0.071	0.097	0.086	-0.001	-0.231	-0.209	0.081
vsurf_Cp	-0.553	-0.563	-0.466	-0.687	-0.615	-0.470	-0.144	-0.322	-0.434
vsurf_D1	0.063	0.026	-0.025	-0.005	0.017	0.001	-0.368	-0.230	-0.169
vsurf_G	0.105	0.089	0.105	0.120	0.101	-0.016	-0.161	-0.188	0.146
vsurf_W1	0.309	0.267	0.189	0.339	0.301	0.044	-0.243	-0.148	0.248

Table 3.6. Linear regression analysis of the full data set (all 24 drugs) summarizing the resulting Pearson's correlation coefficients (r-values). Values between |0.5| and |0.7| are highlighted in yellow and indicate **moderate correlations** and values greater than |0.7| are highlighted in green and indicate **strong correlations**. Nine moderate correlations were identified, but no strong correlations were observed.

Standardized Drug Correlations	Ocular and Visceral Tissues								
	Cornea	Iris/CB	Lens	NR	RPE/C	Brain	SN	Kidney	Liver
Apol	0.130	0.097	0.070	0.084	0.269	-0.183	0.037	-0.209	0.244
ASA	0.122	0.091	0.063	0.099	0.249	-0.197	0.028	-0.198	0.286
ASA_H	-0.082	-0.079	-0.108	-0.305	0.043	0.002	0.243	-0.234	-0.328
ASA_P	0.168	0.135	0.121	0.258	0.230	-0.119	-0.088	-0.079	0.449
CASA+	0.333	0.288	0.183	0.344	0.427	-0.185	-0.151	-0.186	0.314
CASA-	0.343	0.317	0.128	0.324	0.381	-0.194	-0.105	-0.220	0.434
Dipole	0.204	0.144	0.316	0.255	0.392	-0.056	-0.237	-0.112	0.198
FASA_H	-0.158	-0.125	-0.162	-0.331	-0.203	0.140	0.184	0.005	-0.454
FASA_P	0.158	0.125	0.162	0.331	0.203	-0.140	-0.184	-0.005	0.454
Kier1	0.192	0.153	0.094	0.195	0.292	-0.180	-0.040	-0.179	0.374
LogP	-0.426	-0.378	-0.207	-0.479	-0.485	0.136	0.249	0.127	-0.286
LogS	0.299	0.265	0.270	0.401	0.368	-0.064	-0.271	0.084	-0.059
PM3	0.115	0.060	0.132	0.128	0.251	-0.098	-0.249	-0.266	0.195
SLogP	-0.365	-0.325	-0.165	-0.409	-0.417	0.177	0.193	0.151	-0.381
SMR	0.156	0.121	0.079	0.120	0.287	-0.185	0.012	-0.209	0.280
vsurf_Cp	-0.325	-0.290	-0.300	-0.497	-0.363	-0.153	-0.017	-0.322	-0.375
vsurf_D1	0.119	0.085	0.006	0.048	0.257	-0.134	0.050	-0.230	0.061
vsurf_G	0.123	0.109	0.115	0.147	0.259	-0.195	0.013	-0.188	0.329
vsurf_W1	0.269	0.218	0.142	0.308	0.347	-0.195	-0.143	-0.148	0.400

Table 3.7. Linear regression analysis of the mathematically standardized data sets summarizing the resulting Pearson's correlation coefficients (r-values). Drugs excluded from the data sets included HK-15 in the cornea, iris/CB, lens, and NR; HK-15 and HK-2 in the RPE/C; HK-15 and JHX-6 in the brain; JHX-1 and JHX-5 in the SN; and JHX-5 in the liver. No correlations were identified.

3.4.4 Clustered Correlations

Due to the inconclusive results obtained from the linear regression analyses, and the absence of strong correlations, cluster analysis was also employed to identify additional correlations. The clusters were calculated using hierarchical cluster analysis (HCA), an algorithm that studies the relationships between data by testing all possible hierarchical permutations present in a data set, in OriginPro™ using the Euclidean (2D straight line) distance metric and both average-linkage and complete-linkage clustering, the most popular distance metrics in HCA. This method allows for the minimization of

intra-cluster distances while maximizing inter-cluster distances using two different linkage criteria. A minimum of 5 drugs in a cluster was required for further analysis.

Figure 3.1 shows an example of the resulting HCA dendrograms for the ocular tissues and brain versus the physicochemical parameters Apol (hydrophilic) and Kier1 (structural). For each dendrogram (one per tissue per descriptor), the x-axis illustrates an arbitrary position of each of the 24 drug levels in 2D space, and the y-axis measures the 2D geometric distance between each coordinate pair ($x = \text{drug level}$, $y = \text{calculated descriptor value}$, or *vice-versa*). Drug coordinate pairs in closer proximity to each other are represented by linkages closer to the X-axis. Each subsequent linkage is representative of the formation of a larger cluster comprising all previously linked data points under. This process is continued until one final cluster remains. Each of the color coded groups for each tissue indicates a post-process specified cluster. Clusters with less than 5 data points were excluded from further analysis, and clusters with 5 or more data points were isolated into their respective groups and analyzed using linear regression analysis. Though many clusters looked similar between tissues and between descriptors, their correlations were generally not similar. The correlation results from the HCA clusters were separated into tables containing structural, hydrophilic, and hydrophobic parameters for both data sets with both average-linkage and complete-linkage cluster metrics. **Table 3.8** shows the cluster correlations for the structural parameters of the full data sets, while **Table 3.9** shows the resulting cluster correlations for the structural parameters of the standardized data sets. **Tables 3.12** and **3.13** show the cluster correlations for the hydrophilic parameters of the full data set, while **Tables 3.14** and **3.15** show the cluster correlations for the hydrophilic parameters of the standardized data set. Finally, **Tables 3.16** and **3.17** show the cluster correlations for the hydrophobic parameters of the full data

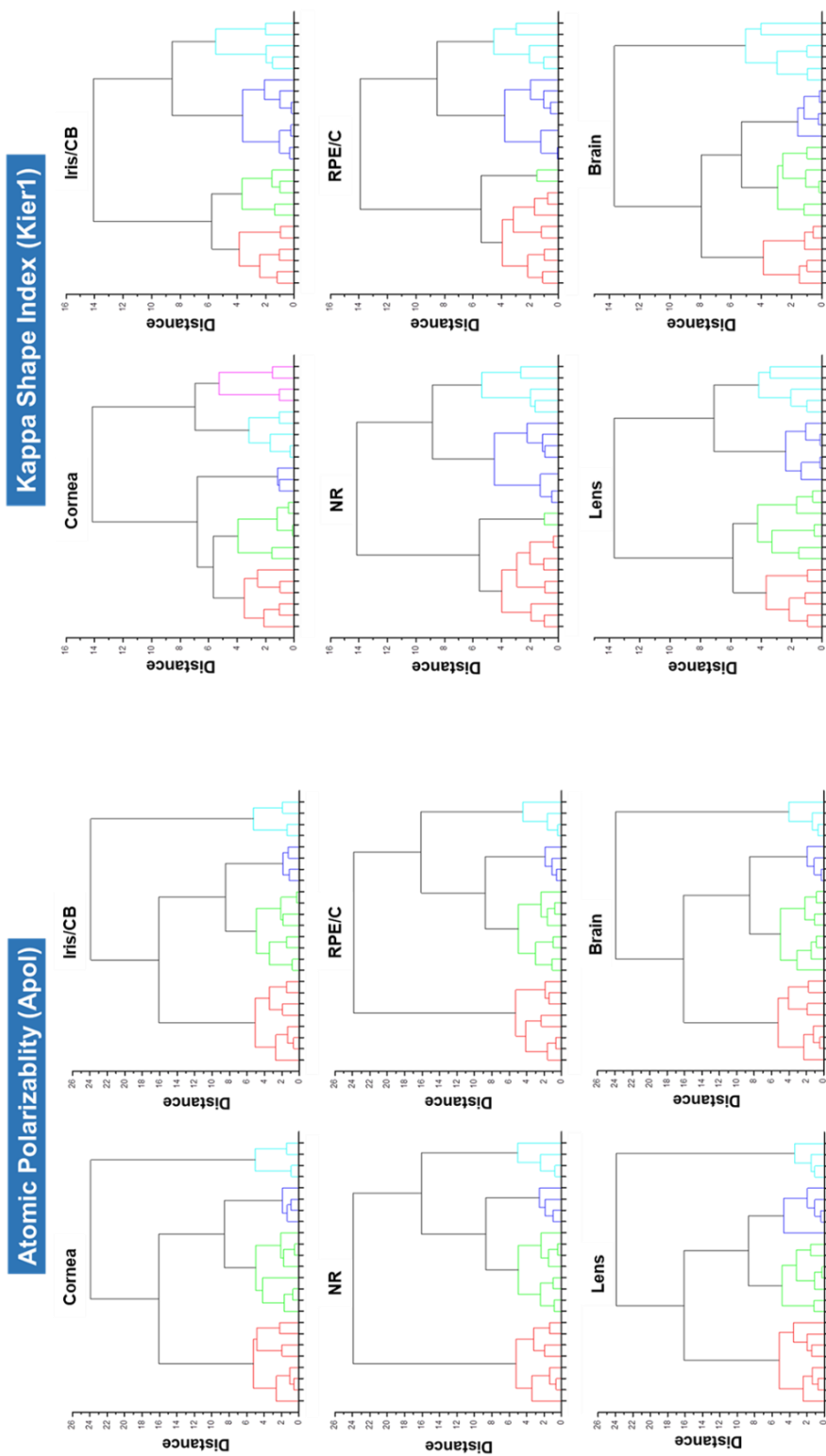


Figure 3.1. Examples of the resulting dendrograms after applying the HCA algorithm. Here are shown the dendrograms upon clustering 24 drug levels in the cornea, iris/CB, NR, RPE/C, lens, and brain drug levels against calculated physicochemical parameters for each drug. Each dendrogram chart shows the linkage of each data point on a 2D plane (drug level, calculated descriptor). Each data point is treated as its own individual cluster, and they are collectively connected until one large cluster remains. The different colors within each dendrogram (*i.e.*, red, green, blue, cyan, purple) represent a unique cluster of compounds, and clusters containing less than 5 drugs were excluded from further analysis. Each of these cluster groups were isolated and subject to linear regression analysis. Some cluster groups look similar, but this does not indicate similar correlation values.

set, while **Tables 3.18** and **3.19** show the cluster correlations for the hydrophobic parameters of the standardized data set.

Structural Parameter Cluster Correlations		Full Data Set Using Average-Linkage Algorithm								
		Cornea	Iris/CB	NR	RPE/C	Lens	Brain	Kidney	Liver	SN
Kier1	Cluster 1	0.620	0.650	0.426	0.761	0.372	0.681	-0.094	0.310	0.743
	Cluster 2	-0.344	0.630	0.744	0.059	0.660	0.702	0.403	-0.132	0.289
	Cluster 3	0.769	-	-0.575	-	-	0.342	0.397	-	0.426
SMR	Cluster 1	-0.129	0.335	0.065	-0.460	0.063	0.277	-0.162	0.202	-0.162
	Cluster 2	0.495	-0.752	-0.537	0.048	-0.317	0.670	0.232	-0.701	0.443
	Cluster 3	-	-0.124	-	-	-	-	-	-0.445	-
vsurf_Cp	Cluster 1	-0.613	-0.213	-0.427	-0.262	-0.464	0.189	0.256	-0.287	0.371
	Cluster 2	-0.208	0.916	-0.112	0.129	0.226	0.184	0.274	-0.401	0.767
	Cluster 3	0.023	0.119	-	-	-0.397	-	0.178	-	-
vsurf_G	Cluster 1	0.468	-0.220	0.320	0.258	-0.316	-0.425	-0.464	0.134	-0.510
	Cluster 2	0.045	0.188	-0.171	0.075	0.290	0.765	-0.490	-0.365	-0.593
	Cluster 3	-0.584	-0.169	-	-	-	-	-0.346	-0.393	-

Table 3.8. Cluster correlations for the structural parameters of the full data set for each tissue using the average-linkage algorithms. Cells shaded in **yellow** and **green** are moderate and strong cluster correlations, and cells shaded in **blue** are identical cluster correlations between both average-linkage and complete-linkage algorithms (**Table 3.9**). Additionally, cells shaded in **pink** are eliminated cluster correlations due to a non-linear distribution of data points. The drugs in each accepted cluster are listed below.

Kier1	Cornea	Cluster 3: HK-1, 2, 5, 9, 10, 13, 14
Kier1	Iris/CB	Cluster 1: JHX-1, 2, 3, 4; HK-3, 4, 6, 7, 8, 11, 12, 16
Kier1	Iris/CB	Cluster 2: HK-1, 2, 5, 9, 10, 13, 14
Kier1	NR	Cluster 2: HK-1, 2, 5, 9, 10, 13, 14
Kier1	NR	Cluster 3: JHX-2, 3, 4, 5, 6, 7, 8; HK-8
Kier1	RPE/C	Cluster 1: JHX-1, 2, 3, 4; HK-3, 4, 6, 7, 8, 11, 12, 16
Kier1	Lens	Cluster 2: HK-1, 2, 5, 9, 10, 13, 14
Kier1	Brain	Cluster 1: JHX-1, 2, 3; HK-3, 4, 6, 7, 8, 11, 12, 15, 16
Kier1	Brain:	Cluster 2: HK-1, 2, 5, 9, 10, 13, 14
Kier1	SN	Cluster 1: JHX-2, 3, 4; HK-3, 4, 8, 15
SMR	NR	Cluster 2: JHX-2, 3, 4, 5, 6, 7, 8; HK-8
SMR	Brain	Cluster 2: JHX-4, JHX-5, JHX-7, JHX-8, HK-6, HK-15
SMR	Liver	Cluster 2: HK-3, 6, 7, 11, 12, 15, 16
Cp	Iris/CB	Cluster 2: JHX-5; HK-4, 6, 9, 11, 16
Cp	SN	Cluster 2: JHX-2, 3, 4; HK-1, 3, 4, 6, 8, 9, 10, 11, 14, 15
G	SN	Cluster 1: JHX-2, 3, 4; HK-1, 3, 4, 6, 8, 9, 10, 11, 14, 15
G	SN	Cluster 2: JHX-6, 7, 8; HK-2, 5, 7, 12, 13, 16

Structural Parameter Cluster Correlations		Full Data Set Using Complete-Linkage Algorithm								
		Cornea	Iris/CB	NR	RPE/C	Lens	Brain	Kidney	Liver	SN
Kier1	Cluster 1	0.620	0.115	0.426	0.529	0.341	0.681	0.123	-0.302	-0.002
	Cluster 2	-0.344	0.630	0.744	0.695	0.660	0.702	0.403	-0.132	0.289
	Cluster 3	0.769	-0.291	-0.575	-0.503	-0.391	0.342	0.422	-0.045	0.426
SMR	Cluster 1	-0.129	-0.063	0.065	-0.460	-0.868	0.277	-0.356	0.212	0.776
	Cluster 2	0.718	-0.248	-0.537	0.048	-0.280	0.670	0.710	-0.400	0.443
	Cluster 3	0.495	-0.696	-	-	0.098	-	0.232	-	-
vsurf_Cp	Cluster 1	-0.775	0.135	-0.427	-0.367	-0.464	0.189	-0.231	-0.287	0.371
	Cluster 2	-0.170	-0.089	-0.474	-0.178	-0.397	0.184	0.924	-0.401	0.767
	Cluster 3	-0.795	-	-0.406	-	-0.609	-	0.178	-	-
vsurf_G	Cluster 1	0.086	0.172	0.320	0.486	-0.316	-0.425	-0.276	0.134	-0.510
	Cluster 2	0.344	0.225	-0.738	0.075	0.290	0.765	-0.381	0.144	-0.593
	Cluster 3	-0.308	-	0.619	-0.445	-	-	-0.346	-	-

Table 3.9. Cluster correlations for the structural parameters of the full data set for each tissue using the complete-linkage algorithms. Cells shaded in yellow and green are moderate and strong cluster correlations, and cells shaded in blue are identical cluster correlations between both average-linkage and complete-linkage algorithms (Table 3.8). Additionally, cells shaded in pink are eliminated cluster correlations due to a non-linear distribution of data points. The drugs in each accepted cluster are listed below.

Kier1	Cornea	Cluster 3: HK-1, 2, 5, 9, 10, 13, 14
Kier1	Iris/CB	Cluster 2: HK-1, 2, 5, 9, 10, 13, 14
Kier1	NR	Cluster 2: HK-1, 2, 5, 9, 10, 13, 14
Kier1	NR	Cluster 3: JHX-2, 3, 4, 5, 6, 7, 8; HK-8
Kier1	RPE/C	Cluster 1: JHX-1; HK-3, 4, 6, 7, 11, 12, 16
Kier1	RPE/C	Cluster 2: HK-1, 2, 5, 9, 10, 13, 14
Kier1	RPE/C	Cluster 3: JHX-2, 3, 4, 5, 6, 7, 8; HK-8
Kier1	Lens	Cluster 2: HK-1, 2, 5, 9, 10, 13, 14
Kier1	Brain	Cluster 1: JHX-1, 2, 3; HK-3, 4, 6, 7, 8, 11, 12, 15, 16
Kier1	Brain:	Cluster 2: HK-1, 2, 5, 9, 10, 13, 14
SMR	Cornea	Cluster 2: JHX-5, 8; HK 4, 15, 16
SMR	NR	Cluster 2: JHX-2, 3, 4, 5, 6, 7, 8; HK-8
SMR	Brain	Cluster 2: JHX-4, 5, 7, 8; HK-6, 15
SMR	Kidney	Cluster 2: JHX-2; HK-3, 4, 7, 8, 11, 15, 16
SMR	SN	Cluster 1: JHX-2, 3, 4, 6, 7, 8; HK-3, 4, 8, 15
Cp	SN	Cluster 2: JHX-2, 3, 4; HK-1, 3, 4, 6, 8, 9, 10, 11, 14, 15
G	NR	Cluster 3: JHX-3, 4, 7; HK-5, 12, 14
G	SN	Cluster 1: JHX-2, 3, 4; HK-1, 3, 4, 6, 8, 9, 10, 11, 14, 15
G	SN	Cluster 2: JHX-6, 7, 8; HK-2, 5, 7, 12, 13, 16

Structural Parameter Cluster Correlations		Standardized Data Set Using Average-Linkage Algorithm								
		Cornea	Iris/CB	NR	RPE/C	Lens	Brain	Kidney	Liver	SN
Kier1	Cluster 1	0.647	0.657	0.462	0.785	0.425	0.572	-0.094	0.310	0.756
	Cluster 2	0.769	0.630	0.744	0.549	0.660	-0.195	0.403	-0.132	0.426
	Cluster 3	-	-	-	-	-	-	0.397	-	0.289
SMR	Cluster 1	-0.747	0.209	0.065	0.156	0.063	-0.549	-0.162	0.358	-0.162
	Cluster 2	-0.827	-0.752	-0.537	0.048	-0.116	0.970	0.232	-0.400	-0.263
	Cluster 3	0.495	0.502	-	-	-	-	-	-	-0.187
vsurf_Cp	Cluster 1	-0.613	-0.213	0.070	-0.100	-0.527	0.253	0.256	-0.353	0.487
	Cluster 2	-0.208	0.916	-0.474	-0.030	0.226	-0.112	0.274	-0.401	0.767
	Cluster 3	0.023	0.119	-0.406	-0.343	-0.397	-	0.178	-	-
vsurf_G	Cluster 1	0.468	-0.220	0.320	0.486	0.170	-0.017	-0.464	0.134	-0.204
	Cluster 2	0.233	0.188	-0.738	-0.011	0.472	0.498	-0.490	-0.365	-0.593
	Cluster 3	-0.584	-0.169	0.619	0.075	0.452	-	-0.346	-0.393	-

Table 3.10. Cluster correlations for the structural parameters of the standardized data set for each tissue using the average-linkage algorithms. Cells shaded in yellow and green are moderate and strong cluster correlations, and cells shaded in blue are identical cluster correlations between both average-linkage and complete-linkage algorithms (Table 3.11). Additionally, cells shaded in pink are eliminated cluster correlations due to a non-linear distribution of data points. The drugs in each accepted cluster are listed below.

Kier1	Cornea	Cluster 1: JHX-1, 2, 3, 4; HK-3, 4, 6, 7, 8, 11, 12, 16
Kier1	Cornea	Cluster 2: HK-1, 2, 5, 9, 10, 13, 14
Kier1	Iris/CB	Cluster 1: JHX-1, 2, 3, 4; HK-3, 4, 6, 7, 8, 11, 12, 16
Kier1	Iris/CB	Cluster 2: HK-1, 2, 5, 9, 10, 13, 14
Kier1	NR	Cluster 2: HK-1, 2, 5, 9, 10, 13, 14
Kier1	RPE/C	Cluster 1: JHX-1, 2, 3, 4; HK-3, 4, 6, 7, 8, 11, 12, 16
Kier1	Lens	Cluster 2: HK-1, 2, 5, 9, 10, 13, 14
Kier1	SN	Cluster 1: JHX-2, 3, 4; HK-4, 8
SMR	Cornea	Cluster 1: JHX-1; HK-1, 2, 3, 5, 7, 11, 12, 13, 14
SMR	Cornea	Cluster 2: HK-4, 6, 9, 10, 16
SMR	NR	Cluster 2: JHX-2, 3, 4, 5, 6, 7, 8; HK-8
SMR	Brain	Cluster 1: JHX-1; HK-1, 2, 3, 4, 5, 9, 10, 11, 12, 13, 14
Cp	Iris/CB	Cluster 2: JHX-5; HK-4, 6, 9, 11, 16
Cp	SN	Cluster 2/3: JHX-6, 7, 8; HK-2, 5, 7, 12, 13, 16
G	NR	Cluster 3: JHX-3, 4, 7; HK-5, 12, 14
G	SN	Cluster 2/3: JHX-6, 7, 8; HK-2, 5, 7, 12, 13, 16

Structural Parameter Cluster Correlations		Standardized Data Set Using Complete-Linkage Algorithm								
		Cornea	Iris/CB	NR	RPE/C	Lens	Brain	Kidney	Liver	SN
Kier1	Cluster 1	0.143	-0.010	0.462	0.529	0.281	0.572	0.123	0.310	0.756
	Cluster 2	0.769	0.630	0.744	0.549	0.660	-0.195	0.403	-0.132	0.426
	Cluster 3	-0.257	-0.291	-0.575	-0.183	-0.391	-	0.422	-	0.289
SMR	Cluster 1	-0.747	0.190	0.065	0.156	-0.868	0.590	-0.356	-0.429	-0.162
	Cluster 2	-0.827	-0.696	-0.096	0.048	-0.280	0.003	0.710	0.358	-0.263
	Cluster 3	0.495	0.502	-	-	0.443	0.970	0.232	-0.103	-0.187
vsurf_Cp	Cluster 1	-0.775	-0.590	-0.314	-0.030	-0.527	0.718	-0.231	-0.353	-0.914
	Cluster 2	-0.293	-0.663	-0.474	0.847	0.226	-0.555	0.924	-0.401	0.096
	Cluster 3	0.023	0.030	-0.406	-0.121	-0.397	-0.112	0.178	-	0.767
vsurf_G	Cluster 1	0.086	0.461	0.412	0.486	-0.218	-0.580	-0.276	0.286	-0.410
	Cluster 2	0.430	0.815	-0.738	-0.011	0.472	-0.315	-0.381	-0.531	-0.232
	Cluster 3	-0.584	0.187	0.619	0.075	0.452	0.498	-0.346	0.091	-0.593

Table 3.11. Cluster correlations for the structural parameters of the standardized data set for each tissue using the complete-linkage algorithms. Cells shaded in yellow and green are moderate and strong cluster correlations, and cells shaded in blue are identical cluster correlations between both average-linkage and complete-linkage algorithms (Table 3.10). Additionally, cells shaded in pink are eliminated cluster correlations due to a non-linear distribution of data points. The drugs in each accepted cluster are listed below.

Kier1	Cornea	Cluster 2: HK-1, 2, 5, 9, 10, 13, 14
Kier1	Iris/CB	Cluster 2: HK-1, 2, 5, 9, 10, 13, 14
Kier1	NR	Cluster 2: HK-1, 2, 5, 9, 10, 13, 14
Kier1	Lens	Cluster 2: HK-1, 2, 5, 9, 10, 13, 14
Kier1	SN	Cluster 1: JHX-2, 3, 4; HK-4, 8
SMR	Cornea	Cluster 1: JHX-1; HK-1, 2, 3, 5, 7, 11, 12, 13, 14
SMR	Cornea	Cluster 2: HK-4, 6, 9, 10, 16
SMR	Kidney	Cluster 2: JHX-2; HK-3, 4, 7, 8, 11, 15, 16
Cp	Brain	Cluster 1: JHX-1, 8; HK-3, 4, 9, 10, 12
Cp	SN	Cluster 2/3: JHX-6, 7, 8; HK-2, 5, 7, 12, 13, 16
G	Iris/CB	Cluster 2: JHX-2, 3, 4; HK-5, 12, 14
G	NR	Cluster 3: JHX-3, 4, 7; HK-5, 12, 14
G	SN	Cluster 2/3: JHX-6, 7, 8; HK-2, 5, 7, 12, 13, 16

Hydrophilic Parameter Cluster Correlations		Full Data Set Using Average Linkage Algorithm								
		Cornea	Iris/CB	NR	RPE/C	Lens	Brain	Kidney	Liver	SN
Apol	Cluster 1	0.345	0.342	0.390	0.502	0.492	0.165	-0.243	-0.032	-0.444
	Cluster 2	-0.063	-0.168	-0.454	-0.476	-0.461	-0.410	-0.161	-0.170	0.105
	Cluster 3	-	-	-	-	-	-	-	-	-
ASA	Cluster 1	0.374	0.380	0.441	0.528	0.535	0.128	-0.328	0.099	-0.423
	Cluster 2	-0.002	-0.128	-0.185	-0.215	-0.344	-0.445	0.077	0.015	-0.074
	Cluster 3	-	-	-	-	-	-	-	-	-
ASA_P	Cluster 1	-0.513	-0.453	-0.361	-0.244	-0.408	-0.507	-0.540	-0.525	-0.550
	Cluster 2	0.578	0.439	0.254	0.185	0.331	0.334	-0.356	0.143	-0.904
	Cluster 3	0.496	0.420	0.176	0.185	-0.066	0.295	0.289	0.582	0.743
CASA+	Cluster 1	0.864	0.937	0.890	0.720	0.573	0.776	0.820	0.891	0.930
	Cluster 2	0.195	0.196	0.520	0.479	0.409	0.473	0.334	0.220	0.089
	Cluster 3	-0.211	-0.061	0.257	0.202	0.447	0.283	-0.134	-0.487	-0.224
CASA-	Cluster 1	-0.280	-0.301	-0.158	-0.084	-0.045	-0.264	-0.074	0.318	-0.370
	Cluster 2	-0.463	-0.389	-0.256	-0.270	0.036	-0.157	-0.007	-0.025	0.014
	Cluster 3	-	-	-	-	-	-	-	-	-
Dipole	Cluster 1	0.227	-0.261	0.547	0.346	-0.298	-0.694	-0.332	-0.047	-0.124
	Cluster 2	0.542	-0.116	-0.856	0.210	-0.038	0.675	-0.178	0.030	-0.315
	Cluster 3	-0.692	-0.318	0.715	-	-	-	0.130	-	-
FASA_P	Cluster 1	0.450	-0.117	0.244	0.365	-0.283	-0.566	-0.382	0.093	-0.586
	Cluster 2	0.524	-0.196	-0.209	-0.294	0.540	0.477	-0.596	0.612	-0.631
	Cluster 3	-0.379	-0.095	0.567	-	-	-	-0.148	0.299	-
LogS	Cluster 1	-0.167	0.153	0.151	0.023	-0.570	-0.408	0.150	-0.220	0.355
	Cluster 2	0.246	0.751	0.391	-0.094	-0.367	0.528	0.446	-0.495	0.305
	Cluster 3	0.912	-0.411	-	-	-	-	0.727	0.305	-
PM3	Cluster 1	-0.002	0.459	0.200	-0.091	-0.480	-0.620	-0.480	-0.264	0.165
	Cluster 2	-0.751	0.050	-0.486	-0.327	0.102	0.067	-0.802	-0.724	-0.552
	Cluster 3	-0.239	-0.632	-	-	-0.227	-0.314	0.808	0.549	-0.419
vsurf_W1	Cluster 1	0.190	0.041	0.052	0.102	0.094	-0.036	-0.625	-0.426	-0.813
	Cluster 2	-0.087	-0.151	0.014	-0.053	-0.013	-0.185	0.006	-0.170	-0.418
	Cluster 3	-0.082	-0.064	-0.390	-0.372	-0.420	-0.373	0.104	0.335	0.718

Table 3.12. Cluster correlations for the hydrophilic parameters of the full data set for each tissue using the average-linkage algorithms. Cells shaded in yellow and green are moderate and strong cluster correlations, and cells shaded in blue are identical cluster correlations between both average-linkage and complete-linkage algorithms (Table 3.13). Additionally, cells shaded in pink are eliminated cluster correlations due to a non-linear distribution of data points. The drugs in each accepted cluster are listed below.

Apol	RPE/C	Cluster 1: JHX-1, 2, 3, 4; HK-3, 4, 7, 8, 11, 12, 15, 16
ASA	RPE/C	Cluster 1: JHX-1, 2, 3, 4; HK-3, 4, 7, 8, 11, 12, 15, 16
ASA	Lens	Cluster 1: JHX-1, 2, 3, 4; HK-3, 4, 7, 8, 11, 12, 15, 16
ASA_P	Cornea	Cluster 1: JHX-1; HK-1, 5, 6, 10, 11, 14, 15
ASA_P	Cornea	Cluster 2: JHX-2, 3; HK-2, 3, 7, 8, 12, 16
ASA_P	Brain	Cluster 1: JHX-1; HK-1, 5, 6, 10, 11, 14, 15
ASA_P	Kidney	Cluster 1: JHX-1; HK-1, 5, 6, 10, 11, 14, 15

ASA_P	Liver	Cluster 1: JHX-1; HK-1, 5, 6, 10, 11, 14, 15
ASA_P	SN	Cluster 2: JHX-2, 3; HK-2, 3, 7, 8, 12, 16
ASA_P	SN	Cluster 3: JHX-4, 5, 6, 7, 8; HK-4
CASA+	Cornea	Cluster 1: JHX-1, 2, 3, 5, 6, 7
CASA+	NR	Cluster 2: HK-1, 5, 7, 9, 10, 11, 12, 13, 14, 15, 16
CASA+	Brain	Cluster 1: JHX-1, 2, 3, 5, 6, 7
CASA+	Kidney	Cluster 1: JHX-1, 2, 3, 5, 6, 7
CASA+	SN	Cluster 1: JHX-1, 2, 3, 5, 6, 7
Dipole	Cornea	Cluster 2: JHX-2, 3, 4, 7; HK-1, 2, 5, 8, 13, 14
Dipole	Cornea	Cluster 3: JHX-5; HK-4, 6, 9, 16
Dipole	NR	Cluster 1: JHX-1, 5, 8; HK-3, 4, 6, 7, 9, 10, 11, 13, 16
Dipole	NR	Cluster 3: JHX-3, 4, 7; HK-5, 12, 14
Dipole	Brain	Cluster 1: JHX-1, 7, 8; HK-3, 4, 5, 9, 10, 11, 12, 13, 14
Dipole	Brain	Cluster 2: JHX-2, 3, 6; HK-1, 2, 7, 8, 16
FASA_P	Cornea	Cluster 2: JHX-2, 3, 4, 7; HK-1, 2, 5, 8, 13, 14
FASA_P	NR	Cluster 3: JHX-3, 4, 7; HK-5, 12, 14
FASA_P	Lens	Cluster 2: JHX-2, 3, 4, 6; HK-1, 2, 8, 14, 16
FASA_P	Brain	Cluster 1: JHX-1, 7, 8; HK-3, 4, 5, 9, 10, 11, 12, 13, 14
FASA_P	Kidney	Cluster 2: JHX-2; HK-1, 3, 4, 5, 6, 7, 8, 13, 14, 16
FASA_P	SN	Cluster 1: JHX-3, 4; HK-1, 3, 6, 9, 10, 11, 14, 15
FASA_P	SN	Cluster 2: JHX-6, 7, 8; HK-2, 5, 7, 12, 13, 16
LogS	Cornea	Cluster 3: JHX-5; HK-4, 6, 9, 16
LogS	Iris/CB	Cluster 2: JHX-5; HK-4, 6, 9, 16
LogS	Lens	Cluster 1: JHX-1, 2, 3, 4, 6; HK-1, 2, 8, 14, 16
LogS	Brain	Cluster 2: JHX-2, 3, 6; HK-1, 2, 7, 8, 16
PM3_Dipole	Cornea	Cluster 2: HK-1, 2, 3, 5, 12, 13
PM3_Dipole	Iris/CB	Cluster 3: JHX-2, 3, 4, 6, 7; HK-8
PM3_Dipole	Brain	Cluster 1: JHX-1, 4, 5, 7, 8; HK-3, 4, 11, 12
PM3_Dipole	Liver	Cluster 2: JHX-3, 4, 6, 7, 8; HK-8
PM3_Dipole	Liver	Cluster 3: HK-1, 2, 3, 5, 6, 9, 10, 13, 14
W1	Kidney	Cluster 1: JHX-1; HK-2, 3, 4, 6, 7, 8, 12, 16
W1	SN	Cluster 1: JHX-1; HK-2, 3, 4, 6, 7, 8, 12, 16
W1	SN	Cluster 3: JHX-2, 3, 4, 5, 6, 7, 8

Hydrophilic Parameter Cluster Correlations		Full Data Set Using Complete Linkage Algorithm								
		Cornea	Iris/CB	NR	RPE/C	Lens	Brain	Kidney	Liver	SN
Apol	Cluster 1	0.345	0.342	0.390	0.502	0.492	0.165	-0.243	-0.032	-0.444
	Cluster 2	-0.063	-0.168	-0.454	-0.476	-0.461	-0.410	-0.161	-0.170	0.105
	Cluster 3	-	-	-	-	-	-	-	-	-
ASA	Cluster 1	0.374	0.380	0.441	0.528	0.535	0.128	-0.328	0.099	-0.423
	Cluster 2	-0.002	-0.128	-0.185	-0.215	-0.344	-0.445	0.077	0.015	-0.074
	Cluster 3	-	-	-	-	-	-	-	-	-
ASA_P	Cluster 1	-0.172	-0.093	0.045	0.129	0.096	0.131	0.106	0.260	0.274
	Cluster 2	-0.013	0.078	-0.087	-0.046	-0.164	-0.235	0.145	0.140	0.641
	Cluster 3	-	-	-	-	-	-	-	-	-
CASA+	Cluster 1	0.305	0.330	0.160	-0.038	0.068	-0.063	0.065	0.677	0.801
	Cluster 2	0.195	0.196	0.520	0.479	0.409	0.473	0.334	0.220	0.089
	Cluster 3	-0.211	-0.061	0.257	0.202	0.447	0.283	-0.134	-0.487	-0.224
CASA-	Cluster 1	-0.280	-0.301	-0.158	-0.084	-0.045	-0.264	-0.074	0.318	-0.370
	Cluster 2	-0.463	-0.389	-0.256	-0.270	0.036	-0.157	-0.007	-0.025	0.014
	Cluster 3	-	-	-	-	-	-	-	-	-
Dipole	Cluster 1	0.558	-0.261	0.547	0.443	0.008	-0.443	-0.332	0.146	0.193
	Cluster 2	0.542	-0.116	-0.856	0.210	0.711	0.377	-0.178	-0.188	-0.312
	Cluster 3	-	-0.318	0.715	-0.568	-0.039	-	0.130	-	-0.315
FASA_P	Cluster 1	0.450	0.356	0.244	0.369	-0.283	-0.566	-0.382	0.093	-0.289
	Cluster 2	0.515	-0.196	-0.209	-0.294	0.540	0.477	-0.596	0.612	0.218
	Cluster 3	0.029	0.318	0.567	0.289	-	-	-0.148	0.299	-
LogS	Cluster 1	-0.246	0.153	-0.430	0.369	-0.081	-0.519	-0.696	0.138	0.371
	Cluster 2	0.246	0.751	0.218	-0.178	0.678	0.377	0.984	0.530	-0.046
	Cluster 3	-	-0.411	0.048	-	0.768	-	0.438	-	-
PM3	Cluster 1	0.034	-0.006	0.200	0.394	0.558	-0.620	-0.480	-0.264	0.165
	Cluster 2	0.540	-0.484	-0.486	-0.405	-0.227	0.067	-0.802	-0.724	0.459
	Cluster 3	-0.061	-0.141	-	-	-0.186	-0.314	0.808	0.549	0.747
vsurf_W1	Cluster 1	0.219	0.182	0.168	0.083	0.082	-0.113	-0.480	-0.571	-0.800
	Cluster 2	-0.078	-0.070	0.117	-0.001	0.022	-0.161	0.204	-0.097	-0.141
	Cluster 3	-0.082	-0.064	-0.390	-0.372	-0.420	-0.373	0.104	0.335	0.718

Table 3.13. Cluster correlations for the hydrophilic parameters of the full data set for each tissue using the complete-linkage algorithms. Cells shaded in yellow and green are moderate and strong cluster correlations, and cells shaded in blue are identical cluster correlations between both average-linkage and complete-linkage algorithms (Table 3.12). Additionally, cells shaded in pink are eliminated cluster correlations due to a non-linear distribution of data points. The drugs in each accepted cluster are listed below.

Apol	RPE/C	Cluster 1: JHX-1, 2, 3, 4; HK-3, 4, 7, 8, 11, 12, 15, 16
ASA	RPE/C	Cluster 1: JHX-1, 2, 3, 4; HK-3, 4, 7, 8, 11, 12, 15, 16
ASA	Lens	Cluster 1: JHX-1, 2, 3, 4; HK-3, 4, 7, 8, 11, 12, 15, 16
ASA_P	SN	Cluster 2: JHX-2, 3, 4, 5, 6, 7, 8; HK-3, 4, 8
CASA+	NR	Cluster 2: HK-1, 5, 7, 9, 10, 11, 12, 13, 14, 15, 16
CASA+	SN	Cluster 1: JHX-1, 2, 3, 4, 5, 6, 7, 8
Dipole	Cornea	Cluster 1: JHX-1, 8; HK-3, 6, 7, 9, 10, 11, 12

Dipole	Cornea	Cluster 2: JHX-2, 3, 4, 7; HK-1, 2, 5, 8, 13, 14
Dipole	NR	Cluster 1: JHX-1, 5, 8; HK-3, 4, 6, 7, 9, 10, 11, 13, 16
Dipole	NR	Cluster 3: JHX-3, 4, 7; HK-5, 12, 14
Dipole	Lens	Cluster 2: JHX-5, 8; HK-3, 6, 7, 10, 15
FASA_P	Cornea	Cluster 2: JHX-2, 3, 4, 6, 7; HK-1, 2, 5, 8, 13, 14
FASA_P	NR	Cluster 3: JHX-3, 4, 7; HK-5, 12, 14
FASA_P	Lens	Cluster 2: JHX-2, 3, 4, 6; HK-1, 2, 8, 14, 16
FASA_P	Brain	Cluster 1: JHX-1, 7, 8; HK-3, 4, 5, 9, 10, 11, 12, 13, 14
FASA_P	Kidney	Cluster 2: JHX-2; HK-1, 3, 4, 5, 6, 7, 8, 13, 14, 16
LogS	Iris/CB	Cluster 2: JHX-5; HK-4, 6, 9, 16
LogS	Lens	Cluster 2: JHX-5, 8; HK-3, 6, 10, 15
LogS	Lens	Cluster 3: JHX-7; HK-4, 5, 7, 9, 11, 12, 13
LogS	Brain	Cluster 1: JHX-1, 4, 5, 7, 8; HK-3, 4, 6, 9, 10, 11, 12
LogS	Kidney	Cluster 1: JHX-1, 3, 4, 5, 8; HK-4, 7, 8
LogS	Liver	Cluster 2: JHX-3, 4, 6, 7, 8; HK-2, 3, 7, 8, 10, 13, 16
PM3_Dipole	Lens	Cluster 1: JHX-1, 5, 7, 8; HK-3, 4, 6, 7, 11, 12, 15
PM3_Dipole	Brain	Cluster 1: JHX-1, 4, 5, 7, 8; HK-3, 4, 11, 12
PM3_Dipole	Liver	Cluster 2: JHX-3, 4, 6, 7, 8; HK-8
PM3_Dipole	Liver	Cluster 3: HK-1, 2, 3, 5, 6, 9, 10, 13, 14
PM3_Dipole	SN	Cluster 3: HK-1, 2, 5, 9, 13
W1	Liver	Cluster 1: JHX-1; HK-2, 3, 4, 6, 7, 8, 16
W1	SN	Cluster 1: JHX-1; HK-2, 3, 4, 6, 7, 8, 16
W1	SN	Cluster 3: JHX-2, 3, 4, 5, 6, 7, 8

Hydrophilic Parameter Cluster Correlations		Standardized Data Set Using Average-Linkage Algorithm								
		Cornea	Iris/CB	NR	RPE/C	Lens	Brain	Kidney	Liver	SN
Apol	Cluster 1	0.448	0.479	0.768	0.766	-0.802	0.236	-0.243	-0.032	-0.306
	Cluster 2	-0.063	-0.168	0.775	-0.317	0.328	-0.410	-0.161	-0.170	0.759
	Cluster 3	-	-	-0.454	-	-0.461	-	-	-	0.105
ASA	Cluster 1	0.446	0.484	0.583	0.749	0.604	0.135	-0.328	0.099	-0.328
	Cluster 2	-0.002	-0.128	-0.185	-0.247	-0.344	-0.445	0.077	0.015	-0.074
	Cluster 3	-	-	-	-	-	-	-	-	-
ASA_P	Cluster 1	-0.620	-0.497	-0.303	-0.128	-0.358	-0.549	-0.540	-0.525	-0.630
	Cluster 2	0.801	0.439	0.254	0.660	0.611	-0.664	-0.356	-0.317	-0.242
	Cluster 3	0.496	0.420	0.176	0.185	-0.066	-	0.289	-	-
CASA+	Cluster 1	0.864	0.937	0.890	0.720	0.573	0.677	0.820	0.640	0.440
	Cluster 2	0.073	0.069	0.527	0.289	0.366	0.620	0.334	0.220	0.089
	Cluster 3	-0.211	-0.061	0.257	-	0.447	0.283	-0.134	-0.487	-0.224
CASA-	Cluster 1	-0.280	-0.301	-0.158	-0.439	-0.045	-0.264	-0.074	0.318	-0.370
	Cluster 2	-0.401	-0.298	-0.083	-0.075	0.335	0.228	-0.007	-0.025	0.014
	Cluster 3	-	-	-	-	-	-	-	-	-
Dipole	Cluster 1	0.227	-0.261	0.547	0.443	0.008	-0.443	-0.332	-0.047	-0.124
	Cluster 2	0.542	-0.116	-0.856	-0.385	0.667	0.595	-0.178	0.034	-0.315
	Cluster 3	-0.692	-0.318	0.715	0.099	0.701	-	0.130	0.497	-
FASA_P	Cluster 1	0.450	-0.117	0.321	0.369	-0.069	-0.305	-0.382	0.093	-0.586
	Cluster 2	0.524	-0.196	-0.209	-0.019	0.047	0.076	-0.596	0.612	-0.631
	Cluster 3	-0.379	-0.095	0.567	-0.294	0.750	-	-0.148	0.299	-
LogS	Cluster 1	-0.167	0.153	-0.098	0.815	-0.081	-0.107	0.150	-0.220	0.355
	Cluster 2	0.168	0.751	-0.153	-0.331	0.307	0.507	0.446	-0.495	0.305
	Cluster 3	0.912	0.072	-	-	0.768	-	0.727	0.305	-
PM3	Cluster 1	-0.002	0.459	0.200	0.281	-0.480	-0.620	-0.480	-0.152	-0.552
	Cluster 2	-0.412	0.050	-0.486	-0.327	-0.589	0.603	-0.802	-0.724	-0.492
	Cluster 3	-0.394	-0.632	-	-	-0.227	-0.314	0.808	0.549	-
vsurf_W1	Cluster 1	0.219	0.182	0.168	0.513	0.082	-0.113	-0.625	-0.426	0.797
	Cluster 2	0.241	0.245	0.449	0.402	0.311	0.196	0.006	-0.170	0.305
	Cluster 3	-0.082	-0.064	-0.390	-0.372	-0.420	-0.519	0.104	0.171	-0.799

Table 3.14. Cluster correlations for the hydrophilic parameters of the standardized data set for each tissue using the average-linkage algorithms. Cells shaded in yellow and green are moderate and strong cluster correlations, and cells shaded in blue are identical cluster correlations between both average-linkage and complete-linkage algorithms (Table 3.15). Additionally, cells shaded in pink are eliminated cluster correlations due to a non-linear distribution of data points. The drugs in each accepted cluster are listed below.

Apol
Apol

NR
RPE/C

Cluster 2: HK-3, 4, 7, 8, 12
Cluster 1: JHX-1, 2, 3, 4; HK-3, 4, 7, 8, 11, 12, 16

Apol	Lens	Cluster 1: JHX-1, 2, 3, 4; HK-8, 16
ASA	NR	Cluster 1: JHX-1, 2, 3, 4; HK-3, 4, 7, 8, 11, 12, 16
ASA	RPE/C	Cluster 1: JHX-1, 2, 3, 4; HK-3, 4, 7, 8, 11, 12, 16
ASA	Lens	Cluster 1: JHX-1, 2, 3, 4; HK-3, 4, 7, 8, 11, 12, 16
ASA_P	Cornea	Cluster 1: JHX-1; HK-1, 5, 6, 10, 11, 14
ASA_P	Cornea	Cluster 2: JHX-2, 3; HK-2, 3, 7, 8, 12, 15, 16
ASA_P	Brain	Cluster 1: JHX-1; HK-1, 5, 6, 10, 11, 14
ASA_P	Brain	Cluster 2: JHX-2, 3, 4, 5; HK-2, 3, 4, 7, 8, 12, 16
ASA_P	Kidney	Cluster 1: JHX-1; HK-1, 5, 6, 10, 11, 14, 15
ASA_P	Liver	Cluster 1: JHX-1; HK-1, 5, 6, 10, 11, 14, 15
ASA_P	SN	Cluster 1: JHX-2, 3; HK-2, 3, 4, 6, 7, 8, 12, 16
CASA+	Brain	Cluster 2: HK-1, 5, 7, 9, 10, 11, 12, 13, 14, 16
CASA+	Kidney	Cluster 1: JHX-1, 2, 3, 5, 6, 7
Dipole	Cornea	Cluster 2: JHX-2, 3, 4, 7; HK-1, 2, 5, 8, 13, 14
Dipole	Cornea	Cluster 3: JHX-5; HK-4, 6, 9, 16
Dipole	NR	Cluster 1: JHX-1, 5, 8; HK-3, 4, 6, 7, 9, 10, 11, 13, 16
Dipole	NR	Cluster 3: JHX-3, 4, 7; HK-5, 12, 14
Dipole	Lens	Cluster 3: JHX-3, 6; HK-1, 2, 8, 16
FASA_P	Cornea	Cluster 2: JHX-2, 3, 4, 7; HK-1, 2, 5, 8, 13, 14
FASA_P	NR	Cluster 3: JHX-3, 4, 7; HK-5, 12, 14
FASA_P	Lens	Cluster 3: JHX-3, 6; HK-1, 2, 8, 16
FASA_P	Kidney	Cluster 2: JHX-2; HK-1, 3, 4, 5, 6, 7, 8, 13, 14, 16
FASA_P	SN	Cluster 1: JHX-3, 4; HK-1, 3, 6, 9, 10, 11, 14, 15
FASA_P	SN	Cluster 2: JHX-6, 7, 8; HK-2, 5, 7, 12, 13, 16
LogS	Cornea	Cluster 2: JHX-2, 3, 4, 7; HK-1, 2, 5, 8, 13, 14
LogS	Iris/CB	Cluster 2: JHX-5; HK-4, 6, 9, 16
LogS	Lens	Cluster 3: JHX-7; HK-4, 5, 7, 9, 11, 12, 13
PM3_Dipole	Iris/CB	Cluster 3: JHX-2, 3, 4, 6, 7; HK-8
PM3_Dipole	Brain	Cluster 1: JHX-1, 4, 5, 7, 8; HK-3, 4, 11, 12
PM3_Dipole	Liver	Cluster 2: JHX-3, 4, 6, 7, 8; HK-8
PM3_Dipole	Liver	Cluster 3: HK-1, 2, 3, 5, 6, 9, 10, 13, 14
W1	Kidney	Cluster 1: JHX-1; HK-2, 3, 4, 6, 7, 8, 12, 16
W1	SN	Cluster 1: JHX-2, 3, 4, 6, 7, 8

Hydrophilic Parameter Cluster Correlations		Standardized Data Set Using Complete Linkage Algorithm								
		Cornea	Iris/CB	NR	RPE/C	Lens	Brain	Kidney	Liver	SN
Apol	Cluster 1	0.448	0.479	0.560	0.766	-0.802	-0.325	-0.243	-0.032	-0.284
	Cluster 2	-0.063	-0.168	-0.454	-0.317	0.328	-0.410	-0.161	-0.170	0.105
	Cluster 3	-	-	-	-	-0.461	-	-	-	-
ASA	Cluster 1	0.446	0.484	0.583	0.749	0.604	0.135	-0.328	0.099	-0.328
	Cluster 2	-0.002	-0.128	-0.185	-0.247	-0.344	-0.445	0.077	0.015	-0.074
	Cluster 3	-	-	-	-	-	-	-	-	-
ASA_P	Cluster 1	-0.275	-0.178	0.020	-0.089	0.083	0.142	0.106	0.260	-0.600
	Cluster 2	-0.013	-0.149	-0.136	-0.105	0.021	-0.764	0.145	0.009	0.805
	Cluster 3	-	-	-	-	-	-	-	-	-0.242
CASA+	Cluster 1	0.864	0.937	0.890	0.720	0.573	0.677	0.065	0.562	0.440
	Cluster 2	0.073	0.069	0.527	0.515	0.366	0.620	0.334	0.220	0.089
	Cluster 3	-0.211	-0.061	0.257	-	0.447	0.283	-0.134	-0.487	-0.224
CASA-	Cluster 1	-0.280	-0.301	-0.158	-0.439	-0.045	-0.264	-0.074	0.318	-0.370
	Cluster 2	-0.401	-0.298	-0.083	-0.075	0.335	0.228	-0.007	-0.025	0.014
	Cluster 3	-	-	-	-	-	-	-	-	-
Dipole	Cluster 1	0.558	-0.261	0.680	0.443	0.008	-0.443	-0.332	-0.360	-0.312
	Cluster 2	0.542	-0.116	-0.856	-0.385	0.667	0.377	-0.178	-0.188	-0.315
	Cluster 3	-	-0.318	0.715	0.099	-0.901	-	0.130	-	-
FASA_P	Cluster 1	0.450	0.356	0.321	0.369	-0.283	-0.305	-0.382	0.093	-0.006
	Cluster 2	0.524	0.828	-0.209	-0.019	-	0.076	-0.596	0.612	0.417
	Cluster 3	-0.379	0.200	0.567	-0.294	0.750	-	-0.148	0.299	0.728
LogS	Cluster 1	-0.167	0.153	-0.430	-0.270	0.682	0.557	-0.696	0.138	0.371
	Cluster 2	0.912	0.751	0.218	-0.106	-0.081	0.227	0.984	-0.220	-0.046
	Cluster 3	-0.621	-0.411	0.048	-0.178	-0.379	-	0.438	-0.257	-
PM3	Cluster 1	0.034	-0.632	0.200	0.120	0.472	-0.620	-0.480	-0.152	0.780
	Cluster 2	-0.412	-0.484	-0.486	-0.900	-0.227	0.603	-0.802	-0.724	0.747
	Cluster 3	-0.157	-0.172	-	-0.405	0.102	-0.445	0.808	0.549	-
vsurf_W1	Cluster 1	0.219	0.182	0.168	0.780	0.082	-0.113	-0.480	0.505	0.219
	Cluster 2	0.241	0.245	0.449	0.171	0.311	0.196	0.204	0.465	-
	Cluster 3	-0.082	-0.064	-0.390	-0.372	-0.420	-0.519	0.104	-	-

Table 3.15. Cluster correlations for the hydrophilic parameters of the standardized data set for each tissue using the complete-linkage algorithms. Cells shaded in yellow and green are moderate and strong cluster correlations, and cells shaded in blue are identical cluster correlations between both average-linkage and complete-linkage algorithms (Table 3.14). Additionally, cells shaded in pink are eliminated cluster correlations due to a non-linear distribution of data points. The drugs in each accepted cluster are listed below.

Apol	NR	Cluster 1: JHX-1, 2, 3, 4; HK-3, 4, 7, 8, 11, 12, 16
Apol	RPE/C	Cluster 1: JHX-1, 2, 3, 4; HK-3, 4, 7, 8, 11, 12, 16
Apol	Lens	Cluster 1: JHX-1, 2, 3, 4; HK-8, 16

ASA	NR	Cluster 1: JHX-1, 2, 3, 4; HK-3, 4, 7, 8, 11, 12, 16
ASA	RPE/C	Cluster 1: JHX-1, 2, 3, 4; HK-3, 4, 7, 8, 11, 12, 16
ASA	Lens	Cluster 1: JHX-1, 2, 3, 4; HK-3, 4, 7, 8, 11, 12, 16
ASA_P	Brain	Cluster 1: JHX-1; HK-1, 2, 5, 6, 7, 10, 11, 12, 14, 16
ASA_P	SN	Cluster 1: JHX-2, 3; HK-2, 3, 6, 7, 8, 12, 16
CASA+	Brain	Cluster 2: HK-1, 5, 7, 9, 10, 11, 12, 13, 14, 16
Dipole	Cornea	Cluster 1: JHX-1, 8; HK-3, 6, 7, 9, 10, 11, 12
Dipole	Cornea	Cluster 2: JHX-2, 3, 4, 7; HK-1, 2, 5, 8, 13, 14
Dipole	NR	Cluster 1: JHX-1, 5, 8; HK-3, 4, 7, 9, 13
Dipole	NR	Cluster 3: JHX-3, 4, 7; HK-5, 12, 14
Dipole	Lens	Cluster 3: JHX-2, 4; HK-1, 2, 16
FASA_P	Cornea	Cluster 2: JHX-2, 3, 4, 7; HK-1, 2, 5, 8, 13, 14
FASA_P	Iris/CB	Cluster 2: JHX-5; HK-4, 6, 9, 16
FASA_P	NR	Cluster 3: JHX-3, 4, 7; HK-5, 12, 14
FASA_P	Lens	Cluster 3: JHX-3, 6; HK-1, 2, 8, 16
FASA_P	Kidney	Cluster 2: JHX-2; HK-1, 3, 4, 5, 6, 7, 8, 13, 14, 16
LogS	Cornea	Cluster 2: JHX-2, 3, 4, 7; HK-1, 2, 5, 8, 13, 14
LogS	Cornea	Cluster 3: JHX-4, 7; HK-1, 5, 8, 13, 14
LogS	Iris/CB	Cluster 2: JHX-5; HK-4, 6, 9, 16
LogS	Lens	Cluster 1: JHX-1, 2, 4; HK-4, 5, 9, 12, 13, 14
LogS	Kidney	Cluster 1: JHX-1, 3, 4, 5, 8; HK-4, 7, 8
LogS	Kidney	Cluster 2: JHX-6, 7; HK-2, 10, 12
PM3_Dipole	Iris/CB	Cluster 3: JHX-2, 3, 4, 6, 7; HK-8
PM3_Dipole	RPE/C	Cluster 2: JHX-2, 3, 4, 6; HK-8
PM3_Dipole	Brain	Cluster 1: JHX-1, 4, 5, 7, 8; HK-3, 4, 11, 12
PM3_Dipole	Liver	Cluster 2: JHX-3, 4, 6, 7, 8; HK-8
PM3_Dipole	Liver	Cluster 3: HK-1, 2, 3, 5, 6, 9, 10, 13, 14
W1	RPE/C	Cluster 1: JHX-1; HK-3, 4, 6, 7, 8

Hydrophobic Parameter Cluster Correlations		Full Data Set Using Average-Linkage Algorithm								
		Cornea	Iris/CB	NR	RPE/C	Lens	Brain	Kidney	Liver	SN
ASA_H	Cluster 1	0.014	-0.015	0.083	0.291	0.473	0.447	-0.136	-0.241	-0.115
	Cluster 2	0.096	0.037	-0.275	-0.375	-0.095	-0.229	-0.665	0.006	-0.663
	Cluster 3	-	-	-	-	-	-	-	-	-
FASA_H	Cluster 1	-0.450	0.117	-0.244	-0.365	0.283	0.566	0.382	-0.093	0.586
	Cluster 2	-0.524	0.196	0.209	0.294	-0.540	-0.477	0.596	-0.612	0.631
	Cluster 3	0.379	0.095	-0.567	-	-	-	0.148	-0.299	-
LogP	Cluster 1	0.259	-0.987	-0.523	0.462	-0.764	-0.275	-0.163	0.240	0.676
	Cluster 2	0.177	-0.304	-0.345	0.243	0.565	-0.200	0.586	0.745	0.478
	Cluster 3	-0.355	0.688	0.606	-	-	-	0.113	0.199	-
SLogP	Cluster 1	0.069	0.002	-0.114	0.625	0.566	-0.093	0.876	0.356	0.213
	Cluster 2	0.182	0.420	0.796	0.326	0.492	-0.543	0.098	-0.636	0.572
	Cluster 3	-0.188	-	-	-	-0.516	-	-	0.451	-
vsurf_D1	Cluster 1	-0.302	-0.173	-0.090	-0.072	0.067	-0.157	-0.127	-0.376	-0.405
	Cluster 2	-0.305	-0.290	-0.305	-0.218	0.025	-0.348	-0.392	-0.365	-0.440
	Cluster 3	0.031	0.127	-0.079	-0.158	0.183	0.196	-0.141	-0.139	0.068

Table 3.16. Cluster correlations for the hydrophobic parameters of the full data set for each tissue using the average-linkage algorithms. Cells shaded in yellow and green are moderate and strong cluster correlations, and cells shaded in blue are identical cluster correlations between both average-linkage and complete-linkage algorithms (Table 3.17). Additionally, cells shaded in pink are eliminated cluster correlations due to a non-linear distribution of data points. The drugs in each accepted cluster are listed below.

FASA_H	Cornea	Cluster 2: JHX-2, 3, 4, 7; HK-1, 2, 5, 8, 13, 14
FASA_H	NR	Cluster 3: JHX-3, 4, 7; HK-5, 12, 14
FASA_H	Lens	Cluster 2: JHX-2, 3, 4, 6; HK-1, 2, 8, 14, 16
FASA_H	Brain	Cluster 1: JHX-1, 7, 8; HK-3, 4, 5, 9, 10, 11, 12, 13, 14
FASA_H	Kidney	Cluster 2: JHX-2; HK-1, 3, 4, 5, 6, 7, 8, 13, 14, 16
FASA_H	SN	Cluster 1: JHX-3, 4; HK-1, 3, 6, 9, 10, 11, 14, 15
FASA_H	SN	Cluster 2: JHX-6, 7, 8; HK-2, 5, 7, 12, 13, 16
LogP	Iris/CB	Cluster 1: JHX-1, 5, 8; HK-4, 6
LogP	Iris/CB	Cluster 3: JHX-2, 3, 4, 6, 7; HK-1, 2
LogP	NR	Cluster 3: JHX-2, 3, 4, 6, 7; HK-1, 2, 8
LogP	Lens	Cluster 1: JHX-1, 2, 3, 4, 5, 7, 8
LogP	Lens	Cluster 2: HK-3, 4, 5, 6, 7, 9, 10, 11, 12, 13, 14, 16
LogP	Kidney	Cluster 2: HK-1, 3, 4, 5, 6, 7, 8, 10, 12, 13
LogP	Liver	Cluster 2: HK-1, 3, 4, 5, 6, 7, 8, 10
SLogP	NR	Cluster 2: JHX-2, 3, 4, 6, 7, 8; HK-1, 2, 8
SLogP	RPE/C	Cluster 1: JHX-1, 2, 3, 4, 6, 7, 8; HK-1, 2, 8
SLogP	Brain	Cluster 2: HK-1, 2, 5, 7, 8, 9, 10, 11, 12, 13, 14, 16
SLogP	Kidney	Cluster 1: JHX-1; HK-1, 3, 4, 5, 6, 7, 8
SLogP	Liver	Cluster 2: HK-2, 3, 7, 8, 10
SLogP	SN	Cluster 2: HK-1, 3, 4, 5, 6, 7, 8, 9, 10, 11, 12, 13, 14, 15, 16

Hydrophobic Parameter Cluster Correlations		Full Data Set Using Complete-Linkage Algorithm								
		Cornea	Iris/CB	NR	RPE/C	Lens	Brain	Kidney	Liver	SN
ASA_H	Cluster 1	-0.296	-0.348	0.083	-0.452	-0.554	0.447	-0.262	-0.635	-0.115
	Cluster 2	-0.110	-0.116	-0.275	-0.201	-0.187	-0.229	0.434	0.026	-0.663
	Cluster 3	-	-	-	-	-	-	-	-	-
FASA_H	Cluster 1	-0.450	-0.356	-0.244	-0.369	0.283	0.566	0.382	-0.093	0.289
	Cluster 2	-0.515	0.196	0.209	0.294	-0.540	-0.477	0.596	-0.612	-0.218
	Cluster 3	-0.029	-0.338	-0.567	-0.289	-	-	0.148	-0.299	-
LogP	Cluster 1	0.214	0.375	0.583	0.646	-0.073	-0.275	0.031	0.240	-0.204
	Cluster 2	0.142	0.492	-0.587	-0.243	-0.448	-0.277	-0.195	0.745	-0.251
	Cluster 3	-0.269	-	-0.144	-	-0.388	0.215	0.554	0.199	-
SLogP	Cluster 1	-0.081	-0.343	-0.114	0.335	-0.146	-0.093	-0.056	0.503	0.593
	Cluster 2	-0.619	0.169	0.796	0.326	0.239	-0.543	-0.499	-0.417	0.572
	Cluster 3	-0.141	-	-	-	-	-	-	0.427	-
vsurf_D1	Cluster 1	-0.302	-0.173	-0.090	-0.072	0.067	-0.157	-0.127	-0.376	-0.405
	Cluster 2	-0.156	-0.205	-0.374	-0.255	-0.126	-0.231	-0.302	0.388	-0.065
	Cluster 3	0.246	0.249	-0.010	-0.084	0.159	0.415	0.235	-0.008	-0.073

Table 3.17. Cluster correlations for the hydrophobic parameters of the full data set for each tissue using the complete-linkage algorithms. Cells shaded in yellow and green are moderate and strong cluster correlations, and cells shaded in blue are identical cluster correlations between both average-linkage and complete-linkage algorithms (Table 3.16). Additionally, cells shaded in pink are eliminated cluster correlations due to a non-linear distribution of data points. The drugs in each accepted cluster are listed below.

ASA_H	Lens	Cluster 1: JHX-1, 2, 3, 5, 6, 7; HK-9, 11, 13, 14, 15, 16
ASA_H	Liver	Cluster 1: JHX-1, 2, 3, 5, 6, 7; HK-9, 11, 13, 14, 15, 16
FASA_H	Cornea	Cluster 2: JHX-2, 3, 4, 6, 7; HK-1, 2, 5, 8, 13, 14
FASA_H	NR	Cluster 3: JHX-3, 4, 7; HK-5, 12, 14
FASA_H	Lens	Cluster 2: JHX-1, 5, 7, 8; HK-4, 5, 7, 9, 10, 11, 12, 13
FASA_H	Brain	Cluster 1: JHX-1, 7, 8; HK-3, 4, 5, 9, 10, 11, 12, 13, 14
FASA_H	Kidney	Cluster 2: JHX-2; HK-1, 3, 4, 5, 6, 7, 8, 13, 14, 16
LogP	NR	Cluster 1: JHX-1, 2, 3, 4, 6, 7, 8; HK-1, 2
LogP	NR	Cluster 2: JHX-5; HK-3, 4, 6, 9, 10, 11, 13, 16
LogP	RPE/C	Cluster 1: JHX-1, 2, 3, 4, 6, 7; HK-1, 2
LogP	Kidney	Cluster 3: JHX-3, 4, 5, 8; HK-3, 4, 9, 11, 15, 16
LogP	Liver	Cluster 2: HK-1, 3, 4, 5, 6, 7, 8, 10
SLogP	Cornea	Cluster 1: JHX-1, 2, 3, 4, 7, 8
SLogP	NR	Cluster 2: JHX-2, 3, 4, 6, 7, 8; HK-1, 2, 8
SLogP	Brain	Cluster 2: HK-1, 2, 5, 7, 8, 9, 10, 11, 12, 13, 14, 16
SLogP	Liver	Cluster 1: JHX-1, 2, 5; HK-1, 4, 6
SLogP	SN	Cluster 2: JHX-3, 4, 6, 7, 8; HK-2

Hydrophobic Parameter Cluster Correlations		Standardized Data Set Using Average-Linkage Algorithm								
		Cornea	Iris/CB	NR	RPE/C	Lens	Brain	Kidney	Liver	SN
ASA_H	Cluster 1	0.014	-0.015	0.083	-0.371	0.473	0.314	0.136	-0.241	-0.115
	Cluster 2	0.096	0.037	-0.275	0.651	-0.095	-0.229	-0.665	0.006	-0.281
	Cluster 3	-	-	-	0.393	-	-	-	-	-
FASA_H	Cluster 1	-0.450	0.117	-0.321	-0.369	0.069	0.305	0.382	-0.093	0.586
	Cluster 2	-0.524	0.196	0.209	0.019	-0.047	-0.076	0.596	-0.612	0.631
	Cluster 3	0.379	0.095	-0.567	0.294	-0.750	-	0.148	-0.299	-
LogP	Cluster 1	0.259	-0.987	-0.523	-0.254	-0.764	-0.275	-0.163	0.240	-0.084
	Cluster 2	-0.355	-0.449	-0.345	0.243	0.407	-0.200	0.586	0.745	-0.251
	Cluster 3	0.263	0.688	0.606	-	-	-	0.113	0.199	-
SLogP	Cluster 1	0.069	0.169	-0.114	0.171	0.566	-0.093	0.876	0.356	0.474
	Cluster 2	0.182	0.420	0.811	0.326	0.086	-0.543	0.098	-0.636	-0.286
	Cluster 3	-0.188	-	-	-	0.492	-	-	0.451	-
vsurf_D1	Cluster 1	-0.302	-0.173	-0.090	0.757	0.067	0.202	-0.127	0.226	-0.440
	Cluster 2	0.199	0.168	-0.045	0.193	0.163	0.415	-0.392	-0.365	0.068
	Cluster 3	0.246	0.249	-0.010	-	0.159	-	-0.141	-0.139	-

Table 3.18. Cluster correlations for the hydrophobic parameters of the standardized data set for each tissue using the average-linkage algorithms. Cells shaded in yellow and green are moderate and strong cluster correlations, and cells shaded in blue are identical cluster correlations between both average-linkage and complete-linkage algorithms (Table 3.19). Additionally, cells shaded in pink are eliminated cluster correlations due to a non-linear distribution of data points. The drugs in each accepted cluster are listed below.

FASA_H	Cornea	Cluster 2: JHX-2, 3, 4, 7; HK-1, 2, 5, 8, 13, 14
FASA_H	NR	Cluster 3: JHX-3, 4, 7; HK-5, 12, 14
FASA_H	Lens	Cluster 3: JHX-3, 6; HK-1, 2, 8, 16
FASA_H	Kidney	Cluster 2: JHX-2; HK-1, 3, 4, 5, 6, 7, 8, 13, 14, 16
FASA_H	SN	Cluster 1: JHX-3, 4; HK-1, 3, 6, 9, 10, 11, 14, 15
FASA_H	SN	Cluster 2: JHX-6, 7, 8; HK-2, 5, 7, 12, 13, 16
LogP	Iris/CB	Cluster 1: JHX-1, 5, 8; HK-4, 6
LogP	Iris/CB	Cluster 3: JHX-2, 3, 4, 6, 7; HK-1, 2
LogP	NR	Cluster 3: JHX-2, 3, 4, 6, 7; HK-1, 2, 8
LogP	Lens	Cluster 1: JHX-1, 3, 4, 5, 7, 8
LogP	Kidney	Cluster 2: HK-1, 3, 4, 5, 6, 7, 8, 10, 12, 13
LogP	Liver	Cluster 2: HK-1, 3, 4, 5, 6, 7, 8, 10
SLogP	NR	Cluster 2: JHX-2, 3, 4, 6, 7; HK-1, 2, 8
SLogP	Brain	Cluster 2: HK-1, 2, 5, 7, 8, 9, 10, 11, 12, 13, 14, 16
SLogP	Kidney	Cluster 1: JHX-1; HK-1, 3, 4, 5, 6, 7, 8
SLogP	Liver	Cluster 2: HK-2, 3, 7, 8, 10

Hydrophobic Parameter Cluster Correlations		Standardized Data Set Using Complete-Linkage Algorithm								
		Cornea	Iris/CB	NR	RPE/C	Lens	Brain	Kidney	Liver	SN
ASA_H	Cluster 1	-0.338	-0.400	0.083	-0.371	-0.215	0.314	-0.262	-0.717	0.073
	Cluster 2	-0.110	-0.116	-0.275	0.651	-0.187	-0.229	0.434	0.026	-0.360
	Cluster 3	-	-	-	0.393	-	-	-	-	-0.281
FASA_H	Cluster 1	-0.450	-0.356	-0.321	-0.369	0.283	0.305	0.382	-0.093	0.006
	Cluster 2	-0.524	-0.828	0.209	0.019	-	-0.076	0.596	-0.612	-0.417
	Cluster 3	0.379	-0.200	-0.567	0.294	-0.750	-	0.148	-0.299	-0.728
LogP	Cluster 1	0.214	0.375	0.583	0.537	-0.764	-0.275	0.031	0.240	-0.084
	Cluster 2	0.142	-0.716	-0.587	-0.243	-0.448	-0.404	-0.195	0.745	-0.251
	Cluster 3	0.299	-0.019	-0.144	-	0.369	0.405	0.554	0.199	-
SLogP	Cluster 1	0.069	-0.343	0.620	0.335	-0.004	-0.093	-0.056	0.434	0.667
	Cluster 2	0.182	0.169	0.485	-0.740	0.475	-0.543	-0.499	-0.417	0.986
	Cluster 3	-0.188	-	0.300	-0.431	-	-	-	0.427	-
vsurf_D1	Cluster 1	-0.302	-0.173	-0.090	-0.072	0.067	0.202	-0.127	0.226	-0.815
	Cluster 2	0.199	0.168	-0.045	0.187	0.163	0.415	-0.302	-0.188	0.069
	Cluster 3	0.246	0.249	-0.010	-	0.159	-	0.235	0.872	-0.073

Table 3.19. Cluster correlations for the hydrophobic parameters of the standardized data set for each tissue using the complete-linkage algorithms. Cells shaded in yellow and green are moderate and strong cluster correlations, and cells shaded in blue are identical cluster correlations between both average-linkage and complete-linkage algorithms (Table 3.18). Additionally, cells shaded in pink are eliminated cluster correlations due to a non-linear distribution of data points. The drugs in each accepted cluster are listed below.

FASA_H	Cornea	Cluster 2: JHX-2, 3, 4, 7; HK-1, 2, 5, 8, 13, 14
FASA_H	Iris/CB	Cluster 2: JHX-2, 3, 4; HK-5, 12, 14
FASA_H	NR	Cluster 3: JHX-3, 4, 7; HK-5, 12, 14
FASA_H	Lens	Cluster 3: JHX-3, 6; HK-1, 2, 8, 16
FASA_H	Kidney	Cluster 2: JHX-2; HK-1, 3, 4, 5, 6, 7, 8, 13, 14, 16
LogP	NR	Cluster 1: JHX-1, 2, 3, 4, 6, 7, 8; HK-1, 2
LogP	Lens	Cluster 1: JHX-1, 3, 4, 5, 7, 8
LogP	Kidney	Cluster 3: JHX-3, 4, 5, 8; HK-3, 4, 9, 11, 15, 16
LogP	Liver	Cluster 2: HK-1, 3, 4, 5, 6, 7, 8, 10
SLogP	NR	Cluster 1: JHX-1, 5; HK-3, 4, 5, 6, 7, 12, 14
SLogP	Brain	Cluster 2: HK-1, 2, 5, 7, 8, 9, 10, 11, 12, 13, 14, 16
SLogP	SN	Cluster 2: HK-5, 7, 12, 13, 16
D1	SN	Cluster 1: JHX-3, 4; HK-7, 11, 15, 16

All cluster correlations shown in **Tables 3.8 to 3.19** represent the linear relationship between the clustered drugs using Pearson's r-value where an r-value between ± 0.5 and ± 0.7 denotes a **moderate correlation** and an r-value between ± 0.7 and ± 1.0 denotes a **strong correlation**. These metrics are common statistical cut-offs which here denote the strength of the linear relationship between the drug tissue levels and their calculated physicochemical descriptors. In order to develop the most accurate and predictable models for the tissue distribution of these drugs from these clusters, all correlation values which resulted in an $r^2 \leq 0.5$ (*i.e.*, $|r| < 0.707$) were excluded. Thus, only **strong correlations** were considered for model development. P-values were also calculated for these cluster correlations and clusters with a p-value > 0.05 were also excluded. A model with a significant p-value (*i.e.*, $p < 0.05$) is more likely to be meaningful because this supports the notion that the changes observed between the drug tissue levels and the calculated physicochemical descriptors are more likely to be directly related. The final clustered linear correlations are shown in **Figures 3.2 to 3.10**.

In **Figure 3.2**, the clustered correlations for the cornea are reported. Four positive correlations were calculated for the cornea, where the log concentrations of drugs found in the cornea were positively correlated with the hydrophilic parameters **CASA+** ($r^2 = +0.746$, $p = 0.026$), **ASA_P** ($r^2 = +0.641$, $p = 0.009$), and **LogS** ($r^2 = +0.831$, $p = 0.031$), and the structural parameter **SMR** ($r^2 = +0.515$, $p = 0.017$). These results suggest that larger, polar, and hydrophilic compounds possessing are more likely to distribute into the cornea.

In **Figure 3.3**, the clustered correlations for the iris/CB are reported. Three positive and two negative correlations were calculated. The log concentrations of drugs found in the iris/CB were positively correlated with the hydrophilic parameter **FASA_P** ($r^2 = +0.685$,

$p = 0.042$) and the structural parameter **vsurf_G** ($r^2 = 0.664$, $p = 0.048$), and negatively correlated with hydrophobic parameters **FASA_H** ($r^2 = -0.685$, $p = 0.042$) and **LogP** ($r^2 = -0.974$, $p = 0.002$). This suggests that globular, polar, and hydrophilic compounds are more likely to distribute into the iris/CB.

Cornea Cluster Correlations by Hierarchical Cluster Analysis

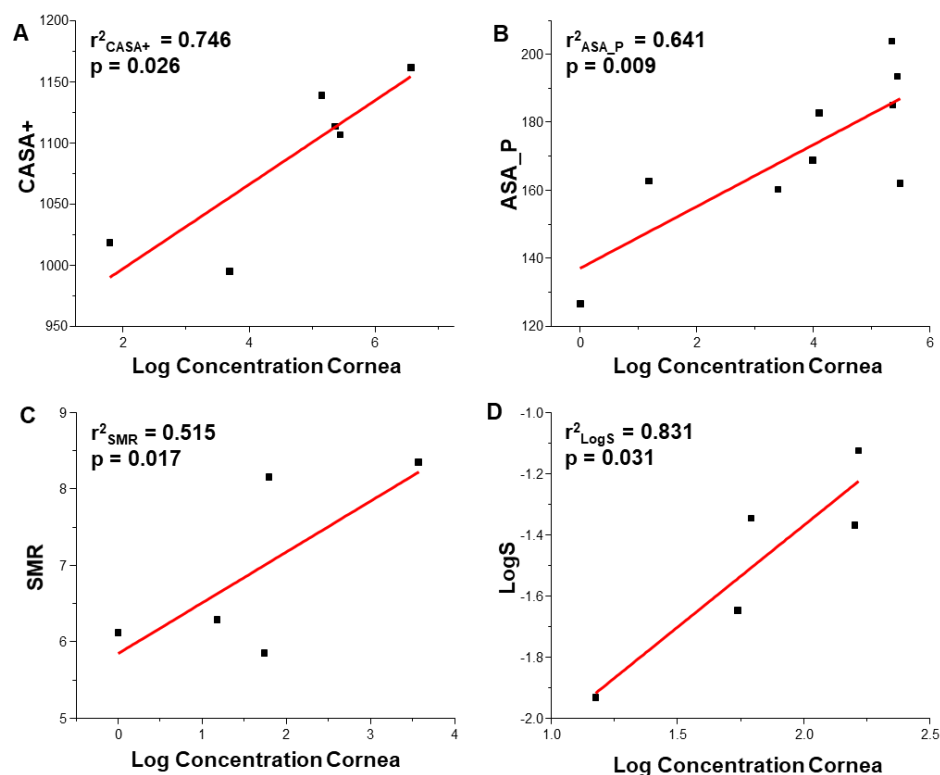


Figure 3.2. Linear regression models between physicochemical descriptors and drug levels in the cornea where (A) corresponds to Cluster 1 between cornea and CASA+ in **Table 3.12**, (B) corresponds to the Cluster 2 between cornea and ASA_P in **Table 3.14**, (C) corresponds to Cluster 2 between cornea and SMR in **Table 3.9**, and (D) corresponds to Cluster 3 between cornea and LogS in **Table 3.14**. The hydrophilic parameters ASA_P, and LogS, and the structural parameter SMR, were all positively correlated with drug levels in the cornea and exhibit both an $r^2 \geq 0.5$ and $p < 0.05$, indicating strong relationships between these descriptors and drug levels in the cornea. These results suggest that larger, polar, and hydrophilic compounds are more likely to distribute into the cornea.

Iris/CB Cluster Correlations by Hierarchical Cluster Analysis

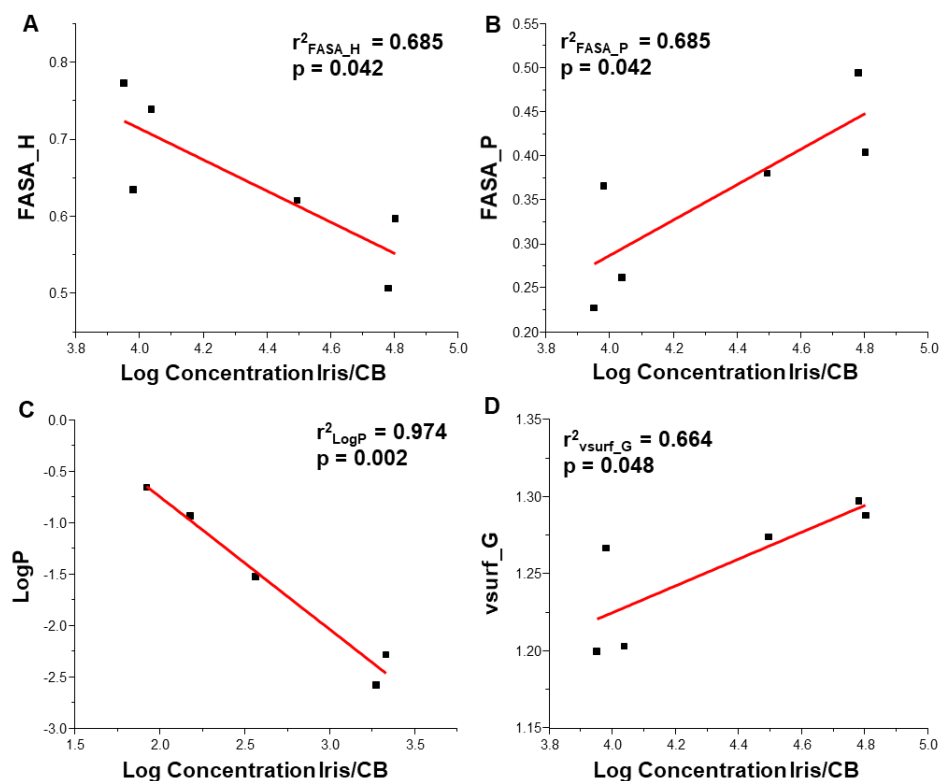


Figure 3.3. Linear regression models between physicochemical descriptors and drug levels in the iris/CB where (A) corresponds to Cluster 2 between iris/CB and FASA_H in **Table 3.19**, (B) corresponds to Cluster 2 between iris/CB and FASA_P in **Table 3.15**, (C) corresponds to Cluster 1 between iris/CB and LogP in both **Table 3.16** and **Table 3.18**, and (D) corresponds to Cluster 2 between iris/CB and vsurf_G in **Table 3.11**. The hydrophilic parameters FASA_P and LogS, and the structural parameter vsurf_G, were positively correlated, while the hydrophobic parameter LogP was negatively correlated, with drug levels in the iris/CB. All of these correlations exhibit an $r^2 \geq 0.5$ and $p < 0.05$, indicating a strong relationship between these descriptors and drug levels in the iris/CB. These results suggest that globular, polar, and hydrophilic compounds are more likely to distribute into the iris/CB.

In **Figure 3.4**, the clustered correlations for the lens are reported where two positive and two negative correlations were found. The log concentrations of drugs found in the lens were positively correlated with the hydrophilic parameters **FASA_P** ($r^2 = +0.562$, $p = 0.047$) and **LogS** ($r^2 = +0.589$, $p = 0.026$), and negatively correlated with hydrophobic parameters **FASA_H** ($r^2 = -0.562$, $p = 0.047$) and **LogP** ($r^2 = -0.583$, $p =$

0.045). This data suggests that more polar, hydrophilic compounds are more likely to distribute into the lens.

Lens Cluster Correlations by Hierarchical Cluster Analysis

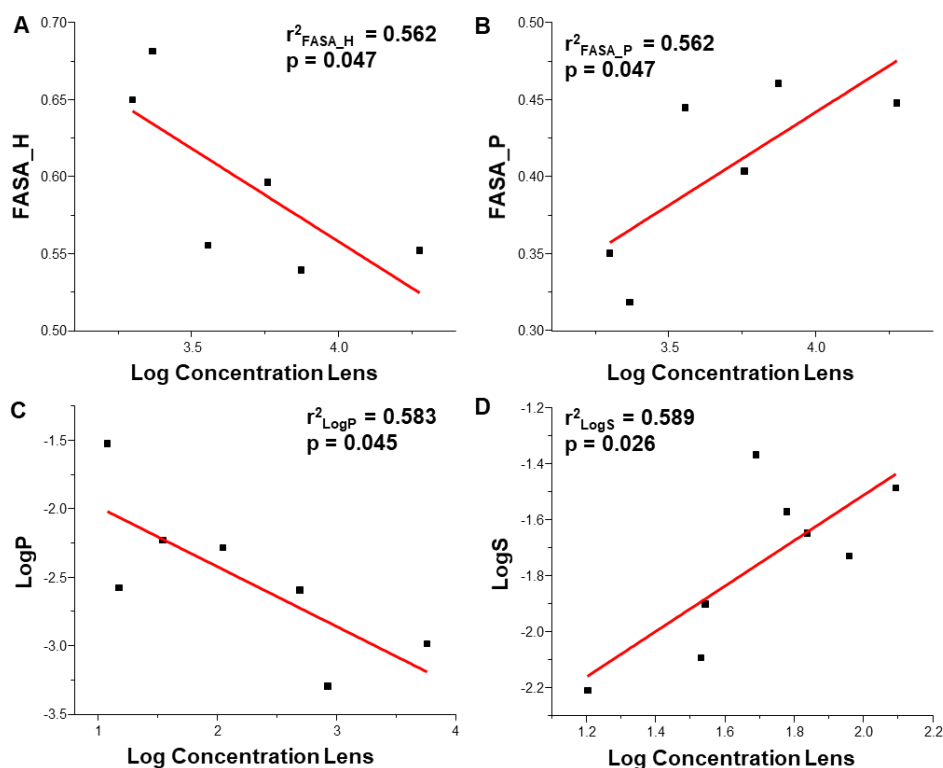


Figure 3.4. Linear regression models between physicochemical descriptors and drug levels in the lens where (A) corresponds to Cluster 3 between lens and FASA_H in **Tables 3.18** and **3.19**, (B) corresponds to Cluster 2 between lens and FASA_P in **Tables 3.14** and **3.15**, (C) corresponds to Cluster 1 between lens and LogP in **Tables 3.16** and **3.18**, and (D) corresponds to Cluster 3 between lens and LogS in **Tables 3.13** and **3.14**. The hydrophilic parameters FASA_P and LogS were positively correlated, while the hydrophobic parameter FASA_H and LogP were negatively correlated, with drug levels in the lens. All of these correlations exhibit an $r^2 \geq 0.5$ and $p < 0.05$, indicating a strong relationship between these descriptors and drug levels in the lens. These results suggest that more polar, hydrophilic compounds are more likely to distribute into the lens.

In **Figure 3.5**, the clustered correlations for the neural retina (NR) are reported. Three positive correlations were found, with two correlations of the same parameter. The log concentrations of drugs found in the NR were positively correlated with the

hydrophobic parameter **SLogP** ($r^2 = +0.633$, $p = 0.010$; $r^2 = +0.657$, $p = 0.015$) and the structural parameter **Kier1** ($r^2 = +0.554$, $p = 0.046$). This suggests that compounds which are larger, branched, and lipophilic are more likely to distribute into the NR.

Neural Retina Cluster Correlations by Hierarchical Cluster Analysis

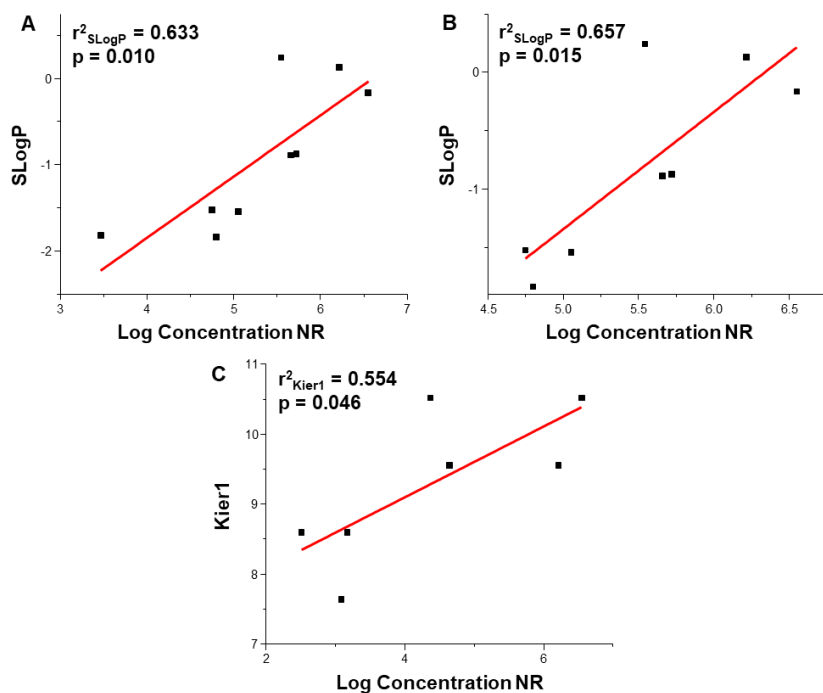


Figure 3.5. Linear regression models between physicochemical descriptors and drug levels in the NR where (A) corresponds to Cluster 2 between NR and SLogP in **Tables 3.16** and **3.17**, (B) corresponds to Cluster 2 between NR and SLogP in **Table 3.18**, and (C) corresponds to Cluster 2 between NR and Kier1 in **Tables 3.8, 3.9, 3.10, and 3.11**. The hydrophobic parameter SLogP, which resulted in two models, and the structural parameter Kier1 were both positively correlated with drug levels in the NR. All of these correlations exhibit an $r^2 \geq 0.5$ and $p < 0.05$, indicating a strong relationship between these descriptors and drug levels in the NR. These results suggest that larger, branched, and hydrophobic compounds are more likely to distribute into the NR.

In **Figure 3.6**, the clustered correlations for the RPE/C are reported where four positive correlations were identified. The log concentrations of drugs found in the RPE/PS were positively correlated with the hydrophilic parameters **Apol** ($r^2 = +0.587$, $p = 0.006$),

ASA ($r^2 = +0.561$, $p = 0.047$), **LogS** ($r^2 = +0.664$, $p = 0.044$), and **vsurf_W1** ($r^2 = +0.608$, $p = 0.037$). This suggests that compounds which are more water soluble, polar, and possess a larger hydrophilic surface area are more likely to distribute into the RPE/C.

RPE/C Cluster Correlations by Hierarchical Cluster Analysis

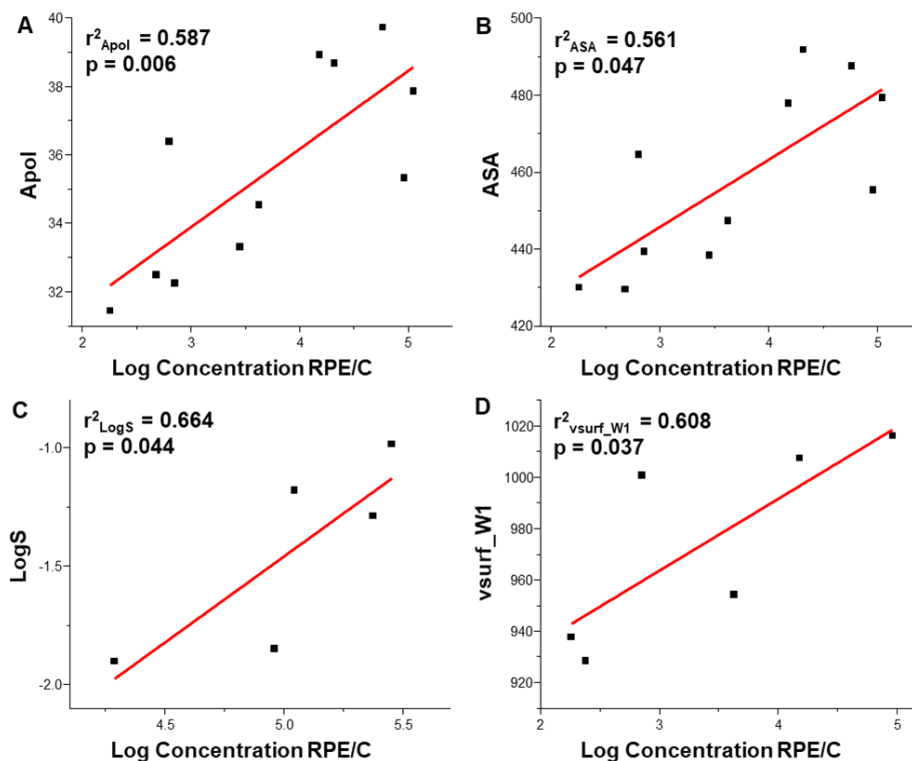


Figure 3.6. Linear regression models between physicochemical descriptors and drug levels in the RPE/C where (A) corresponds to Cluster 1 between RPE/C and Apol in **Tables 3.14** and **3.15**, (B) corresponds to Cluster 1 between RPE/C and ASA in **Tables 3.14** and **3.15**, (C) corresponds to Cluster 3 between RPE/C and LogS in **Table 3.14**, and (D) corresponds to Cluster 1 between RPE/C and vsurf_W1 in **Table 3.15**. The hydrophilic parameters Apol, ASA, LogS, and vsurf_W1 are all positively correlated with drug levels in the RPE/C. All of these correlations exhibit an $r^2 \geq 0.5$ and $p < 0.05$, indicating a strong relationship between these descriptors and drug levels in the RPE/C. These results suggest that more polar hydrophilic compounds are more likely to distribute into the RPE/C.

The single cluster correlation for the brain is shown in **Figure 3.7**, where drug concentration in the brain is positively correlated with the structural parameter **vsurf_Cp** ($r^2 = +0.515$, $p = 0.050$), suggesting that compounds which are more micellar in shape may more likely to distribute into the brain.

Brain Cluster Correlation by Hierarchical Cluster Analysis

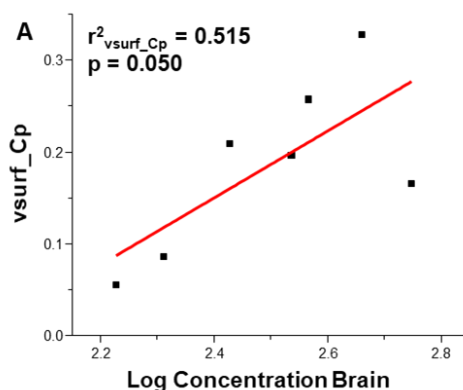


Figure 3.7. Linear regression model between physicochemical descriptors and drug levels in the brain where (A) corresponds to Cluster 1 between brain and vsurf_Cp in **Table 3.11**. The structural parameter vsurf_Cp is positively correlated with drug levels in the brain and exhibits an $r^2 \geq 0.5$ and $p < 0.05$, indicating a strong relationship between vsurf_Cp and drug levels in the RPE/C. This result suggests that compounds resembling more micellar shapes are more likely to distribute into the brain.

The cluster correlations for the sciatic nerve (SN) are reported in **Figure 3.8** where two positive and two negative correlations were identified. The log concentrations of drugs found in the SN were positively correlated with the hydrophobic parameter **SLogP** ($r^2 = +0.972$, $p = 0.002$) and the structural parameter **vsurf_Cp** ($r^2 = +0.588$, $p = 0.016$), and negatively correlated with hydrophilic parameters **ASA_P** ($r^2 = -0.817$, $p = 0.002$) and **vsurf_W1** ($r^2 = -0.661$, $p = 0.008$). These results suggest that compounds which are less polar, more hydrophobic, and micellar-shaped are more likely to distribute into the SN.

Sciatic Nerve Cluster Correlations by Hierarchical Cluster Analysis

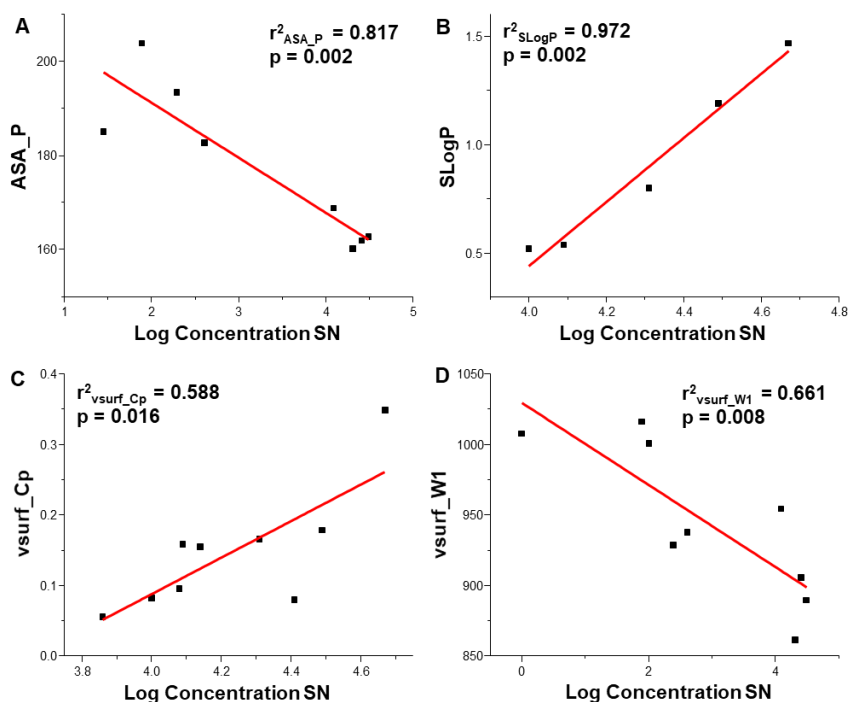


Figure 3.8. Linear regression models between physicochemical descriptors and drug levels in the SN where (A) corresponds to Cluster 2 between SN and ASA_P in **Table 3.12**, (B) corresponds to Cluster 2 between SN and SLogP in **Table 3.19**, (C) corresponds to Cluster 2 between SN and vsurf_Cp in **Tables 3.8, 3.9, and 3.10**, as well as Cluster 3 between SN and vsurf_Cp in **Table 3.11**, and (D) corresponds to Cluster 1 between SN and vsurf_W1 in **Table 3.12**. The hydrophilic parameters ASA_P and vsurf_W1 are negatively correlated, while the hydrophobic parameter SLogP and structural parameters Kier1 and vsurf_Cp are positively correlated, with drug levels in the SN. All of these correlations exhibit an $r^2 \geq 0.5$ and $p < 0.05$, indicating a strong relationship between these descriptors and drug levels in the SN. These results suggest that less polar and more hydrophobic compounds resembling a micellar shape are more likely to distribute into the SN.

Figure 3.9 reports the cluster correlations for the kidney where two positive correlations were identified. The log concentrations of drugs found in the kidney were positively correlated with the hydrophilic parameters **CASA+** ($r^2 = +0.672$, $p = 0.046$) and **SMR** ($r^2 = +0.504$, $p = 0.048$). This suggests that larger polar compounds with a greater positively-charged surface area are more likely to distribute into the kidney.

Kidney Cluster Correlations by Hierarchical Cluster Analysis

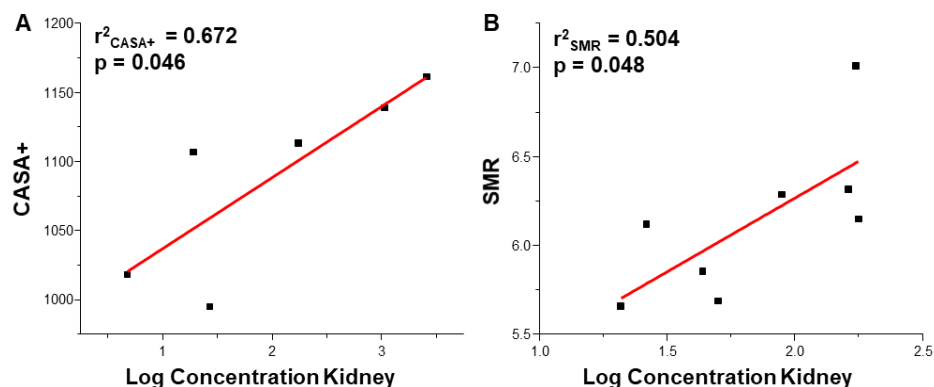


Figure 3.9. Linear regression models between physicochemical descriptors and drug levels in the kidney where (A) corresponds to Cluster 1 between kidney and CASA+ in **Table 3.12**, and (B) corresponds to Cluster 2 between kidney and SMR in **Table 3.9**. The hydrophilic parameter CASA+ and the structural parameter SMR are both positively correlated with drug levels in the kidney. Both of these correlations exhibit an $r^2 \geq 0.5$ and $p < 0.05$, indicating a strong relationship between these descriptors and drug levels in the kidney. These results suggest that larger hydrophilic compounds with a greater positively-charged surface area are more likely to distribute into the kidney.

The cluster correlations for the liver are reported in **Figure 3.10** where one positive correlation and one negative correlation was identified. The log concentrations of drugs found in the liver were positively correlated with the hydrophobic parameter **LogP** ($r^2 = +0.555$, $p = 0.034$) and negatively correlated with the hydrophilic parameter **PM3_Dipole** ($r^2 = -0.524$, $p = 0.049$). This suggests that more hydrophobic, less polar molecules are more likely to distribute into the liver.

Liver Cluster Correlations by Hierarchical Cluster Analysis

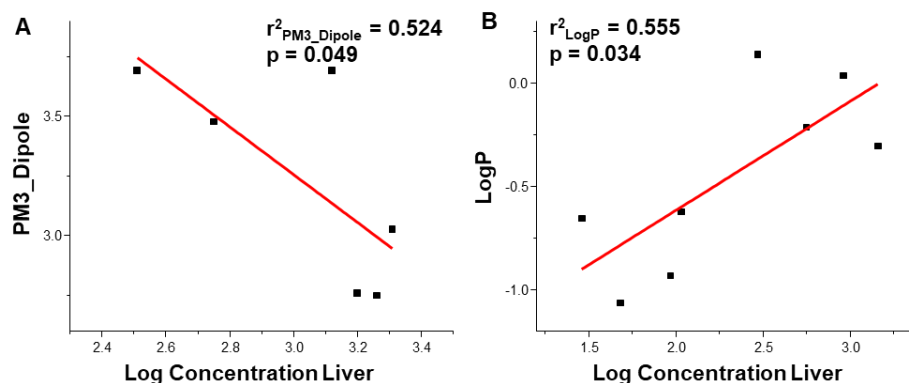


Figure 3.10. Linear regression models between physicochemical descriptors and drug levels in the Liver where (A) corresponds to Cluster 2 between liver and PM3_Dipole in **Tables 3.12, 3.13, 3.14, and 3.15**, and (B) corresponds to Cluster 2 between liver and LogP in **Tables 3.16, 3.17, 3.18, and 3.19**. The hydrophilic parameter PM3_Dipole is negatively correlated, and the hydrophobic parameter LogP is positively correlated, with drug levels in the liver. Both of these correlations exhibit an $r^2 \geq 0.5$ and $p < 0.05$, indicating a strong relationship between these descriptors and drug levels in the liver. These results suggest hydrophobic compounds are more likely to distribute into the liver.

3.4.5 Confirmation of HCA Clusters using QSAR Algorithms

Initial efforts at investigating predictive models for drug delivery upon oral distribution using HCA and linear regression analysis led to the identification of multiple relationships between the calculated physicochemical parameters and drug levels in various ocular, neural, and visceral tissues (**Figures 3.2 through 3.10**). To investigate the accuracy of these models, the same data were subject to the “QuaSAR” algorithm in MOE™. Although many of the same cluster correlations were identified, some were excluded due to different p-values, suggesting the statistical methods between OriginPro and MOE may be different. Results using the MOE™ “QuaSAR” algorithm are shown in **Table 3.20** along with the calculated mean absolute error (MAE), root mean square error (RMSE), cross-validated root mean square error (XRMSE), and cross-validated coefficient of determination (Xr^2). Clusters matching those calculated by HCA are indicated (*).

Tissue	Drugs in Cluster	Measured Parameter	r ²	MAE	RMSE	XRMSSE	Xr ²
Cornea*	JHX: 2,3; HK: 2,3,7,8,12,15,16	ASA_P	0.643	0.853	1.127	1.407	0.452
Cornea*	JHX: 1,2,3,5,6,7	CASA+	0.747	0.648	0.773	1.411	0.365
Cornea*	JHX: 5; HK: 4,6,9,16	LogS	0.833	0.139	0.155	0.246	0.597
IrisCB	JHX: 1,2,3,5,6,7	CASA+	0.878	0.275	0.351	0.648	0.653
IrisCB*	JHX: 2,3,4; HK: 5,12,14	FASA_P	0.685	0.140	0.205	0.256	0.536
IrisCB	JHX: 2,3,4; HK: 5,12,14	LogP	-0.934	0.081	0.094	0.135	0.868
IrisCB*	JHX: 2,3,4; HK: 5,12,14	vsurf_G	0.663	0.151	0.212	0.276	0.465
IrisCB*	JHX: 1,5,8; HK: 4,6	LogP	-0.973	0.074	0.092	0.169	0.917
Lens*	JHX: 1,2,3,4,5,7,8	LogP	-0.586	0.481	0.594	0.780	0.372
Lens*	JHX: 7; HK: 4,5,7,9,11,12,13	LogS	0.591	0.143	0.168	0.245	0.240
NR*	JHX: 2,3,4,6,7,8; HK: 1,2,8	SLogP ₁	0.633	0.416	0.524	0.721	0.372
NR*	JHX: 2,3,4,6,7; HK: 1,2,8	SLogP ₂	0.656	0.267	0.355	0.506	0.383
RPE/C*	JHX: 1,2,3,4; HK: 3,4,7,8,11,12,16	Apol	0.588	0.451	0.607	0.693	0.469
RPE/C*	JHX: 1,2,3,4; HK: 3,4,7,8,11,12,16	ASA	0.561	0.491	0.626	0.725	0.424
RPE/C	JHX: 1,2,3,4; HK: 3,4,7,8,11,12,16	vsurf_W1	0.608	0.562	0.663	0.800	0.335
SN*	JHX: 2,3; HK: 2,3,7,8,12,16	ASA_P	-0.817	0.373	0.505	0.681	0.696
SN	JHX: 2,3; HK: 2,3,7,8,12,16	Kier1	-0.557	0.720	0.785	1.014	0.357
SN*	HK: 5,7,12,13,16	SLogP	0.972	0.033	0.041	0.063	0.937
SN*	JHX: 6,7,8; HK: 2,5,7,12,13,16	vsurf_Cp	0.588	0.125	0.157	0.191	0.424
SN*	JHX: 1; HK: 2,3,4,6,7,8,12,16	vsurf_W1 ₁	-0.661	0.737	0.842	1.075	0.473
SN	JHX: 1; HK: 2,3,4,6,7,8,16	vsurf_W1 ₂	-0.639	0.747	0.864	1.124	0.419
SN	HK: 2,3,4,6,7,8,12,16	vsurf_W1 ₃	-0.639	0.527	0.646	0.766	0.504
Kidney*	JHX: 1,2,3,5,6,7	CASA+	0.673	0.489	0.557	0.897	0.334
Kidney*	JHX: 2; HK: 3,4,7,8,11,15,16	SMR	0.504	0.202	0.247	0.330	0.297
Liver*	HK: 1,3,4,5,6,7,8,10	LogP	0.555	0.300	0.386	0.493	0.340

Table 3.20. Cross-validated linear regression models obtained with the MOE™ QuaSAR algorithm, many of which are the same as those obtained using OriginPro™ HCA algorithm and subsequent linear regression analysis (indicated with *). The clusters that were not identified by MOE™ that were identified by OriginPro™ include cornea vs. SMR, NR vs. Kier1, and brain vs. vsurf_Cp. However, a few clusters were identified by MOE™ that were not identified by OriginPro™, including iris/CB vs. CASA+, iris/CB vs. LogP, RPE/C vs. vsurf_W1, SN vs. Kier1, and SN vs. vsurf_W1. An r² value with a (-) sign indicates a negative correlation.

3.4.6 Extended QSAR Analysis using Validated Clustered Correlations

Could these determined clusters, which were identified using two different mathematical approaches with OriginPro™ and MOE™, be correlated with other physicochemical descriptors? To investigate this possibility, the “QuaSAR” algorithm in

MOE™ was again employed. All identified cluster correlations in **Table 3.20** were re-evaluated against all physicochemical descriptors (**Table 3.1**) to confirm whether these clusters can be used to further identify relationships between tissue drug levels and the calculated physicochemical descriptors. The results in **Tables 3.21** through **3.28** report the newly calculated clusters where clusters highlighted in green were accepted and clusters highlighted in red were rejected by the internal validation algorithm. The rejection criteria included the resulting calculations with a weak cross-validated coefficient of determination ($Xr^2 < 0.5$), a large cross-validated error ($XRMSE \geq 1.2$), or a non-linear distribution of data points.

The results from the validated cornea cluster correlations (**Table 3.20, cornea**) are presented in **Table 3.21**, where the extended relationships between cornea and ASA_P, CASA+, and LogS clusters were examined. The clusters were initially chosen based on their calculated r^2 values, and then subjected to the internal cross-validation algorithm. For the cornea, this yielded four acceptable clustered correlations: **FASA_H** ($Xr^2 = -0.647$), **FASA_P** ($Xr^2 = +0.647$), **vsurf_Cp** ($Xr^2 = +0.631$), and **LogS** ($Xr^2 = +0.597$). The graphed results of these extended QSAR models are shown in **Figure 3.11**.

The results from the validated iris/CB cluster correlations (**Table 3.20, iris/CB**) are presented in **Table 3.22**, where the extended relationships between iris/CB and CASA+, FASA_H, FASA_P, and LogP clusters were examined. The clusters were initially chosen based on calculated r^2 values, and then subjected to the internal cross-validation algorithm. For the iris/CB, this yielded eight acceptable clustered correlations: **vsurf_Cp** ($Xr^2 = +0.660$), **ASA** ($Xr^2 = +0.536$), **ASA_P** ($Xr^2 = +0.609$), **CASA-** ($Xr^2 = +0.949$), **FASA_H** ($Xr^2 = -0.536$), **FASA_P** ($Xr^2 = +0.536$), **Kier1** ($r^2 = +0.815$), and **LogP** ($Xr^2 = +0.917$). The graphed results of these extended QSAR models are shown in **Figure 3.12**.

Tissue	Cluster Parameter	Drugs in Cluster	Measured Parameter	r^2	MAE	RMSE	XRMSSE	Xr^2
Cornea	ASA_P	JHX: 2,3; HK: 2,3,7,8,12,15,16	FASA_H	-0.752	0.775	0.939	1.126	0.647
Cornea	ASA_P	JHX: 2,3; HK: 2,3,7,8,12,15,16	FASA_P	0.752	0.775	0.939	1.126	0.647
Cornea	ASA_P	JHX: 2,3; HK: 2,3,7,8,12,15,16	LogP	-0.671	0.983	1.082	1.446	0.459
Cornea	ASA_P	JHX: 2,3; HK: 2,3,7,8,12,15,16	SLogP	-0.684	0.939	1.06	1.547	0.431
Cornea	ASA_P	JHX: 2,3; HK: 2,3,7,8,12,15,16	vsurf_Cp	0.597	0.882	1.197	4.25	0.505
Cornea	ASA_P	JHX: 2,3; HK: 2,3,7,8,12,15,16	vsurf_W1	0.533	1.073	1.289	1.654	0.289
Cornea	CASA+	JHX: 1,2,3,5,6,7	ASA_H	-0.538	0.884	1.045	1.58	0.175
Cornea	CASA+	JHX: 1,2,3,5,6,7	vsurf_Cp	0.784	0.586	0.714	0.941	0.631
Cornea	LogS	JHX: 5; HK: 4,6,9,16	LogS	0.833	0.139	0.155	0.246	0.597

Table 3.21. Extended and cross-validated QSAR models relating to the measured parameters with clustered drug tissue levels in the cornea. An r^2 value with a (-) sign indicates a negative correlation. The clusters in green (4) were accepted, and the clusters in pink (5) were rejected due to $Xr^2 < 0.5$, $XRMSSE \geq 1.2$, or a non-linear distribution of data points. The accepted clusters are shown in Figure 3.11.

Extended Cornea Cluster Correlations Identified by QuaSAR Algorithm

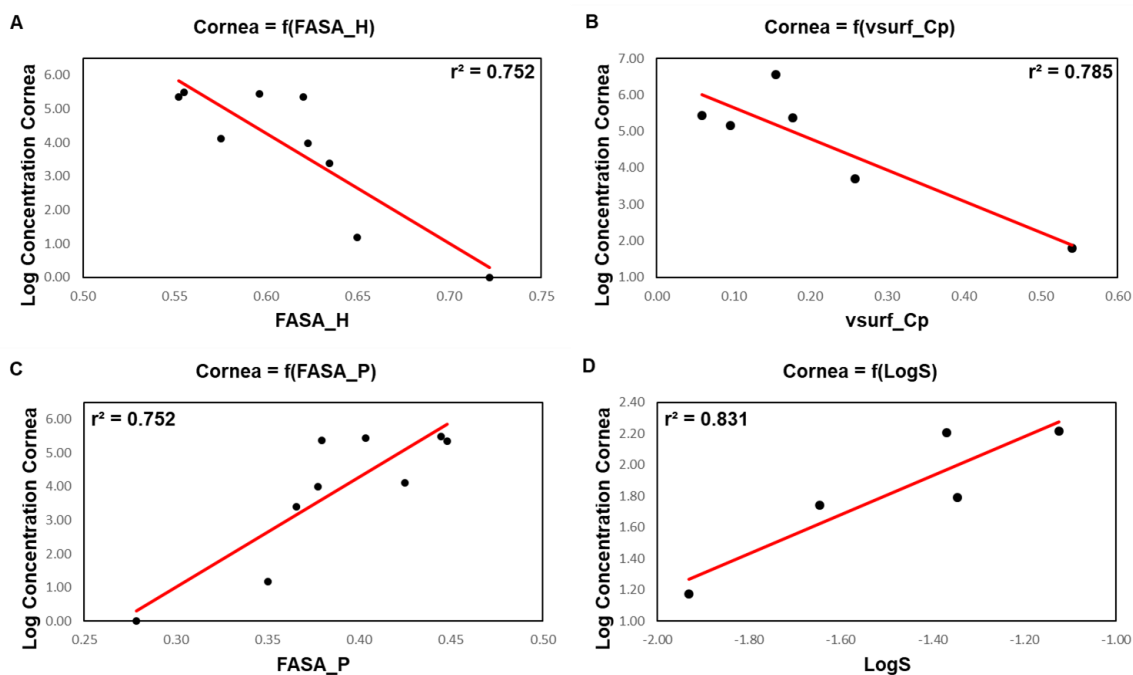


Figure 3.11. Cross-validated linear regression models between physicochemical descriptors and drug levels in the cornea where (A) and (B) correspond to the new FASA_H and vsurf_Cp cluster correlations identified from Cluster 1 between cornea and CASA+ in Table 3.14, (C) corresponds to the new FASA_P cluster correlation identified from Cluster 1 between cornea and CASA+ in Table 3.14, and (D) corresponds to the validated Cluster 3 between cornea and LogS in Table 3.14. These results suggest that non-micellar hydrophilic compounds are more likely to distribute into the cornea, which agrees with the trends observed and reported for the cornea using HCA in Figure 3.2.

Tissue	Cluster Parameter	Drugs in Cluster	Measured Parameter	r^2	MAE	RMSE	XRMSE	Xr^2
IrisCB	CASA+	JHX: 1,2,3,5,6,7	ASA_H	0.672	0.456	0.577	0.845	0.39
IrisCB	CASA+	JHX: 1,2,3,5,6,7	CASA+	0.878	0.275	0.351	0.648	0.653
IrisCB	CASA+	JHX: 1,2,3,5,6,7	vsurf_Cp	0.777	0.348	0.475	0.685	0.660
IrisCB	FASA_H/_P	JHX: 2,3,4; HK: 5,12,14	Apol	0.708	0.182	0.198	0.284	0.474
IrisCB	FASA_H/_P	JHX: 2,3,4; HK: 5,12,14	ASA	0.729	0.16	0.191	0.26	0.536
IrisCB	FASA_H/_P	JHX: 2,3,4; HK: 5,12,14	ASA_P	0.74	0.13	0.187	0.234	0.609
IrisCB	FASA_H/_P	JHX: 2,3,4; HK: 5,12,14	CASA+	0.939	0.062	0.09	0.128	0.879
IrisCB	FASA_H/_P	JHX: 2,3,4; HK: 5,12,14	CASA-	0.972	0.048	0.061	0.089	0.949
IrisCB	FASA_H/_P	JHX: 2,3,4; HK: 5,12,14	FASA_H	-0.685	0.144	0.205	0.256	0.536
IrisCB	FASA_H/_P	JHX: 2,3,4; HK: 5,12,14	FASA_P	0.685	0.14	0.205	0.256	0.536
IrisCB	FASA_H/_P	JHX: 2,3,4; HK: 5,12,14	Kier1	0.897	0.093	0.117	0.161	0.815
IrisCB	FASA_H/_P	JHX: 2,3,4; HK: 5,12,14	LogP	-0.934	0.081	0.094	0.135	0.868
IrisCB	FASA_H/_P	JHX: 2,3,4; HK: 5,12,14	PM3_Dipole	0.624	0.19	0.224	0.298	0.399
IrisCB	FASA_H/_P	JHX: 2,3,4; HK: 5,12,14	SLogP	-0.982	0.045	0.049	0.077	0.957
IrisCB	FASA_H/_P	JHX: 2,3,4; HK: 5,12,14	SMR	0.796	0.144	0.165	0.233	0.625
IrisCB	FASA_H/_P	JHX: 2,3,4; HK: 5,12,14	vsurf_G	0.663	0.151	0.212	0.276	0.465
IrisCB	FASA_H/_P	JHX: 2,3,4; HK: 5,12,14	vsurf_W1	0.923	0.084	0.102	0.141	0.855
IrisCB	LogP	JHX: 1,5,8; HK: 4,6	CASA+	0.706	0.269	0.307	0.442	0.471
IrisCB	LogP	JHX: 1,5,8; HK: 4,6	Dipole	0.551	0.322	0.38	0.915	0.215
IrisCB	LogP	JHX: 1,5,8; HK: 4,6	LogP	-0.973	0.074	0.092	0.169	0.917
IrisCB	LogP	JHX: 1,5,8; HK: 4,6	SLogP	-0.569	0.28	0.372	0.642	0.325

Table 3.22. Extended and cross-validated QSAR models relating to the measured parameters with clustered drug tissue levels in the iris/CB. An r^2 value with a (-) sign indicates a negative correlation. The clusters in green (8) were accepted, and the clusters in pink (13) were rejected due to $Xr^2 < 0.5$, $XRMSE \geq 1.2$, or a non-linear distribution of data points. The accepted clusters are shown in **Figure 3.12**.

Extended Iris/CB Cluster Correlations Identified by QuaSAR Algorithm

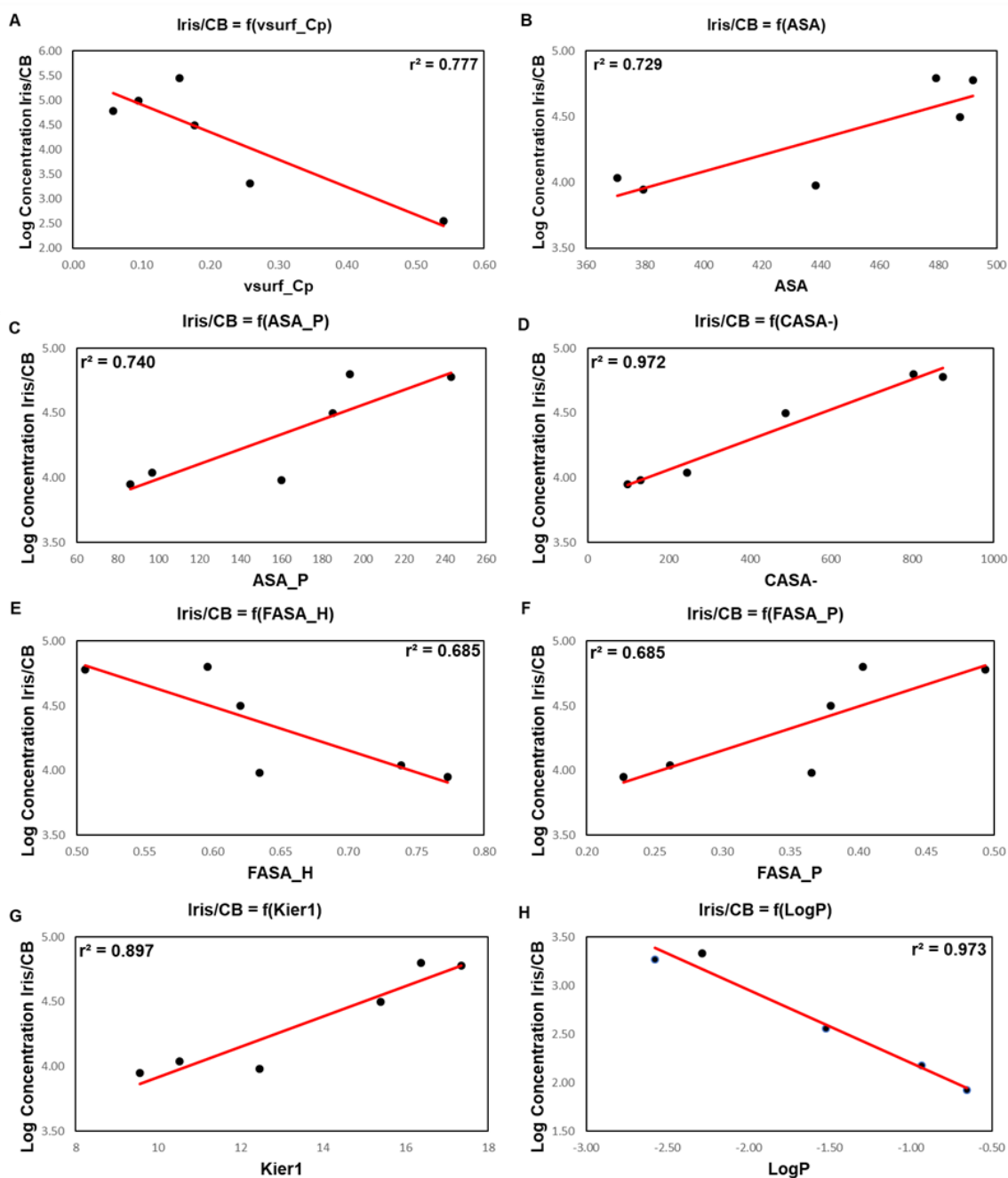


Figure 3.12. Cross-validated linear regression models between physicochemical descriptors and drug levels in the iris/CB where (A) corresponds to a newly identified vsurf_Cp cluster correlation between iris/CB and CASA+, (B) through (G) correspond to the new calculated ASA, ASA_P, CASA-, ASA_H, FASA_P, and Kier1 clusters from iris/CB and FASA_H in **Table 3.19** or FASA_P in **Table 3.15**, and (H) corresponds to the validated Cluster 1 between iris/CB and LogP in **Table 3.18**. These results suggest that globular, hydrophilic compounds are more likely to distribute into the iris/CB, which agrees with the trends observed and reported for the iris/CB using HCA in **Figure 3.3**.

The results from the validated lens cluster correlations (**Table 3.20, lens**) are presented in **Table 3.23**, where it is shown that one new cluster correlations was identified but rejected due to $Xr^2 \leq 0.5$.

Tissue	Cluster Parameter	Drugs in Cluster	Measured Parameter	r^2	MAE	RMSE	XRMSSE	Xr^2
Lens	LogP	JHX: 1,2,3,4,5,7,8	vsurf_D1	-0.545	0.506	0.622	0.799	0.309

Table 3.23. Extended and cross-validated QSAR model relating to the measured parameters with clustered drug tissue levels in the lens. An r^2 value with a (-) sign indicates a negative correlation. The identified cluster in pink was rejected due to an $Xr^2 < 0.5$.

The results from the validated NR cluster correlations (**Table 3.20, NR**) are presented in **Table 3.24**, where the extended relationships between NR and SLogP were examined. The difference between the clusters for SLogP₁ and SLogP₂ is the presence or absence of compound JHX-8. Though many clusters were identified based on r^2 value, only **CASA₋₁** ($Xr^2 = -0.509$) and **CASA₋₂** ($Xr^2 = -0.636$) were identified, suggesting that the cluster without JHX-8 yielded a stronger relationship between drug levels in the NR and the calculated physicochemical parameters. The graphed results of these identified QSAR models are shown in **Figure 3.13**.

Tissue	Cluster Parameter	Drugs in Cluster	Measured Parameter	r^2	MAE	RMSE	XRMSE	Xr^2
NR	SLogP ₁	JHX: 2,3,4,6,7,8; HK: 1,2,8	Apol	-0.509	0.444	0.606	0.797	0.228
NR	SLogP ₁	JHX: 2,3,4,6,7,8; HK: 1,2,8	ASA	-0.552	0.432	0.579	0.770	0.273
NR	SLogP ₁	JHX: 2,3,4,6,7,8; HK: 1,2,8	ASA_P	-0.656	0.398	0.508	0.697	0.397
NR	SLogP ₁	JHX: 2,3,4,6,7,8; HK: 1,2,8	CASA+	-0.559	0.449	0.574	0.737	0.317
NR	SLogP ₁	JHX: 2,3,4,6,7,8; HK: 1,2,8	CASA-	-0.710	0.373	0.466	0.619	0.509
NR	SLogP ₁	JHX: 2,3,4,6,7,8; HK: 1,2,8	Kier1	-0.682	0.379	0.488	0.656	0.456
NR	SLogP ₁	JHX: 2,3,4,6,7,8; HK: 1,2,8	SMR	-0.555	0.423	0.577	0.758	0.289
NR	SLogP ₁	JHX: 2,3,4,6,7,8; HK: 1,2,8	vsurf_G	-0.623	0.381	0.532	0.721	0.36
NR	SLogP ₁	JHX: 2,3,4,6,7,8; HK: 1,2,8	vsurf_W1	-0.676	0.382	0.493	0.687	0.436
NR	SLogP ₂	JHX: 2,3,4,6,7; HK: 1,2,8	Apol	-0.501	0.356	0.428	0.592	0.175
NR	SLogP ₂	JHX: 2,3,4,6,7; HK: 1,2,8	ASA	-0.519	0.344	0.42	0.581	0.198
NR	SLogP ₂	JHX: 2,3,4,6,7; HK: 1,2,8	ASA_P	-0.506	0.336	0.426	0.56	0.239
NR	SLogP ₂	JHX: 2,3,4,6,7; HK: 1,2,8	CASA+	-0.566	0.358	0.399	0.525	0.301
NR	SLogP ₂	JHX: 2,3,4,6,7; HK: 1,2,8	CASA-	-0.793	0.190	0.276	0.371	0.636
NR	SLogP ₂	JHX: 2,3,4,6,7; HK: 1,2,8	Kier1	-0.652	0.284	0.358	0.478	0.419
NR	SLogP ₂	JHX: 2,3,4,6,7; HK: 1,2,8	PM3_Dipole	-0.506	0.392	0.426	0.555	0.267
NR	SLogP ₂	JHX: 2,3,4,6,7; HK: 1,2,8	SMR	-0.547	0.341	0.408	0.558	0.243
NR	SLogP ₂	JHX: 2,3,4,6,7; HK: 1,2,8	vsurf_G	-0.595	0.323	0.386	0.54	0.299
NR	SLogP ₂	JHX: 2,3,4,6,7; HK: 1,2,8	vsurf_W1	-0.666	0.325	0.350	0.479	0.440

Table 3.24. Extended and cross-validated QSAR models relating to the measured parameters with clustered drug tissue levels in the NR. An r^2 value with a (-) sign indicates a negative correlation. The clusters in green (2) were accepted, and the clusters in pink (17) were rejected either due to $Xr^2 < 0.5$, $XRMSE \geq 1.2$, or a non-linear distribution of data points. The accepted clusters are shown in **Figure 3.13**.

Extended NR Cluster Correlations Identified by QuaSAR Algorithm

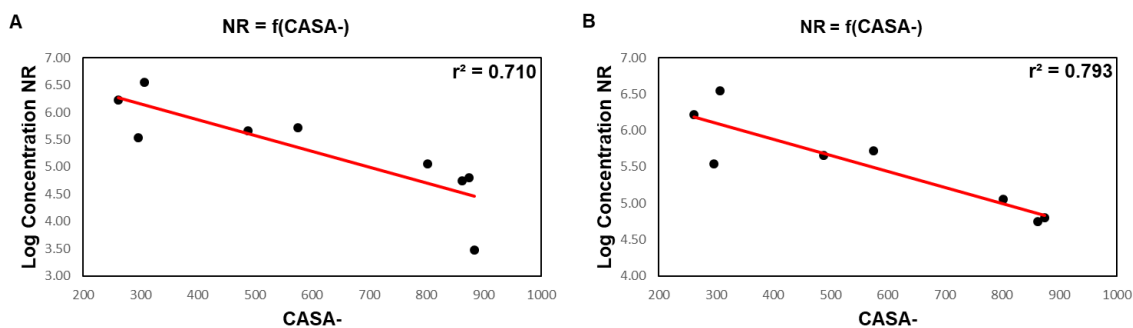


Figure 3.13. Cross-validated linear regression models between physicochemical descriptors and drug levels in the NR where (A) corresponds to the newly calculated CASA- clusters from Cluster 2 between NR and SLogP in **Tables 3.16** and **3.17**, and (B) corresponds to the newly calculated cluster from Cluster 2 between NR and SLogP in **Table 3.18**. These results suggest that hydrophilic molecules with less negatively charged surface area are more likely to distribute into the NR, which support the trends observe and reported in **Figure 3.5** demonstrating larger hydrophobic molecules are more likely to distribute into the NR.

The results from the validated RPE/C cluster correlations (**Table 3.20, RPE/C**) are presented in **Table 3.25**, where the extended relationships between RPE/C and Apol, ASA, and vsurf_W1 were examined. No clustered correlations were identified from the ASA and vsurf_W1 clusters because no new relationships were identified with an $r^2 \geq 0.5$. The Apol clusters were initially chosen based on r^2 values, and then subject to the internal cross-validation algorithm. For the RPE/C, this yielded three acceptable clustered correlations with **Dipole** ($Xr^2 = +0.584$), **PM3_Dipole** ($Xr^2 = +0.690$) and **SMR** ($Xr^2 = +0.539$). The graphed results of these extended QSAR models are shown in **Figure 3.14**.

Tissue	Cluster Parameter	Drugs in Cluster	Measured Parameter	r^2	MAE	RMSE	XRMSSE	Xr^2
RPE/C	Apol	JHX: 1,2,3,4; HK: 3,4,7,8,11,12,16	ASA	0.561	0.491	0.626	0.725	0.424
RPE/C	Apol	JHX: 1,2,3,4; HK: 3,4,7,8,11,12,16	Dipole	0.681	0.423	0.534	0.617	0.584
RPE/C	Apol	JHX: 1,2,3,4; HK: 3,4,7,8,11,12,16	Kier1	0.552	0.577	0.633	0.773	0.381
RPE/C	Apol	JHX: 1,2,3,4; HK: 3,4,7,8,11,12,16	PM3_Dipole	0.775	0.328	0.448	0.531	0.69
RPE/C	Apol	JHX: 1,2,3,4; HK: 3,4,7,8,11,12,16	SMR	0.651	0.435	0.558	0.647	0.539
RPE/C	Apol	JHX: 1,2,3,4; HK: 3,4,7,8,11,12,16	vsurf_W1	0.608	0.562	0.663	0.800	0.335

Table 3.25. Extended and cross-validated QSAR models relating to the measured parameters with clustered drug tissue levels in the RPE/C. An r^2 value with a (-) sign indicates a negative correlation. The clusters in green (3) were accepted, and the clusters in pink (3) were rejected due to $Xr^2 < 0.5$. The accepted clusters are shown in **Figure 3.14**.

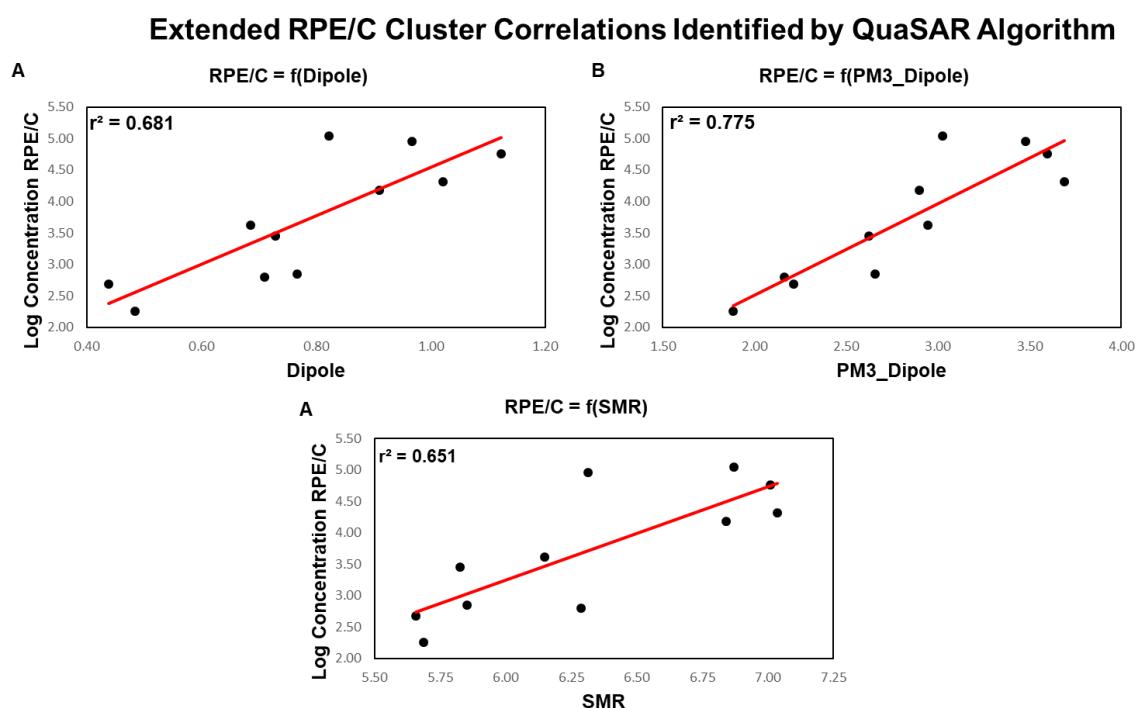


Figure 3.14. Cross-validated linear regression models between physicochemical descriptors and drug levels in the RPE/C where (A) through (C) corresponds to the newly calculated Dipole, PM3_Dipole, and SMR clusters from Cluster 1 between RPE/C and Apol in **Tables 3.14** and **3.15**. These results suggest that larger, polar hydrophilic molecules are more likely to distribute into the RPE/C, supporting the trends observed and reported for the RPE/C in **Figure 3.6** demonstrating more polar hydrophilic molecules are more likely to distribute into the RPE/C.

The results from the validated SN cluster correlations (**Table 3.20, SN**) are presented in **Table 3.26**, where the extended relationships between SN and ASA_P, SLogP, vsurf_Cp, and three different vsurf_W1 clusters were examined. The clusters were accepted based on initial r^2 values and subjected to the internal cross-validation algorithm. For the SN, this yielded six acceptable clustered correlations with **ASA_P** ($Xr^2 = -0.696$), **vsurf_W1** ($Xr^2 = -0.600$; $Xr^2 = -0.504$), **ASA_H** ($Xr^2 = +0.654$), **SLogP** ($Xr^2 = +0.937$), and **vsurf_Cp** ($Xr^2 = +0.596$). The graphed results of these extended QSAR models are shown in **Figure 3.15**.

The results from the validated kidney cluster correlations (**Table 3.20, kidney**) are presented in **Table 3.27**, where the extended relationships between kidney and SMR were examined. The clusters were initially accepted based on r^2 values, and then subject to the internal cross-validation algorithm. This yielded one acceptable clustered correlation between the kidney and **Kier1** ($Xr^2 = +0.656$). The graphed result of this extended QSAR models is shown in **Figure 3.16**.

Finally, the results from the validated liver cluster correlations (**Table 3.20, liver**) are presented in **Table 3.28**, where the extended relationships between liver and LogP were examined and no acceptable cluster correlations were identified.

Tissue	Cluster Parameter	Drugs in Cluster	Measured Parameter	r^2	MAE	RMSE	XRMSSE	Xr^2
SN	ASA_P	JHX: 2,3; HK: 2,3,7,8,12,16	ASA_P	-0.817	0.373	0.505	0.681	0.696
SN	ASA_P	JHX: 2,3; HK: 2,3,7,8,12,16	CASA+	-0.529	0.702	0.809	1.006	0.318
SN	ASA_P	JHX: 2,3; HK: 2,3,7,8,12,16	Kier1	-0.557	0.720	0.785	1.014	0.357
SN	ASA_P	JHX: 2,3; HK: 2,3,7,8,12,16	vsurf_W1	-0.742	0.531	0.599	0.762	0.600
SN	SLogP	HK: 5,7,12,13,16	ASA_H	0.836	0.094	0.100	0.188	0.654
SN	SLogP	HK: 5,7,12,13,16	CASA+	-0.562	0.119	0.164	0.211	0.298
SN	SLogP	HK: 5,7,12,13,16	CASA-	-0.856	0.090	0.094	0.169	0.608
SN	SLogP	HK: 5,7,12,13,16	LogP	0.700	0.115	0.136	0.199	0.486
SN	SLogP	HK: 5,7,12,13,16	SLogP	0.972	0.033	0.041	0.063	0.937
SN	SLogP	HK: 5,7,12,13,16	vsurf_Cp	0.772	0.100	0.118	0.225	0.596
SN	vsurf_Cp	JHX: 6,7,8; HK: 2,5,7,12,13,16	CASA-	-0.512	0.146	0.171	0.215	0.278
SN	vsurf_Cp	JHX: 6,7,8; HK: 2,5,7,12,13,16	SLogP	0.520	0.144	0.169	0.209	0.295
SN	vsurf_Cp	JHX: 6,7,8; HK: 2,5,7,12,13,16	vsurf_Cp	0.588	0.125	0.157	0.191	0.424
SN	vsurf_Cp	JHX: 6,7,8; HK: 2,5,7,12,13,16	vsurf_W1	-0.517	0.143	0.170	0.216	0.257
SN	vsurf_W1 ₁	JHX: 1; HK: 2,3,4,6,7,8,12,16	CASA+	-0.727	0.661	0.755	1.082	0.622
SN	vsurf_W1 ₁	JHX: 1; HK: 2,3,4,6,7,8,12,16	CASA-	-0.630	0.697	0.879	1.109	0.432
SN	vsurf_W1 ₁	JHX: 1; HK: 2,3,4,6,7,8,12,16	SLogP	0.537	0.708	0.983	1.292	0.257
SN	vsurf_W1 ₂	JHX: 1; HK: 2,3,4,6,7,8,16	CASA+	-0.697	0.702	0.792	1.164	0.579
SN	vsurf_W1 ₂	JHX: 1; HK: 2,3,4,6,7,8,16	CASA-	-0.602	0.748	0.908	1.302	0.342
SN	vsurf_W1 ₃	HK: 2,3,4,6,7,8,12,16	CASA+	-0.507	0.565	0.755	0.913	0.307
SN	vsurf_W1 ₃	HK: 2,3,4,6,7,8,12,16	vsurf_W1	-0.639	0.527	0.646	0.766	0.504

Table 3.26. Extended and cross-validated QSAR models relating to the measured parameters with clustered drug tissue levels in the SN. An r^2 value with a (-) sign indicates a negative correlation. The clusters in green (6) were accepted, and the clusters in pink (15) were rejected due to $Xr^2 < 0.5$. The accepted clusters are shown in **Figure 3.15**.

Extended SN Cluster Correlations Identified by QuaSAR Algorithm

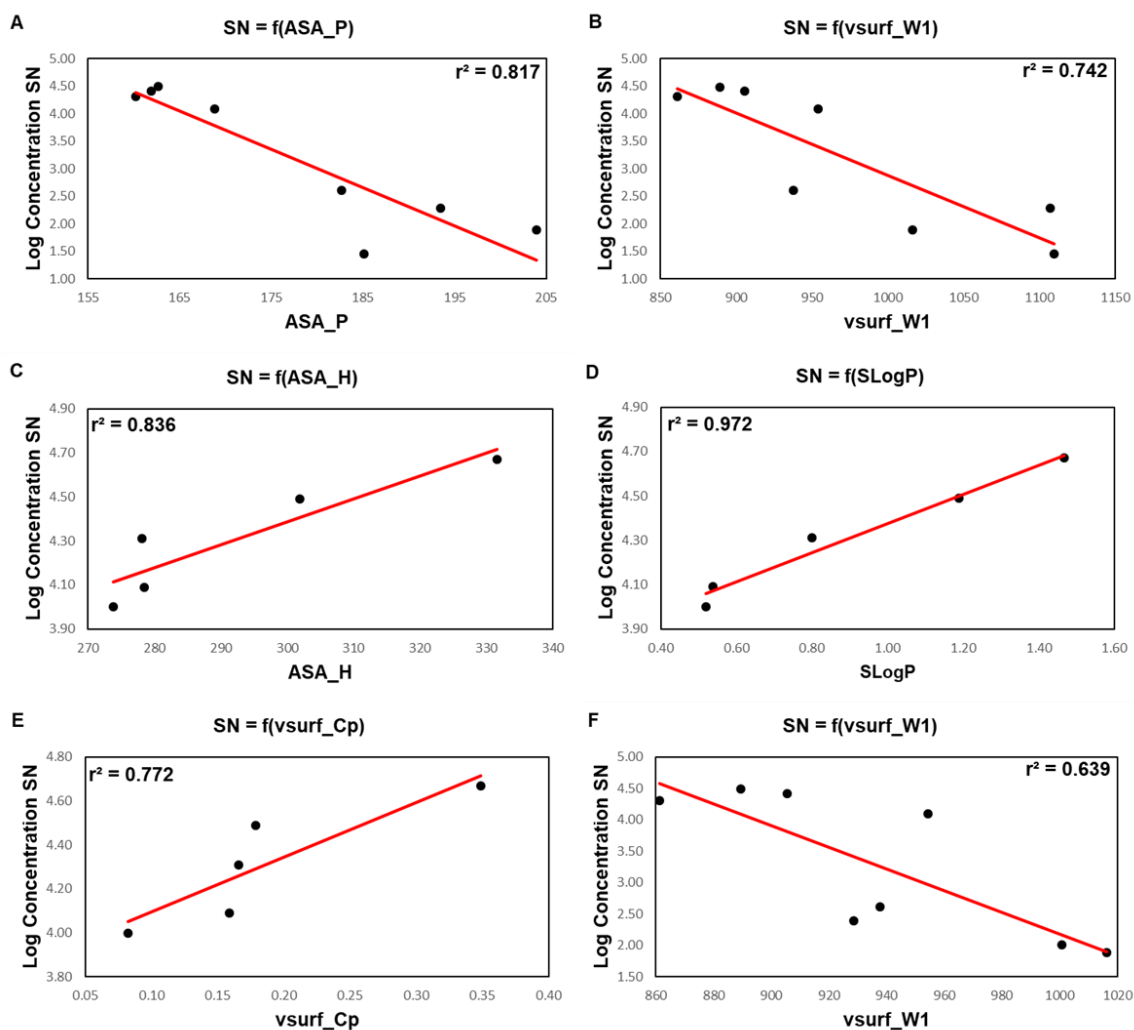


Figure 3.15. Cross-validated linear regression models between physicochemical descriptors and drug levels in the SN where (A) and (B) correspond to the newly calculated ASA_P and vsurf_W1 clusters from Cluster 2 between SN and ASA_P in **Tables 3.12**, (C) through (E) correspond to the validated SLogP cluster and new calculated ASA_H and vsurf_P clusters from Cluster 2 between SN and SLogP in **Table 3.19**, and (F) corresponds to the validated vsurf_W1 cluster from Cluster 1 between SN and vsurf_W1 in **Table 3.12**. These results suggest that hydrophobic molecules with micellar-shape are more likely to distribute into the SN, which supports the trends observed and reported in **Figure 3.8**.

Tissue	Cluster Parameter	Drugs in Cluster	Measured Parameter	r^2	MAE	RMSE	XRMSSE	Xr^2
Kidney	SMR	JHX: 2; HK: 3,4,7,8,11,15,16	Dipole	0.648	0.17	0.208	0.257	0.49
Kidney	SMR	JHX: 2; HK: 3,4,7,8,11,15,16	Kier1	0.753	0.128	0.174	0.207	0.656
Kidney	SMR	JHX: 2; HK: 3,4,7,8,11,15,16	PM3_Dipole	0.62	0.182	0.216	0.265	0.451
Kidney	SMR	JHX: 2; HK: 3,4,7,8,11,15,16	vsurf_Cp	-0.566	0.203	0.231	0.297	0.353
Kidney	SMR	JHX: 2; HK: 3,4,7,8,11,15,16	vsurf_W1	0.58	0.198	0.227	0.278	0.393

Table 3.27. Extended and cross-validated QSAR models relating to the measured parameters with clustered drug tissue levels in the kidney. An r^2 value with a (-) sign indicates a negative correlation. The cluster in green (1) was accepted, and the clusters in pink (4) were rejected due to $Xr^2 < 0.5$. The accepted cluster is shown in Figure 3.15.

Extended Kidney Cluster Correlation Identified by QuaSAR Algorithm

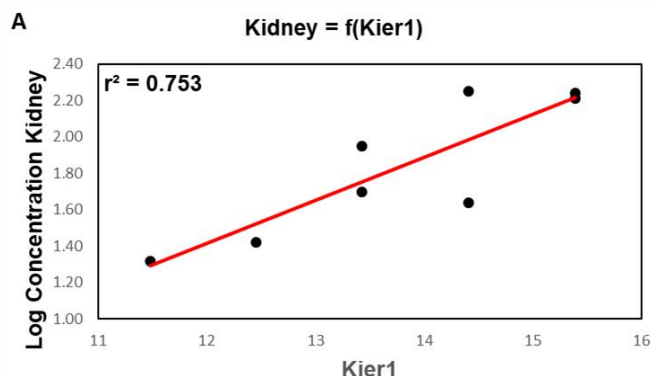


Figure 3.16. Cross-validated linear regression model between physicochemical descriptor Kier1 and drug levels in the Kidney where (A) corresponds to the newly calculated Kier1 cluster from Cluster 2 between kidney and SMR in Table 3.9. This result suggests that larger, more branched molecules are more likely to distribute into the kidney, which supports the trends observed and reported in Figure 3.9 that indicate larger, polar molecules with a greater positively-charged surface area are more likely to distribute into the kidney.

Tissue	Cluster Parameter	Drugs in Cluster	Measured Parameter	r^2	MAE	RMSE	XRMSSE	Xr^2
Liver	LogP	HK: 1,3,4,5,6,7,8,10	vsurf_Cp	0.525	0.299	0.399	0.502	0.288

Table 3.28. Extended and cross-validated QSAR model relating to the measured parameter vsurf_Cp with clustered drug tissue levels in the liver. An r^2 value with a (-) sign indicates a negative correlation. The identified cluster in pink was rejected due to an $Xr^2 < 0.5$.

3.5 Discussion

3.5.1 Initial Linear Regression Analysis

The possibility that predictive models of drug distribution using the 24 orally-active multifunctional antioxidants (MFAO), their monofunctional free radical scavengers (FRS) and bio-active transition metal chelators (CHL), and their nonfunctional parent (NF) analogs, could be developed was investigated. Initially, the results for the compounds found in the greatest concentrations per functional family were plotted against the calculated physicochemical parameters of those compounds, followed by linear regression analysis. These compounds included the NFs JHX-1 and HK-13, the FRS JHX-6, the CHLs JHX-3 and HK-1, and the MFAOs HK-2 and HK-8. The calculated physicochemical parameters each represent a general molecular attribute and are categorized as lipophilic, hydrophilic, or structural terms, which are used to develop physiologically-relevant modeling equations [22]. The classifications of each for each physicochemical parameter are reported in **Table 3.1**.

The preliminary correlations reported in **Tables 3.2 to 3.5** are meaningless without understanding the general properties of molecules required to pass through tissues [23]. Just like the calculated physicochemical parameters are assigned a property, so are the physiological barriers in tissues which also possess different degrees of lipophilicity or hydrophilicity. With the preliminary correlation data set including the NF compound (no antioxidant activity), two strong correlations (“r” value between ± 0.7 and ± 1.0) which followed physiologically-known trends were observed: **lens** with ASA_P ($r = +0.801$) and **RPE/C** with ASA_H ($r = -0.818$). The data set excluding NFs found 10 strong correlations following physiologically-known trends: **cornea** with Dipole ($r = +0.777$), Apol ($r = +0.833$),

ASA ($r = +0.848$), ASA_P ($r = +0.912$), and SMR ($r = +0.825$); **lens** with Dipole ($r = +0.810$) and PM3_Dipole ($r = +0.905$); **NR** with PM3_Dipole ($r = -0.801$); **brain** with ASA_H ($r = +0.840$) and Kier1 ($r = +0.818$). Due to the identification of many correlations which followed physiologically-known trends, it appeared that the creation of predictive models was plausible [14].

Linear regression analysis of the full data set suggested that there may be some relationships between the 24 compounds and various calculated physicochemical descriptors (**Table 3.6**), and unfortunately the linear regression analysis on the mathematically standardized data set provided more questions rather than answers as no moderate correlations nor strong correlations were identified (**Table 3.7**). Hence, attention was turned towards two common data mining techniques, hierarchical cluster analysis (HCA) followed by linear regression analysis and quantitative structure activity relationship (QSAR) analysis, to investigate whether it was possible to elucidate unknown relationships between the drug levels found in tissues and their calculated physicochemical descriptors. These two techniques were applied to confirm whether using different strategic approaches resulted in similar clusters and/or correlation outcomes.

3.5.2 Clustered Correlations and Cluster Confirmations using QSAR Algorithms

HCA was conducted on both data sets using average-linkage and complete-linkage distance measures with the Euclidean distance metric. The HCA method employed here is called *agglomerative clustering*, also known as a “bottom-up” approach, where each data point in 2D space (*i.e.*, an (x,y) coordinate where x = tissue level of drug and y = calculated physicochemical parameter of drug, or *vice-versa*) is treated as its own individual cluster. Based on the linkage algorithm, each of the points are successively

combined until one large cluster with all data points remains. For cluster analysis, the linkage algorithm is important because it can be used to help understand the (dis)similarities between cluster groups. Both complete-linkage and average-linkage measures were used. The complete-linkage measure is an algorithm which merges the points of two clusters with the smallest *maximum* distance, which has been shown to maximize the probability that the most dissimilar clusters will be identified through its sensitivity to outliers [24]. In contrast, the average-linkage measure is a combined algorithm using aspects of both complete-linkage and single-linkage measures to create a balanced group of clusters, though more weight is given to the complete-linkage algorithm [25]. These two linkage algorithms are the most popular distance metrics in hierarchical clustering. The single-linkage measure was not used due to its tendency to compact data sets into very similar groups [26]. Additionally, the distance metric chosen for clustering was Euclidean distance because it measures the 2D linear distance between two clusters.

For both the full and standardized data sets, the drug levels for each tissue were plotted against the calculated physicochemical parameter of the drugs. These were then subject to HCA using both average-linkage and complete-linkage algorithms. An example of the results from these algorithm calculations are illustrated in **Figure 3.1** which shows two model groups of dendrograms for the Apol and Kier1 parameters. Each dendrogram chart represents the clustered data of the specified tissue's drug levels and the calculated physicochemical parameter of the drugs. The different colors within each dendrogram (*i.e.*, red, green, blue, cyan, purple) represent a unique cluster of compounds identified by the algorithm within a specific data set. Any clusters containing less than 5 drugs were excluded from further analysis because such clusters do not meet the minimum Hansch analysis criteria of 5-6 drugs per cluster per descriptor [23]. Though these dendrograms

may look similar between tissues, this did not indicate that the same drugs were clustered together, nor that the correlations of these clusters were similar. Each calculated cluster identified by HCA analysis that met Hansch analysis criteria was further subject to linear regression analysis, and the results for all clustered correlations are shown in **Tables 3.8** to **3.11** for *structural* parameters, **Tables 3.12** to **3.15** for *hydrophilic* parameters, and **tables 3.16** to **3.19** for *hydrophobic* parameters.

The clustered correlation values (*i.e.*, Pearson's r-value) for the full data set of the structural parameters using average-linkage and complete-linkage algorithms, respectively, are shown in **Tables 3.8 and 3.9**. Each of these clustered correlations were graphed and those with a non-linear distribution of data points (*i.e.*, data points localized at two extremes) were eliminated. Though many clusters did not appear to indicate even modest relationships, there were a large number of clusters which appeared to suggest robust relationships. Clusters highlighted in yellow indicate a moderate correlation ("r" value between ± 0.5 and ± 0.7), while clusters highlighted in green indicate a strong correlation ("r" value between ± 0.7 and ± 1.0) for the respective linkage algorithms. Clusters highlighted in blue were found to be identical clusters between both average-linkage and complete-algorithms for that tissue/descriptor cluster set, and clusters highlighted in pink were eliminated due to a non-linear distribution of data points. This method was also applied to the standardized data set of the structural parameters (**Tables 3.10 and 3.11**) and both data sets of the hydrophilic and hydrophobic parameters (**3.12 to 3.19**).

For cluster correlations to have any predictive merit, two major criteria must be met. The first criterion is that the r^2 value, also known as the coefficient of determination, must meet or exceed a value of 0.5. The r^2 value is a statistical measure of the strength

of the regression prediction and the degree of influence both variables have on each other [27]. In the case of an r^2 value of 0.5, this means that 50% of the variation in the correlation/model is due to the variability between the measured variables, while 50% of the variation is attributed to external factors. Because greater r^2 values suggest model robustness, all correlations with Pearson's r -values with an absolute value less than 0.707 were eliminated. The second criterion is that the p -value of the cluster correlations must be less than 0.05. The p -value is statistically defined as the probability, under a specified statistical model, that the statistical summary of the data would be equal to or more extreme than its observed value [28]. A predictive model with a calculated p -value of less than 0.05 also suggests greater model robustness. The final clustered correlations by means of HCA and linear regression analysis that meet these two criteria are presented, per tissue, in **Figures 3.2 to 3.10**.

3.5.2a. Blood-Aqueous Barrier Penetration

For a drug in systemic circulation to distribute into the cornea, iris/CB, or lens, it must penetrate the blood-aqueous barrier (BAB), a network of tight junctions in the non-pigmented epithelium of the ciliary process and the endothelial cells in the iris vasculature [29]. These cell layers prevent drug entry into aqueous humor and the intraocular tissues of the anterior segment due to the presence of tight junctions which regulate solute passage [30, 31]. The clustered correlations for the cornea, iris/CB, and lens are shown in **Figures 3.2, 3.3, and 3.4**, respectively.

The vasculature of the ciliary body is supplied by the anterior ciliary arteries and the long posterior ciliary arteries, forming the major arterial circle near the root of the iris wherefrom branches supply the iris, ciliary body, and the anterior choroid. The ciliary body

vasculature is also fenestrated to allow passage of plasma proteins and molecules into the stroma as part of aqueous humor production [32]. The non-pigmented cell layer of the ciliary epithelium, and the endothelial cells of iris blood vessels, are believed to make up the blood-aqueous barrier (BAB). Tight junctions are present in the non-pigmented cell layer of the ciliary epithelium, suggesting its role as the physical barrier to drug movement across the ciliary body [33]. Therefore, distribution of drugs to the cornea and lens require transit through the iris/CB. According to **Figure 3.3**, parameters strongly correlated with iris/CB drug levels include the hydrophilic parameter **FASA_P**, the structural parameter **vsurf_G**, and the hydrophobic parameters **FASA_H** and **LogP**. All hydrophilic and structural parameters are positively correlated, and all hydrophobic parameters negatively correlated, with iris/CB drug levels, suggesting that globular hydrophilic drugs with a greater polar surface area have a greater probability of distributing into the iris/CB.

Upon transit through the iris/CB, the drugs enter circulation of the aqueous humor which flows from the ciliary body, into the anterior chamber, and out through the trabecular meshwork and Schlemm's canal. During aqueous circulation, the drugs can distribute to the lens through the lens epithelial cells. Drug distribution to isolated lenses have been extensively studied with various compounds such as pilocarpine [34], dexamethasone [35], epinephrine [35], and timolol [36], and suggest that lipophilic drugs are able to distribute into the lens. One comprehensive study with 13 small molecule xenobiotics and amino acids investigated *in vitro* drug partition through rabbit lenses and linked lipophilicity with increased lens uptake rate, suggesting that lipophilic drugs penetrate the lens better than more polar, hydrophilic compounds [37]. Another study investigated various drugs and dyes and found consistent distribution to the lens capsule, epithelium, and cortex of the porcine lens, but not to the lens nucleus [38]; these findings agree with other reported *in vivo* and *in vitro* results [37, 39].

Unfortunately, drug distribution studies to the lens are limited in literature and it is difficult to assess what factors contribute to overall lens uptake. It was initially assumed that more lipophilic drug characteristics were desired in order to penetrate into the lens. The opposite was observed in our studies, both in a preliminary distribution study in mice by Kawada and my distribution study in rats (Chapter 2). The lens distribution results herein (**Figure 3.4**) reveal that the hydrophilic parameters **FASA_P** and **LogS** are positively correlated with lens distribution, while the hydrophobic parameter **LogP** is negatively correlated with lens distribution. This is a similar trend to the one observed in the iris/CB, where it was also observed that hydrophilic drugs with a greater polar surface area have a higher likelihood of distributing to the iris/CB. It is possible that a balance of lipophilic and hydrophilic characteristics are required for lens distribution, but future investigations must be done to determine whether this is the case.

From aqueous circulation, drugs may also enter the cornea through the corneal endothelial cells. Few oral drug treatments have been shown to deliver to the diseased cornea such as miltefosine [40], cyclosporin [41], tetracycline [42], and prednisolone [43]. However, studies comparing the effects of different routes of administration on corneal drug delivery are limited, especially since the most convenient route for treating corneal ailments is by topical application; scarce are models predicting corneal permeability upon oral distribution. Araki-Sasaki and colleagues demonstrated in healthy rabbits that corticosteroids reached the cornea in higher concentrations upon topical application (dexamethasone) than upon oral administration (prednisolone). Though this was expected, it was also found that both oral and topical administration of these corticosteroids resulted in similar distributions to the conjunctiva [44]. Furthermore, Sharma and colleagues developed a novel QSPR model using molecular descriptors to

predict the penetration of nine fluoroquinolones, though this was based on topical administration and corneal predictability was found to be unachievable [45]. Whether hydrophilicity or lipophilicity is a greater factor in corneal permeation remains to be determined as results continue to be conflicting and based solely on topical formulations [45-49]. Our results indicate that corneal drug levels are positively correlated with the hydrophilic parameters **CASA+**, **ASA_P**, and **LogS**, and the structural parameter **SMR**. SMR is an indirect measure of molecular size (*i.e.*, larger SMR suggests to greater molecular size) and is strongly correlated with hydrophilicity and polarizability. These data, reported in **Figure 3.2**, suggest that larger, polar, hydrophilic molecules with a greater positively-charged surface area have a greater likelihood of distributing into the cornea. These findings agree with other reported hydrophilic trends for corneal drug penetration through different routes of administration [50, 51].

3.5.2b. Blood-Retinal Barrier Penetration

For drugs in systemic circulation to distribute into the neural retina or retinal pigmented epithelium and choroid (RPE/C), they must penetrate the blood-retinal barrier (BRB). Like the BAB in the anterior segment, the BRB is the major barrier of ocular drug delivery to the posterior segment from the blood. By means of tight junctions, the BRB regulates fluids and molecular movement between the ocular vascular beds and retinal tissues, prevents leakage of macromolecules and other potentially harmful agents into the retina, and maintains the microenvironment of the retina [52]. The BRB consists of two parts, the inner BRB (iBRB) formed by non-fenestrated retinal capillary endothelial cells, and the outer BRB (oBRB) formed by the tight junctions of the retinal pigmented epithelial cells with support from Bruch's membrane that prevent passage of large molecules from the choriocapillaris [53]. The clustered correlations for the neural retina (NR) and retinal

pigmented epithelium with choroid (RPE/C) are shown in **Figures 3.5** and **3.6**, respectively.

The RPE comprises the oBRB and is situated between the retinal photoreceptors and choroid. It has several essential functions, namely absorbing scattered light, phagocytosis of photoreceptor outer segment membranes, and maintaining the homeostasis between the neural retina and circulating blood. Due to its large surface area, the RPE is considered an important route of passage of small molecular weight drugs, especially in their elimination [54], because small molecules may cross the RPE both transcellularly and paracellularly [55]. Though drugs may cross the RPE by passive diffusion and/or active transport, evidence suggests that passive permeability is the main mechanism of drug distribution across the BRB [56-58]. It has been shown that drugs in the bloodstream rapidly equilibrate with the extravascular space of the choroid because the choriocapillaris is fenestrated, and the RPE limits the permeation of drugs from the choroid to the retina [59, 60]. Additionally, the inward permeability of more hydrophilic drugs, such as the beta blockers atenolol and nadolol, were found to penetrate greater than the more hydrophobic drugs pindolol, metoprolol, timolol, and betaxolol [31, 61, 62]. In agreement with these reports, the cluster correlations for the RPE/C (**Figure 3.6**) illustrate positive correlations between RPE/C drug levels and the hydrophilic parameters **Apol**, **ASA**, **LogS**, and **vsurf_W1**, indicating that large, polar, hydrophilic drugs with a greater polar surface area are more likely to distribute to the RPE/C.

Consequently, the iBRB prevents the free diffusion of substances between the neural retina (NR) and the circulating endoneurial blood [63]. Transcellular transport by retinal capillary endothelial cells is required for a variety of low molecular weight compounds such as amino acids and D-glucose [64, 65]. When a drug is administered

systemically, it must pass the iBRB to reach therapeutic levels in the neural retina. Drug penetration across the iBRB depends on various factors including plasma protein binding of the drug, plasma concentration of the drug, and the drug's volume of distribution (pharmacokinetic parameter representing a drug's tendency to remain in plasma or distribute to a tissue) [66]. It is well-known that hydrophilic molecules are impermeable through the iBRB and, in general, drugs with more lipophilic characteristics penetrate the iBRB better. The data in **Figure 3.5** agree with this general presumption, where it is reported that drug levels in the NR are positively correlated with the hydrophobic parameter **SLogP** and the structural parameter **Kier1**, indicating that larger, branched, hydrophobic molecules are more likely to distribute into the NR.

3.5.2c. Blood-Brain and Blood-Nerve Barrier Penetration

The blood-brain barrier (BBB) and blood-nerve barrier (BNB) constitute a complex interface between the blood, the central nervous system (CNS), and the peripheral nervous system (PNS). The BBB protects the brain by controlling molecule exchange from the blood and regulates the transmigration of immune cells. It is mainly composed of brain microvascular endothelial cells, pericytes, astrocytes, and basement membranes [67, 68]. Like the BAB and BRB, the BBB is comprised of tight junctions. The BNB has a similar structure to the BBB except that it lacks supporting astrocytes [69]. Despite the lack of astrocytes, reports indicate that the BNB has similar properties to the BBB which suggests that the specific structural components of the basement membrane at the BNB affects barrier function [69, 70]. Both the BBB and BNB play crucial roles in maintaining homeostasis of the CNS and PNS, respectively [71].

Molecules cross the BBB both paracellularly and transcellularly. For the paracellular pathway, ions and solutes use concentration gradients to pass the BBB by passive diffusion. The transcellular pathway includes passive diffusion and transcytosis. Physicochemical factors that influence BBB permeability include molecular weight, charge, hydrophobicity, surface activity, and relative molecular size [72], yet the BBB prevents entry into the brain of most drugs from the blood. While it is assumed that small molecules are freely transported across the BBB, *ca.* 98% are not; however, almost all drugs for the brain in the clinic are highly lipid soluble small molecules with a molecular weight < 400 Da [73-75]. Unfortunately, only one cluster correlation was identified for the brain. The data presented in **Figure 3.7** shows that drug concentration in the brain is positively correlated with **vsurf_Cp**, a structural parameter which measures micellar shape of molecules. Molecular structure has not been well documented for BBB passage, nor used in predictive BBB models.

The PNS and CNS constantly transmit signals between each other which is critical for normal human sensory and motor function. To ensure proper function of peripheral nerves, the maintenance of homeostasis is required for the endoneurial environment. This is endowed by the presence of the BNB which is located at the innermost layer of the perineurium and at the endoneurial microvessels within the nerve fascicles in the PNS [76, 77]. The tight junctions between the endothelial cells and pericytes in the endoneurial vasculature isolate the endoneurium from the blood, thereby preventing uncontrollable leakage of molecules and ions from the circulatory system to the peripheral nerves. Evidence from various physiological and morphological studies indicates that BNB exchange occurs predominantly through endoneurial capillaries and that perineurial passage constitutes a minor route [78-81]. For drug targets located in peripheral nerves,

the BNB can be problematic because of its potential to restrict or prevent drugs from reaching their site of action [81, 82].

Little is known about the impact of the blood-nerve barrier (BNB) on drug distribution into peripheral nerves. Previous studies indicate that the distal trunks of peripheral nerves, such as the sciatic nerve, are relatively impermeable to hydrophilic small molecules and many large molecules due to limited intercellular diffusion [83-85]. Despite some basic drug passage studies, a systematic and quantitative evaluation of the distribution of small molecule drugs into peripheral nerves is still absent. Compared to BBB penetration, the physicochemical and transport properties governing the drug distribution into peripheral nerves remains largely unexplored. One recent study from GlaxoSmithKline by Liu and colleagues shows that the sciatic nerve is more permeable to small, lipophilic molecules with structural diversity compared to the BBB [86]. Our reported cluster correlations in **Figure 3.8** support this finding and show that SN concentration is positively correlated with the hydrophobic parameter **SLogP** and the structural parameters **Kier1** and **vsurf_Cp**, and negatively correlated with the hydrophilic parameters **ASA_P** and **vsurf_W1**. This suggests that large, branched, micelle-like hydrophobic molecules are more likely to distribute into the SN.

3.5.2d. Peripheral Tissue Distribution

The liver and kidneys are two vital organs responsible for the metabolism and excretion of drugs, respectively. However, there is a lack of site-specific delivery of drugs to both hepatocytes and nephrons [87, 88]. Most discussions concerning the liver and kidney come from a toxicological perspective, such as drug-induced liver injury and drug-induced kidney injury, as these organs are rarely the direct targets of therapeutic drugs

[89-91]. As a result, there are limited, if any, models for drug distribution to the liver and kidney. **Figures 3.9** and **3.10** illustrate the predictive cluster correlations of the MFAOs and their analogs to the kidney and liver, respectively. It was observed that drug concentration in the kidney is positively correlated with the hydrophilic parameter **CASA+** and the structural parameter **SMR**, while the liver is negatively correlated with the hydrophilic parameter **PM3_Dipole** and positively correlated with the hydrophobic parameter **LogP**. These reports indicate that larger, polar, hydrophilic drugs with a larger positively-charged surface area are more likely to distribute into the kidney, and that more nonpolar hydrophobic drugs preferentially distribute into the liver. These results support the general known trends of drug distribution in the body. The liver is the primary site of metabolism and contains the necessary enzymes to metabolize drugs [92]. Most drugs are lipophilic, and upon oral administration they eventually reach the liver and readily undergo first-pass metabolism to increase their hydrophilicity [93]. These modifications are necessary for excretion by the kidneys, since the kidneys cannot efficiently filter and excrete lipophilic drugs [94]. However, drugs can also be excreted from the liver into bile which get released into the gastrointestinal tract, where drugs can then be reabsorbed into systematic circulation.

3.5.2e. Verification of HCA Clustered Correlations

To verify the HCA clustered correlations, the data sets were also subject to the intrinsic “QuaSAR” algorithm in MOE™. Most of the clustered correlations identified by OriginPro™ were also identified with MOE™. Though a few correlations were eliminated due to p-value exclusion criteria (*i.e.*, $p > 0.05$), a few new correlations were identified. These resulting clustered correlations are shown in **Table 3.20** along with the drugs in the clusters, the mean average error (MAE), the root-mean standard error (RMSE), cross-

validated RMSE (XRMSE) and cross-validated r^2 (Xr^2) values. Unlike the results from HCA analysis using OriginPro™, no models were found for the brain. This approach validated the HCA methods of analysis by means of a more mathematically rigorous algorithm and was able to eliminate less robust models.

3.5.3 *Extended Linear Regression Using QSAR-Derived Clustered Correlations*

Could these determined clusters, which were identified using two different mathematical approaches with OriginPro™ and MOE™, be correlated with other physicochemical descriptors? To investigate this possibility, the “QuaSAR” algorithm in MOE™ was employed. All identified cluster correlations in **Table 3.20** were re-evaluated against all physicochemical descriptors (**Table 3.1**) to confirm whether these clusters can be used to further identify relationships between tissue drug levels and the calculated physicochemical descriptors. The results in **Tables 3.21** through **3.28** report the identified clusters where clusters highlighted in green were accepted and clusters highlighted in red were rejected by the internal validation algorithm. The rejection criteria included the resulting calculations with a weak cross-validated coefficient of determination ($Xr^2 < 0.5$), a large cross-validated error ($XRMSE \geq 1.2$), or a non-linear distribution of data points.

The accepted clusters after intrinsic cross-validation for the cornea, iris/CB, NR, RPE/C, SN, and kidney are reported in **Figures 3.11** to **3.16**. These models agree with the reported HCA trends for the cornea (**Figure 3.2**), iris/CB (**Figure 3.3**), NR (**Figure 3.5**), RPE/C (**Figure 3.6**), SN (**Figure 3.8**), and kidney (**Figure 3.9**). No models were identified for the lens, brain, or liver, but these results indicated that there are multiple physicochemical descriptors that can be used to develop predictive models for drug distribution to various tissues. Though many of the parameters used herein have been

commonly used in QSAR and computational studies, many of them have not been widely accepted or standardized since they cannot be validated experimentally. For example, the hydrophobic parameter LogP is the partition coefficient of a drug which can be determined experimentally by measuring its concentration in octanol vs. water. However, a structural parameter like Kier1 or a hydrophilic parameter like CASA+ cannot be determined experimentally as their values are based on theoretical calculations.

Using the QuaSAR algorithms, four predictive models were identified for the cornea as reported in **Figure 3.11**. Drug levels in the cornea were found to be a function of **FASA_H** ($r^2 = -0.752$), **vsurf_Cp** ($r^2 = -0.785$), **FASA_P** ($r^2 = +0.752$), and **LogS** ($r^2 = +0.831$). Just like the results from HCA (**Figure 3.2**), these models show that increased hydrophilicity of a drug increases the probability of drug distribution to the cornea. The same trend is observed in the iris/CB in **Figure 3.12** where iris/CB drug levels were found to be a function of **vsurf_Cp** ($r^2 = -0.777$), **ASA** ($r^2 = +0.729$), **ASA_P** ($r^2 = +0.740$), **CASA-** ($r^2 = +0.972$), **FASA_H** ($r^2 = -0.685$), **FASA_P** ($r^2 = +0.685$), **Kier1** ($r^2 = +0.897$), **LogP** ($r^2 = -0.973$), and **SLogP** ($r^2 = -0.982$). These predictive models also agree with the calculated HCA results (**Figure 3.3**), further supporting the premise that more hydrophilic compounds are required to permeate the BAB and deliver to tissues of the anterior segment.

Two predictive models were identified for the NR as reported in **Figure 3.13**. Both models identified a negative correlation between NR drug levels and the hydrophilic parameter **CASA-** ($r^2 = -0.710$; $r^2 = -0.793$). Though this model is different compared to calculated HCA results (**Figure 3.5**), which found positive correlations between the hydrophobic parameter **SLogP** and the structural parameter **Kier1**, the same overall trend was identified where molecules with more lipophilic properties are more likely to distribute

into the NR. Additionally, **Figure 3.14** demonstrated the positive correlation between RPE/C drug levels and the hydrophilic parameters **Dipole** ($r^2 = +0.681$), **PM3_Dipole** ($r^2 = +0.775$), and **SMR** ($r^2 = +0.651$), while HCA calculations showed positive correlation between RPE/C and the hydrophilic parameters **Apol**, **ASA**, **LogS**, and **vsurf_W1** (**Figure 3.6**). These results support the calculated HCA results, demonstrating that drugs with greater hydrophilic characteristics are more likely to distribute into the RPE/C. These models suggest that compounds possessing hydrophilic characteristics are more likely to pass the oBRB and distribute to the RPE/C, while compounds with lipophilic properties are required for iBRB passage for delivering to the NR.

No predictive models were identified for the brain using the MOE™ QuaSAR algorithm. In contrast, all calculated predictive models using the QuaSAR algorithm for the SN are shown in **Figure 3.15**. SN drug levels are positively correlated with the hydrophobic parameters **ASA_H** ($r^2 = +0.836$) and **SLogP** ($r^2 = +0.972$) and the structural parameter **vsurf_Cp** ($r^2 = +0.772$), and negatively correlated with the hydrophilic parameters **ASA_P** ($r^2 = -0.817$) and **vsurf_W1** ($r^2 = -0.639$). Interestingly, the identified parameters and their trends are very similar to those seen in the calculated HCA cluster correlations (**Figure 3.8**), suggesting that these cluster correlations may have strong predictability. Since drug distribution to the SN and peripheral nerves is underexplored, this is one of the first predictive models for SN drug distribution which suggests that drugs with more lipophilic characteristics that resemble a micellar shape are more likely to pass the BNB and deliver to the SN.

Finally, there was only one predictive model identified for the visceral tissues. Unlike the HCA cluster correlations which showed kidney drug distribution positively correlated to **CASA+** and **SMR** (**Figure 3.10**), **Figure 3.17** reported one positive

correlation between kidney drug levels and the structural parameter **Kier1** ($r^2 = 0.753$). These models agree with each other and suggest that larger, branched, hydrophilic drugs with a greater positively-charged surface area are more likely to distribute to the kidney.

3.6 Conclusion

Both Hierarchical Cluster Analysis (HCA) and Quantitative Structure Activity Relationship (QSAR) analysis algorithms were employed herein to determine whether predictive models could be created for 24 orally-administered multifunctional antioxidants (MFAOs), their monofunctional free radical scavenging (FRS) and bio-active transition metal chelating (CHL) analogs, and their nonfunctional (NF) analogs. Using both methods, multiple correlative relationships with several similar, if not identical, trends were identified. More importantly, the present results agree with observations of the requirement of lipophilic or hydrophilic drug passage through the various physiological barriers such as the BAB, BRB, BBB, and BNB, and their respective tissues. This study not only demonstrates the feasibility of developing predictive models for the oral administration of compounds into the ocular, neural, and visceral tissue, but also provides the foundation for future oral/systemic compound administration biodistribution studies.

3.7 References

1. Adam, N.R., R. Wieder, and D. Ghosh, *Data science, learning, and applications to biomedical and health sciences*. Ann N Y Acad Sci, 2017. **1387**(1): p. 5-11.
2. Nantasenamat, C., et al., *AutoWeka: toward an automated data mining software for QSAR and QSPR studies*. Methods Mol Biol, 2015. **1260**: p. 119-47.
3. Sanchez-Pinto, L.N., Y. Luo, and M.M. Churpek, *Big Data and Data Science in Critical Care*. Chest, 2018. **154**(5): p. 1239-1248.
4. Piir, G., et al., *Best Practices for QSAR Model Reporting: Physical and Chemical Properties, Ecotoxicity, Environmental Fate, Human Health, and Toxicokinetics Endpoints*. Environ Health Perspect, 2018. **126**(12): p. 126001.
5. Caron, G. and G. Ermondi, *Updating molecular properties during early drug discovery*. Drug Discov Today, 2017. **22**(6): p. 835-840.
6. Alonso-Betanzos, A. and V. Bolon-Canedo, *Big-Data Analysis, Cluster Analysis, and Machine-Learning Approaches*. Adv Exp Med Biol, 2018. **1065**: p. 607-626.
7. Kimes, P.K., et al., *Statistical significance for hierarchical clustering*. Biometrics, 2017. **73**(3): p. 811-821.
8. Pagnuco, I.A., et al., *Analysis of genetic association using hierarchical clustering and cluster validation indices*. Genomics, 2017. **109**(5-6): p. 438-445.
9. Finch, H., *Comparison of Distance Measures in Cluster Analysis with Dichotomous Data*. Journal of Data Science, 2005. **3**: p. 85-100.
10. DeFays, D., *An efficient algorithm for a complete link method*. The Computer Journal of the British Computer Society, 1977. **20**(4): p. 364-366.
11. Bratchell, N., *Cluster analysis*. Chemometrics and Intelligent Laboratory Systems, 1989. **6**(2): p. 105-125.

12. Kwon, S., et al., *Comprehensive ensemble in QSAR prediction for drug discovery*. BMC Bioinformatics, 2019. **20**(1): p. 521.
13. Cardoso-Silva, J., L.G. Papageorgiou, and S. Tsoka, *Network-based piecewise linear regression for QSAR modelling*. J Comput Aided Mol Des, 2019. **33**(9): p. 831-844.
14. Gini, G., *QSAR Methods*. Methods Mol Biol, 2016. **1425**: p. 1-20.
15. *CRC Handbook of Chemistry and Physics*, ed. C. Press. 1994.
16. *The Molecular Connectivity Chi Indexes and Kappa Shape Indexes in Structure-Property Modeling*, in *Reviews in Computational Chemistry*. p. 367-422.
17. LaBute, P. *MOE LogP(Octanol/Water) Model*. 1998.
18. Hou, T.J., et al., *ADME evaluation in drug discovery. 4. Prediction of aqueous solubility based on atom contribution approach*. J Chem Inf Comput Sci, 2004. **44**(1): p. 266-75.
19. Stewart, J.J.P., *MOPAC Manual (7th Edition)*, ed. MOPAC. 1993.
20. Wildman, S.A. and G.M. Crippen, *Prediction of Physicochemical Parameters by Atomic Contributions*. Journal of Chemical Information and Computer Sciences, 1999. **39**(5): p. 868-873.
21. LaBute, P., *MOE Molar Refractivity Model*, in *Source code in \$MOE/lib/svl/quasar.svl/q_mref.svl Unpublished*, Editor. 1998.
22. Roy, K. and R.N. Das, *A review on principles, theory and practices of 2D-QSAR*. Curr Drug Metab, 2014. **15**(4): p. 346-79.
23. Verma, J., V.M. Khedkar, and E.C. Coutinho, *3D-QSAR in drug design--a review*. Curr Top Med Chem, 2010. **10**(1): p. 95-115.
24. Mamun, A.A., R. Asetine, and S. Rajasekaran, *Efficient Record Linkage Algorithms Using Complete Linkage Clustering*. PLoS One, 2016. **11**(4): p. e0154446.

25. Hahus, I., et al., *Using Cluster Analysis to Compartmentalize a Large Managed Wetland Based on Physical, Biological, and Climatic Geospatial Attributes*. Environ Manage, 2018. **62**(3): p. 571-583.
26. Ultsch, A. and J. Lotsch, *Machine-learned cluster identification in high-dimensional data*. J Biomed Inform, 2017. **66**: p. 95-104.
27. Draper, N.a.S., H., *Applied Regression Analysis*, ed. Wiley-Interscience. 1998.
28. Grabowski, B., "*P < 0.05*" *Might Not Mean What You Think: American Statistical Association Clarifies P Values*. J Natl Cancer Inst, 2016. **108**(8).
29. Coca-Prados, M., *The blood-aqueous barrier in health and disease*. J Glaucoma, 2014. **23**(8 Suppl 1): p. S36-8.
30. Sakamoto, H., et al., *Aqueous and vitreous penetration of levofloxacin after topical and/or oral administration*. Eur J Ophthalmol, 2007. **17**(3): p. 372-6.
31. Pitkanen, L., et al., *Permeability of retinal pigment epithelium: effects of permeant molecular weight and lipophilicity*. Invest Ophthalmol Vis Sci, 2005. **46**(2): p. 641-6.
32. Stewart, P.A. and U.I. Tuor, *Blood-eye barriers in the rat: correlation of ultrastructure with function*. J Comp Neurol, 1994. **340**(4): p. 566-76.
33. Sonsino, J., et al., *Co-localization of junction-associated proteins of the human blood--aqueous barrier: occludin, ZO-1 and F-actin*. Exp Eye Res, 2002. **74**(1): p. 123-9.
34. Miller, S.C., K.J. Himmelstein, and T.F. Patton, *A physiologically based pharmacokinetic model for the intraocular distribution of pilocarpine in rabbits*. J Pharmacokinet Biopharm, 1981. **9**(6): p. 653-77.
35. Heyrman, T.P., et al., *Drug uptake and release by a hydrogel intraocular lens and the human crystalline lens*. J Cataract Refract Surg, 1989. **15**(2): p. 169-75.

36. Menon, I.A., et al., *Binding of timolol to iris-ciliary body and melanin: an in vitro model for assessing the kinetics and efficacy of long-acting antiglaucoma drugs*. J Ocul Pharmacol, 1989. **5**(4): p. 313-24.
37. Tang-Liu, D.D., J.B. Richman, and S.S. Liu, *Lenticular uptake and distribution of xenobiotics and amino acids*. J Ocul Pharmacol, 1992. **8**(3): p. 267-77.
38. Heikkinen, E.M., et al., *Distribution of Small Molecular Weight Drugs into the Porcine Lens: Studies on Imaging Mass Spectrometry, Partition Coefficients, and Implications in Ocular Pharmacokinetics*. Mol Pharm, 2019. **16**(9): p. 3968-3976.
39. Ahmed, I., et al., *The kinetics of timolol in the rabbit lens: implications for ocular drug delivery*. Pharm Res, 1989. **6**(9): p. 772-8.
40. Dewan, N., et al., *Oral Miltefosine as Adjunctive Treatment for Recalcitrant Acanthamoeba Keratitis*. Cornea, 2019. **38**(7): p. 914-917.
41. Patel, D. and S. Wairkar, *Recent advances in cyclosporine drug delivery: challenges and opportunities*. Drug Deliv Transl Res, 2019. **9**(6): p. 1067-1081.
42. Hope-Ross, M.W., et al., *Oral tetracycline in the treatment of recurrent corneal erosions*. Eye (Lond), 1994. **8 (Pt 4)**: p. 384-8.
43. Araki-Sasaki, K., et al., *The effects of oral and topical corticosteroid in rabbit corneas*. BMC Ophthalmol, 2016. **16**(1): p. 160.
44. Araki-Sasaki, K., et al., *The effects of oral and topical corticosteroid in rabbit corneas*. BMC Ophthalmology, 2016. **16**(1): p. 160.
45. Sharma, C., et al., *Development of novel in silico model to predict corneal permeability for congeneric drugs: a QSPR approach*. J Biomed Biotechnol, 2011. **2011**: p. 483869.
46. Tirucherai, G.S., C. Dias, and A.K. Mitra, *Corneal permeation of ganciclovir: mechanism of ganciclovir permeation enhancement by acyl ester prodrug design*. J Ocul Pharmacol Ther, 2002. **18**(6): p. 535-48.

47. Civile, C., et al., *Ocular permeability screening of dexamethasone esters through combined cellular and tissue systems*. J Ocul Pharmacol Ther, 2004. **20**(1): p. 75-84.
48. Suhonen, P., et al., *Different effects of pH on the permeation of pilocarpine and pilocarpine prodrugs across the isolated rabbit cornea*. Eur J Pharm Sci, 1998. **6**(3): p. 169-76.
49. Burstein, N.L. and J.A. Anderson, *Corneal penetration and ocular bioavailability of drugs*. J Ocul Pharmacol, 1985. **1**(3): p. 309-26.
50. Sridhar, M.S., *Anatomy of cornea and ocular surface*. Indian J Ophthalmol, 2018. **66**(2): p. 190-194.
51. Bourne, W.M., *Biology of the corneal endothelium in health and disease*. Eye (Lond), 2003. **17**(8): p. 912-8.
52. Cunha-Vaz, J., R. Bernardes, and C. Lobo, *Blood-retinal barrier*. Eur J Ophthalmol, 2011. **21 Suppl 6**: p. S3-9.
53. Diaz-Coranguez, M., C. Ramos, and D.A. Antonetti, *The inner blood-retinal barrier: Cellular basis and development*. Vision Res, 2017. **139**: p. 123-137.
54. Del Amo, E.M., et al., *Pharmacokinetic aspects of retinal drug delivery*. Prog Retin Eye Res, 2017. **57**: p. 134-185.
55. del Amo, E.M., et al., *Intravitreal clearance and volume of distribution of compounds in rabbits: In silico prediction and pharmacokinetic simulations for drug development*. Eur J Pharm Biopharm, 2015. **95**(Pt B): p. 215-26.
56. Pelkonen, L., et al., *LC-MS/MS Based Quantitation of ABC and SLC Transporter Proteins in Plasma Membranes of Cultured Primary Human Retinal Pigment Epithelium Cells and Immortalized ARPE19 Cell Line*. Mol Pharm, 2017. **14**(3): p. 605-613.

57. Dahlin, A., et al., *Gene expression profiling of transporters in the solute carrier and ATP-binding cassette superfamilies in human eye substructures*. Mol Pharm, 2013. **10**(2): p. 650-63.
58. Vellonen, K.S., et al., *Expression, activity and pharmacokinetic impact of ocular transporters*. Adv Drug Deliv Rev, 2018. **126**: p. 3-22.
59. Ramsay, E., et al., *Role of retinal pigment epithelium permeability in drug transfer between posterior eye segment and systemic blood circulation*. Eur J Pharm Biopharm, 2019. **143**: p. 18-23.
60. Cunha-Vaz, J.G., *The blood-retinal barriers system. Basic concepts and clinical evaluation*. Exp Eye Res, 2004. **78**(3): p. 715-21.
61. Marmor, M.F., A. Negi, and D.M. Maurice, *Kinetics of macromolecules injected into the subretinal space*. Exp Eye Res, 1985. **40**(5): p. 687-96.
62. Araie, M. and D.M. Maurice, *The loss of fluorescein, fluorescein glucuronide and fluorescein isothiocyanate dextran from the vitreous by the anterior and retinal pathways*. Exp Eye Res, 1991. **52**(1): p. 27-39.
63. Hosoya, K. and M. Tachikawa, *Inner blood-retinal barrier transporters: role of retinal drug delivery*. Pharm Res, 2009. **26**(9): p. 2055-65.
64. Niemeyer, G., *Glucose concentration and retinal function*. Clin Neurosci, 1997. **4**(6): p. 327-35.
65. Tachikawa, M., et al., *A novel relationship between creatine transport at the blood-brain and blood-retinal barriers, creatine biosynthesis, and its use for brain and retinal energy homeostasis*. Subcell Biochem, 2007. **46**: p. 83-98.
66. Tyagi, A., Sharma, P.K., and Malviya, R., *Role of Blood Retinal Barrier in Drug Absorption*. Pharmaceutica Analytica Acta, 2018. **9**(5).
67. Weil, Z.M., et al., *Time-of-day determines neuronal damage and mortality after cardiac arrest*. Neurobiol Dis, 2009. **36**(2): p. 352-60.

68. Daneman, R. and A. Prat, *The blood-brain barrier*. Cold Spring Harb Perspect Biol, 2015. **7**(1): p. a020412.
69. Weerasuriya, A. and A.P. Mizisin, *The blood-nerve barrier: structure and functional significance*. Methods Mol Biol, 2011. **686**: p. 149-73.
70. Wu, C., et al., *Endothelial basement membrane laminin alpha5 selectively inhibits T lymphocyte extravasation into the brain*. Nat Med, 2009. **15**(5): p. 519-27.
71. Nakatsuji, Y., *What is the difference between the blood-nerve barrier and blood-brain barrier?* Clinical and Experimental Neuroimmunology, 2017. **8**(1): p. 13-14.
72. Goyal, D., et al., *Rationally Designed Peptides and Peptidomimetics as Inhibitors of Amyloid-beta (Abeta) Aggregation: Potential Therapeutics of Alzheimer's Disease*. ACS Comb Sci, 2017. **19**(2): p. 55-80.
73. Ghose, A.K., V.N. Viswanadhan, and J.J. Wendoloski, *A knowledge-based approach in designing combinatorial or medicinal chemistry libraries for drug discovery. 1. A qualitative and quantitative characterization of known drug databases*. J Comb Chem, 1999. **1**(1): p. 55-68.
74. Lipinski, C.A., *Drug-like properties and the causes of poor solubility and poor permeability*. J Pharmacol Toxicol Methods, 2000. **44**(1): p. 235-49.
75. Ajay, G.W. Bemis, and M.A. Murcko, *Designing libraries with CNS activity*. J Med Chem, 1999. **42**(24): p. 4942-51.
76. Montgomery, K.L., et al., *Beyond the brain: Optogenetic control in the spinal cord and peripheral nervous system*. Sci Transl Med, 2016. **8**(337): p. 337rv5.
77. Langert, K.A. and E.M. Brey, *Strategies for Targeted Delivery to the Peripheral Nerve*. Front Neurosci, 2018. **12**: p. 887.
78. Maiuolo, J., et al., *The Role of Endothelial Dysfunction in Peripheral Blood Nerve Barrier: Molecular Mechanisms and Pathophysiological Implications*. Int J Mol Sci, 2019. **20**(12).

79. Reina, M.A., et al., *[The blood-nerve barrier in peripheral nerves]*. Rev Esp Anesthesiol Reanim, 2003. **50**(2): p. 80-6.
80. Khazaei, M., F. Moien-Afshari, and I. Laher, *Vascular endothelial function in health and diseases*. Pathophysiology, 2008. **15**(1): p. 49-67.
81. Abe, M., et al., *Establishment and characterization of human peripheral nerve microvascular endothelial cell lines: a new in vitro blood-nerve barrier (BNB) model*. Cell Struct Funct, 2012. **37**(2): p. 89-100.
82. Maiuolo, J., et al., *The Role of Endothelial Dysfunction in Peripheral Blood Nerve Barrier: Molecular Mechanisms and Pathophysiological Implications*. International journal of molecular sciences, 2019. **20**(12): p. 3022.
83. Rechthand, E., Q.R. Smith, and S.I. Rapoport, *Transfer of nonelectrolytes from blood into peripheral nerve endoneurium*. Am J Physiol, 1987. **252**(6 Pt 2): p. H1175-82.
84. Abram, S.E., et al., *Permeability of injured and intact peripheral nerves and dorsal root ganglia*. Anesthesiology, 2006. **105**(1): p. 146-53.
85. Poduslo, J.F., G.L. Curran, and C.T. Berg, *Macromolecular permeability across the blood-nerve and blood-brain barriers*. Proc Natl Acad Sci U S A, 1994. **91**(12): p. 5705-9.
86. Liu, H., et al., *Drug Distribution into Peripheral Nerve*. J Pharmacol Exp Ther, 2018. **365**(2): p. 336-345.
87. Mishra, N., et al., *Efficient hepatic delivery of drugs: novel strategies and their significance*. Biomed Res Int, 2013. **2013**: p. 382184.
88. Haas, M., et al., *Specific drug delivery to the kidney*. Cardiovasc Drugs Ther, 2002. **16**(6): p. 489-96.
89. David, S. and J.P. Hamilton, *Drug-induced Liver Injury*. US Gastroenterol Hepatol Rev, 2010. **6**: p. 73-80.

90. Khan, S., V. Loi, and M.H. Rosner, *Drug-Induced Kidney Injury in the Elderly*. *Drugs Aging*, 2017. **34**(10): p. 729-741.
91. Wu, H. and J. Huang, *Drug-Induced Nephrotoxicity: Pathogenic Mechanisms, Biomarkers and Prevention Strategies*. *Curr Drug Metab*, 2018. **19**(7): p. 559-567.
92. Poelstra, K., J. Prakash, and L. Beljaars, *Drug targeting to the diseased liver*. *J Control Release*, 2012. **161**(2): p. 188-97.
93. Almazroo, O.A., M.K. Miah, and R. Venkataramanan, *Drug Metabolism in the Liver*. *Clin Liver Dis*, 2017. **21**(1): p. 1-20.
94. Masereeuw, R. and F.G. Russel, *Mechanisms and clinical implications of renal drug excretion*. *Drug Metab Rev*, 2001. **33**(3-4): p. 299-351.

CHAPTER 4

Failure of Oxysterols such as Lanosterol to Restore Lens Clarity from Cataract

4.1 Summary

The paradigm that cataracts are irreversible and that vision from cataracts can only be restored through surgery has recently been challenged by reports that oxysterols, such as lanosterol and 25-hydroxycholesterol, can restore vision by binding to the α B-crystallin chaperone protein to dissolve or disaggregate lenticular opacities. To confirm this premise, *in vitro* rat lens studies along with *in vitro* human lens protein solubilization studies were conducted. Cataracts were induced in viable rat lenses cultured for 48 hours in TC-199 bicarbonate media through physical trauma, 10 mM ouabain as Na^+/K^+ ATPase ion transport inhibitor, or 1 mM of an experimental compound that induces water influx into the lens. Subsequent 48-hour incubation with 15 mM of lanosterol liposomes failed to either reverse these lens opacities or prevent the further progression of cataracts to the nuclear stage. Similarly, 3-day incubation of 47-year-old human lenses in media containing 0.20 mM lanosterol, or 60-year-old human lenses in 0.25 and 0.50 mM 25-hydroxycholesterol, failed to increase the levels of soluble lens proteins or decrease the levels of insoluble lens proteins. These binding studies were followed up with *in silico* docking studies of lanosterol, 25-hydroxycholesterol, and ATP as a control to two wild type (**2WJ7** and **2KLR**) and one R120G mutant (**2Y1Z**) α B-crystallins using MOE™ (Molecular Operating Environment)™ and Schrödinger's Maestro software. Results confirmed that, compared to ATP, both oxysterols failed to reach the acceptable threshold binding scores for good predictive binding to the α B-crystallins. Additional *in silico* studies were also conducted on six novel multifunctional antioxidants which exhibited superior

binding compared to the oxysterols. In summary, all three studies failed to provide evidence that lanosterol or 25-hydroxycholesterol have either anti-cataractogenic activity or bind aggregated lens protein to dissolve cataracts. This study has already been published, but the additional MFAO results and discussions were added for this thesis [1].

4.2 Introduction

The ocular lens is a transparent organ whose function is to focus light onto the retina. It is composed of epithelial cells that are enclosed in a thick capsule formed from epithelial basement membrane [2]. At its anterior surface, the lens contains a single layer of proliferating epithelial cells. As these cells reach the equator, they elongate and differentiate into fiber cells that then make up the bulk of the lens. These elongated fiber cells become completely internalized with their ends joined by collagen at sutures that run from the lens center to anterior and posterior poles. The lens grows throughout life with new fiber cells continually laid on top of the older fiber cells so that the fiber cell depth within the lens is directly related to the age and stage of lens development [3-5]. The transparent lens is unique because this “enclosed bag of regularly ordered cells and proteins” has evolved into an internal micro-circulatory system composed of ions that are coupled to fluid movement that causes the lens to demonstrate behavior similar to that of a single cell [6-8].

The lens is transparent because light scattering within the lens is minimized. It lacks blood vessels that can scatter and absorb light as well as light scattering cellular organelles such as nuclei, mitochondria, and endoplasmic reticula that are removed during differentiation of the epithelial cells into fiber cells. Light scattering is further minimized by the specialized organization and composition of the tightly packed fiber cells which contain

structural crystallin proteins that also assist in maintaining the proper refractive index in the lens [9, 10]. Since the lens fiber cells lack the capacity for protein turnover and repair, specific antioxidant defenses and protein chaperones are present within these fiber cells to protect lens proteins from post-translational changes and aggregation [9, 11-14]. Among these are the small heat shock protein (sHSP) α -crystallins with chaperone-like activity that play a central role in maintaining lens transparency by trapping the denaturing or unfolding proteins responsible for light scattering in the highly ordered lens fibers [15-18].

Cataracts develop from the loss of lens transparency associated with increased light scattering and changes in refractive properties. The protective lens antioxidant defenses and the molecular chaperone reserves of α -crystallin decrease with age so that the aging lens can no longer adequately protect itself from post-translational modifications of lens proteins. This leads to increased light scattering as a function of protein aggregation of post-translationally modified structural proteins which has been experimentally and clinically established in pre-cataractous lenses by dynamic light scattering [15, 19, 20]. Since this aggregation and denaturation of lens proteins appears irreversible, the surgical removal of the opaque lens is currently the only treatment for restoring vision loss from cataracts [14]. As a result, the development of anti-cataract agents has primarily focused on supplementing the lens with biochemical intermediates or redox agents to reduce or prevent the post-translational modifications that eventually result in irreversible changes in lens protein structure and aggregation. An exception is the pharmacological prevention of diabetic cataracts where a specific enzyme that initiates sugar cataracts has been identified [21-23].

The paradigm that vision can only be restored through cataract surgery has recently been challenged by Zhao *et al.* [24] and Makley *et al.* [25]. It is reported that interaction of lanosterol or 25-hydroxycholesterol with α -crystallin chaperones enhance the ability of these chaperones to restore lens clarity by increasing their ability to physically dissolve protein aggregates and/or the denatured amyloid-like fibril proteins present in cataractous lenses. These reports have subsequently been expanded to include dissolving aggregated proteins in cataracts from two additional congenital mouse models [26, 27]. The striking possibility of a non-surgical cataract removal has received worldwide coverage by the news media and encouraged investigators to focus on developing anti-cataract drugs that reverse rather than prevent cataract formation. It has also led to the commercialization of lanosterol eye drops [28-30]. However, the ability of these compounds to restore lens clarity has not been independently confirmed. For example, a recent report has shown that culturing lens nuclei from 40 age-related cataractous human lenses with 25 mM lanosterol for 6 days at room temperature failed to either dissolve the aggregated proteins or restore the clarity of the lens nuclei [31]. Similarly, clinically administering eye drops containing 5 mM lanosterol dissolved in olive oil two times daily for the first week, followed by three times daily for the next seven weeks, to a patient with idiopathic unilateral juvenile nuclear cataracts failed to produce any relevant clinical effect in reversing either the cataract or halting the progressive worsening of visual acuity with an increasing of myopic shift [32]. Triparanol, an inhibitor of the conversion of lanosterol to cholesterol, has also been shown to not only induce cataract formation, but also increase tissue lanosterol levels [33-35]. The presence of 25-hydroxycholesterol in human lenses has also been linked to the presence rather than absence of cataracts [36].

To clarify these contrasting findings, we pursued a series of *in vitro* studies to evaluate whether oxysterols such as lanosterol or 25-hydroxycholesterol can reverse

experimentally induced cataracts or to re-dissolve aggregated lens crystallin proteins. We also explored if either oxysterol adequately bound to α B-crystallin chaperones at the molecular level *in silico*. In addition, six novel multifunctional antioxidants (MFAOs) were also examined *in silico* since previous studies from our laboratory have indicated that a parent MFAO analog, JHX-1, was able to significantly delay in the advanced progression of sugar cataract formation *in vivo* without sorbitol dehydrogenase or aldose reductase inhibition, suggesting it may have inherent chaperone activity [37].

4.3 Materials and Methods

All procedures involving live animals were performed in accordance with the National Institutes of Health Guide for the Care and Use of Laboratory Animals and the Association for Research in Vision and Ophthalmology Statement for the Use of Animals in Ophthalmic and Vision Research and approved by the Institutional Animal Care and Use Committee (IACUC) of the University of Nebraska Medical Center. Human lenses were obtained from donor eyes from the Saving Sight Eye Bank, Kansas City, MO and stored at -85°C prior to use.

***In Vitro* Lenses Culture Studies.** Eyes from young (125 g, 5-week old) Sprague Dawley rats were immediately enucleated upon death from carbon dioxide asphyxiation. The intact lens from each eye was removed by careful dissection from a posterior approach and cultured as previously described in sterile TC-199 bicarbonate media containing 30 mM fructose and 20 U/mL of penicillin-streptomycin in a humidified incubator under an atmosphere of 95% air and 5% CO_2 at 37°C [38-40].

Following overnight pre-incubation to ensure intact lenses were not damaged during dissection, all clear lenses were transferred into 24-well culture plates containing 2 mL of the standard culture media for 48 hours according to the following 4 groups (6 lenses/group). The first group served as the untreated control, while each lens in the second group was squeezed at the equator with forceps to induce blunt trauma opacities. In the third group, opacities were induced by addition of 10 mM of the Na⁺/K⁺ ATPase inhibitor, ouabain, and in the fourth group opacities were induced by culture with 1 mM of an experimental toxic glycoprotein chaperone that induces osmotic cataract. After 48 hours, the culture media for each lens was replaced with fresh TC-199 bicarbonate media containing 15 mM of lanosterol liposomes and the lenses were cultured for an additional 48 hours. At the end of the second 48-hour culture period, each lens was carefully washed with PBS solution and transferred to culture plates containing PBS solution. The appearance of each lens was immediately photo-documented by placing the lens over a light source containing a grid. Each photograph was then standardized by adjusting the pixel densities of each outer grid line to a standard value.

Liposome Preparation. Lanosterol (Alpha Chem) was dissolved in a 250 mL round bottom flask containing acetonitrile and the solvent was removed under vacuum in a rotary evaporator. The resulting glassine layer of lanosterol coating the inner surface of the round bottom flask was then removed by scraping with a spatula, followed by addition of an appropriate amount of TC-199 bicarbonate media to give a 15 mM solution. The lanosterol sheets were converted to liposomes by sonication using a micro homogenizer tip (MISONIX Fisher Scientific Sonicator Ultrasonic Processor XL) until the solution appeared homogenous (ca. 5 minutes). Equal aliquots of 2 mL were pipetted into the 24-well culture plates for experimental use.

Solubilization of proteins from human lens fragments with lanosterol. Two human lenses from a 47-year-old donor were cut through the center into four equal quadrants and weighed. One piece from each lens tissue was placed in PBS media composed of 137 mM NaCl, 2.7 mM KCl, 10 mM Na₂HPO₄, and 1.5 mM KH₂PO₄, pH 7.4, containing 0.03% sodium azide. Lanosterol dissolved in 12.5 μL of ethanol was then added to some of the lens pieces in PBS to give a 0.20 mM lanosterol test solution in a total volume of 500 μL. All lens pieces, with or without lanosterol, were incubated at 37 °C in the dark for 72 hours and then homogenized. The soluble and insoluble protein fractions were separated by centrifugation at 13,000 rpm for 20 minutes at room temperature in an Eppendorf centrifuge. The protein content of the soluble protein in the supernatant was determined using the Bio-Rad Protein Assay (Hercules, CA). Control samples were similarly prepared using only 12.5 μL ethanol (These studies were conducted by Dr. Sharma's group from the University of Missouri, Columbia).

Solubilization of proteins from human lens fragments with 25-hydroxycholesterol. Six frozen lenses from 60-year-old donors were each cut into three equal pie shapes with each sample composed of two pie shapes from different lenses. These nine samples were each immersed into 500 μL of PBS containing 0.03% sodium azide and 10% ethanol containing either 0.0, 0.25 or 0.50 mM of 25-hydroxycholesterol. The samples were then incubated at 37 °C for 72 hours in the dark. Following incubation, the samples were homogenized, and the water-soluble fraction was separated from the insoluble fractions by centrifugation at 13,000 rpm for 20 min at room temperature. The water-insoluble fractions were treated with 100 μL of 0.1 M NaOH for 2 hours to solubilize the proteins. The protein content in all samples was measured using the Bio-Rad Protein Assay. Samples incubated only with 10% ethanol served as controls (These studies were conducted by Dr. Sharma's group from the University of Missouri, Columbia, MO).

Solubilization of proteins from human lens homogenates with lanosterol.

Attempts to solubilize lens proteins by lanosterol and 25-hydroxycholesterol were also carried out using lens homogenates prepared from 72-year-old human lenses. Tissue homogenates containing 0.25 and 1.0 mg protein in 0.5 mL PBS (containing protease inhibitor cocktail) and oxysterols at a final concentration of 0, 100, or 200 μ M were incubated at 37 °C for 24 hours. At the end of the incubation, the tubes were centrifuged at 13,000 rpm for 15 min at 4 °C. The protein content in soluble and insoluble fractions was measured using Bio-Rad protein assay reagent. These experiments were conducted three times separately using homogenates prepared from a pair of lenses (These studies were conducted by Dr. Sharma's group from the University of Missouri, Columbia, MO).

Molecular Modeling Studies. The Chemical Computing Group's Molecular Operating Environment 2016 (MOE) and Schrödinger LLC's program, Maestro 11, were used for this study. The structures (**Figure 4.1**) of ATP, 25-hydroxycholesterol, lanosterol, JHX-4, JHX-8, HK-2, HK-4, HK-6, and HK-8 were built and minimized in MOE [41]. To investigate the binding activities of these three compounds to α B-crystallins, docking studies were conducted using MOE's internal dock and Schrödinger's Glide dock [42]. The target proteins were three resolved model α B-crystallins (cryAB) obtained from the Protein Data Bank (PDB): a human wild type dimer **2WJ7** [43], a human wild type α B-crystallin **2KLR** [44], and a R120G mutant, **2Y1Z** [45].

All three proteins, wildtype **2WJ7**, wildtype **2KLR**, and R120G mutant **2Y1Z**, were uploaded from the PDB into MOE. The first cryAB examined was the wildtype **2WJ7** used by Makley *et al.* [25]. The dimer containing chains A/B was isolated for binding studies, and residues ASP 46 and ARG 57 on this protein were identified to be synonymous with

residues ASP 109 and ARG 120 described in Makley *et al.* [25] These residues are located at the dimer interface where the carboxylic group of ASP 46 on one chain and the guanidine group of ARG 57 on the opposite chain form a salt bridge that contributes to the

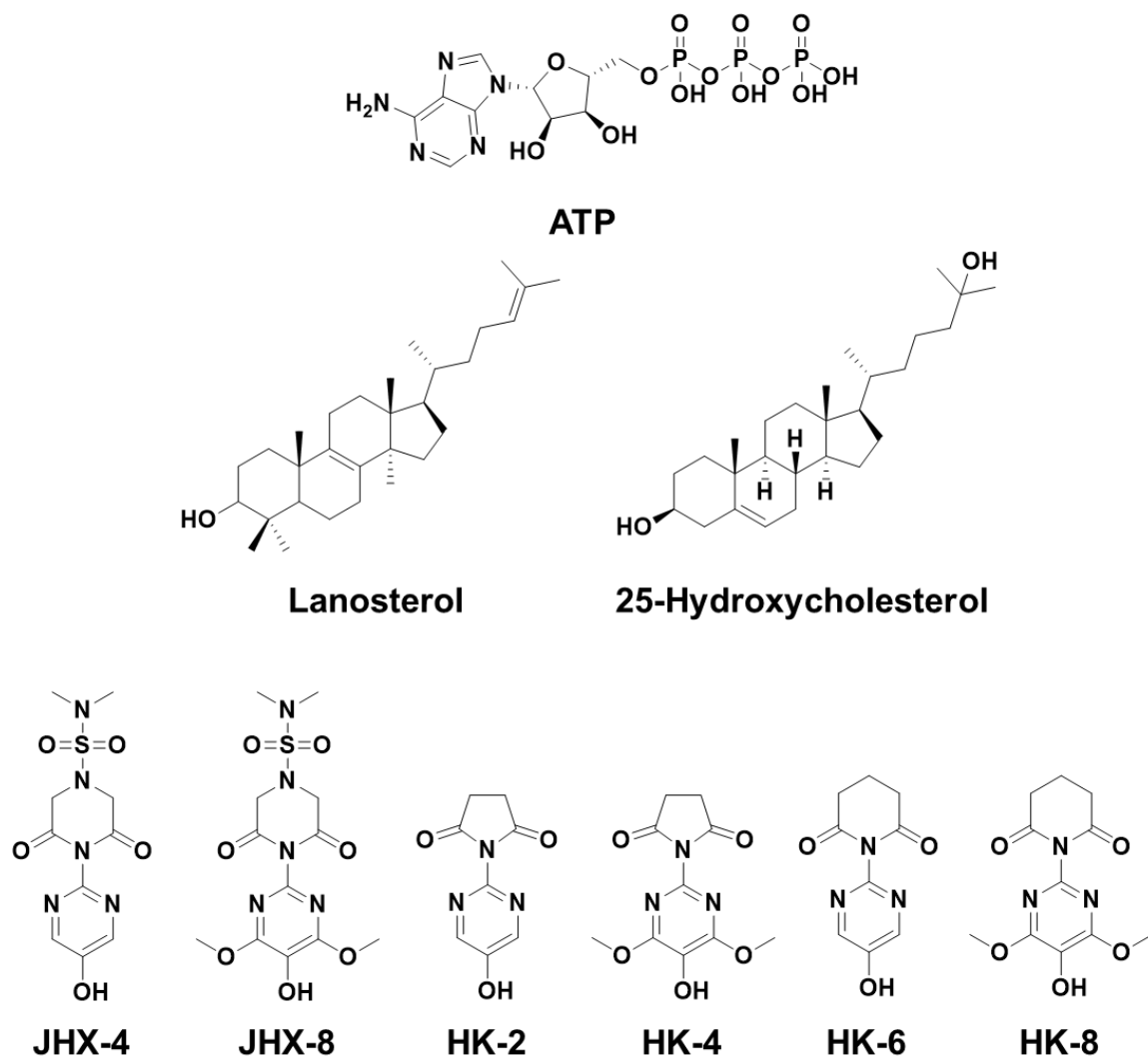


Figure 4.1. Structures of molecules used in the docking studies with the human cryAB wildtypes, **2WJ7** and **2KLR**, and the R120G mutant, **2Y1Z**. These molecules were modeled in MOE and energy minimized using the MMFF94x forcefield.

protein's stability. Salt bridges are defined as noncovalent hydrogen bonds or electrostatic interactions between two ionized sites with distances ≤ 4.0 Å. Despite the absence of a

ligand, the dimer also contains water molecules. **2WJ7** was prepared, corrected, and protonated using the Protonate3D function which runs an optimization routine to determine overall lowest potential energy configuration for the protein's side chains. Next, the protein backbone was selected, inverted, and minimized using Amber14:EHT forcefield with a 0.05 gradient, followed by an unrestricted minimization using the same forcefield and gradient. In this mathematical process of energy minimization, the potential energy surface minimum of the protein is determined by changing the geometry of the protein in a step-wise fashion until a local or global minimum is reached. The slope of this step-wise change is defined as the gradient, and the minimization is terminated when the slope change is less than the specified threshold of 0.05. During the energy minimization, the protein structure was stabilized by retaining water molecules attached to the protein so that major 3D configurational perturbations were avoided. These water molecules were then removed for the docking experiments. A similar process was used for the other two cryABs, wildtype **2KLR** and mutant **2Y1Z**. The same proteins were then imported into Maestro and re-prepared using the Protein Preparation Wizard. Proteins were pre-processed with original hydrogens removed and water molecules beyond 5 Å from het groups deleted. Next, the proteins were refined and optimized, followed by a backbone-constrained minimization of side chains and an unconstrained minimization with the OPLS3e forcefield.

Docking Studies. Two binding pockets were defined for the docking studies. The first binding pocket was at the dimer interface binding site as defined by Makley *et al.* [25] on wildtype **2WJ7**. **2WJ7** is an apoprotein without any ligand binding information, and Makley *et al.* did not specify ligand binding residues. We identified PHE 55 on the "A" chain of **2WJ7** as the centroid for the binding pocket and extended the docking space by 25 Å on each side. We defined the same binding pocket for the 2KLR wildtype, and PHE

118 was identified as the centroid for the R120G mutant dimer, **2Y1Z**. The second binding pocket was the binding site for ATP that was experimentally determined and defined by Ghosh *et al.* [46] in the β 4- β 8 groove. ATP binds to an amino acid sequence part of a Walker-B ATP-binding motif which contains the cryAB sequence ⁸²KHFSPEELKVKVLGD⁹⁶. This motif has also been found in several ATP-binding proteins, including HSP90 and HSP104 [47, 48]. Furthermore, the Walker-B motif is highly conserved in the α -crystallin core domain of the sHSP family.

The MOE™ docking studies were conducted using the “Triangle Matcher” placement method with the flexible “Induced Fit” placement algorithm which simulates physiological conditions by allowing the residues in the receptor pocket and the ligand to freely perturb. The output from this method was a London Δ G binding score, and predicted **K_d** values were calculated based on the following equation:

$$K_d \text{ (unit, } \mu\text{M)} = e^{(\text{docking score} \cdot 1000 / (1.98 \cdot 298.15))} / 10^{-6} \text{ (eq. 1)}$$

The Maestro docking studies were conducted using Glide Dock by first defining the binding pocket using the Glide Grid Generation method using centroids identified above for all three proteins: wildtypes **2WJ7** and **2KLR**, and the R120G mutant **2Y1Z**. This was followed by Glide dock with the Extra Precision (XP) scoring function. The docking scores of each protein-ligand docked complex were expressed in kcal/mol, with a value of -9 kcal/mol approximated to an IC₅₀ or K_d in the high nM/low μ M. A more negative docking score indicated stronger ligand binding to the protein.

4.4 Results

Organ Culture Studies. The new paradigm suggests that lanosterol and other oxysterols can clear cataracts, presumably by boosting the α -crystallin's chaperone activity to dissolve the light scattering, denatured, aggregated lens proteins responsible for opacification. Since transparency and biochemical viability can be maintained for up to two weeks, lens organ culture has become a valuable technique in investigating the mechanisms of both lens homeostasis and cataractogenesis [49, 50]. Therefore, lens culture studies were conducted to investigate the ability of lanosterol to reduce lens opacities. Cataracts were experimentally induced with blunt trauma, by ATPase ion transport inhibition with 10 mM of ouabain, or by osmotic stress induced with 1 mM of a toxic experimental compound that induces water influx into the lens. Untreated lenses were used as the control. Within 48 hours of culture, all the lenses developed opacities except the control untreated group. As illustrated in **Figure 4.2**, trauma-induced cataracts appeared as localized opacities that varied because of the levels of blunt physical trauma applied, while the ouabain-treated lenses developed cortical opacities and the osmotic inducer produced dramatic refractive index changes associated with significant lens swelling. All lenses were then transferred to similar TC-199 bicarbonate media containing 15 mM of lanosterol liposomes. Incubation for an additional 48 hours in the lanosterol liposome media resulted in an apparent penetration of the amber liposomes into the lenses as noted by the slight color changes, especially around the nucleus as all treated lenses progressed to the mature nuclear cataract stage. Over the 48-hour period, there was also liposome clumping at the surface of the collagen capsule, which was difficult to rinse off presumably because of the sticky nature of the liposomes. While transparency in the control lenses appeared to be minimally affected, lanosterol failed to reverse opacities or halt the progression of cataracts in all treated lenses. In fact, lens opacities

in all treated lenses exposed to lanosterol progressed to the more advanced mature cataract stage with apparent nuclear involvement.

Protein Binding Studies. The described lens culture studies suggest that lanosterol either inadequately binds to lens proteins or that the chaperone activity of the assumed bound lanosterol to α -crystallin complex is not adequate to reverse or alter the progression of cataracts as previously proposed. To evaluate this possibility, two lenses from a 47-year-old human were equally divided into 4 pie shaped portions and incubated in the dark for 3 days at 37 °C in media containing 0.2 mM lanosterol dissolved in 10% ethanol. As shown in **Figure 4.3**, incubation with lanosterol did not result in either an anticipated increase in the level of soluble lens proteins or decrease the levels of insoluble proteins. This indicates that lanosterol failed to solubilize the insoluble lens proteins present in the cataractous lens. Similar results were obtained with three lenses from 70-year-old humans analyzed separately (data not shown).

Since in our experiments lanosterol failed to increase soluble protein levels, the binding studies were expanded to include 25-hydroxycholesterol whose binding power has been reported to be superior to that of lanosterol [25]. For these studies, 6 frozen lenses from three 60-year-old donors were each cut into three equal pie shaped fragments, thawed and incubated in the dark for 3 days at 37 °C in media containing either 0.0, 0.25 or 0.50 mM of 25-hydroxycholesterol. For each group, two pieces from different lenses were combined for each experiment. The percentage of protein in soluble and insoluble fractions were estimated separately for all samples in each group and averaged.

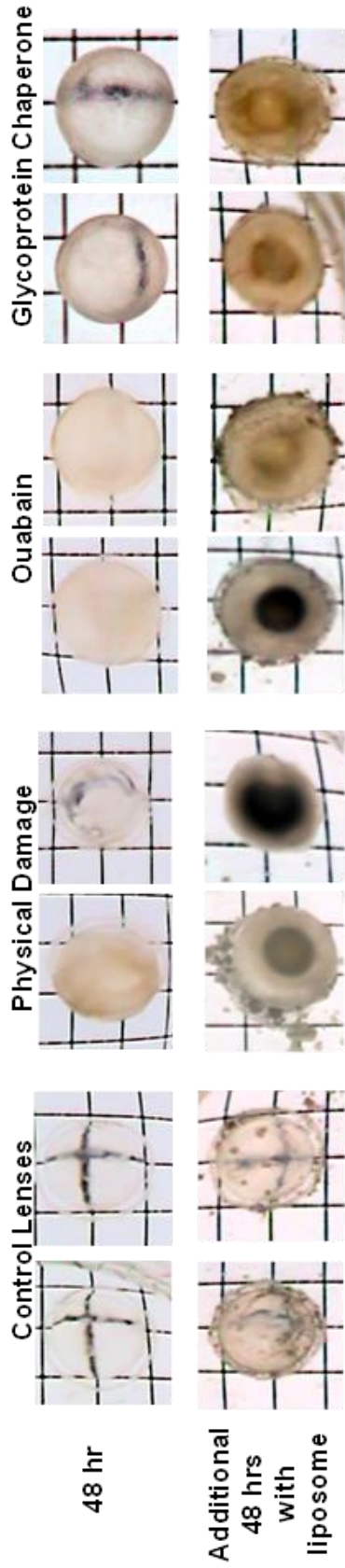


Figure 4.2. Appearance of rat lenses after 48-hour incubation following the induction of cataract and subsequent additional incubation with 15 mM of lanosterol liposomes. While the control lenses appear relatively clear after 48-hour exposure to lanosterol, the presence of lanosterol did not halt the further progression of cataracts. Lens photos were taken over a grid with special care to standardize the outer grid size and intensity in comparison to the control lenses since changes in intensity can affect the apparent levels of lens opacity.

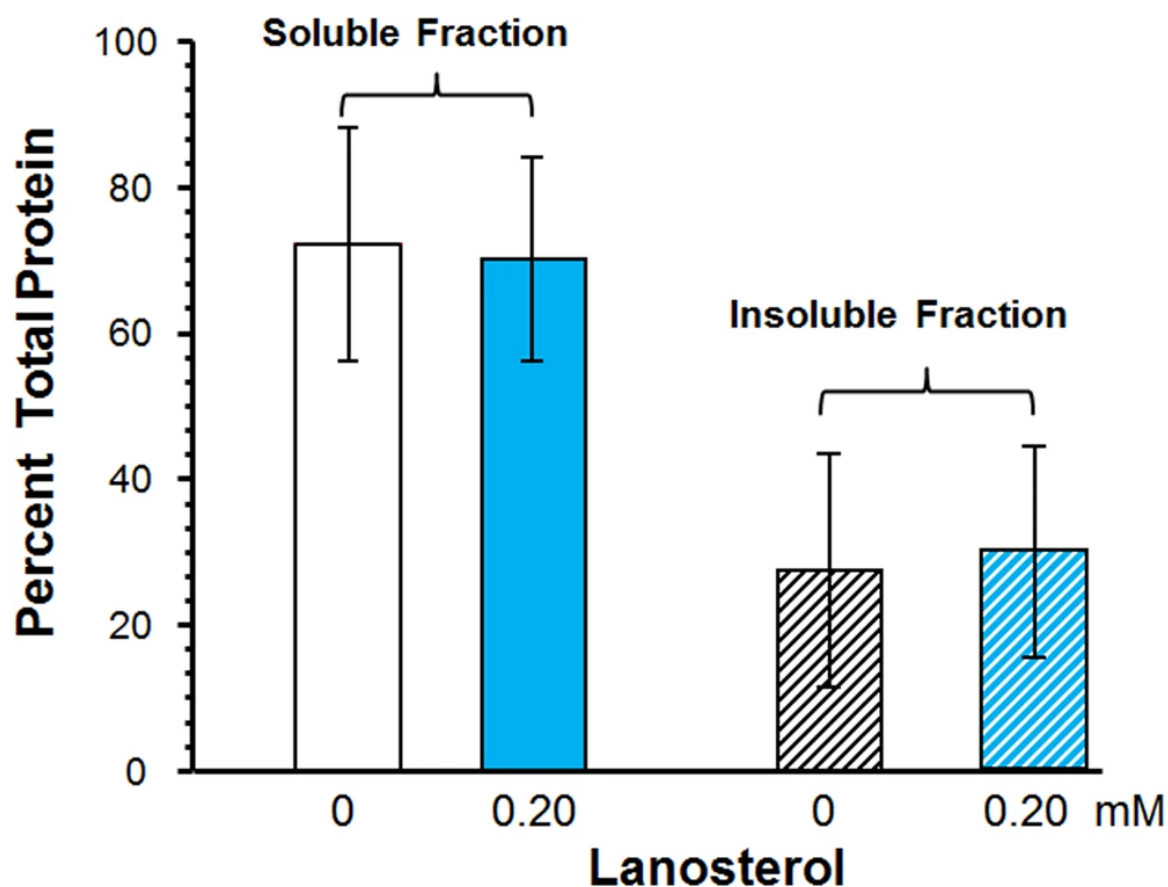


Figure 4.3. Change in protein levels from 47-year-old human lens fragments after 3 days incubation at 37 °C in media containing 0.20 mM lanosterol. There is no change in the levels of proteins in the soluble and insoluble fractions with or without the presence of lanosterol. $p > 0.5$ ANOVA single factor analysis and $n = 4 \pm$ S.D.

As summarized in **Figure 4.4**, no significant difference in soluble protein levels (p -value of 0.79, by ANOVA single factor analysis) was observed between the non-treated and 25-hydroxycholesterol-treated lenses. If the aggregated proteins were solubilized, then the levels of proteins in the insoluble fractions should have been lowered in the 25-hydroxycholesterol treated lenses. Instead, the insoluble protein levels in the control and the groups treated with either 0.25 or 0.50 mM 25-hydroxycholesterol showed no difference.

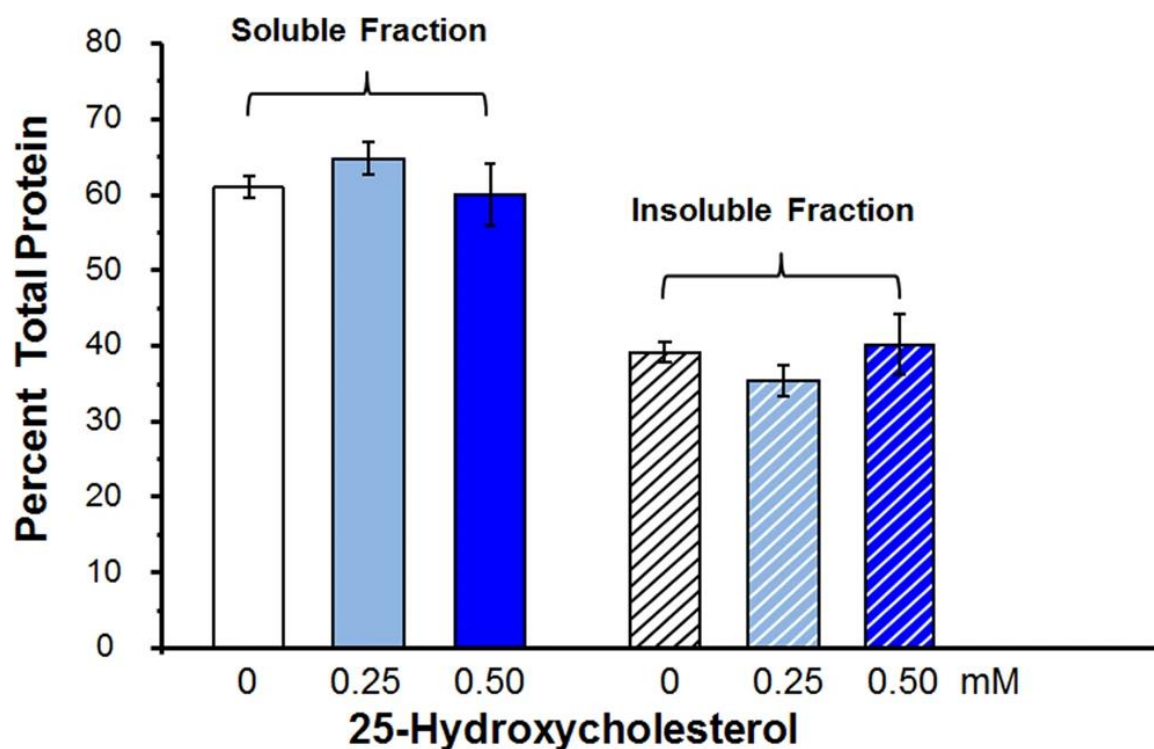


Figure 4.4. Change in soluble/insoluble protein levels of 60-year-old human lens homogenate after 3 days incubation at 37 °C in media containing either 0.0, 0.25 or 0.50 mM of 25-hydroxycholesterol. There is no change in the levels of proteins in the soluble and insoluble fraction. $n = 3 \pm$ S.D. $p = 0.79$ by ANOVA single factor analysis.

The lack of binding demonstrated by both oxysterols could possibly be due to the failure of both oxysterols to adequately penetrate the lens fibers in the incubated lens fragments. To investigate this possibility, protein solubilization studies with 100 and 200 μ M concentrations of lanosterol and 25-hydroxycholesterol were carried out with lens homogenates of 0.5 and 2.0 mg/mL protein concentrations in PBS (containing protease inhibitor cocktail) prepared from 72-year-old human lenses. Changes in the soluble protein levels after 24-hour incubation at 37 °C are illustrated in **Figure 4.5**. The results confirm that lanosterol and 25-hydroxycholesterol do not affect lens protein solubilization when lens homogenate was used.

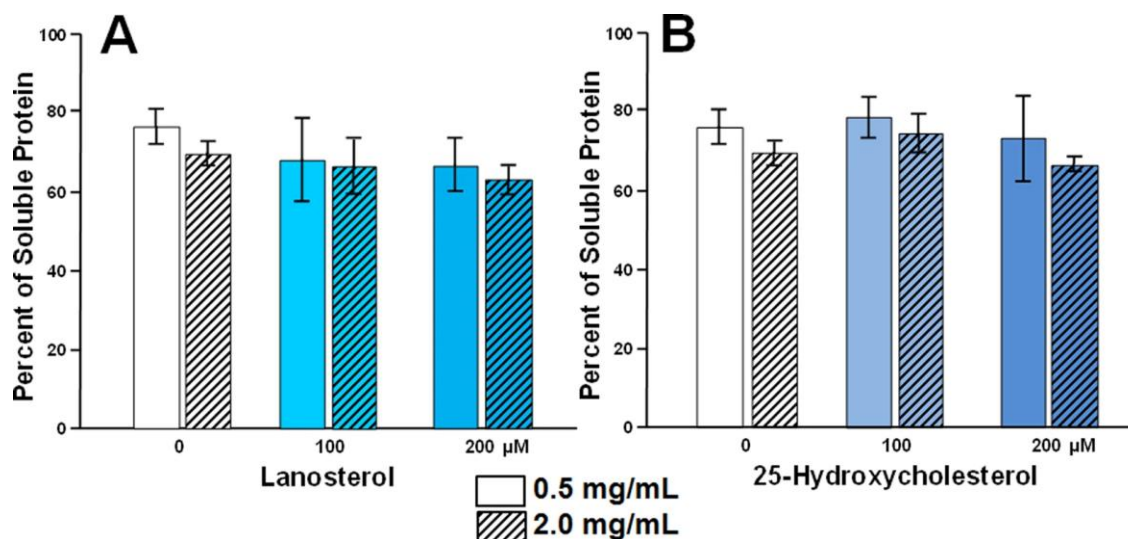


Figure 4.5. The solubility of human lens proteins in the presence of (A) lanosterol and (B) 25-hydroxycholesterol. Tissue homogenates from 72-year-old human lenses containing 0.5 or 2.0 mg protein in 1.0 mL of PBS were incubated with 0.0, 100 and 200 μM lanosterol or 25-hydroxycholesterol at 37 °C for 24 hours. The values shown are the percentage of protein remaining in the soluble fraction after incubation. N = 3 ± S.D. and $p > 0.05$ ANOVA single factor analysis.

Molecular Modeling Studies. Since both oxysterols failed to increase the anticipated soluble protein levels in lenses or lens homogenates where age-related protein denaturation had occurred, this suggests that oxysterol binding to the crystallin chaperones may be inadequate. Therefore, additional *in silico* studies to gain insight into chaperone binding to lanosterol and 25-hydroxycholesterol at the molecular level were conducted. As specified in the Method Section, lanosterol and 25-hydroxycholesterol were docked to three small αB-crystallins heat shock chaperones, two human wild type dimers, **2WJ7** [43] and **2KLR** [44], and an ARG120GLY mutant, **2Y1Z** [45]. As an internal control, ATP, which has been reported to bind these αB-crystallins, was also examined. Additionally, the novel MFAOs were investigated because the parent scaffold of these compounds was observed to have anti-cataract activity without aldose reductase or sorbitol dehydrogenase activity *in vivo* [37]. Molecular modeling and docking studies were conducted using MOE dock and Schrödinger Glide dock standard docking methods. The

appropriate binding modes were determined by docking the ligands to two potential pockets, an ATP pocket and the dimer interface. The top five docked poses were collected and the best docking scores along with predicted K_d values are presented. The MOE dock scores are reported as London ΔG binding scores which generally indicate that a value of -12.00 corresponds to the low nM range and a dissociation constant, K_d , of -12.3 kcal/mol, a value of -8.00 corresponds to the low μ M range and a K_d of -8.2 kcal/mol, and a value of -4.00 corresponds to the low mM range and a K_d of -4.1 kcal/mol.

The MOETM docking results summarized in **Table 4.1** demonstrate good binding of ATP to the ATP binding pocket in wildtypes **2WJ7** and **2KLR** (*ca.* -12.0 kcal/mol). This indicates that the methods employed successfully predicted the expected feasible nanomolar range binding of ATP to its binding pocket on these chaperones. However, ATP binding to mutant **2Y1Z** appeared to be slightly weaker as observed by the higher docking score (-9.82 kcal/mol), though still with high affinity. In contrast, the results of the oxysterols suggested weak binding to the dimer interface containing the PHE centroid in the wildtype **2WJ7**, with lanosterol (-4.33 kcal/mol) and 25-hydroxycholesterol (-6.75 kcal/mol) binding with much lower affinity. Compared to the oxysterols, the MFAOs all exhibited much stronger binding to the **2WJ7** dimer interface. The binding of the bulkier and slightly larger MFAOs JHX-4 (-11.62 kcal/mol) and JHX-8 (-13.08 kcal/mol) to the **2WJ7** dimer interface was stronger than the HK series. However, HK-2 (-9.11 kcal/mol), HK-4 (-9.80 kcal/mol), HK-6 (-9.18 kcal/mol), and HK-8 (-10.10 kcal/mol) also bound stronger than the oxysterols. The methoxy derivatives JHX-8, HK-4, and HK-8 all exhibited stronger binding than the non-methoxy derivatives, suggesting the added bulkiness of the methoxy groups on the pyrimidine bottom ring in addition to their smaller size may help to

increase binding affinity at the dimer interface. Against the **2KLR** wildtype, the slightly bulkier methoxy compounds JHX-8 (-10.15 kcal/mol) and HK-4 (-8.71 kcal/mol) exhibited slightly stronger binding than their non-methoxy derivatives JHX-4 (-9.71 kcal/mol) and HK-2 (-7.92 kcal/mol). However, the non-methoxy HK-4 (-8.71 kcal/mol) bound slightly stronger than the methoxy HK-8 (-8.36 kcal/mol). Against the mutant **2Y1Z**, JHX-4 (-9.79 kcal/mol) and JHX-8 (-10.26 kcal/mol) were found to bind tighter than HK-2 (-6.08 kcal/mol), HK-4 (-7.91 kcal/mol), HK-6 (-5.92 kcal/mol), and HK-8 (-7.86 kcal/mol), suggesting the size of the JHX-series is better for binding to the **2Y1Z** mutant model. Comparatively, the results for lanosterol (+2.34 kcal/mol; +17.80 kcal/mol) and 25-hydroxycholesterol (+0.11 kcal/mol; +11.33 kcal/mol) at both **2KLR** and **2Y1Z** dimer interfaces, respectively, predict that no binding is anticipated. The positive docking scores suggest unfavorable binding which is most likely due to the size and hydrophobicity of the oxysterols. All MFAOs are shown to bind well at all dimer interfaces and the data suggest that they are small enough to successfully bind to the closed groove of **2Y1Z**.

Compounds	2WJ7 Wildtype		2KLR Wildtype		2Y1Z Mutant	
	Best	K _d (Pred)	Best	K _d (Pred)	Best	K _d (Pred)
ATP	-12.72	438.78 pM	-11.48	3.59 nM	-9.82	59.66 nM
25-Hydroxycholesterol	-6.75	10.82 μM	0.11	n.d.	11.33	n.d.
Lanosterol	-4.33	652.44 μM	2.34	n.d.	17.80	n.d.
JHX-4	-11.62	2.84 nM	-9.71	72.01 nM	-9.79	63.31 nM
JHX-8	-13.08	239.99 pM	-10.15	34.30 nM	-10.26	28.41 nM
HK-2	-9.11	198.87 nM	-7.92	1.49 μM	-6.08	33.77 μM
HK-4	-9.80	62.05 nM	-8.71	390.78 nM	-7.91	1.51 μM
HK-6	-9.18	177.53 nM	-8.29	792.02 nM	-5.92	44.43 μM
HK-8	-10.10	37.36 nM	-8.36	712.49 nM	-7.86	1.65 μM

Table 4.1. MOETM docking scores of all compounds (**Figure 4.1**) to the dimer interface on PHE 55 of wildtypes, **2WJ7** and **2KLR**, and the R120G mutant, **2Y1Z**. ATP was docked to the ATP binding pocket of each protein as the internal control. Positive binding scores indicate that a feasible binding value in the docking data could not be determined.

In order to verify these docking results, a similar strategy was employed using Schrodinger's Maestro and these results are summarized in **Table 4.2**. Compared to MOE™, the Maestro docking scores and predicted K_d values were more positive and comparable to reported experimental data of both ATP and the oxysterols. ATP again showed good binding at the ATP binding site of wildtype **2WJ7** (-8.23 kcal/mol). Surprisingly, the binding of ATP to wildtype **2KLR** was weaker (-5.57 kcal/mol) compared to **2WJ7**, and binding of ATP to mutant **2Y1Z** was stronger (-9.65 kcal/mol) than to both wildtypes **2WJ7** and **2KLR**. Both oxysterols demonstrated weak binding to all dimer interfaces with strength of binding decreasing from **2WJ7** > **2KLR** > **2Y1Z**. Lanosterol was shown to bind weakly to the wildtypes **2WJ7** (-3.33 kcal/mol) and **2KLR** (-1.54 kcal/mol), and no docking information could be extracted for **2Y1Z** (n.d.). On the other hand, 25-hydroxycholesterol bound stronger than lanosterol to **2WJ7** (-4.40 kcal/mol), **2KLR** (-3.96 kcal/mol), and **2Y1Z** (-2.87 kcal/mol), albeit poorly. This trend follows the MOE™ results, though no feasible docking poses were found for both oxysterols on **2KLR** or **2Y1Z**. Unlike the MOE™ results of MFAOs docked to the **2WJ7** dimer interface, the

Compounds	2WJ7 Wildtype		2KLR Wildtype		2Y1Z Mutant	
	Best	K_d (Pred)	Best	K_d (Pred)	Best	K_d (Pred)
ATP	-8.23	881.90 nM	-5.57	79.86 μ M	-9.65	79.57 nM
25-Hydroxycholesterol	-4.40	579.49 μ M	-3.96	1.22 mM	-2.87	7.74 mM
Lanosterol	-3.33	3.55 mM	-1.54	73.63 mM	n.d.	n.d.
JHX-4	-7.36	3.85 μ M	-4.27	722.24 μ M	n.d.	n.d.
JHX-8	-6.49	16.81 μ M	n.d.	n.d.	n.d.	n.d.
HK-2	-7.39	3.66 μ M	-5.78	55.95 μ M	-5.84	50.54 μ M
HK-4	-6.09	33.09 μ M	n.d.	n.d.	-5.43	101.23 μ M
HK-6	-7.55	2.79 μ M	-5.56	81.22 μ M	-4.77	309.63 μ M
HK-8	-5.80	53.99 μ M	n.d.	n.d.	-4.52	472.89 μ M

Table 4.2. Maestro docking scores of all compounds (**Figure 4.1**) to the dimer interface on PHE 55 of wildtypes, **2WJ7** and **2KLR**, and the R120G mutant, **2Y1Z**. ATP was docked to the ATP binding pocket of each protein as the internal control. A binding score of "n.d." indicates that a feasible binding value in the docking data could not be assessed.

Maestro results exhibited an opposite effect where the methoxy derivatives JHX-8 (-6.49 kcal/mol), HK-4 (-6.09 kcal/mol), and HK-8 (-5.80 kcal/mol) bound weaker than the non-methoxy derivatives JHX-4 (-7.36 kcal/mol), HK-2 (-7.39 kcal/mol), and HK-6 (-7.55 kcal/mol). Not only do the non-methoxy derivatives bind tighter than the methoxy derivatives, they also bind with similar affinity to the dimer interface. These scores suggest that the added bulkiness from the methoxy groups decrease the strength of binding, and that the general size of the MFAOs is ideal for fitting into the dimer interface of **2WJ7**. Interestingly, docking to the interface of **2KLR** only identified successful binding of the non-methoxy compounds JHX-4 (-4.27 kcal/mol), HK-2 (-5.78 kcal/mol), and HK-6 (-5.56 kcal/mol). None of the methoxy derivatives were able to bind to the **2KLR** dimer interface, further suggesting that the bulkiness of the methoxy groups decreases MFAO binding affinity. Additionally, HK-2 and HK-6 were calculated to bind ~1.4 kcal/mol stronger than JHX-4, suggesting the smaller size of the HK compounds is favorable for binding to the **2KLR** dimer interface. This may be explained by the fact that the wildtype **2KLR** model does not have an “open” dimer interface like the wildtype **2WJ7** model. Instead, the protein is curved, and the dimer interface is smaller and less-accessible by larger molecules. Finally, it was observed that neither JHX-4 nor JHX-8 could bind to the dimer interface of mutant **2Y1Z**, but HK-2 (-5.84 kcal/mol), HK-4 (-5.43 kcal/mol), HK-6 (-4.77 kcal/mol), and HK-8 (-4.52 kcal/mol) were all able to bind, also suggesting that the smaller size of the HK compounds may be favorable for mutant dimer interface binding.

Could the oxysterol and MFAO binding perhaps occur at the ATP binding site? To investigate this question, these compounds were also docked to the ATP interactive binding region, which is known as the β 4- β 8 groove, and these results are shown in **Table 4.3**. As already reported in the binding studies on the dimer interface (**Table 4.2**), adequate binding values for ATP binding to the ATP binding pocket of the

wildtype **2WJ7** and **2Y1Z** mutant models were obtained but not for the wildtype **2KLR**. The oxysterols were unable to adequately bind at the dimer interface, and it was observed that they were also unable to adequately bind to the ATP binding pockets of these α B-crystallins. 25-hydroxycholesterol exhibited poor binding (-3.20 kcal/mol) to the **2WJ7** wildtype ATP-binding pocket. On the other hand, the MFAOs demonstrated modest but better binding than the oxysterols. HK-2 (-5.78 kcal/mol; -5.19 kcal/mol) and HK-6 (-5.56 kcal/mol; -5.25 kcal/mol) both bind tighter to the **2KLR** dimer interface than the ATP binding region, respectively, whereas JHX-4 (-4.27 kcal/mol; -4.98 kcal/mol) was predicted to have greater affinity at the **2KLR** ATP binding region. Surprisingly, JHX-4 (-4.78 kcal/mol) and JHX-8 (-4.76 kcal/mol) both exhibited similar affinity to the ATP binding region of **2Y1Z**, but neither of them were able to bind to the **2Y1Z** dimer interface. All HK MFAOs demonstrated greater binding affinity to the **2Y1Z** dimer interface except for HK-4 (-5.73 kcal/mol), which seems to have slight preference to the ATP binding region of **2Y1Z**. Interestingly, all MFAOs bound within ~1 kcal/mol to each other to the **2WJ7** ATP binding pocket, ~0.5 kcal/mol to the **2KLR** ATP binding pocket, and ~2 kcal/mol to the **2Y1Z** ATP binding pocket, suggesting that the binding affinity of these compounds may be due to their similar properties and sizes. Furthermore, the deviation of the binding scores of each MFAO to each of the protein ATP-binding pockets are close, suggesting that the compounds are able to similarly bind to the ATP binding pockets of each model α B-crystallin.

Overall, **Tables 4.1, 4.2, and 4.3** summarize the binding studies conducted using MOE dock and Schrödinger Glide dock methods, and these results support the protein binding studies which indicated that lanosterol or 25-hydroxycholesterol do not appear to adequately bind to α B-crystallins.

Compounds	β 4- β 8 Groove, ATP interactive binding region					
	2WJ7 Wildtype		2KLR Wildtype		2Y1Z Mutant	
	Best	Pred Kd	Best	Pred Kd	Best	Pred Kd
ATP	-8.23	881.90 nM	-5.57	79.86 μ M	-9.65	79.57 nM
25-Hydroxycholesterol	-3.20	4.42 mM	n.d.	n.d.	n.d.	n.d.
Lanosterol	n.d.	n.d.	n.d.	n.d.	n.d.	n.d.
JHX-4	-5.33	119.91 μ M	-4.98	216.95 μ M	-4.78	304.43 μ M
JHX-8	-5.11	174.07 μ M	-5.10	177.04 μ M	-4.76	314.92 μ M
HK-2	-6.06	34.82 μ M	-5.19	152.01 μ M	-5.51	88.40 μ M
HK-4	-5.25	137.32 μ M	-4.87	261.38 μ M	-5.73	60.90 μ M
HK-6	-5.78	55.95 μ M	-5.25	137.32 μ M	-4.10	963.26 μ M
HK-8	-4.73	331.34 μ M	-4.96	224.42 μ M	-4.25	747.13 μ M

Table 4.3. Maestro docking scores and predicted K_d values of ATP, oxysterols, and MFAOs to wildtypes **2WJ7** and **2KLR**, and mutant **2Y1Z**. All compounds were docked to the ATP interactive binding region containing the Walker-B motif. A value of “n.d.” indicates that no docking data could be acquired after 30 iterations.

4.5 Discussion

The mammalian lens contains millions of densely packed fiber cells that are continuously formed throughout life from differentiating lens epithelial cells. These fiber cells contain three major crystallin proteins families: α -crystallin, which resembles small heat shock proteins, and β - and γ -crystallins, that have structural and functional roles in maintaining transparency and the high refractive index of the lens. Increased light scattering leading to the appearance of lens opacities is directly linked to lens protein aggregation of the β - and γ -crystallins. To counteract this aggregation, Horwitz has proposed that small heat-shock proteins, α A- and α B-crystallins, serve as chaperones that protect the lens against protein aggregation [17, 18, 51]. The protein unfolding hypothesis for age-related cataract postulates that the progressive modifications of β - and γ -crystallins reduce their free energies of unfolding and promote their binding to α -crystallin. By binding to α -crystallins, lanosterol and 25-hydroxycholesterol have been proposed to

enhance the ability of α -crystallin to bind to the unfolded (aggregated) β - and γ -crystallins. Solubilizing these insoluble, light scattering aggregated lens proteins should result in an increase of soluble proteins and a decrease in insoluble proteins, *i.e.* “the cataract should be dissolved”.

Cholesterol derivatives, in addition to interacting with crystallins, also play an integral role in the regulation of cholesterol-dependent processes in fiber cell plasma membranes and in the maintenance of fiber cell membrane homeostasis [52]. With the loss of its organelles during fiber cell differentiation, the plasma membrane forming the external boundary of the fiber cell cytoplasm becomes the only remaining membrane in mature fiber cells [53]. Its extremely high cholesterol content makes this membrane one of the most saturated and ordered (stiff) membranes in the human body. While the need for this high lipid content is unclear, disturbances of cholesterol homeostasis can lead to cataract formation.

The first synthetic cholesterol lowering drug associated with irreversible cataract formation was triparanol (MER-29) [54]. This compound inhibited cholesterol synthesis at the desmosterol step, several steps downstream of lanosterol and resulted in the cellular accumulation of lanosterol [34, 35]. Although lens lanosterol levels were never specifically measured after triparanol administration, it can be assumed that downstream inhibition of cholesterol synthesis would similarly increase lanosterol levels in the lens. Therefore, altered cholesterol homeostasis may lead to cataract formation despite an increase in lanosterol. Similarly, cataracts have been associated with the lenticular accumulation of cholesterol oxides such as 25-hydroxycholesterol [36]. Cataract formation has also developed with other cholesterol lowering agents such as statins and fibrates. Several clinical studies report that patients undergo cataract surgery at higher rates with long-term

statin or fibrate administration [39, 55-57]. Statins inhibit cholesterol biosynthesis at the initial mevalonic acid level, while fibrates modify lipids, decrease triglycerides, and alter cholesterol levels of HDL/LDL by activating alpha peroxisome proliferator-activated receptors (PPAR- α). Studies suggest that cataract formation is induced by statins because they lower the isoprenylation of small GTPases [58, 59]. At present, the relationship between the regulation of cholesterol-dependent processes in lens fiber cells and their plasma membranes and cataract formation is not well established and more studies in this area are required.

In vitro organ culture of lenses has become a powerful experimental tool for not only investigating the relationship between lens metabolism and lens clarity, but also for elucidating the mechanism(s) of cataract formation by drugs and biochemical agents [49, 60]. These culture studies require carefully excised lenses that are cultured in specially buffered and osmotically compensated culture media at 37 °C in order to maintain their viability and clarity [61, 62]. Moreover, because the use of freshly excised lenses is ideally required, the majority of culture studies employ readily available rat lenses. Rat lens organ culture studies have been used to elucidate the effect of statins on cataract formation [39, 59], the role of osmotic changes on sugar cataract formation [40, 63], and the role of oxidative stress on oxidation-induced cataracts [64, 65].

In the present organ culture studies, freshly excised clear rat lenses were incubated under established conditions. During the initial 48-hour culture period, cataracts were induced in select groups of these clear lenses with either physical blunt trauma, inhibition of ATP, or experimentally induced osmotic stress. Blunt traumatic injury results in localized lens membrane damage and increased oxidative stress [66, 67], while ouabain alters the intracellular Na⁺ and K⁺ levels and affects the anabolism and catabolism of

protein during cataract formation [68]. Experimentally induced osmotic changes initiate increased endoplasmic reticulum (ER) stress in lens epithelial cells that subsequently results in the generation of reactive oxygen species (ROS) and oxidative stress [69-71]. These biochemical insults all lead to similar protein destabilization, the presence of partially unfolded aggregation-prone intermediates, and the formation of insoluble, light-scattering protein aggregates that appear as lens opacities [14]. Subsequent 48-hour exposure of these lenses to 15 mM of lanosterol liposomes failed to decrease the insoluble, light-scattering protein aggregates that had developed into lens opacities. More importantly, the presence of lanosterol during this 48-hour period also had no effect on influencing the further progression of protein aggregate development as evidenced by lens opacity progression to the advanced nuclear stage (**Figure 4.2**). Similarly, Shen *et al.* observed that lanosterol failed to prevent opacities induced by U18666A, an agent that induces cataracts in part by inhibiting the formation of lanosterol [72]. This is in contrast to the report by Zhao *et al.* who report that the clarity of cataractous rabbit lenses was improved in culture [24]. Their culture condition was quite different from ours as we ensure the viability of the cultured lenses by incubating under 37 °C physiological temperature. We also paid extra attention to ensure that the lens photos (**Figure 4.2**) taken after incubation were standardized to the same contrast, exposure, and pixel density by adjusting the outer grid lines to a standard value.

These lens organ culture results, which strongly suggest that there was no apparent interaction between lanosterol and the experimentally aggregated lens proteins, concur with the subsequent protein binding studies (**Figures 4.3, 4.4, 4.5**) where lanosterol or the presumably more potent 25-hydroxycholesterol both failed to interact with aggregated proteins in human lenses to increase the levels of soluble proteins by decreasing the levels of insoluble proteins. These results confirm those of Shanmugam *et*

al. in which the authors also failed to show any change in soluble protein levels in 40 nuclear cataracts cultured with lanosterol [31]. It is well-known that fully denatured proteins lack both tertiary and secondary structure and exist as so-called random coils where the only fixed relationship between the amino acids is the peptide bond between adjacent residues. While Zhao *et al.* [24] and Makley *et al.* [25] both focused on the misfolded crystallins only existing as amyloid fibrils characterized by intermolecular cross- β -sheet formations and relatively ordered morphologies [73, 74], crystallin aggregates can also adopt alternative amorphous forms other than amyloid fibrils [75-77]. This may explain, in part, the observed inability of aggregated lens proteins to be re-dissolved in the present studies. A recent study reported that sonicated human lens homogenates were partially solubilized by lanosterol and 25-hydroxycholesterol when the samples were kept in a shaker for 14 days [78]. Since it is known that sonication disaggregates and solubilizes water-insoluble lens proteins [79], it is unclear whether the prior sonication of the sample and several days of shaking contributed to the ability of sterols to partially solubilize the lens proteins. In another study, treatment of sonicated bovine lens extract with 50–500 μ M of 25-hydroxycholesterol for two days did not result in significant reduction of turbidity [80]. Further, it is yet to be determined whether the results of lens protein solubilization observed after sonication and shaking with sterols can be interpreted as *in vivo* therapeutic potential of the sterols since both sonication and shaking are not treatment modalities.

Failure of lanosterol in our studies to alter the appearance of formation of cataracts, along with the inability of oxysterols to reduce insoluble protein levels, prompted us to examine if oxysterols can bind to the crystallin chaperones at the molecular level to enhance chaperone function to re-dissolve aggregated proteins. Using both MOE™ dock and Schrödinger's Glide dock programs, *in silico* docking studies confirmed that both

lanosterol and 25-hydroxycholesterol failed to reach the therapeutically significant low micromolar range binding (docking score ≤ -8.00 kcal/mol) with the wildtypes **2WJ7** and **2KLR**, and the mutant **2Y1Z** α B-crystallins chaperones (**Tables 4.1, 4.2, and 4.3**). To confirm our methodology, the present studies used ATP as a control since ATP has a known binding site on the α B-crystallin chaperones [46, 48]. While the overall docking scores from the MOE dock program (**Table 4.1**) appeared to overestimate binding compared to the Glide dock program (**Table 4.2**), feasible binding with ATP was observed by both programs. Glide dock docking scores (**Table 4.2**) for **2KLR** provided an ATP binding scores (-5.57 kcal/mol) that was in good agreement with Palmisano *et al.* [81] who reported the binding constant of ATP to α -crystallin to be $K_a = 8.1 \times 10^3 \text{ M}^{-1}$, which corresponds to -5.33 kcal/mol when converted to ΔG . Significantly better ATP binding scores were obtained for binding at the ATP binding pocket of both **2WJ7** and **2Y1Z** (-8.23 kcal/mol and -9.65 kcal/mol, respectively). In contrast to ATP, the present MOETM and Glide docking scores suggest that lanosterol and 25-hydroxycholesterol binding to α -crystallin is unlikely at less than micromolar concentrations (**Tables 4.1 and 4.2**). For example, the K_d for lanosterol and 25-hydroxycholesterol, respectively, are predicted to be $653 \mu\text{M}$ and $11 \mu\text{M}$ (**Table 4.1, MOETM**) and 3.55 mM and $579 \mu\text{M}$ (**Table 4.2, Glide**) against wildtype **2WJ7**. For 25-hydroxycholesterol, the predicted K_d for **2Y1Z** is at a concentration of 7.74 mM (**Table 4.2**). It is unlikely that these high micromolar or even millimolar concentrations can be clinically achieved in the lens.

Our docking results were not contradictory to previously reported data in Makley *et al.* and Zhao *et al.* In Makley *et al.*, $100 \mu\text{M}$ concentration of drugs were used and at this concentration, 56% recovery versus wildtype in T_m was observed [25]. In Zhao's report, the observation of "reduction in cataract severity" was achieved in using 25 mM

concentration of lanosterol [24]. The free energy ΔG for K_d of 25 mM range would be ca. -2.48 kcal/mol. A ligand with a K_d above 10 μ M (docking score more positive than -6.8 kcal/mol) is normally considered to be low affinity. Both our docking results, and the fact that the Makley's and Zhao's experiments used high concentration (from 100 μ M to 15 mM), suggest that under 10 μ M concentrations are unlikely for the oxysterols to have significant and specific binding to α -crystallin.

Additional protein-ligand interactions in our studies further disclosed the underlying cause for the poor binding of oxysterols, such as lanosterol, to the current α B-crystallins models. The human wild-type dimer **2WJ7** contains residues ASP 109 and ARG 120, (**Figure 4.6**) which were identified to be synonymous with those described in Makley *et al.* [25]. These residues are located at the dimer interface where the carboxylic group of ASP 109 on one chain and the guanidine group of ARG 120 on the opposite chain form a salt bridge that contributes to the protein's stability. This open groove binding pocket is shown to be hydrophobic (white) and surrounded by positively charged residues (blue). Inspection of this dimer interface reveals that the central open groove binding pocket identified in **2WJ7** becomes narrower in **2KLR** and is blocked in **2Y1Z**. **2KLR** has a second salt bridge between ASP 80 and ARG 107 which further stabilizes the dimer interface so that a closed-groove conformation can be maintained. Such a scenario may result in a poor binding environment for both lanosterol and 25-hydroxycholesterol. This structural difference helps to explain why the docking scores of ATP and oxysterols are smaller in **2KLR** than in **2WJ7**. Similarly, the open-structure observed in wildtype **2WJ7** is disrupted in the ARG120GLY mutant **2Y1Z**, thereby making it impossible to form a stabilizing salt bridge between ARG120 and ASP109. Instead, salt bridges between ASP

80 and HIS 83 are formed where the side chains of these two residues block the central groove/pocket so that no suitable binding with either oxysterol can occur.

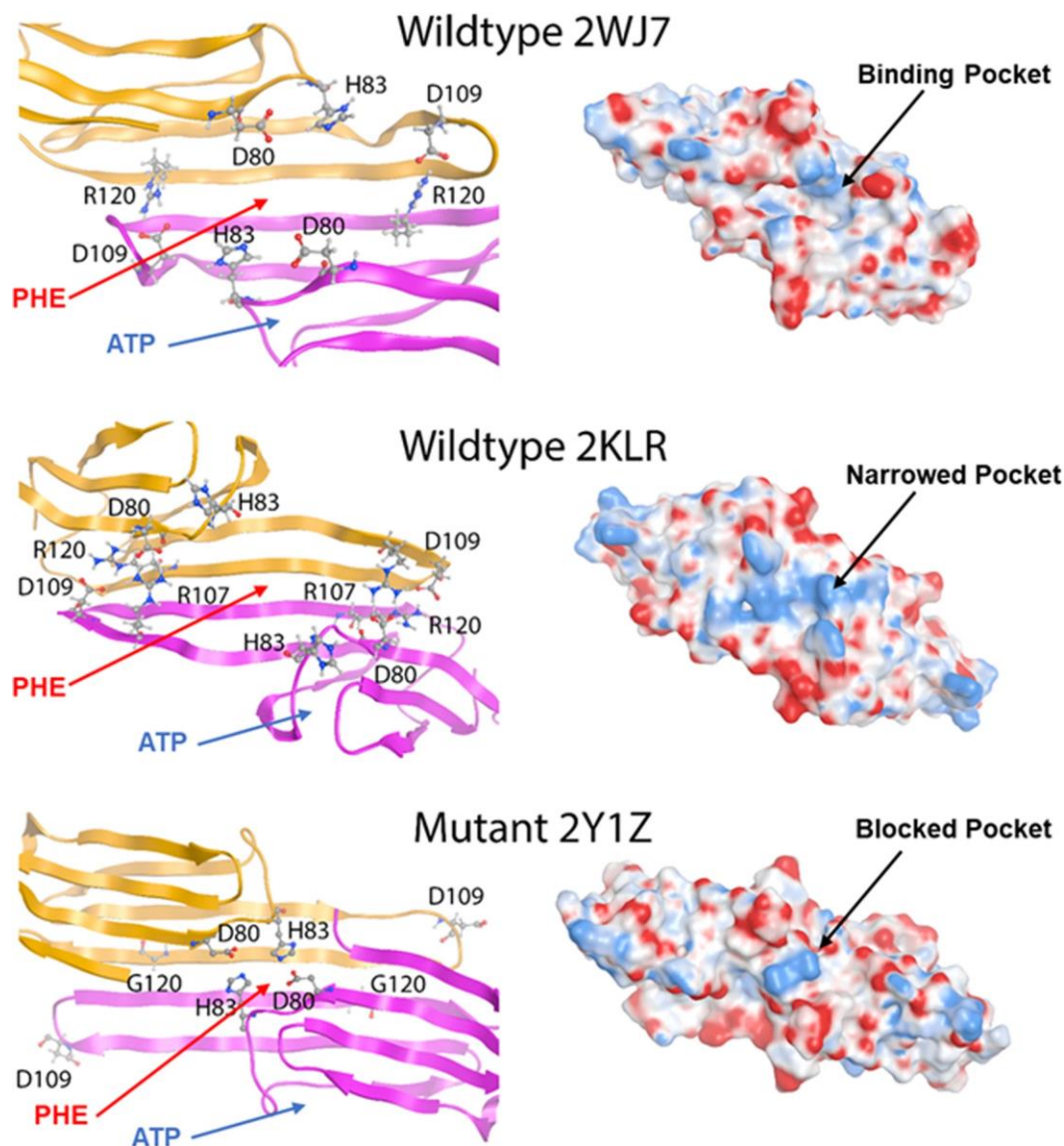


Figure 4.6. Comparison of the surface and charge differences (sphere structure), along with the location of key amino acid residues (ribbon structure) between the α B-crystallin wildtypes **2WJ7** and **2KLR** and the ARG120GLY mutant **2Y1Z**. Locations of the defined ATP pocket and PHE 55 binding regions for docking studies are marked with arrows on the ribbon structures. The experimentally determined ATP-binding site is in the β 4- β 8 pocket where the amino acid sequence ⁸²KHFSPEELKVKVLGD⁹⁶ resembles the Walker-B ATP-binding motif. PHE 55 is in the centroid of the dimer interface. Note the presence of the open groove at the dimer interface in **2WJ7**, which is nonexistent in **2KLR** and shielded by the ASP 80/HIS 83 salt bridge in **2Y1Z**. These protein models agree with previously reported results [45].

Since no crystal structures of the α B-crystallin/oxysterol complex are available, and the published papers, including that of Makley *et al.*[25], have not identified specific binding residues used for docking oxysterols to α B-crystallins, residue PHE 55 of the “A” chain was chosen as the centroid to define the binding pocket for the dimer interface in **2WJ7**, **2KLR** and **2Y1Z**. In addition, the Walker-B ATP-binding motifs containing the sequence ⁸²KHFSPEELKVKVLGD⁹⁶ were used for docking on both wildtypes, **2WJ7** and **2KLR**, and mutant, **2Y1Z**, to determine whether the oxysterols can also bind to the ATP binding pocket. This ATP binding pocket was previously reported by Ghosh *et al.* [46], and both binding regions are marked in **Figure 4.6**.

Because an ATP binding site on the α B-crystallins has previously been identified, successful binding of ATP to this site was easily and successfully achieved. As discussed above, the Glide docking scores were in better agreement with the experimental data than those from the MOE dock method [81]. Depending on the α B-crystallin model employed, the binding constant for ATP was estimated to be in the range of 0.1 to 80 μ M (**Table 4.2**). However, achieving similar binding results for the oxysterols was more difficult. No suitable binding pose for lanosterol was identified. For 25-hydroxycholesterol, the predicted K_d values were ca. 4.4 mM and 27.6 mM for the **2WJ7** and the **2Y1Z** models, respectively. It is not surprising that the narrowed pocket on the dimer interface (**Figure 4.6**) is unable to accommodate the larger oxysterol molecules. For the larger dimer interface, a docked pose for 25-hydroxycholesterol was identified; however, the predicted K_d values for **2WJ7**, **2KLR**, and **2Y1Z**, were 579 μ M, 1.22 mM, and 7.74 mM, respectively. Binding results for lanosterol in the dimer interface were even worse, with K_d values for **2WJ7** and **2KLR** of 3.55 mM and 73.63 mM; K_d values for **2Y1Z** could not be determined. In addition, no suitable docked pose for the **2Y1Z** mutant was identified.

Inspection of the protein structures and docked ligands showed that the 3-hydroxyl group of 25-hydroxycholesterol can form a favorable hydrogen-bond with ARG 57, which is missing in the similar binding of lanosterol. This hydrogen-bond was absent in the **2KLR** and **2Y1Z** models (**Figure 4.7**). Therefore, 25-hydroxycholesterol showed even worse binding activity (mM range, **Table 4.2**). Furthermore, blocking of the dimer interface in the **2Y1Z** model due to the salt bridge between ASP 80 and HIS 83 made it unlikely for either oxysterol to bind (**Figures 4.6** and **4.7**). The only interaction between the oxysterols and the dimer interface was perpendicular to the interface pocket (**Figure 4.7**).

Previous *in vivo* studies in our laboratory have found that the MFAO parent analog, JHX-1, was observed to delay the formation of sugar cataracts *in vivo* [37]. Because JHX-1 did not affect lens polyol levels, it was evident that it did not have aldose reductase or sorbitol dehydrogenase activity. This study suggested that JHX-1 may have inherent chaperone activity which was observed as a delay in cataract formation. Because the MFAO derivatives showed therapeutic efficacy in various ocular pathologies, their binding capabilities *in silico* were also investigated. As with the oxysterols, their binding was examined at the dimer interface of multiple α B-crystallin models to investigate whether they may also interact with this lens protein, thereby supporting the chaperone hypothesis.

Compared to both ATP and the oxysterols, the MFAOs are smaller molecules. Due to their size, it was thought the MFAOs would fit in the open dimer interface of the **2WJ7** wildtype. This was confirmed upon examining the best docking poses of each the MFAOs to the dimer interface. Reported in **Figure 4.8** are the best docked poses of the MFAOs and their interactions with certain amino-acid residues on the dimer interface.

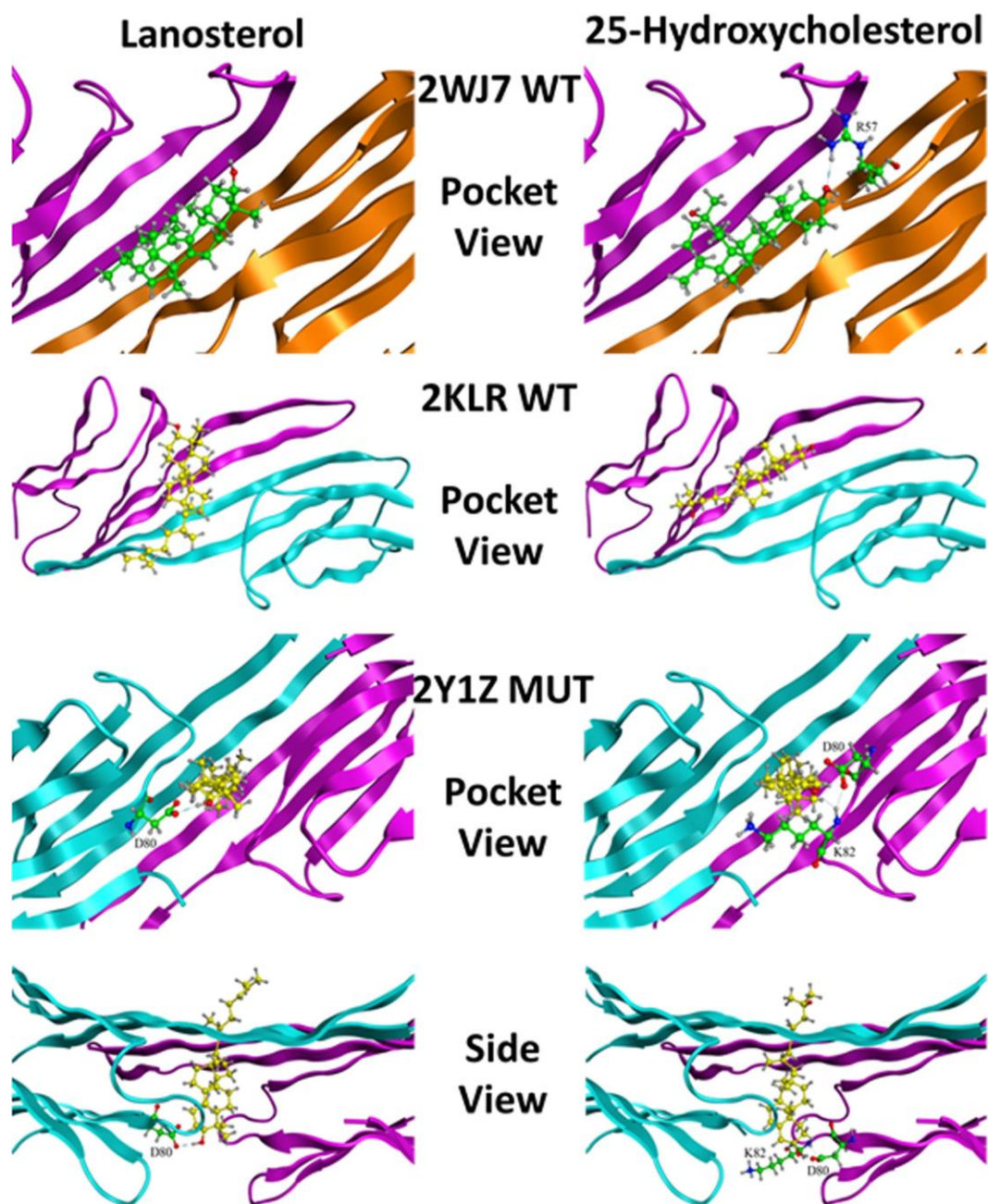


Figure 4.7. MOE ribbon structures depicting the best docked complexes for lanosterol and 25-hydroxycholesterol with the wildtype and mutant α B-crystallins. Note that neither oxysterol could enter the dimer interface on the 2Y1Z mutant, and the only interaction was perpendicular to the interface pocket.

MFAOs docked to the dimer interface of wildtype 2WJ7

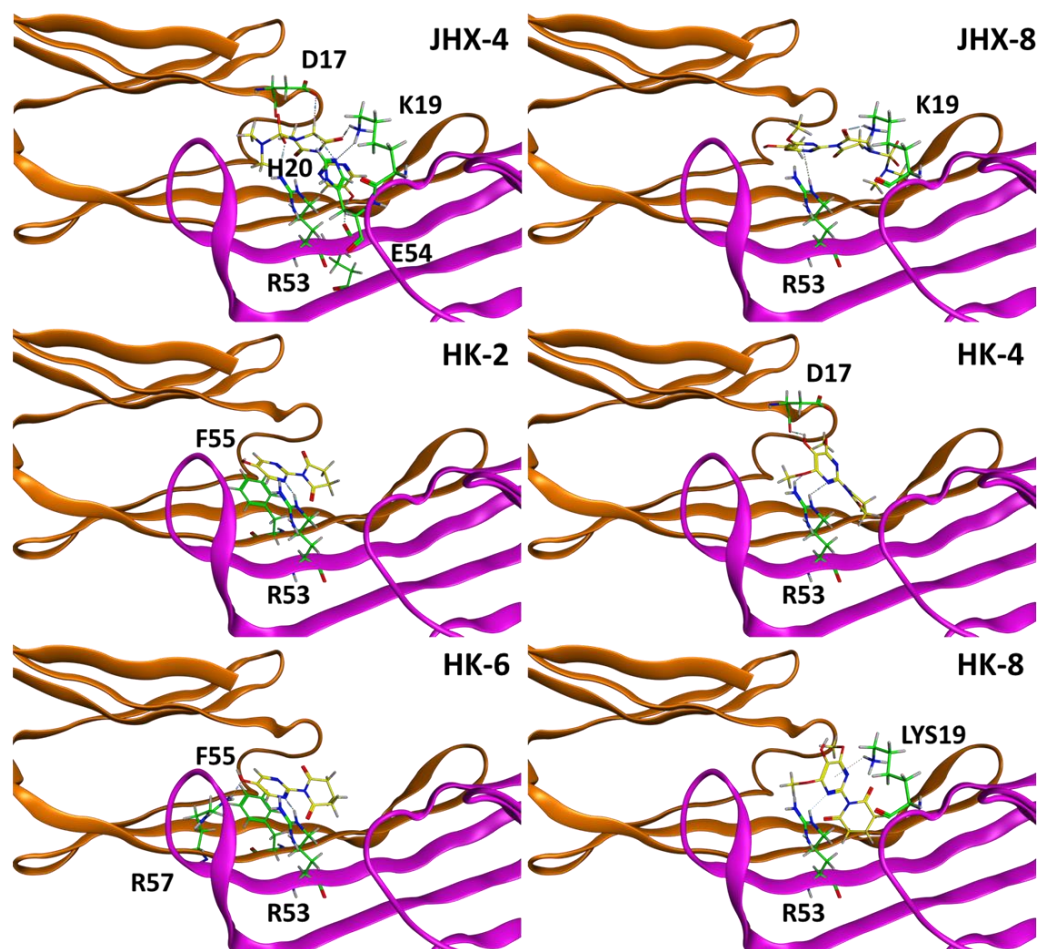


Figure 4.8. MOE ribbon structures depicting the best docked complexes for all MFAOs to the dimer interface of the wildtype α B-crystallin, **2WJ7**. Each of these compounds fit in the binding pocket and were observed to interact with at least two amino acids.

Both JHX-4 (-11.62 kcal/mol) and JHX-8 (-13.08 kcal/mol) bound with higher affinity than the HK series, which suggested that their size and bulkiness may be favorable compared to the smaller HK series and the larger, lipophilic oxysterols. Additionally, compared to the lipophilic oxysterols, all MFAOs have an aromatic ring system and more polar functional groups which may contribute to their favorable binding. JHX-4 participates in hydrogen bonding with ASP 17 on the “A” chain and LYS 19, HIS 20, ARG 53, and GLU 54 on the “B” chain; JHX-8 participates in an arene-cation interaction between the

pyrimidine bottom ring and ARG 53 on the “B” chain and a hydrogen bond with LYS 19 on the “B” chain. The HK series, though weaker binders than the JHX series, are still predicted to bind with low nanomolar affinity (docking scores *ca.* -9 to -10 kcal/mol) and participate in a variety of hydrogen and arene interactions. HK-2 (-9.11 kcal/mol) forms a hydrogen bond with ARG 53 on the “B” chain and has an arene-arene interaction with PHE 55 on the “A” chain; HK-4 (-9.80 kcal/mol) forms hydrogen bonds with ASP 17 on the “A” chain and ARG 53 on the “B” chain; HK-6 (-9.18 kcal/mol) forms hydrogen bonds with ARG 53 and ARG 57 on the “B” chain and an arene-arene interaction with PHE 55 on the “A” chain; HK-8 (-10.10 kcal/mol) forms hydrogen bonds with ASP 17 on the “A” chain and ARG 53 on the “B” chain, and forms an arene-cation interaction between the pyrimidine ring and LYS 19 on the “B” chain.

Relative to the **2WJ7** wildtype, there are significantly less interactions observed between the MFAOs and the **2KLR** wildtype presumably due to the narrowed dimer interface pocket. Based on the docking poses as reported in **Figure 4.9**, it appears the greatest contribution to the strength of the binding scores may be spatial fit. Again, JHX-4 (-9.71 kcal/mol) and JHX-8 (-10.15 kcal/mol) bound with higher affinity to the **2KLR** dimer interface than the HK series, but their tight docking scores are a result of interactions with solely one amino acid residue. JHX-4 forms a hydrogen bond with HIS 83 on the “A” chain, while JHX-8 forms a hydrogen bond with LYS 82 on the “B” chain. Comparatively, HK-2 (-7.92 kcal/mol) forms a hydrogen bond with LYS 82 on the “A” chain and an arene-hydrogen bond with HIS 83 on the “B” chain, and HK-6 (-8.29 kcal/mol) forms a hydrogen bond with LYS 82 on the “B” chain and an arene-hydrogen bond with PHE 84 on the “B” chain. Neither HK-4 (-8.71 kcal/mol) nor HK-8 (-8.36 kcal/mol) exhibit any significant interactions with the protein.

MFAOs docked to the dimer interface of wildtype 2KLR

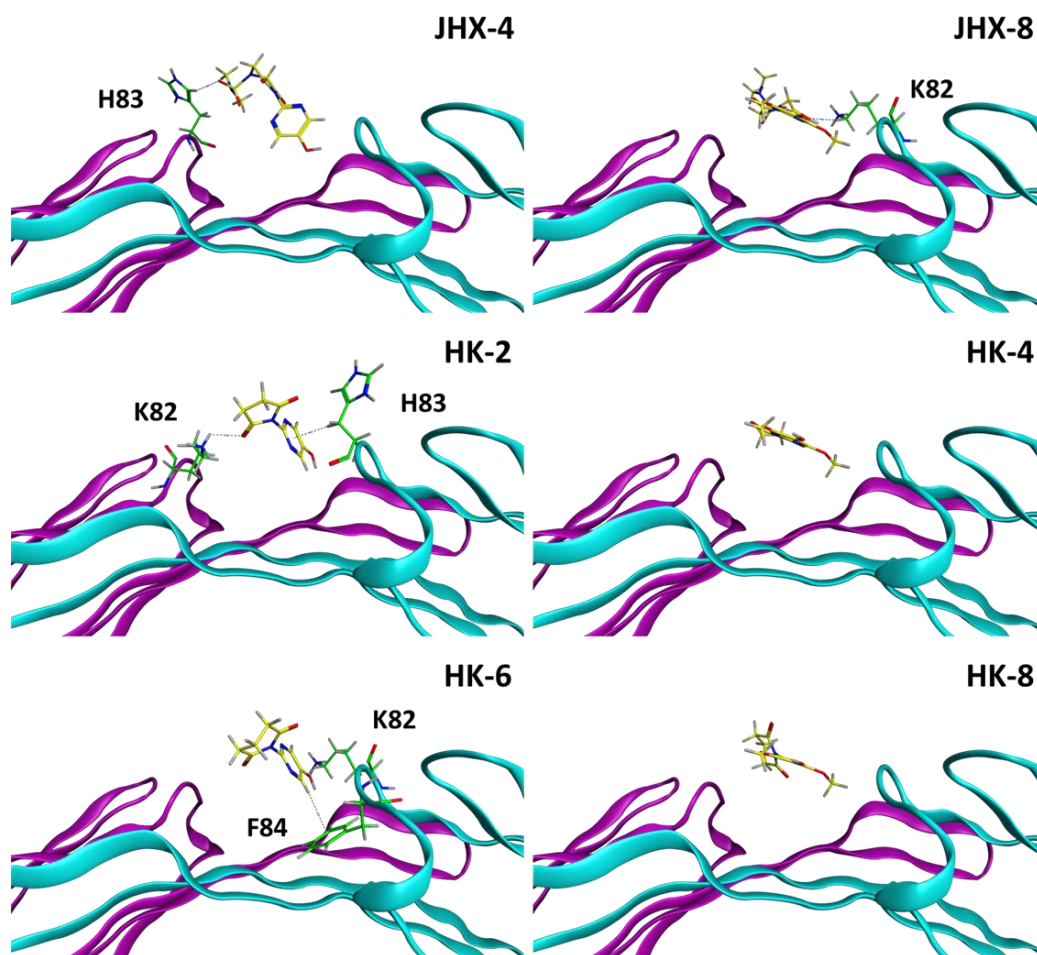


Figure 4.9. MOE ribbon structures depicting the best docked complexes for all MFAOs with the dimer interface of the wildtype α B-crystallin, **2KLR**. Compared to the **2WJ7** wildtype, less interactions with amino acids were observed. Compounds HK-4 and HK-8 were found to have no significant amino acid interactions, while all other MFAOs were observed to have at least one amino acid interaction.

Because most of these interactions do not necessarily indicate significant or selective binding with such strong docking scores, it suggests that size, bulkiness, and spatial arrangement of the MFAOs dictates their binding feasibility. From the **2KLR** binding results, it is evident that the oxysterols are too large and too hydrophobic to bind at the dimer interface, while the MFAOs have favorable size and electrostatic properties. The results for binding of the MFAOs to both wildtype α B-crystallins, **2WJ7**

and **2KLR**, suggest that they may stabilize the wildtype proteins at the dimer interface. However, it is still unknown whether these compounds enhance the chaperone activity of the α B-crystallins, in addition to reducing oxidative stress, as the mechanism through which the *in vivo* observations of cataract prevention was observed.

The majority of the MFAOs were too large to fit into the blocked pocket of the **2Y1Z** mutant protein (**Figure 4.10**) just like the oxysterols. Only HK-4 (-7.91 kcal/mol) appeared to fit in this tight pocket and form a hydrogen bond with PHE 118 on the "A" chain. Analysis of the ligand interaction diagram of HK-4 revealed that one of its methoxy groups on the bottom ring were unable to fit into the closed binding pocket of **2Y1Z**. Further examination of the ligand interaction diagrams of the other MFAOs revealed that the N,N-dimethylsulfamoyl top rings of both JHX-4 (-9.79 kcal/mol) and JHX-8 (-10.26 kcal/mol), not their pyrimidine bottom rings, were preferentially placed into the blocked binding pocket, presumably due to more favorable electrostatics. The same was observed for HK-2 (-6.08 kcal/mol) and HK-6 (-5.92 kcal/mol). In contrast, the bottom ring of HK-8 (-7.86 kcal/mol) was preferentially placed in the binding pocket. These results suggest that even the smaller MFAO compounds are unable to fit into the blocked pocket of the **2Y1Z** mutant dimer interface, suggesting that these molecules may be unable to bind or disrupt aggregation of the R120G mutant of α B-crystallin.

MFAOs docked to the dimer interface of mutant 2Y1Z

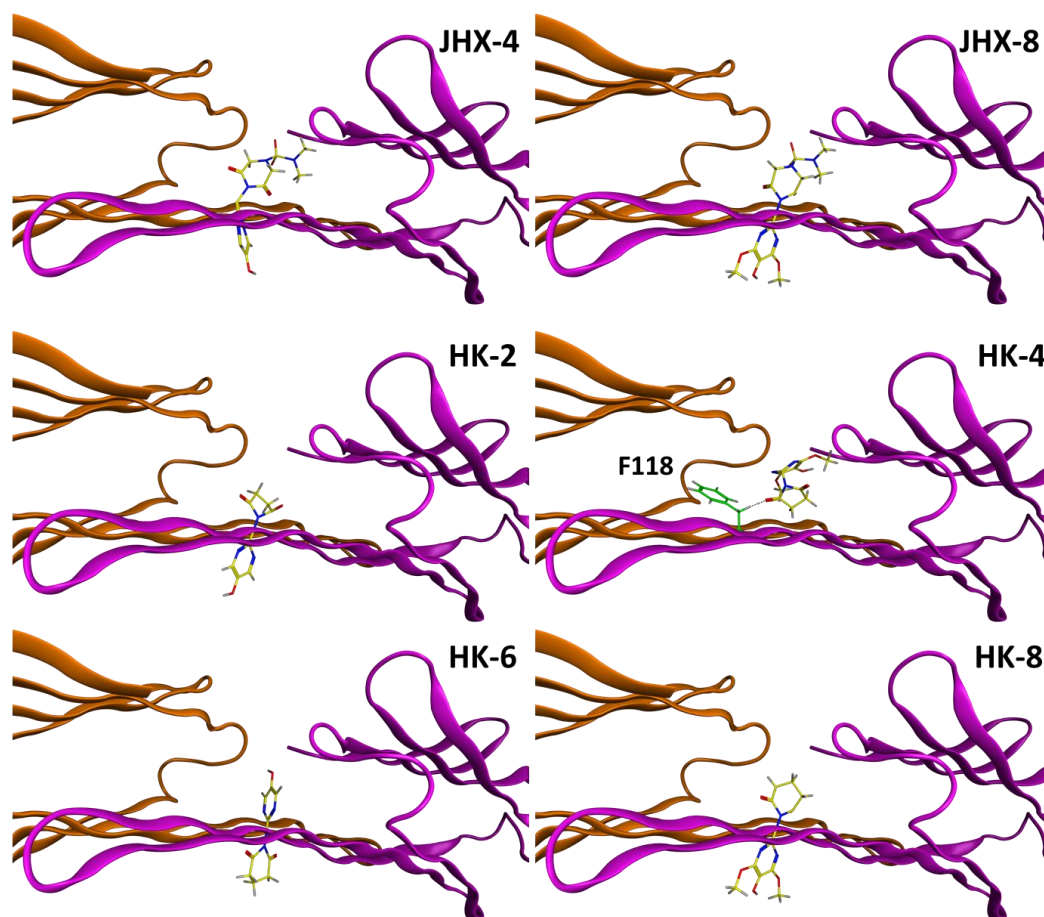


Figure 4.10. MOE ribbon structures depicting the best docked complexes for all MFAOs to the dimer interface of the R120G mutant α B-crystallin, **2Y1Z**. None of the MFAOs showed any amino acid interactions with **2Y1Z** except for HK-4 with F118. Overall, the best docked structural models indicate that the MFAOs are unable to fit in the closed/blocked pocket of **2Y1Z**.

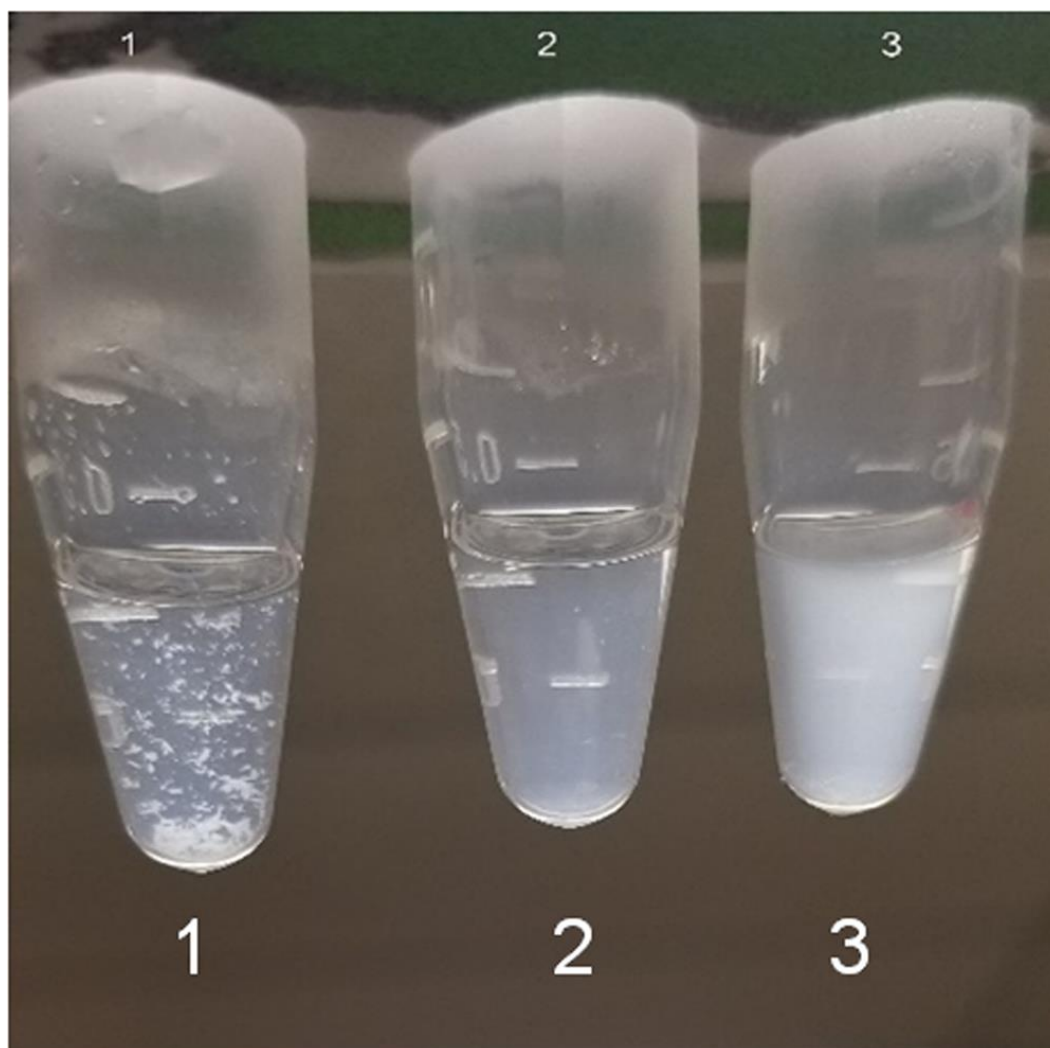


Figure 4.11. Appearance of 25-hydroxycholesterol dissolved in PBS solution with or without the presence of α B-crystallin. (1) 25-hydroxycholesterol (0.25 mM) in PBS. (2) α B-crystallin (2.0 mg/mL) in PBS. (3) 0.25 mM 25-hydroxycholesterol +2.0 mg/mL α B-crystallin.

Despite the poor binding results of 25-hydroxycholesterol with the three α B-crystallin models and the inability of 25-hydroxycholesterol to solubilize lens proteins (**Figures 4.4** and **4.5**), some interaction of α B-crystallin with this oxysterol can occur. As illustrated in **Figure 4.11**, when 25-hydroxycholesterol is placed in a solution of PBS, it remains as a precipitate and fails to dissolve into the solution. However, α B-crystallin does dissolve in PBS. Combining both PBS solutions together results in the formation of

a white turbid solution. While the oxysterol indeed appears to solubilize in the α B-crystallin solution, subsequent multi-angle light scattering (MALS) analysis indicates that the 25-hydroxycholesterol becomes trapped within the oligomers of α B-crystallin. The complex peak showed no significant change in the molar mass (MW) or hydrodynamic radii (R_h) of α B-crystallin incubated with 25-hydroxycholesterol. Consistent with the present docking and binding studies, this suggests that 25-hydroxycholesterol is held within α B-oligomers without any apparent binding interaction with the protein. This interaction may be similar to the partitioning of dexamethasone with α -crystallin as reported by Augusteyn and co-workers and interpreted as a non-functional interaction [82].

Lens protein aggregation occurs within the millions of mature lens fiber cells where α B-crystallin chaperones are located. Therefore, the oxysterols must penetrate within the millions of fiber cells to bind to the α B-crystallin chaperones. While investigators have focused on lens protein aggregation and the role of oxysterol induction of chaperones in reversing lens protein aggregation in solutions, missing is the consideration of the unique properties of the lens fiber membranes and the required demonstration that oxysterols can actually penetrate through the highly saturated, stiff cholesterol containing membranes of these fiber cells which are tightly interconnected through ball and socket junctions. In fact, in the rat lenses cultured with lanosterol liposomes (**Figure 4.2**), the amber appearance of the cortex and surrounding nucleus in the cataractous lenses does not rule out the possibility that the appearance is due only to the presence of liposomes in the extracellular space between the lens fibers. However, the failure of both oxysterols to solubilize lens protein homogenates suggests that studies establishing oxysterol penetration into lens fibers may be moot.

4.6 Conclusion

Using *in vitro* rat lens culture studies, *in vitro* human lens protein solubilization studies, and *in silico* molecular modeling studies, it was determined that the oxysterols lanosterol and 25-hydroxycholesterol failed to prevent the progression of, or clear, lens opacities. These oxysterols also failed to reach acceptable thresholds for good predictive binding at either the protein dimer interface or the ATP binding pocket of three model α B-crystallins. ATP and the MFAOs were found to bind with high affinity to all model α B-crystallins, whereas the oxysterols demonstrated low affinity binding. The results for *in silico* ATP and oxysterol binding closely matched reported experimental data, indicating the computational methods were conducted appropriately. It is presumed that the high affinity binding of the MFAOs to the wildtype α B-crystallin models, **2WJ7** and **2KLR**, is due to their smaller size and the presence of more polar functionalities compared to the larger, neutral, lipophilic oxysterols. However, neither the oxysterols nor the MFAOs were found to successfully fit into the dimer interface pocket of the R120G mutant, **2Y1Z**, suggesting that these compounds most likely do not restoring vision through the proposed mechanism of binding to the R120G-mutated α B-crystallin chaperone protein. Though our oxysterol results do not support the conclusions presented by Zhao *et al.* or Makley *et al.*, the *in silico* MFAO molecular modeling results support our laboratory's previously reported findings which demonstrated that the JHX series was able to delay the formation of cataracts without affecting aldose reductase or sorbitol dehydrogenase, suggesting these compounds may have chaperone activity.

4.7 References

1. Daszynski, D.M., et al., *Failure of Oxysterols Such as Lanosterol to Restore Lens Clarity from Cataracts*. Sci Rep, 2019. **9**(1): p. 8459.
2. Bassnett, S., Y. Shi, and G.F. Vrensen, *Biological glass: structural determinants of eye lens transparency*. Philos Trans R Soc Lond B Biol Sci, 2011. **366**(1568): p. 1250-64.
3. Michael, R. and A.J. Bron, *The ageing lens and cataract: a model of normal and pathological ageing*. Philos Trans R Soc Lond B Biol Sci, 2011. **366**(1568): p. 1278-92.
4. Kuszak, J.R., R.K. Zoltoski, and C.E. Tiedemann, *Development of lens sutures*. Int J Dev Biol, 2004. **48**(8-9): p. 889-902.
5. Bassnett, S. and M.J. Costello, *The cause and consequence of fiber cell compaction in the vertebrate lens*. Exp Eye Res, 2017. **156**: p. 50-57.
6. Mathias, R.T., J.L. Rae, and G.J. Baldo, *Physiological properties of the normal lens*. Physiol Rev, 1997. **77**(1): p. 21-50.
7. Mathias, R.T., J. Kistler, and P. Donaldson, *The lens circulation*. J Membr Biol, 2007. **216**(1): p. 1-16.
8. Mathias, R.T. and J.L. Rae, *Transport properties of the lens*. Am J Physiol, 1985. **249**(3 Pt 1): p. C181-90.
9. Ray, N.J., *Biophysical chemistry of the ageing eye lens*. Biophys Rev, 2015. **7**(4): p. 353-368.
10. Wride, M.A., *Lens fibre cell differentiation and organelle loss: many paths lead to clarity*. Philos Trans R Soc Lond B Biol Sci, 2011. **366**(1568): p. 1219-33.
11. Srivastava, O.P., et al., *Post-translationally modified human lens crystallin fragments show aggregation in vitro*. Biochem Biophys Rep, 2017. **10**: p. 94-131.

12. Truscott, R.J. and M.G. Friedrich, *The etiology of human age-related cataract. Proteins don't last forever*. Biochim Biophys Acta, 2016. **1860**(1 Pt B): p. 192-8.
13. Zhu, X., A. Korlimbinis, and R.J. Truscott, *Age-dependent denaturation of enzymes in the human lens: a paradigm for organismic aging?* Rejuvenation Res, 2010. **13**(5): p. 553-60.
14. Moreau, K.L. and J.A. King, *Protein misfolding and aggregation in cataract disease and prospects for prevention*. Trends Mol Med, 2012. **18**(5): p. 273-82.
15. Andley, U.P., *Effects of alpha-crystallin on lens cell function and cataract pathology*. Curr Mol Med, 2009. **9**(7): p. 887-92.
16. Biswas, A. and K.P. Das, *Role of ATP on the interaction of alpha-crystallin with its substrates and its implications for the molecular chaperone function*. J Biol Chem, 2004. **279**(41): p. 42648-57.
17. Horwitz, J., *Proctor Lecture. The function of alpha-crystallin*. Invest Ophthalmol Vis Sci, 1993. **34**(1): p. 10-22.
18. Horwitz, J., *The function of alpha-crystallin in vision*. Semin Cell Dev Biol, 2000. **11**(1): p. 53-60.
19. Datiles, M.B., 3rd, et al., *Clinical detection of precatactous lens protein changes using dynamic light scattering*. Arch Ophthalmol, 2008. **126**(12): p. 1687-93.
20. Ansari, R.R. and M.B. Datiles, 3rd, *Use of dynamic light scattering and Scheimpflug imaging for the early detection of cataracts*. Diabetes Technol Ther, 1999. **1**(2): p. 159-68.
21. Kinoshita, J.H., *Mechanisms initiating cataract formation. Proctor Lecture*. Invest Ophthalmol, 1974. **13**(10): p. 713-24.

22. Kador, P.F., et al., *Topical KINOSTAT ameliorates the clinical development and progression of cataracts in dogs with diabetes mellitus*. *Vet Ophthalmol*, 2010. **13**(6): p. 363-8.
23. Kador, P.F., M. Wyman, and P.J. Oates, *Aldose reductase, ocular diabetic complications and the development of topical Kinostat((R))*. *Prog Retin Eye Res*, 2016. **54**: p. 1-29.
24. Zhao, L., et al., *Lanosterol reverses protein aggregation in cataracts*. *Nature*, 2015. **523**(7562): p. 607-11.
25. Makley, L.N., et al., *Pharmacological chaperone for alpha-crystallin partially restores transparency in cataract models*. *Science*, 2015. **350**(6261): p. 674-7.
26. Qi, L.B., et al., *Cataract-causing mutation S228P promotes betaB1-crystallin aggregation and degradation by separating two interacting loops in C-terminal domain*. *Protein Cell*, 2016. **7**(7): p. 501-15.
27. Leng, X.Y., et al., *Congenital microcornea-cataract syndrome-causing mutation X253R increases betaB1-crystallin hydrophobicity to promote aggregate formation*. *Biochem J*, 2016. **473**(14): p. 2087-96.
28. Behar-Cohen, F. and T.J. Wolfensberger, *[Ophthalmology: what's new in 2015?]*. *Rev Med Suisse*, 2016. **12**(500): p. 67-70.
29. Quinlan, R.A., *DRUG DISCOVERY. A new dawn for cataracts*. *Science*, 2015. **350**(6261): p. 636-7.
30. Hejtmancik, J.F., *Ophthalmology: Cataracts dissolved*. *Nature*, 2015. **523**(7562): p. 540-1.
31. Shanmugam, P.M., et al., *Effect of lanosterol on human cataract nucleus*. *Indian J Ophthalmol*, 2015. **63**(12): p. 888-90.

32. Felici, A., Mengato, D., Falciani, M. & Bertelli, E., *Lanosterol Eye Drops in a Human Juvenile Nuclear Cataract*. Open Journal of Clinical and Medical Case Reports, 2018. **2**: p. 12-15.
33. Pyrah, I.T., et al., *Toxicologic lesions associated with two related inhibitors of oxidosqualene cyclase in the dog and mouse*. Toxicol Pathol, 2001. **29**(2): p. 174-9.
34. Popjak, G., et al., *Inhibition of cholesterol synthesis and cell growth by 24(R,S),25-iminolanosterol and triparanol in cultured rat hepatoma cells*. J Biol Chem, 1989. **264**(11): p. 6230-8.
35. Seo, S., et al., *Effect of sterol biosynthesis inhibitor, SSF-109, on cholesterol synthesis in isolated rat hepatocytes*. Steroids, 1993. **58**(2): p. 74-8.
36. Girao, H., et al., *Cholesterol oxides accumulate in human cataracts*. Exp Eye Res, 1998. **66**(5): p. 645-52.
37. Kador, P.F., J. Inoue, and K. Blessing, *Anticataract activity of analogs of a sorbitol dehydrogenase inhibitor*. J Ocul Pharmacol Ther, 2004. **20**(4): p. 333-44.
38. Shiono, T., P.F. Kador, and J.H. Kinoshita, *Ornithine accumulation and metabolism in rat lens*. Exp Eye Res, 1985. **40**(3): p. 421-9.
39. Rao, P.V., et al., *Role of small GTP-binding proteins in lovastatin-induced cataracts*. Invest Ophthalmol Vis Sci, 1997. **38**(11): p. 2313-21.
40. Zhang, P., et al., *Osmotic stress, not aldose reductase activity, directly induces growth factors and MAPK signaling changes during sugar cataract formation*. Exp Eye Res, 2012. **101**: p. 36-43.
41. *Molecular Operating Environment (MOE)*. 2016, Chemical Computing Group: 8. ULC, 1010 Sherbooke St West, Suite #910, Montreal, QC, Canada, H3A, 2R7, 201.

42. Wizard, P.P., *Maestro; MacroModel; Glide*. 2018, Schrödinger, LLC: New York, NY.
43. Bagneris, C., et al., *Crystal structures of alpha-crystallin domain dimers of alphaB-crystallin and Hsp20*. J Mol Biol, 2009. **392**(5): p. 1242-52.
44. Jehle, S., et al., *Solid-state NMR and SAXS studies provide a structural basis for the activation of alphaB-crystallin oligomers*. Nat Struct Mol Biol, 2010. **17**(9): p. 1037-42.
45. Clark, A.R., et al., *Crystal structure of R120G disease mutant of human alphaB-crystallin domain dimer shows closure of a groove*. J Mol Biol, 2011. **408**(1): p. 118-34.
46. Ghosh, J.G., et al., *The beta4-beta8 groove is an ATP-interactive site in the alpha crystallin core domain of the small heat shock protein, human alphaB crystallin*. J Mol Biol, 2006. **364**(3): p. 364-75.
47. Chin, D.T., et al., *Sequence of the lon gene in Escherichia coli. A heat-shock gene which encodes the ATP-dependent protease La*. J Biol Chem, 1988. **263**(24): p. 11718-28.
48. Walker, J.E., et al., *Distantly related sequences in the alpha- and beta-subunits of ATP synthase, myosin, kinases and other ATP-requiring enzymes and a common nucleotide binding fold*. Embo j, 1982. **1**(8): p. 945-51.
49. Wormstone, I.M., et al., *A focus on the human lens in vitro*. Environ Toxicol Pharmacol, 2006. **21**(2): p. 215-21.
50. Tumminia, S.J., et al., *The integrity of mammalian lenses in organ culture*. Exp Eye Res, 1994. **58**(3): p. 367-74.
51. Horwitz, J., *Alpha-crystallin can function as a molecular chaperone*. Proc Natl Acad Sci U S A, 1992. **89**(21): p. 10449-53.

52. Widomska, J., et al., *Cholesterol Bilayer Domains in the Eye Lens Health: A Review*. Cell Biochem Biophys, 2017. **75**(3-4): p. 387-398.
53. Borchman, D. and M.C. Yappert, *Lipids and the ocular lens*. J Lipid Res, 2010. **51**(9): p. 2473-88.
54. Kirby, T.J., *Cataracts produced by triparanol. (MER-29)*. Trans Am Ophthalmol Soc, 1967. **65**: p. 494-543.
55. Erie, J.C., et al., *Statin Use and Incident Cataract Surgery: A Case-Control Study*. Ophthalmic Epidemiol, 2016. **23**(1): p. 40-5.
56. Al-Holou, S.N., et al., *The Association of Statin Use with Cataract Progression and Cataract Surgery: The AREDS2 Report Number 8*. Ophthalmology, 2016. **123**(4): p. 916-7.
57. Wise, S.J., et al., *Statin use and risk for cataract: a nested case-control study of 2 populations in Canada and the United States*. Can J Cardiol, 2014. **30**(12): p. 1613-9.
58. MacDonald, J.S., et al., *Preclinical evaluation of lovastatin*. Am J Cardiol, 1988. **62**(15): p. 16j-27j.
59. Cheng, Q.F., P.V. Rao, and J.S. Zigler, Jr., *Effect of perillic acid, a putative isoprenylation inhibitor, on the cultured rat lens*. Exp Eye Res, 2001. **73**(2): p. 239-45.
60. Aleo, M.D., C.M. Doshna, and K.A. Navetta, *Ciglitazone-induced lenticular opacities in rats: in vivo and whole lens explant culture evaluation*. J Pharmacol Exp Ther, 2005. **312**(3): p. 1027-33.
61. Zigler, J.S., Jr., et al., *Effects of lipid peroxidation products on the rat lens in organ culture: a possible mechanism of cataract initiation in retinal degenerative disease*. Arch Biochem Biophys, 1983. **225**(1): p. 149-56.

62. Zigler, J.S., Jr., et al., *Macrophage mediated damage to rat lenses in culture: a possible model for uveitis-associated cataract*. Invest Ophthalmol Vis Sci, 1983. **24**(5): p. 651-4.
63. Kinoshita, J.H., et al., *Aldose reductase in diabetic complications of the eye*. Metabolism, 1979. **28**(4 Suppl 1): p. 462-9.
64. Lou, M.F., G.T. Xu, and X.L. Cui, *Further studies on the dynamic changes of glutathione and protein-thiol mixed disulfides in H₂O₂ induced cataract in rat lenses: distributions and effect of aging*. Curr Eye Res, 1995. **14**(10): p. 951-8.
65. Spector, A., *Oxidative stress-induced cataract: mechanism of action*. Faseb j, 1995. **9**(12): p. 1173-82.
66. Babizhaev, M.A., et al., *[Peroxidation crystalline lens damage--a possible cause of the development of traumatic cataract]*. Biull Eksp Biol Med, 1986. **101**(4): p. 412-3.
67. Hong, M.G., S.Y. Jiang, and J. Wang, *[The dynamic changes in glutathione peroxidase activity and malondialdehyde level in experimental traumatic cataract in rabbit]*. Zhonghua Yan Ke Za Zhi, 1994. **30**(5): p. 379-81.
68. Piatigorsky, J., H.N. Fukui, and J.H. Kinoshita, *Differential metabolism and leakage of protein in an inherited cataract and a normal lens cultured with ouabain*. Nature, 1978. **274**(5671): p. 558-62.
69. Mulhern, M.L., et al., *Cellular osmolytes reduce lens epithelial cell death and alleviate cataract formation in galactosemic rats*. Mol Vis, 2007. **13**: p. 1397-405.
70. Ikesugi, K., et al., *Role of the unfolded protein response (UPR) in cataract formation*. Exp Eye Res, 2006. **83**(3): p. 508-16.
71. Ikesugi, K., et al., *Induction of endoplasmic reticulum stress in retinal pericytes by glucose deprivation*. Curr Eye Res, 2006. **31**(11): p. 947-53.

72. Shen, X., et al., *Lanosterol Synthase Pathway Alleviates Lens Opacity in Age-Related Cortical Cataract*. J Ophthalmol, 2018. **2018**: p. 4125893.
73. Meehan, S., et al., *Amyloid fibril formation by lens crystallin proteins and its implications for cataract formation*. J Biol Chem, 2004. **279**(5): p. 3413-9.
74. Moran, S.D., et al., *Amyloid fiber formation in human gammaD-Crystallin induced by UV-B photodamage*. Biochemistry, 2013. **52**(36): p. 6169-81.
75. Boatz, J.C., et al., *Cataract-associated P23T gammaD-crystallin retains a native-like fold in amorphous-looking aggregates formed at physiological pH*. Nat Commun, 2017. **8**: p. 15137.
76. Moran, S.D. and M.T. Zanni, *How to Get Insight into Amyloid Structure and Formation from Infrared Spectroscopy*. J Phys Chem Lett, 2014. **5**(11): p. 1984-1993.
77. Wu, J.W., et al., *Comparative analysis of human gammaD-crystallin aggregation under physiological and low pH conditions*. PLoS One, 2014. **9**(11): p. e112309.
78. Chen, X.J., et al., *Lanosterol and 25-hydroxycholesterol dissociate crystallin aggregates isolated from cataractous human lens via different mechanisms*. Biochem Biophys Res Commun, 2018. **506**(4): p. 868-873.
79. Ortwerth, B.J., P.R. Olesen, and K.K. Sharma, *Solubilization of the lens water-insoluble fraction by sonication*. Exp Eye Res, 1986. **43**(6): p. 955-63.
80. Chemerovski-Glikman, M., et al., *Rosmarinic Acid Restores Complete Transparency of Sonicated Human Cataract Ex Vivo and Delays Cataract Formation In Vivo*. Sci Rep, 2018. **8**(1): p. 9341.
81. Palmisano, D.V., et al., *Interaction of ATP and lens alpha crystallin characterized by equilibrium binding studies and intrinsic tryptophan fluorescence spectroscopy*. Biochim Biophys Acta, 1995. **1246**(1): p. 91-7.

82. Jobling, A.I., A. Stevens, and R.C. Augusteyn, *Binding of dexamethasone by alpha-crystallin*. Invest Ophthalmol Vis Sci, 2001. **42**(8): p. 1829-32.

CHAPTER 5

Approaches to the Synthesis of Mitochondrial-Targeted JHX-4 and their Preliminary *In Vitro* Evaluation in the HEI-OC1 Cell Line

5.1 Summary

JHX-4 is an orally-active multifunctional antioxidant (MFAO) that has been shown to protect against a wide range of experimentally-induced oxidative stress. Though it is well-established that reducing cytoplasmic ROS is important, studies have suggested that targeting antioxidants directly to the mitochondria may be more beneficial than to the cytoplasm in preventing mitochondrial linked ROS-induced cellular damage. To test this hypothesis, a synthetic procedure was approached to develop a novel series of mitochondrially-targeted antioxidants based on the JHX series. To increase the targeting capability of these compounds to the mitochondria, the main source of ROS in the cell, the N,N-dimethylsulfamoyl head group was replaced with the lipophilic triphenylphosphonium (TPP) cationic group, a well-known mitochondria-targeting linker. The present chapter describes the synthetic approach towards developing this JHX-TPP series. Initial studies of JHX-2 (4-(5-hydroxypyrimidin-2-yl)-N,N-dimethylpiperazine-1-sulfonamide), JHX-3 (N,N-dimethyl-3,5-dioxo-4-(pyrimidin-2-yl)piperazine-1-sulfonamide), JHX-4 (4-(5-hydroxy-pyrimidin-2-yl)-N,N-dimethyl-3,5-dioxopiperazine-1-sulfonamide), the novel non-functional JHX-1-TPP (triphenyl(3-(4-(pyrimidin-2-yl)piperazin-1-yl)propyl)triphenyl-phosphonium bromide), and a novel model monofunctional chelator HK-2-CHL-TPP ((3-(1-(5-(benzyloxy)pyrimidin-2-yl)-2,5-dioxopyrrolidin-3-yl)propyl)triphenylphosphonium bromide) were tested using the rhodamine-123 fluorophore, which measures mitochondrial membrane potential. Our

results indicated that 1 mM of JHX-2, JHX-3, and JHX-4, as well as up to 100 nM of both JHX-1-TPP and HK-2-CHL-TPP are not mitochondriotoxic, demonstrating that further development of this novel compound class is feasible.

5.2 Introduction

The MFAOs scavenge free radicals and independently sequester and re-distribute free transition metals that facilitate the Fenton generation of toxic hydroxyl radicals. As discussed in the previous chapters, MFAOs have been shown to be beneficial for neuroprotection [1-5]. Very recently, it has been suggested that mitochondrial dysfunction occurs in neurodegeneration as one of the main propagating factors [6]. Since mounting experimental studies pinpoint the importance of mitochondrial function in neural tissues, the premise that specifically targeting the mitochondria and preventing mitochondrial dysfunction should have therapeutic merit [7, 8].

The mitochondria are complex intracellular organelles which are extremely critical for cellular function. With the exception of glycolysis, they are the main organelles in cellular respiration through which each step occurs. During the electron transport chain, NADH and FADH₂ are oxidized and through a cascade of multi-enzyme complexes ADP is phosphorylated to form ATP [9]. Throughout this process, ROS are released as byproducts which include superoxide, hydrogen peroxide, and the hydroxyl radicals. Various organelles within the cell can generate ROS as ROS is used for cellular signaling, but the majority of intracellular ROS is created by the mitochondria [10]. Additionally, the mitochondria are a source of iron-sulfur clusters and heme-prosthetic groups utilized by proteins throughout the cell. The post-transcriptional system that mammalian cells use to

regulate intracellular iron homeostasis depends on iron-sulfur cluster synthesis in the mitochondria. Hence, proper mitochondrial function is crucial to cellular iron homeostasis.

The excess production of ROS by mitochondria is one of the primary factors in the pathology of oxidative damage. Specifically, mitochondrial ROS production causes oxidative damage to mitochondrial proteins, membranes, and DNA, impairing the ability of mitochondria to synthesize ATP and carry out their wide range of metabolic functions [11]. Mitochondrial oxidative damage can also activate the cell's apoptotic machinery [12]. Furthermore, it renders the impermeable inner membrane permeable to small molecules in situations such as ischemia/reperfusion injuries [13, 14]. Mitochondria-generated ROS are a major mediator of age-associated cellular damage because the antioxidant enzyme activity within the mitochondria defects with age. Mitochondrial dysfunction, in addition to being linked to a number of neurodegenerations, may also initiate and/or contribute to iron dysregulation that is seen as an increase of iron levels during neurodegeneration.

Mitochondrial dysfunction is linked to apoptotic cell death in not only neurodegeneration, but also many other diseased states [15]. There are currently no therapeutic treatments for preventing or reversing mitochondria dysfunction. Therefore, maintaining functional mitochondria with pharmacological agents able to protect them against increased oxidative stress and promote mtDNA repair offers new strategies for the treatment of neurodegenerations. For neuroprotective approaches to be effective, they must preserve or regenerate normal cell function and counter the toxicity resulting from ROS overproduction [16]. Targeting MFAOs to the mitochondria using established transport carriers, such as the triphenylphosphonium (TPP) group, should increase their therapeutic efficacy to prevent mitochondrial dysfunction.

The aim of this study was to synthesize a novel series of mitochondria-targeting analogs of the MFAOs and compare their activity to the non-targeting analogs to see if they provide superior protection. In addition, an increase of free iron in the mitochondria has been detected during mitochondrial dysfunction, suggesting that targeting chelators may be beneficial to quenching ROS-associated damage in the mitochondria, but this topic is controversial since it has also been reported that mitochondrially-targeted chelators have adverse effects in the mitochondria [17]. To evaluate this premise, the synthesis of the JHX-TPPs derivatives including the nonfunctional parent (JHX-1-TPP, **1**), the monofunctional free radical scavenger (JHX-2-TPP, **2**) and bio-active transition metal chelator (JHX-3-TPP, **3**), and the multifunctional antioxidant containing both free radical scavenging and transition metal chelating activity (JHX-4-TPP, **4**), and evaluated their efficacy against the initial JHX-series in HEI-OC1 inner ear cells was approached. The structures of the JHX-TPP class of compounds are shown in **Figure 5.1**. No adverse effects were anticipated with the free radical scavenger **2**, and no effects were anticipated with the nonfunctional control compound **1**.

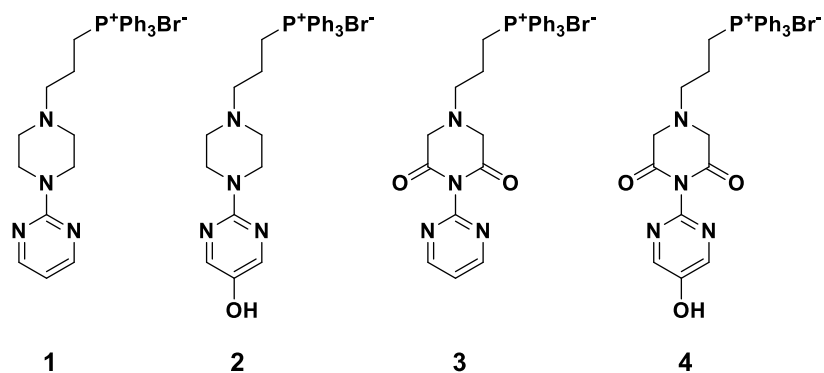


Figure 5.1. Proposed structures of the novel JHX-TPP class of compounds. Compound **1** shows the structure of the JHX-1-TPP (triphenyl(3-(4-(pyrimidin-2-yl)piperazin-1-yl)-propyl)triphenyl-phosphonium bromide), compound **2** shows the structure of the JHX-2-TPP ((3-(4-(5-hydroxypyrimidin-2-yl)piperazin-1-yl)propyl)triphenylphosphonium bromide), compound **3** shows the structure of the JHX-3-TPP ((3-(3,5-dioxo-4-(pyrimidin-2-yl)piperazin-1-yl)propyl)triphenylphosphonium bromide), and compound **4** shows the structure of the JHX-4-TPP ((3-(4-(5-hydroxypyrimidin-1-yl)-3,5-dioxopiperazin-1-yl)-propyl)triphenylphosphonium bromide).

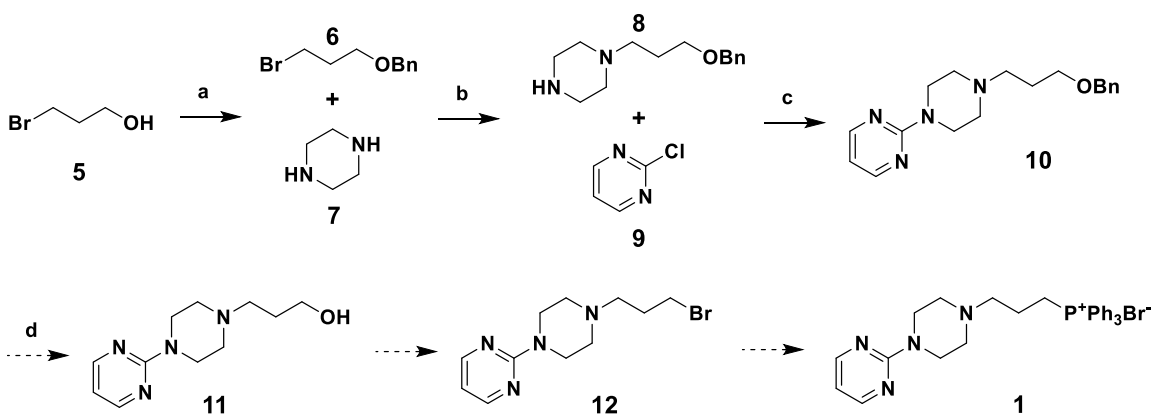
5.3 Results and Discussion

5.3.1 Chemistry

5.3.1a Synthesis of the Parent TPP Compound

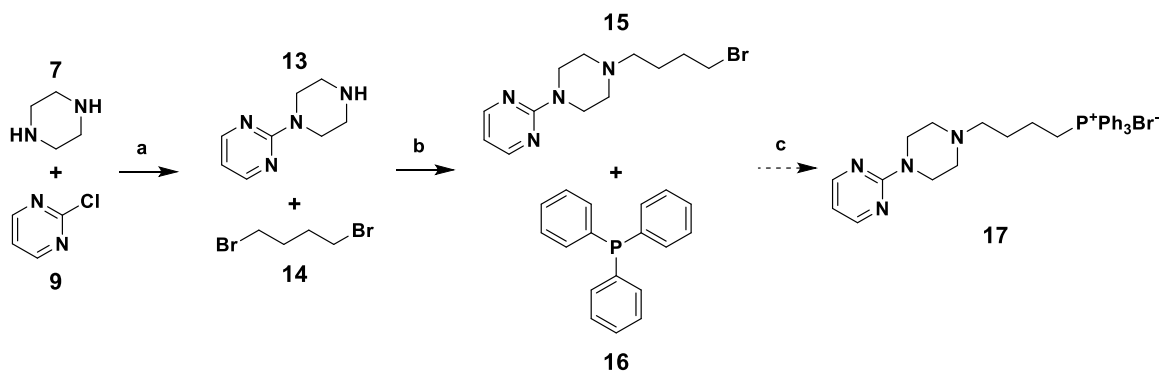
The initial approach towards synthesizing parent-TPP (**1**), triphenyl(3-(4-(pyrimidin-2-yl)piperazin-1-yl)-propyl)triphenyl-phosphonium bromide, is shown in **Scheme 5.1**. The commercially available 3-bromopropanol **5** was benzyl protected with benzyl bromide to give the bromo-benzyl **6**, which underwent nucleophilic substitution with piperazine **7** to yield product **8** according to Capuano [18]. The nucleophilic aromatic substitution of piperazine product **8** with 2-chloropyrimidine **9** yielded the benzyl-protected parent precursor **10**. However, subsequent removal of the benzyl protecting group from **10** under standard hydrogenolysis conditions was unsuccessful. Hydrogenolysis using

Pd/C catalyst at various loading ratios (5-15 wt%) in 95% ethanol under hydrogen balloon for 72 hours were unsuccessful. It was thought that increasing the catalytic loading to 25 wt% would drive the reaction forward, but this was unsuccessful. The solvent systems were also changed because their properties, such as different dielectric constant and polarities, could affect the hydrogenolysis. However, hydrogenolysis reactions using different solvents such as methanol, acetone, ethyl acetate, and dichloromethane with 20 wt% Pd/C under hydrogen balloon for up to 48 hours failed to cleave the benzyl group. Finally, Pd/C was replaced with Pearlman's catalyst ($\text{Pd}(\text{OH})_2/\text{C}$) because it is reported that some hydrogenolysis reactions may be catalyst-selective [19]. Using 20 wt% $\text{Pd}(\text{OH})_2/\text{C}$ with various solvents under hydrogen balloon for up to 48 hours also failed to cleave the benzyl protecting group. These reactions were also unsuccessful. As a final attempt, the hydrogen pressure was increased to 50 psi by placing **10** was under high temperature (120 °C) in a Parr Reactor with 20 wt% Pd/C for 48 hours. This also failed to remove the benzyl protecting group. The reason for this failure to debenzylate are not clear; however, conflicting reports suggest that the presence of amines can adversely affect the cleavage of the benzyl group from alkyl benzyl protected alcohols [20-23].



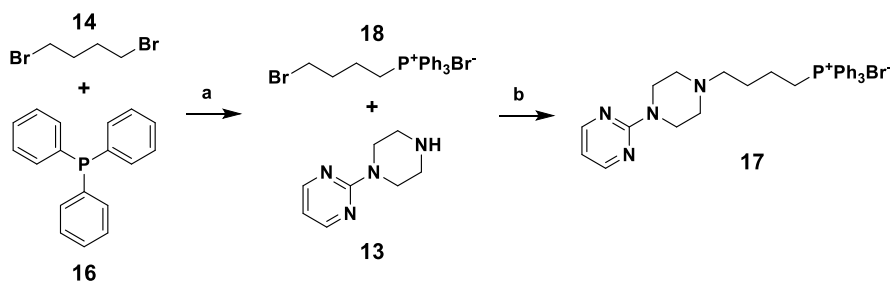
Scheme 5.1. Progress towards the C3-linked JHX-1-TPP (**1**). Reagents and conditions: (a) **5**, BnBr, NaH, DMF, -90 °C to rt, 18 hours; (b) **6**, **7**, toluene, reflux, 4 hours; (c) **8**, **9**, K_3PO_4 , H_2O , reflux, 18 hours; (d) **10**, H_2 , Pd/C, Acetone.

Because the benzyl group on compound **10** failed to cleave, an alternate approach towards compound **1** was investigated as shown in **Scheme 5.2**. This alternate synthetic approach directly conjugates 1,4-dibromobutane with the parent ring scaffold **13** to give **15** which should then react with TPP to give the desired product **17**. A 4-carbon linker rather than the 3-carbon linker was used in this approach because the starting material was readily available in the laboratory. The parent scaffold **13** was prepared according to Mills [24] by nucleophilic aromatic substitution between piperazine **7** with 2-chloropyrimidine **9**. Reaction between equimolar ratios of the parent scaffold **13** and 1,3-dibromobutane **14** under reflux in acetonitrile according to Mou [25] gave the desired product **15**. The low boiling point of **14** required the use of PEG-1000 as a phase-transfer catalyst to facilitate the transition of **14** back into liquid phase. The final addition of TPP installation to yield the 4-carbon-linked parent-TPP **17** was unsuccessful. Initially, an overnight reflux of bromo **17** with TPP yielded only recovery of starting material. Hypothesizing that the reaction may require a higher activation energy, reflux was then extended to 5 days with the reaction and monitored by thin-layer chromatography (TLC). During this 5-day period, no change in product formation was observed. In accordance with the activation energy hypothesis, the reaction energy was then increased by replacing the acetonitrile solvent with higher boiling toluene. This also failed to produce product **17**. This suggests that perhaps an even higher than anticipated temperature is required, or perhaps that steric hindrance of the bromo-parent precursor **15** with the bulky TPP somehow prevented the final nucleophilic reaction.

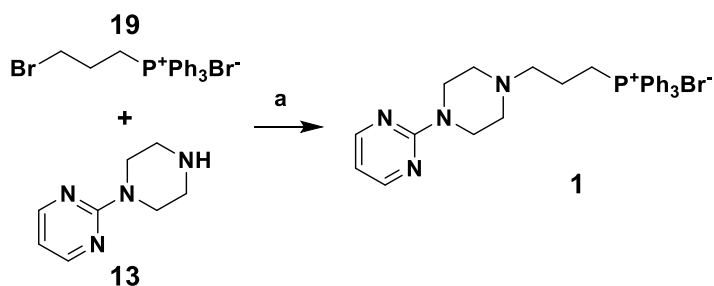


Scheme 5.2. Progress towards the C4-linked JHX-1-TPP (**17**). Reagents and conditions: (a) **7**, **9**, K_2CO_3 , H_2O ; (b) **13**, **14**, K_2CO_3 , PEG-1000, MeCN, reflux; (c) **15**, **16**, MeCN, reflux.

Since the parent scaffold **13** easily reacted with the 1,4-dibromobutane **14**, the possibility of reacting **13** with 4-bromobutyl-TPP salt **18** was investigated to circumvent the failure of TPP to react with **15**. As shown in **Scheme 5.3**, the 4-bromobutyl-TPP salt **18** was formed in 26% yield by refluxing an equimolar ratio of 1,4-dibromobutane **14** and triphenylphosphine **16** under reflux. The 4-bromobutyl-TPP salt **18** then underwent nucleophilic substitution with the parent scaffold **13** in acetonitrile reflux in the presence of K_2CO_3 to form the 4-carbon-linked parent-TPP **17**. This approach was then repeated with the commercially available C3-bromo-TPP **19** and the parent scaffold **13** with the organic base (*N,N*-diisopropylethylamine) at room temperature to yield the initially proposed parent-TPP **1** (**Scheme 4**).



Scheme 5.3. Synthesis of the first C4-linked JHX-1-TPP (**17**). Reagents and conditions: (a) **14**, **16**, toluene, reflux; (b) **13**, **18**, K_2CO_3 , MeCN, reflux.

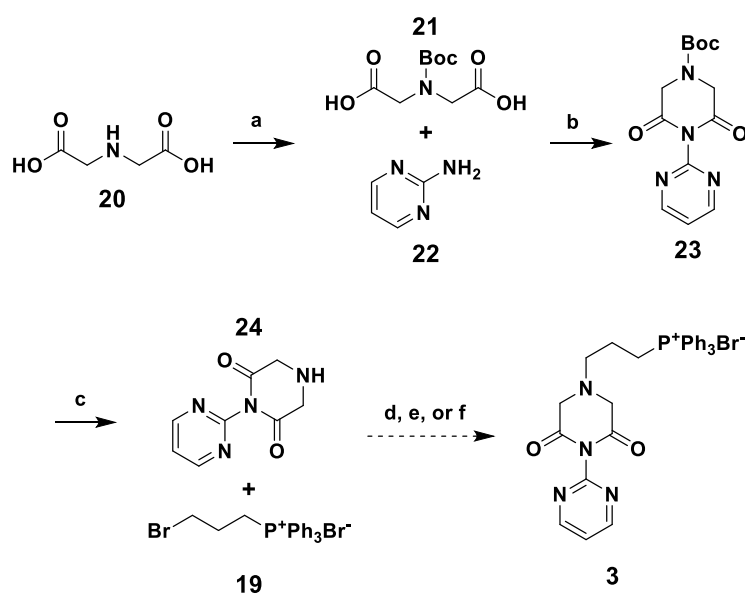


Scheme 5.4. Synthesis of the first C3-linked JHX-1-TPP (**1**). Reagents and conditions: (a) **13**, **19**, DIPEA, MeOH.

5.3.1b Synthesis of the Metal Chelating TPP Compound

The initial desired synthetic approach for making the JHX-3-TPP (**3**), ((3-(3,5-dioxo-4-(pyrimidin-2-yl)piperazin-1-yl)propyl)triphenylphosphonium bromide), is shown in **Scheme 5.5**. This uses a similar final conjugation procedure of the C3-bromo-TPP as shown in **Scheme 5.4**. The di-acid **20** was first Boc-protected to give the Boc-di-acid **21**, which was heated to reflux with 2-aminopyrimidine **22** in toluene to form an amide intermediate *in situ*, followed by ring closure in acetic anhydride (Ac_2O) to form the Boc-protected chelating scaffold **23**. Boc-deprotection of **23** using trifluoroacetic acid in dichloromethane (DCM) gave the chelating precursor **24**. However, the nucleophilic substitution reaction between **24** and 3-bromopropyl-TPP **19** failed to produce JHX-3-TPP (**3**). This was unexpected since the same approach had yielded the JHX-1-TPP (**Scheme 5.4**). It is assumed that in this nucleophilic substitution, the hydrogen from the secondary amine on **24** is first deprotonated by a base (DIPEA), which turns the secondary amine into a strong nucleophile. This amine then attacks the electron-poor carbon adjacent to the bromine on **19**. Because the bromine is the better leaving group during the transition state of this reaction, it eliminates to give product **3**. This formation of product **3** was not

observed because this reaction may also have a high activation energy. No product was formed as indicated by TLC. The base was then removed, thinking that the base may somehow preferentially interact with the 3-bromopropyl-TPP. No product formation was again observed, indicating that the base was not the factor. The reaction was repeated using a higher boiling solvent and sodium hydride, an even stronger base than DIPEA. Again, no product was formed (reflux, up to 72 hours). Since this reaction worked with the amine **13** but failed with the amine **24**, the presence of the 2,6-carbonyl groups may possibly affect the reactivity of the 4-amino group in the piperazine ring [26]. Therefore, an alternate approach will have to be investigated.

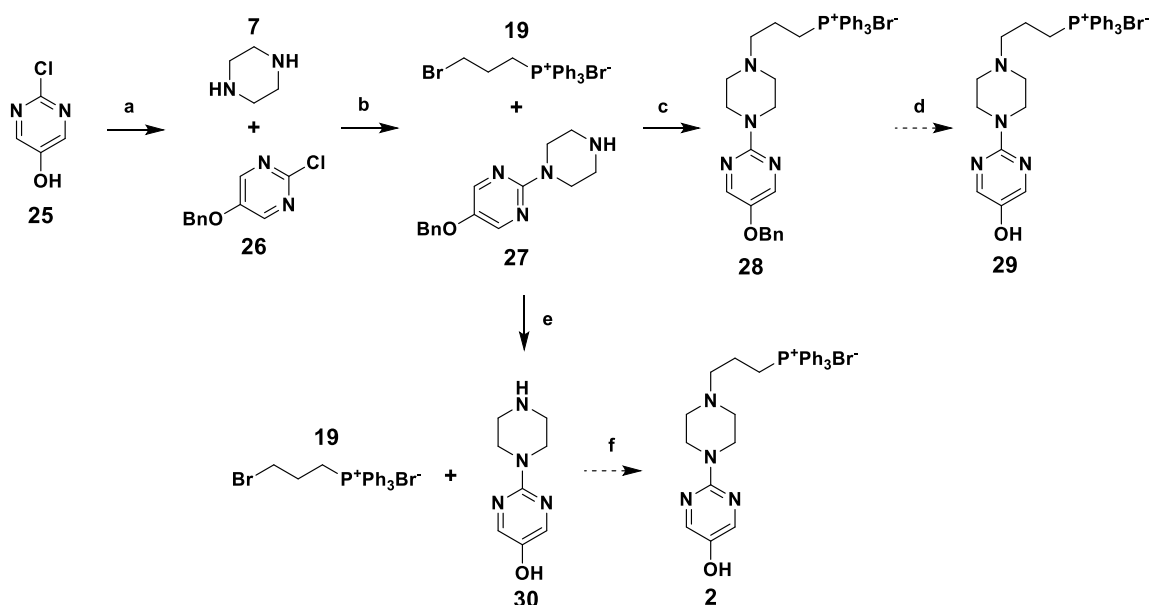


Scheme 5.5. Progress towards the C3-linked JHX-3-TPP (**3**). Reagents and conditions: (a) **20**, Boc_2O , NaOH , Dioxane, H_2O ; (b) **21**, **22**, toluene, Ac_2O , reflux; (c) **23**, TFA, DCM; (d) **24**, **19**, DIPEA, MeOH, reflux; (e) **24**, **19**, toluene, reflux; (f) **24**, **19**, NaH , toluene, reflux.

5.3.1c Progress towards the Free Radical Scavenging TPP Compound

The initial synthetic approach for the JHX-2-TPP, (3-(4-(5-hydroxypyrimidin-2-yl)piperazin-1-yl)propyl)triphenylphosphonium bromide, is shown in **Scheme 5.6**. This approach is similar to the initial route of the JHX-1-TPP (**Scheme 5.3**) where the scaffold is first formed, followed by the nucleophilic substitution of the C3-bromo-TPP and subsequent aryl O-benzyl deprotection to give the final product **2**. Following the benzyl protection of commercially available chloro-alcohol **25** to give the chloro-benzyl **26**, its nucleophilic aromatic substitution with piperazine **7** yielded the scavenging scaffold **27**. The nucleophilic substitution of **27** to the 3-bromopropyl-TPP **19** yielded the scavenging-benzyl **28**. The debenylation was assumed to proceed similar to that of the parent precursor. However, similar to that of the parent precursor **10**, various attempts at debenylation were unsuccessful. Since it has been reported that the presence of phosphorus in **28** can poison the Pd catalyst [27-29], an alternate approach for the synthesis of **2** was investigated. The literature suggests that, in the presence of both an N-H and an O-H group on a compound, the reaction can be modified to selectively N-alkylate or O-alkylate based on the polarity of the solvent. Reactions conducted in more polar solvents are more likely to yield the N-alkylated product [30]. Thus, the O-benzyl group was deprotected from the scavenging scaffold **27** according to Ito [31] to give the conjugated amino-alcohol **30**, which was subsequently subject to nucleophilic substitution under conditions reported to selectively yield the N-alkylated product (aqueous methanol). TLC monitoring and mass spectrum analysis indicated product formation ($m/z = 562.4$), and $^1\text{H NMR}$ suggested that the reaction yielded a mixture which contained the desired product **2**. 5% MeOH/DCM was identified as the best mobile phase for purification by silica gel chromatography, but no final product could be isolated from column chromatography. Instead, a mixed fraction was obtained containing both the desired

product **2** and a di-substituted byproduct (triphenyl(3-(4-(5-(3-(triphenylphosphonio)propoxy)pyrimidin-2-yl)piperazin-1-yl)propyl)phosphonium bromide). Purification was then attempted first using 20% EtOH/DCM column elution, followed by a 100% EtOH elution, but the product was not successfully isolated. The stationary phase was then changed from silica to alumina, and again the purification attempts were unsuccessful at isolating the desired compound **2**. Due to this unsuccessful approach, attention was re-directed towards the JHX-4-TPP while the synthetic approach towards the JHX-2-TPP was re-evaluated.

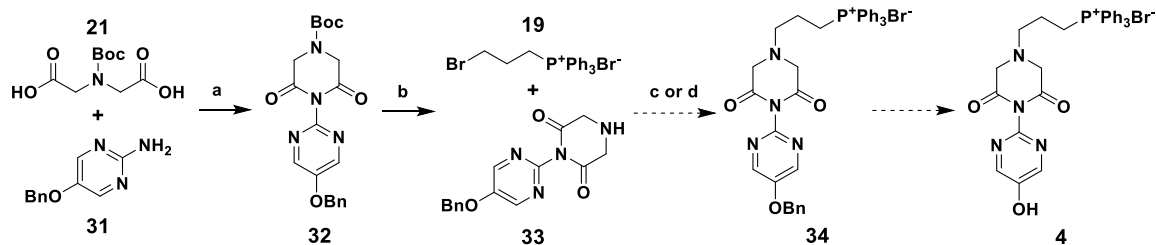


Scheme 5.6. Progress towards the C3-linked JHX-2-TPP (**2**). Reagents and conditions: (a) **25**, BnBr, K₂CO₃, MeCN; (b) **26**, **7**, Et₃N, toluene, reflux; (c) **27**, **19**, MeOH, H₂O; (d) **28**, H₂, Pd(OH)₂/C, EtOAc/EtOH; (e) **27**, H₂, Pd(OH)₂/C, EtOAc/EtOH; (f) **30**, **19**, MeOH, H₂O.

5.3.1d Progress towards the Multifunctional Antioxidant TPP Compound

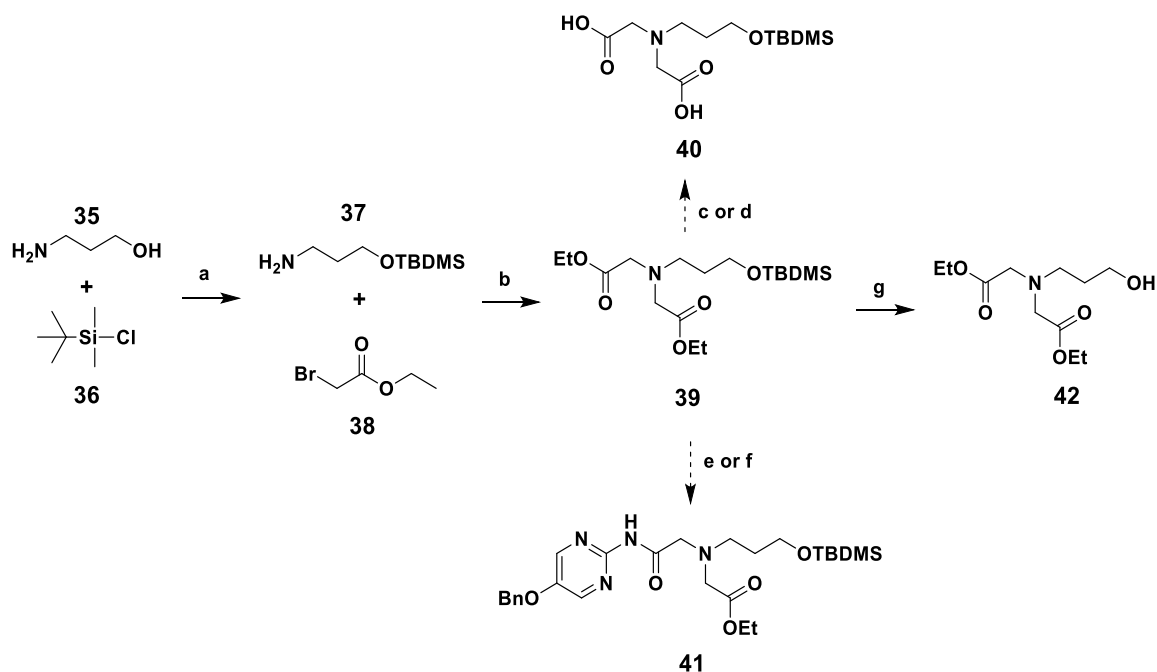
The initial desired synthetic approach towards the JHX-4-TPP, (3-(4-(5-(3-(triphenylphosphonio)propoxy)pyrimidin-1-yl)-3,5-dioxopiperazin-1-yl)-propyl)triphenylphosphonium bromide, is

shown in **Scheme 5.7**. This follows a similar approach for the synthesis of JHX-3-TPP in **Scheme 5.5**. The Boc-di-acid **21** was heated to reflux with 2-amino-5-benzyloxypyrimidine **31** in toluene to form an amide intermediate *in situ*, followed by ring closure in acetic anhydride (Ac_2O) to give the Boc-protected MFAO-benzyl **32**. Boc-deprotection of **32** using trifluoroacetic acid in DCM gave the MFAO-benzyl-precursor **33**. The nucleophilic substitution between the CHL-precursor **24** and C3-bromo-TPP **19** did not give the JHX-3-TPP (**3**) (**Scheme 5.5**). Since the presence of the carbonyls on the top piperazine ring appeared to alter the amine reactivity, perhaps the presence of the O-benzyl group could also alter the reactivity of the molecule. The nucleophilic substitution between the 3-bromopropyl-TPP and the MFAO-benzyl-precursor **33** was conducted and also found to be unsuccessful as indicated by TLC monitoring. In a similar fashion to the approaches described for the synthesis of JHX-3-TPP, higher boiling solvents such as toluene were also used to overcome the activation energy of the reaction. The reactions were run under reflux conditions and monitored by TLC for 5 days without success. Since microwave-assisted synthesis is an alternate, convenient method of conducting high temperature and pressure refluxes, it was performed using both DMF and toluene. Again, no product was observed and only starting material was obtained. These results provided further evidence that suggests that the reactivity of this secondary amine is significantly reduced by the presence of the carbonyl groups, which prevents the nucleophilic substitution from occurring.



Scheme 5.7. Progress towards the C3-linked JHX-4-TPP (**4**). Reagents and conditions: (a) **21**, **31**, toluene, Ac₂O, reflux; (b) **32**, TFA, DCM; (c) **19**, **33**, NaH, THF, reflux; (d) **19**, **33**, CsCO₃, DMF, MW for 30 minutes.

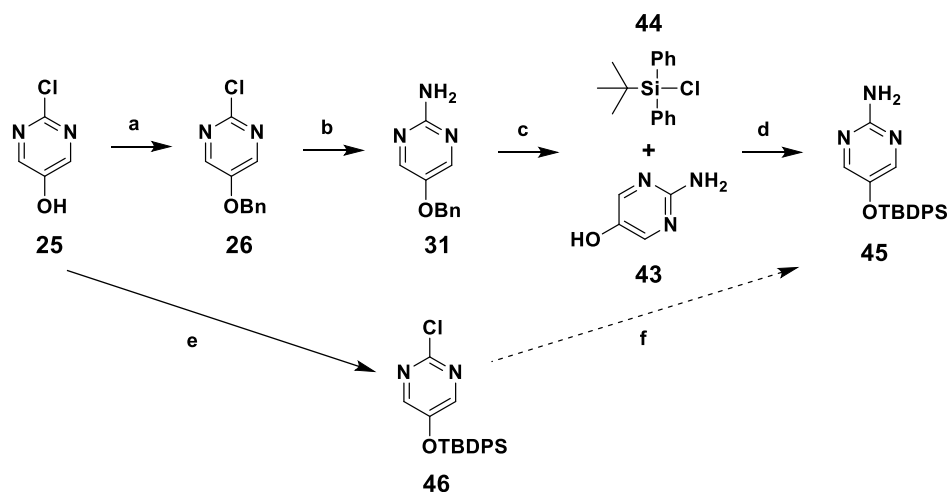
Both **Scheme 5.5** and **Scheme 5.7** provide evidence that the secondary amine precursors (**24** and **33**) are unreactive with the 3-bromopropyl-TPP **19**. Therefore, an alternate approach was required. Instead of starting with the di-acid **20** or the Boc-di-acid **21**, the new approach started with the amine already linked to an alcohol (**Scheme 5.8**). Unlike with the JHX-1-TPP where it was demonstrated that the O-benzyl deprotection did not proceed (**Scheme 5.1**), the more labile *tert*-butyldimethylsilyl (TBDMS) O-protecting group was employed [32]. The amino-alcohol **35** was protected with TBDMS **36** to give TBDMS-amine **37**, followed by the di-nucleophilic substitution with ethyl bromoacetate **38** to obtain the di-ester **39**. Saponification of di-ester **39** under either standard base-catalyzed conditions with NaOH (6 eq.), or milder conditions using trimethyltin hydroxide (2.5 eq.) [33], did not yield the di-acid **40**; only the cleaved TBDMS group was recovered. Direct formation of the amide **41** was next attempted by refluxing the di-ester **39** with 2-amino-5-benzyloxy pyrimidine (**31**) in the presence or absence of K₂CO₃, but this was also unsuccessful. Finally, the saponification was conducted using acid-catalyzed conditions which yielded the O-deprotected di-ester alcohol **42**. This approach suggested that this approach is feasible, however a more stable protecting group is required.



Scheme 5.8. Alternate MFAO-TPP synthesis using the TBDMS protecting group. Reagents and conditions: (a) **35**, **36**, DIPEA, DCM; (b) **37**, **38**, K_2CO_3 , KI, MeCN; (c) **39**, NaOH, H_2O , THF; (d) **39**, Me_3SnOH , DCE, 70 °C; (e) **39**, **31**, K_2CO_3 , MeCN, reflux; (f) **39**, **31**, toluene, reflux; (g) **39**, 12M HCl, EtOH.

At this point in the JHX-4-TPP synthesis, the empirical evidence indicates that neither the benzyl nor the TBDMS protecting groups are optimal. Because the silyl protecting groups are generally easier to work with and are more labile, one of the most stable silyl protecting groups, the *tert*-butyldiphenylsilyl group (TBDPS), was used to protect the hydroxyls in both the top ring and bottom ring. The TBDPS group is reported to have a higher stability in both acidic and basic conditions compared to the TBDMS group, which suggests it may survive saponification of the di-ester and the acetic anhydride reflux ring closure [32]. The synthesis of the TBDPS-protected amino bottom ring is shown in **Scheme 5.9**. The chloro-alcohol **25** was benzyl protected to give the chloro-benzyl **26**. The initial synthesis of chloro-benzyl **26** to amino-benzyl **31** according to Jin [1] is a low-yielding multi-step process. This synthesis was improved to a one-pot reaction by using a high-temperature, high-pressure reaction vessel containing compound

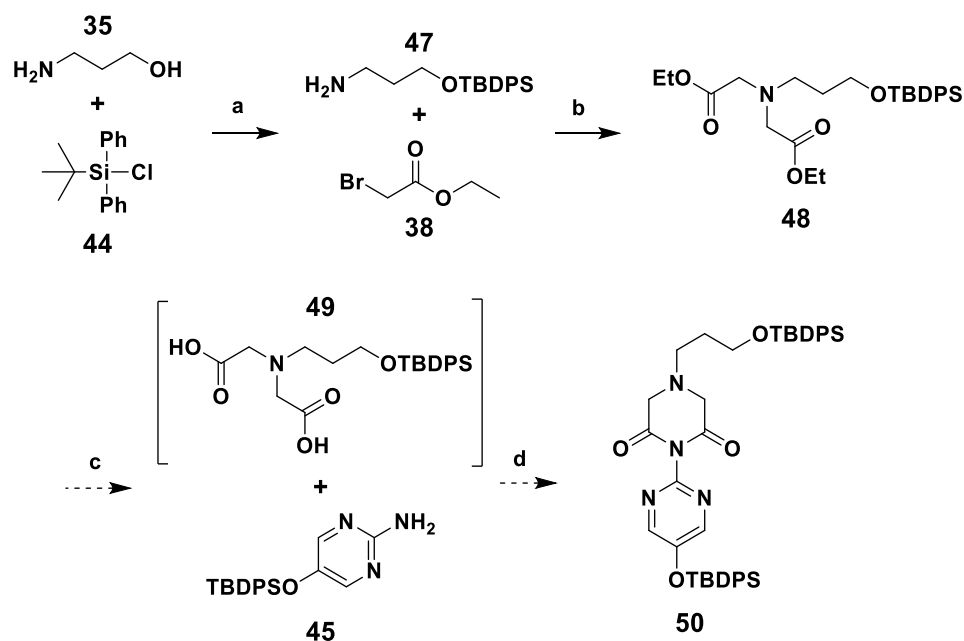
26 dissolved in EtOH with 30% NH₄OH and EtOH. High temperature is necessary for the activation of the nucleophilic aromatic substitution, but these conditions also result in the phase-transition of ammonia to the gaseous phase from liquid ammonium hydroxide. Gaseous ammonia cannot participate in the nucleophilic aromatic substitution, which is why the simultaneous high temperature and pressure of the Parr reactor is advantageous because it forces gaseous ammonia back in the liquid phase to drive the reaction forward according to Le Chatelier's Principle [34]. The amino-benzyl **31** was deprotected by hydrogenolysis with Pearlman's catalyst (Pd(OH)₂/C) to form the aryl amino-alcohol **43**, which was subsequently protected with TBDPS **44** to form the aryl amino-TBDPS **45**. The TBDPS group did not survive the nucleophilic aromatic substitution reaction in the Parr reactor, so the direct conversion of the chloro-TBDPS **46** to the aryl amino-TBDPS **45** is not possible.



Scheme 5.9. Synthesis of the bottom ring intermediates for the MFAO synthesis. Reagents and conditions: (a) **25**, BnBr, K₂CO₃, MeCN; (b) **26**, NH₄OH, EtOH, Parr reactor; (c) **31**, H₂, 20% Pd(OH)₂/C, EtOAc, EtOH; (d) **43**, **44**, DIPEA, DCM; (e) **25**, **44**, DIPEA, DCM; (f) **46**, NH₄OH, EtOH, Parr reactor, 120 °C.

The protection of the bottom ring with O-TBDPS initiated the new approach towards the synthesis of JHX-4-TPP (**4**), shown in **Scheme 5.10**. Unlike the TBDMS

group, which was used in **Scheme 5.8**, the more stable TBDPS group was also employed to protect the top ring alkyl alcohol. The amino-alcohol **35** was protected with TBDPS **44** to give the TBDPS-amine **47**, which subsequently underwent di-nucleophilic substitution with ethyl bromoacetate **38** to give the TBDPS-protected di-ester **48**. The base-catalyzed saponification of di-ester **48** could not be isolated. TLC and mass spectrum analysis ($m/z = 429.3$) indicated in the reaction mixture formation of product **49**, but the compound was unable to be properly characterized by ^1H NMR. Since the TLC and mass spectrum analysis indicated that **49** was present in the reaction mixture, ring closure with the intermediate **49** was conducted. No product was identified and only the TBDPS and the aryl amino-alcohol **43** were recovered, suggesting that acetic anhydride may have deprotected the TBDPS groups.



Scheme 5.10. Progress towards the MFAO-TPP with the TBDPS protecting group. Reagents and conditions: (a) **35**, **44**, DIPEA, DCM; (b) **47**, **38**, K_2CO_3 , KI, MeCN; (c) **48**, NaOH, THF, H_2O ; (d) **49**, **45**, toluene, Ac_2O , reflux.

5.3.2 A New Approach to the TPP compounds using an Ester Linkage

Due to the problems encountered in the unsuccessful synthesis of compounds **2-4**, in which direct conjugation of the alkyl linkage to the secondary amine were employed, the use of an alternate linker was investigated [35, 36]. This not only simplified the chemical approach towards the synthesis of the JHX-TPP series, but the ester linkage could potentially be more advantageous by increasing the ease of metabolism. The structures of these new JHX-TPP-Esters are shown in **Figure 5.2**.

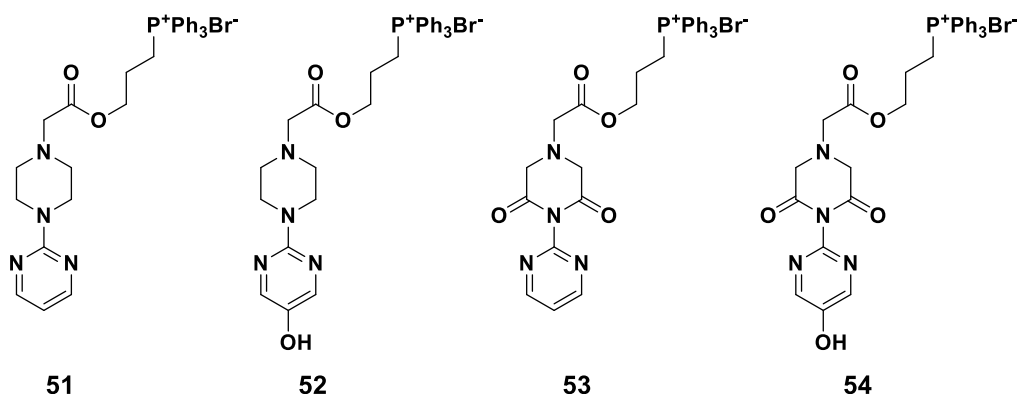
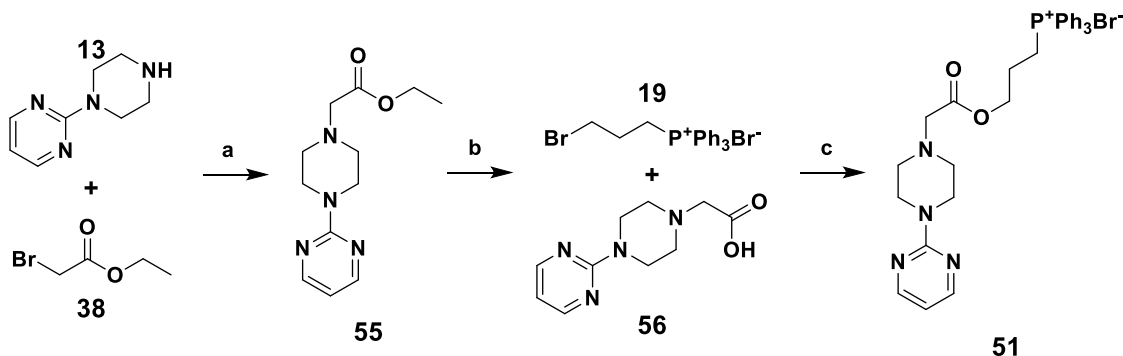


Figure 5.2. Proposed structures of the novel JHX-TPP-Ester class of compounds. Compound **51** shows the structure of the JHX-1-TPP-Ester ((triphenyl(3-(2-(4-(pyrimidin-2-yl)piperazin-1-yl)acetoxyl)propyl)phosphonium bromide), compound **52** shows the structure of the JHX-2-TPP ((3-(2-(4-(5-hydroxypyrimidin-2-yl)piperazin-1-yl)acetoxyl)propyl)triphenylphosphonium bromide), compound **53** shows the structure of the JHX-3-TPP ((3-(2-(3,5-dioxo-4-(pyrimidin-2-yl)piperazin-1-yl)acetoxyl)propyl)triphenylphosphonium bromide), and compound **54** shows the structure of the JHX-4-TPP ((3-(2-(4-(5-hydroxypyrimidin-2-yl)-3,5-dioxopiperazin-1-yl)acetoxyl)propyl)triphenylphosphonium bromide).

5.3.2a Development of the JHX-1-TPP-Ester

Synthesis of the parent scaffold ester linked to the TPP is shown in **Scheme 5.11**. The nucleophilic substitution of parent scaffold **13** and ethyl bromoacetate **38** gave the parent ethyl ester **55**. The acid-catalyzed saponification of **55** yielded the product parent

acid **56**. Nucleophilic substitution of parent acid **56** with the 3-bromopropyl-TPP **19** yielded the JHX-1-TPP-Ester **51**.

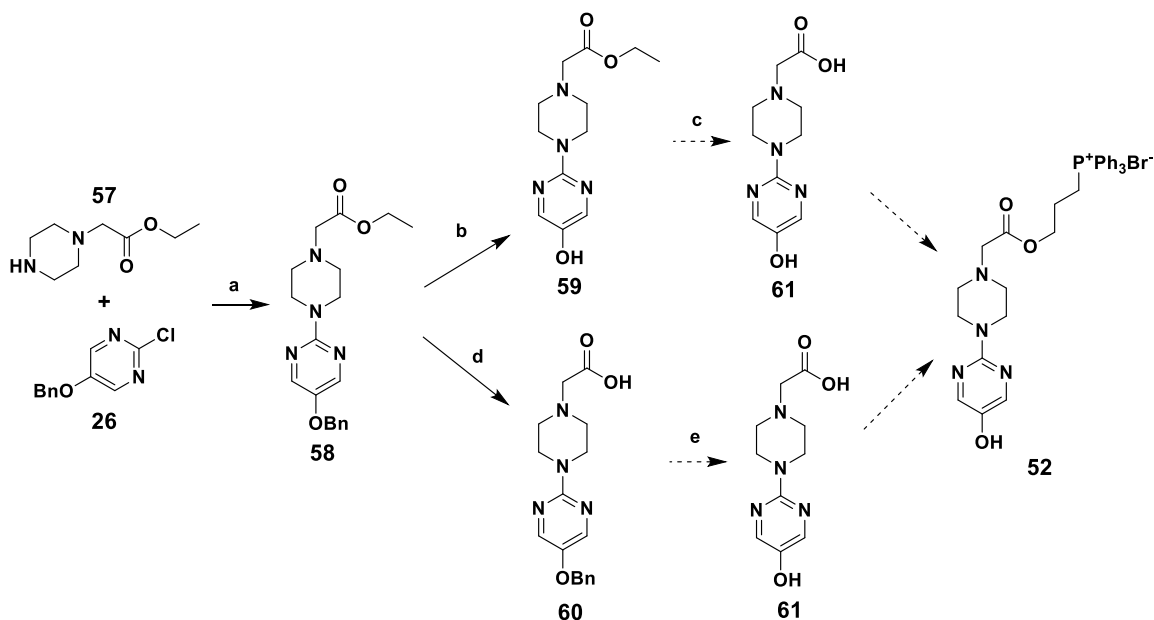


Scheme 5.11. Synthesis of the JHX-1-TPP-Ester (**51**). Reagents and conditions: (a) **13**, **38**, K_2CO_3 , KI, MeCN; (b) **55**, 6M HCl, H_2O ; (c) **56**, **19**, K_2CO_3 , KI, DMF.

5.3.2b Progress towards the JHX-2-TPP-Ester

The synthesis of the JHX-2-TPP-Ester, as shown in **Scheme 5.12**, is similar to that of the JHX-1-TPP Ester (**Scheme 5.11**). The nucleophilic aromatic substitution between commercially available piperazine ethyl ester **57** and chloro-benzyl **26** gave the ester-benzyl **58**. Modifications to this compound were approached two different ways. First, the benzyl protecting group was removed to give the ester-alcohol **59**, but the subsequent base-catalyzed or acid-catalyzed saponification failed to yield the acid-phenol **61**. The second approach, conducted by Mr. Theodor Woolman in the Kador Laboratory, utilized a base-catalyzed saponification of **58** to obtain the benzyloxy acid **60**, but its subsequent O-debenzylation failed to yield the phenolic acid **61**. Both TLC and mass spectrum analysis ($m/z = 238.3$) indicated product formation, however characterization by 1H NMR was inconclusive. The purification of this mixture using both silica and alumina gel chromatography with highly polar solvent systems such as 20% EtOH/DCM and 100%

EtOH were both unsuccessful. Purification by reverse-phase HPLC on a C18 column using 75% aqueous methanol was also unsuccessful. Identifying the contaminants with the product has yet to be elucidated, and further investigations are required.

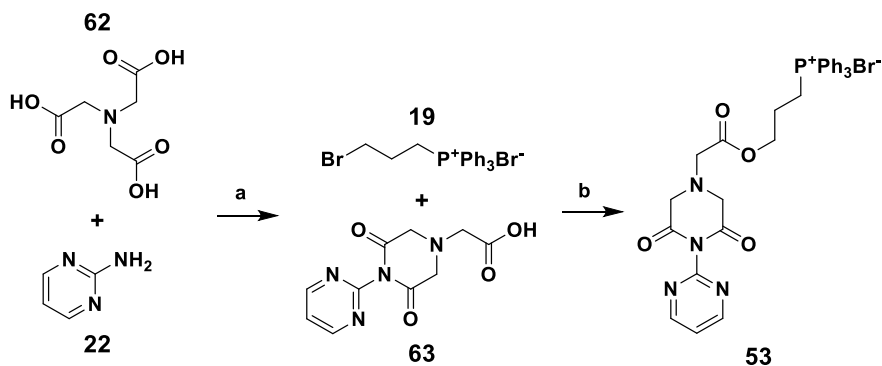


Scheme 5.12. Progress towards the JHX-2-TPP-Ester (**52**). Reagents and conditions: (a) **26**, **57**, Et₃N, toluene, reflux; (b) **58**, H₂, 20% Pd(OH)₂/C, MeOH; (c) **59**, 6M HCl, H₂O, 70 °C; (d) **58**, NaOH, H₂O, THF; (e) **60**, H₂, 20% Pd(OH)₂/C, MeOH.

5.3.2c Development of the JHX-3-TPP-Ester

The approach to synthesizing JHX-3-TPP-Ester (**53**) is outlined in **Scheme 5.7**. To circumvent the problem of the poor reactivity of the 4-amino group in the piperazine-2,6-dione **33** and the potential ring opening of ethyl 2-(3,5-dioxo-4-phenylpiperazin-1-yl)acetate under both acid and base removal of the ethyl ester, a scheme employing commercially available nitrilotriacetic acid **62** was used. As shown in **Scheme 5.13**, refluxing nitrilotriacetic acid **62** in pyridine with acetic anhydride formed an *in situ* anhydride according to Burns [37] that reacted with the 2-aminopyrimidine **22** to give acid

63. The nucleophilic substitution of **63** with 3-bromopropyl-TPP **19** yielded the JHX-3-TPP-Ester **53**.



Scheme 5.13. Synthesis of the JHX-3-TPP-Ester (**53**). Reagents and conditions: (a) **62**, **22**, Ac_2O , Pyridine, reflux; (b) **63**, **19**, K_2CO_3 , KI , DMF.

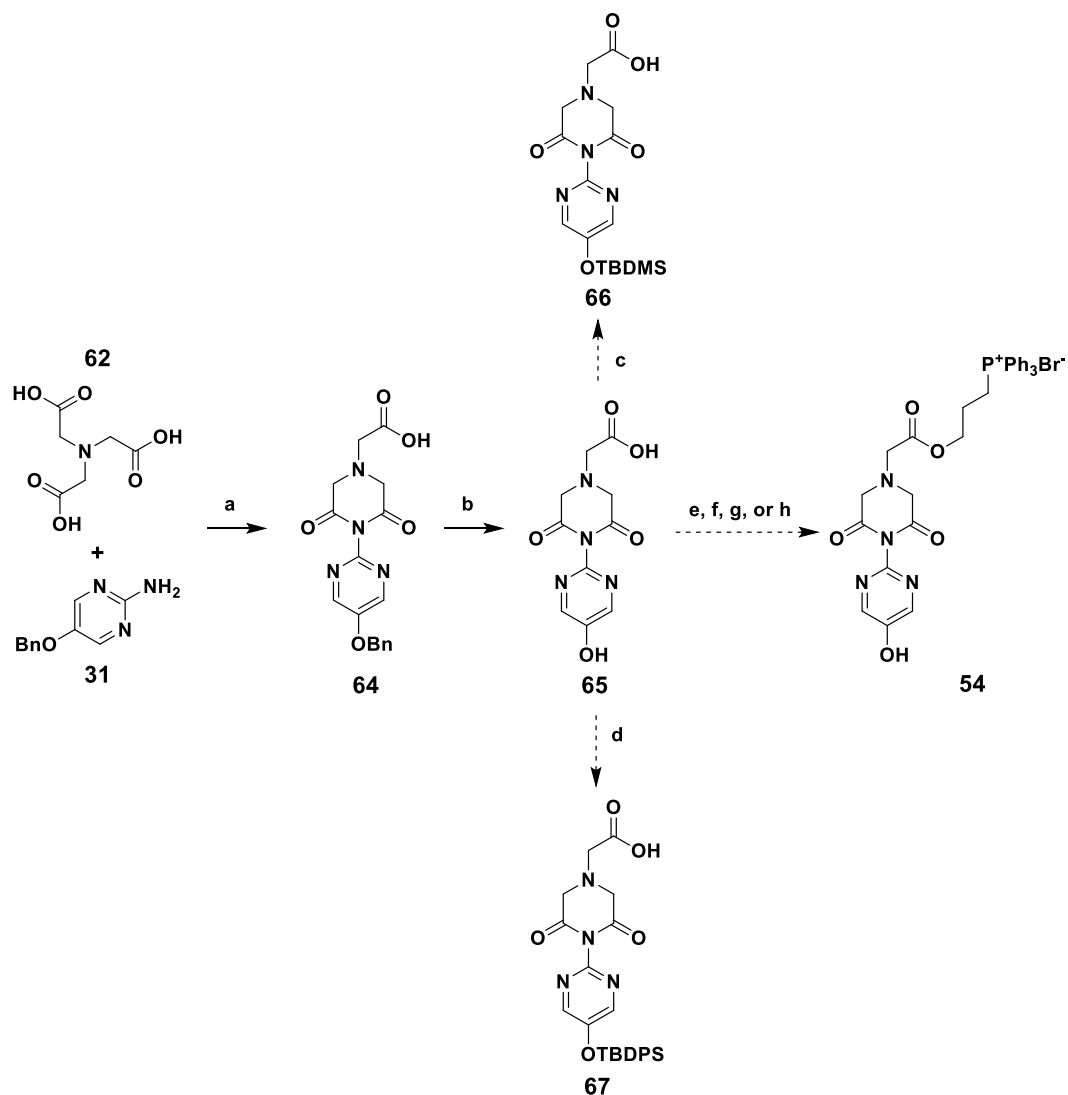
5.3.2d Progress towards the JHX-4-TPP-Ester

After the successful synthesis of the JHX-1-TPP-Ester and the JHX-3-TPP-Ester, attention was turned to the synthesis of the multifunctional analog JHX-4-TPP-Ester **54**. The anhydride of nitrilotriacetic acid **62** was formed *in situ* under reflux with acetic anhydride in pyridine according to Burns [37], followed by reaction with 2-amino-5-benzoxypyrimidine **31** to yield the benzoyloxy-protected pyrimidine **64**. The O-debenzylation of **64** with hydrogen and Pearlman's catalyst ($\text{Pd}(\text{OH})_2/\text{C}$) gave the phenolic acid **65**. To prevent any undesired side products during the nucleophilic substitution to 3-bromopropyl-TPP **19**, protection of the phenol with a labile OH protecting group was investigated [38]. Since the final conjugation of **65** to **19** is not conducted under harsh conditions, and since the silyl groups do not protect carboxylic acids, this approach was used to maximize the ability to obtain the final JHX-4-TPP-Ester (**54**). However, both the reaction of the phenolic acid **65** with TBDMS using Et_3N or DIPEA in DCM to give **66**, and

the reaction of the phenolic acid **65** with TBDPS using Et₃N or DIPEA in DCM to give **67**, failed. Because these protection attempts failed, attempts were made to utilize the significant differences in the pKa values between the carboxylic acid and phenolic functional groups. Since the pKa of the carboxylic acid is ca. 5 and the pKa of the phenol is ca. 9-10, it was postulated that using weak bases would help drive the reaction towards the ester formation and yield the desired product **54**. To do this, K₂CO₃ (pKa ~ 10.3) was added to a stirring mixture of phenolic acid **65** in DMF and was stirred for ca. 1 hour to ensure the full deprotonation of the carboxylic acid. In theory, the carbonate from K₂CO₃ should preferentially strip the proton off of the carboxylic acid, yielding the carboxylate anion and bicarbonate in solution which would not affect the phenolic hydrogen. The resonance on the carboxylate stabilizes the negative charge, which should allow for the nucleophilic attack to the 3-bromopropyl-TPP **19** and yield the JHX-4-TPP **54**. Evidence collected by TLC, mass spectrum analysis (*m/z* = 569.2), and the presence of anticipated ¹H NMR peaks all indicated product formation. However, purification attempts using silica gel chromatography with 20% EtOH/DCM as eluent yielded only a mixed fraction containing a mixture of di-substituted side product ((3-((2-(2,6-dioxo-4-(2-oxo-2-(3-(triphenylphosphonio)propoxy)ethyl)piperazin-1-yl)pyrimidin-5-yl)oxy)propyl)triphenylphosphonium bromide) and desired product **54** which co-eluted. Chromatography was repeated using a longer column to increase the theoretical plates and better resolve the mixed fraction, but again only the co-eluting mixture was obtained. The reaction was then repeated using a weaker base, KHCO₃ (pKa ~ 6), but the TLC, mass spectrum analysis (*m/z* = 436.3), and ¹H NMR indicated only formation of the undesired di-substituted side product. Using pyridine, an even weaker base, yielded no reaction and only starting material was recovered. As an alternative method, a Fischer esterification using a catalytic amount of acid to catalyze the ester formation between the phenolic acid **65** and 3-bromopropyl-TPP **19** was conducted [39, 40]. Reflux for 96 hours in a dean-stark trap

yielded no product. Just as observed with the JHX-2-TPP-Ester (**Scheme 5.12**), these results were unexpected. Since the pKa's of various pyrimidinols have not been well documented, so it is possible that the pKa of the pyrimidinol ring is not as similar to the phenol as anticipated. For example, Nam and colleagues report the pKa's of compounds similar to the bottom ring of the MFAO series, where the pKa of *N*-(4-hydroxyphenyl)acetamide is ca. 9.8, the pKa of 2-(dimethylamino)pyrimidin-5-ol is ca. 8.2, and the pKa of *N*-(5-hydroxypyrimidin-2-yl)acetamide is ca. 5.9, suggesting that the pyrimidinol of the acid-phenol **65** is ca. 1000x more acidic than of a phenol [41]. The properties of phenolic acid **65** should be further investigated to develop a better synthetic approach towards the JHX-4-TPP-Ester (**54**).

In summary, three novel JHX-1-TPP compounds were synthesized as shown in **Schemes 5.3, 5.4, and 5.11**, and one novel JHX-3-TPP was synthesized as shown in **Scheme 5.13**. These developed schemes are shorter, higher-yielding, and greener compared to the initially proposed schemes towards the development of the JHX-TPP series. Additionally, many novel intermediates have also been successfully synthesized which may be used as scaffolds for future novel JHX-based compound series.



Scheme 5.14. Progress towards JHX-4-TPP-Ester (**54**). Reagents and conditions: (a) **62**, **31**, Ac₂O, pyridine, reflux; (b) **64**, H₂, Pd(OH)₂/C, acetone; (c) **65**, **36**, DIPEA, DCM; (d) **65**, **44**, DIPEA, DCM; (e) **65**, **19**, K₂CO₃, DMF; (f) **65**, **19**, KHCO₃, DMF; (g) **65**, **19**, KI, pyridine, DMF; (h) **65**, (3-hydroxypropyl)triphenylphosphonium bromide, (cat.) 12M HCl, DMF.

5.3.3 Preliminary Evaluation of HEI-OC1 Cells

Since the MFAO HK-2 has recently been shown to prevent hearing loss by protecting the cochlear hair cells [42], the synthesized compounds non-functional JHX-1-TPP (**1**, (3-(4-(pyrimidin-2-yl)piperazin-1-yl)propyl)triphenylphosphonium bromide)) and

the metal chelating HK-2-Benzyl-TPP ((3-(1-(5-(benzyloxy)pyrimidin-2-yl)-2,5-dioxopyrrolidin-3-yl)-propyl)triphenylphosphonium bromide), synthesis not shown), as well as the non-conjugated JHX-series [1], were evaluated in the HEI-OC1 cochlear hair cell line present in our laboratory. To confirm that the non-conjugated compounds JHX-2, JHX-3, and JHX-4 were not cytotoxic to the cells, cell viability was measured using the MTS viability assay. Results of this assay indicated that after 24 hours of exposure to 1 mM of JHX-2, JHX-3, or JHX-4 in FBS-free media, there was no significant difference in cell viability compared to controls (**Figure 5.3**).

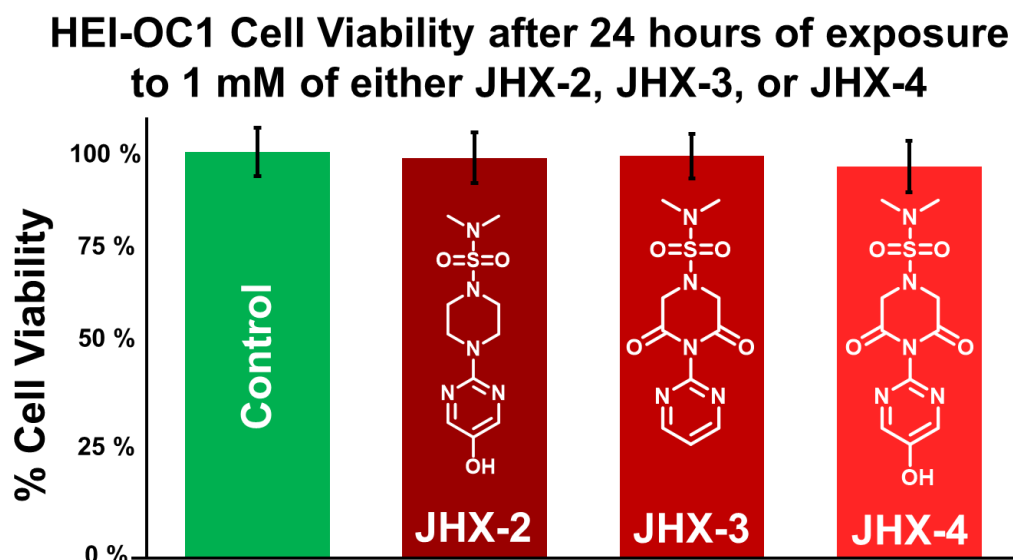
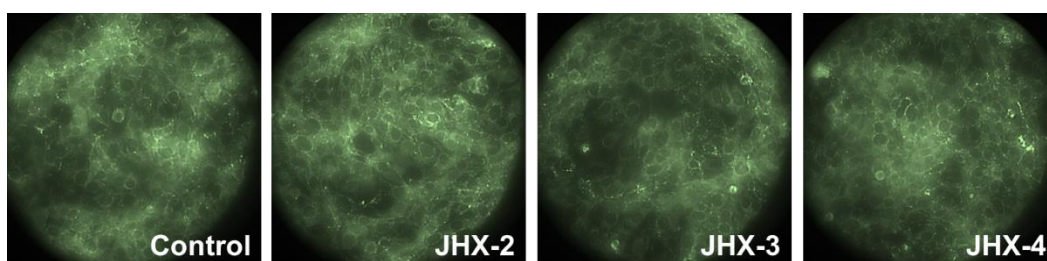


Figure 5.3. HEI-OC1 cytotoxicity with the non-conjugated JHX compounds. HEI-OC1 cell viability, measured by MTS assay, is not significantly affected by exposure to 1 mM of JHX-2, JHX-3, or JHX-4. Statistical significance was determined by ANOVA ($n = 3 \pm SD$).

To assess whether these compounds adversely affected mitochondrial activity, fluorescence measurements were done using the rhodamine-123 dye. Rhodamine-123 is an indicator of mitochondrial membrane potential which indirectly measures mitochondrial activity [43, 44]. After 2 hours of incubation with 1 mM JHX-2, JHX-3, and JHX-4, cells were stained with rhodamine-123 (20 $\mu\text{g}/\text{mL}$). One set of cells was imaged

under a fluorescence microscope, and another set of cells was measured by fluorescence microplate reader. Compared to controls, none of the non-conjugated JHX compounds adversely affected mitochondria activity as indicated by rhodamine-123 staining (**Figure 5.4**).



HEI-OC1 Mitochondria Fluorescence after 2 hours of exposure to 1 mM of either JHX-2, JHX-3, or JHX-4

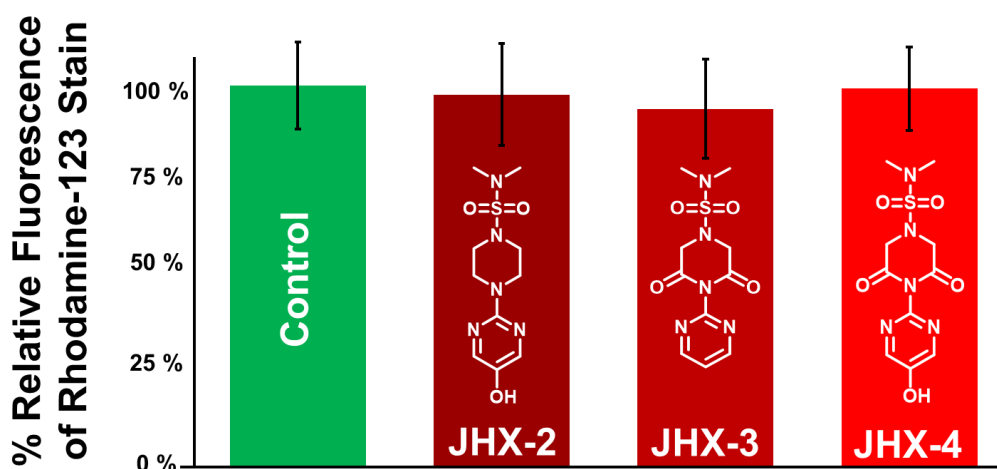


Figure 5.4. HEI-OC1 mitochondriotoxicity study with the non-conjugated JHX compounds. The JHX compounds do not adversely affect mitochondria fluorescence after 2 hours of incubation as measured by rhodamine-123 (20 $\mu\text{g}/\text{mL}$) staining. (Top) Mitochondria fluorescence of HEI-OC1 cells with rhodamine-123 after exposure to 1 mM of JHX-2, JHX-3, or JHX-4 for 2 hours. (Bottom) Fluorescence microplate results of HEI-OC1 cells with rhodamine-123 after exposure to 1 mM of JHX-2, JHX-3, or JHX-4 for 2 hours. No statistically significant differences between treatment groups as determined by ANOVA ($n = 3 \pm \text{SEM}$).

Preliminary cell culture studies with the nonfunctional JHX-1-TPP ((3-(4-(pyrimidin-2-yl)piperazin-1-yl)propyl)triphenylphosphonium bromide) and the metal chelating HK-2-

Benzyl-TPP ((3-(1-(5-(benzyloxy)pyrimidin-2-yl)-2,5-dioxopyrrolidin-3-yl)propyl)triphenylphosphonium bromide) have been conducted using currently available HEI-OC1 cochlear neural cells in our laboratory. The two TPP compounds at concentrations greater than 1 μM rapidly entered the cells, altering the mitochondrial membrane potential so that the uptake of rhodamine-123 stain and cell viability was reduced. **Figure 5.5** shows a dose response study indicating at doses below 1 μM , the 24-hour culture resulted in maintained cell viability in a dose-dependent manner. Similarly, **Figure 5.6** shows that mitochondrial function, measured by rhodamine-123 fluorescence staining, was also maintained in a dose dependent manner. Importantly, there was no difference in cell viability between the JHX-1-TPP and the HK-2-CHL-TPP, indicating that the presence of a chelator within the mitochondria did not lead to mitochondrial dysfunction. This concurs with reports that two new TPP-hydroxybenzoic acid derivatives with antioxidant and iron chelating properties demonstrate low toxicity and that the presence of the chelating moiety does not adversely affect mitochondria function [45].

Dose Response of 1 nM, 10 nM, 100 nM, 1 μ M, or 10 μ M of either JHX-1-TPP or HK-2-Benzyl-TPP on HEI-OC1 Cell Viability

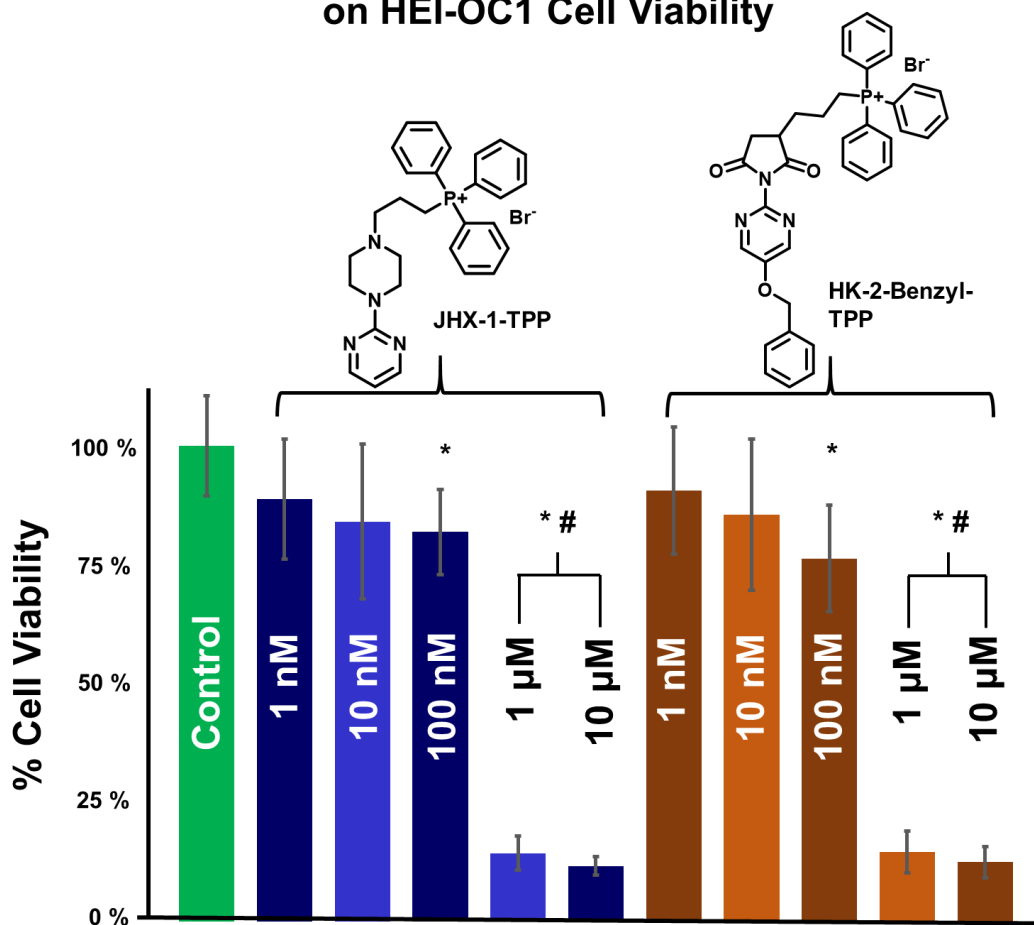
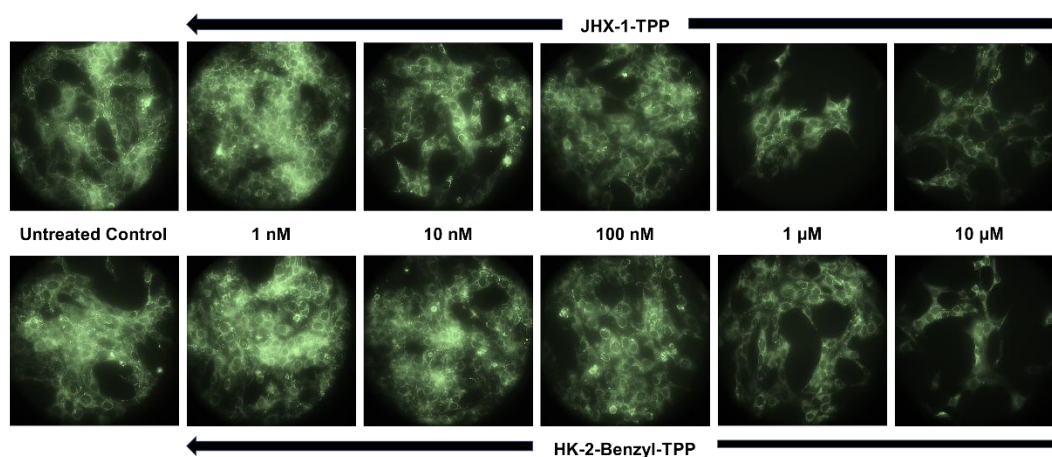


Figure 5.5. Cell viability of HEI-OC1 cells after 24 hours of culture with or without the JHX-1-TPP or HK-2-Benzyl-TPP. Cells were seeded into 96-well plates and incubated at 33 °C and 10% CO₂. Viability was determined using Calcein-AM staining, measured by fluorescence plate reader with results normalized to untreated control cells. The results show that the presence of the chelating group on the HK-2-Benzyl-TPP does not significantly alter cell viability compared to the nonfunctional JHX-1-TPP parent. Statistical significance was identified using ANOVA followed by Post-Hoc t-test with Bonferroni Correction (* indicates statistical significance compared to untreated control; # indicates statistical significance compared to all other treatment groups; n = 3, mean \pm SEM).



Dose Response of 1 nM, 10 nM, 100 nM, 1 μ M, or 10 μ M of either JHX-1-TPP or HK-2-Benzyl-TPP on HEI-OC1 Mitochondria Fluorescence

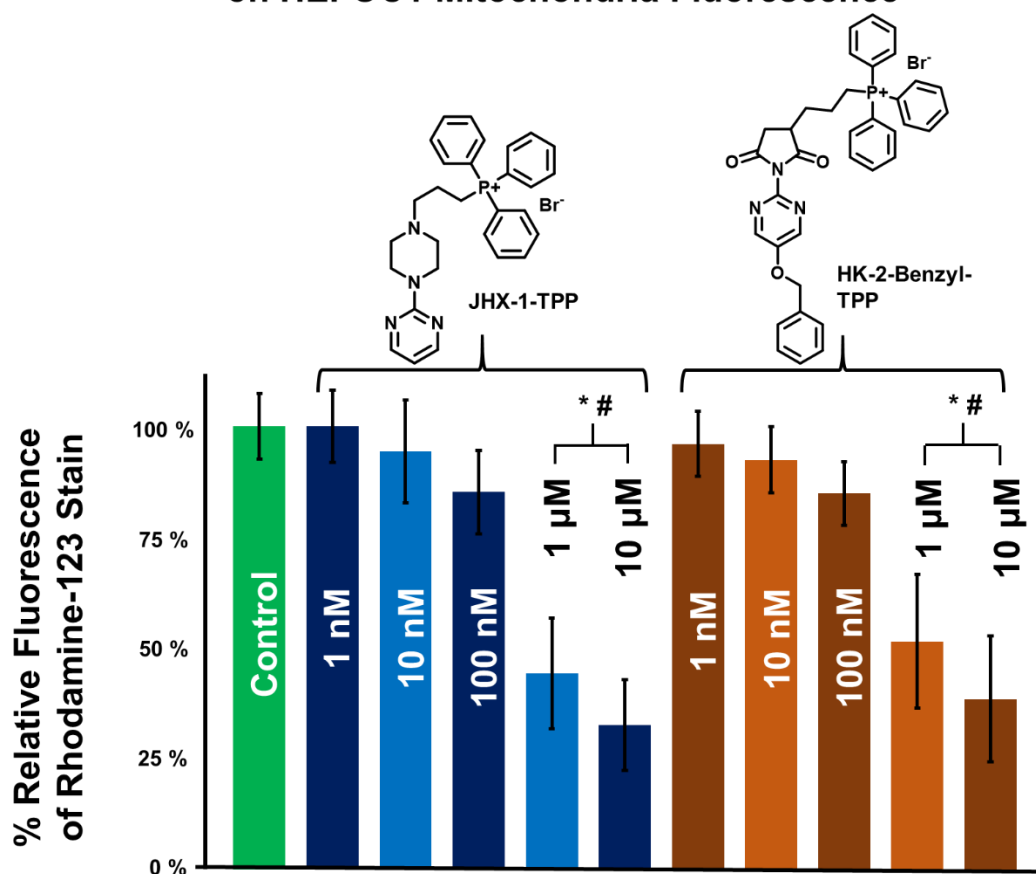


Figure 5.6. Mitochondria membrane potential of HEI-OC1 cells after 8 hours of culture with or without the JHX-1-TPP or HK-2-Benzyl-TPP. Cells were seeded into 96-well plates and incubated at 33 °C and 10% CO₂. Mitochondria membrane potential was determined using rhodamine-123 staining. (Top) Imaged were taken with a fluorescence microscope, and (Bottom) fluorescence was quantified by fluorescence plate reader with results

normalized to untreated control cells. The results indicate that the compounds do not adversely affect the mitochondria membrane potential at sub-micromolar concentrations. Statistical significance was identified using ANOVA followed by Post-Hoc t-test with Bonferroni Correction (* indicates statistical significance compared to untreated control; # indicates statistical significance compared to all other treatment groups; n = 3, mean \pm SEM).

A significant loss of the mitochondrial membrane potential impairs oxidative phosphorylation, depleting cells of energy, and inducing cell death. Translocation of protons from the matrix to the intermembrane space to establish the mitochondrial membrane potential is coupled to the electron transport chain [46]. Inhibition of complex I and/or complex II leads to an increase of ROS and a decrease in ATP production which results in mitochondrial dysfunction [47]. The loss of mitochondrial membrane potential, which can be visualized by fluorescent dyes such as Rhodamine-123, is an early marker of cellular apoptosis [48]. The mitochondria membrane potential was evaluated in order to investigate whether the JHX-series compounds or the TPP compounds could perturb mitochondrial function in the HEI-OC1 cells. In **Figure 5.4**, it was shown that incubation of the HEI-OC1 cells with 1 mM of JHX-2, JHX-3, and JHX-4 do not affect fluorescence staining of the mitochondria, suggesting that these compounds are not mitochondriotoxic and do not affect the mitochondria membrane potential. The TPP compounds at concentrations over 1 μ M alter membrane potentials and indicate mitochondrial dysfunction [49]. This has also been seen with MitoQ, a compound currently undergoing clinical studies [50, 51].

The TPP moiety has been identified as an effective cellular and mitochondrial carrier for many small molecules, but little is known about the pharmacological effects and properties of the TPP. The principles of TPP-assisted drug transport across plasma and mitochondria membranes are well-documented, and the mitochondrial targeting of

antioxidants have been of great interest to researchers since they have proven to be a promising therapeutic strategy towards developing more potent antioxidants [52, 53]. Despite the established importance of TPPs, little is known about their effects on cellular bioenergetics [54]. To date, limited studies have assessed the impact of coupling functional molecules to alkyl-TPP moieties. One group examining the effects of 1 μ M concentrations of MitoQ, MitoTempol, and MitoE and found that the alkyl-TPP chains elicited cellular bioenergetic responses consistent with inhibition of oxidative phosphorylation independent of the functional antioxidant group [55]. Others have shown that conjugation of different length carbon chain linkers between TPP to ubiquinol (MitoQ derivatives) affect retention and accumulation of the TPP in the mitochondria. Longer carbon chain linkers achieving a rapid steady state and contribute to rapid decreases in mitochondrial membrane potential [56-58], suggesting that shorter carbon chain linkers may yield less toxic TPP therapeutics.

The extensive accumulation of lipophilic cations within isolated mitochondria at micromolar concentrations, especially approaching millimolar levels, are known to disrupt membrane integrity and impair respiration and ATP synthesis. Ng and colleagues observed that maintaining mitochondrial membrane potential required sub-micromolar concentrations of MitoQ as low micromolar concentrations were observed to decrease respiration of isolated mitochondria [49]. This similar study was reported by Reily and colleagues who showed that 1 μ M of MitoQ caused a 25% decline in the cellular respiration due to an inhibition of oxidative phosphorylation in as little as 2 hours [55]. Likewise, Rogov and colleagues observed that SkQ1 rapidly destroyed the mitochondrial membrane at concentrations between 1-10 μ M [59]. In the present study, low nanomolar concentrations are not shown to negatively affect HEI-OC1 cell viability or the mitochondrial membrane potential (**Figure 5.5** and **5.6**). The explanation for the protective

effects of the examined novel TPP compounds have yet to be elucidated because the mechanisms by which the TPP compounds affect mitochondria are still unknown. Though, a study has suggested that the TPP-based antioxidants directly affect mitochondrial Ca^{2+} homeostasis by interacting with the $\text{Na}^+/\text{Ca}^{2+}$ or $\text{H}^+/\text{Ca}^{2+}$ calcium exchangers, which are implicated in the regulation of mitochondrial dynamics and sensitivity to apoptotic challenges [60], further investigations are required to understand the intricacies of TPP-based antioxidants on mitochondria health.

5.4 Conclusion

Three novel JHX-1-TPP compounds were synthesized as shown in **Schemes 5.3, 5.4, and 5.11**, and one novel JHX-3-TPP was synthesized as shown in **Scheme 5.13**. With these two compounds, these developed schemes are shorter and higher-yielding than the originally proposed synthetic routes towards the TPP compounds. Although the desired compounds were not obtained, several novel intermediates were successfully synthesized which may be used for future JHX-based compound development. The results from the *in vitro* studies on HEI-OC1 cells with the non-conjugated JHX-2, JHX-3, and JHX-4 compounds, as well as the novel synthesized JHX-1-TPP and the HK-2-Benzyl-TPP compounds, show that compounds with Fe, Cu, or Zn chelating potential entering the mitochondria may not adversely affect mitochondrial function at sub-micromolar concentrations and provide evidence that development of the TPP-based MFAOs should be further explored.

5.5 Materials and Methods

5.5.1 Chemistry Procedures

General. All solvents and reagents were obtained from commercial sources. NMR spectra were obtained with a Bruker 500 MHz or 600 MHz spectrometer. Melting points were obtained with the Melting Point Apparatus MPA-120 EZ-Melt (Stanford Research Systems, Sunnyvale, CA). Column chromatography utilized Sigma Aldrich silica gel (70-230 mesh, 60 Å pore size). UV-visible spectra were measured on a Molecular Devices SpectraMax Plus³⁸⁴ microplate spectrophotometer (Molecular Devices, Sunnyvale, CA). Final compound purities were assessed as $\geq 99\%$ and intermediate compound purities were assessed as $\geq 96\%$ by NMR and ESI-MS on a Thermo Finnigan LCQ (Thermo Fisher Scientific, Waltham, MA), and LRMS data was obtained on a Thermo Finnigan LCQ in positive scanning mode.

((3-bromopropoxy)methyl)benzene (6). To a stirred solution of 3-bromopropan-1-ol (25.0 grams, 179.9 mmol) and benzyl bromide (35.0 grams, 204.6 mmol) in 200 mL DMF at $-90\text{ }^{\circ}\text{C}$ was added 60% NaH in mineral oil (8.7 grams, 215.9 mmol) portionwise. Stirring was continued for another 30 minutes at $-90\text{ }^{\circ}\text{C}$ before the mixture was warmed to room temperature over a period of 18 hours. The mixture was quenched with aqueous NH_4Cl (400 mL) and extracted with ether (3 x 300 mL). Combined organics were washed with brine (3 x 200 mL), dried over MgSO_4 , filtered, and concentrated under reduced pressure. The crude material was purified by silica gel chromatography with 15% ether:pentanes, yielding the product as a pale yellow oil in 45% yield. ^1H NMR (500 MHz, CDCl_3) δ 7.35-7.29 (m, 5H), 4.52 (s, 2H), 3.62-3.60 (t, $J = 5.4\text{ Hz}$, 2H), 3.55-3.52 (t, $J = 7.2\text{ Hz}$, 2H), 2.16-2.12 (m, 2H).

1-(3-(benzyloxy)propyl)piperazine (8). To a flame-dried 100 mL round-bottom flask was added piperazine (1.00 grams, 11.6 mmol) and toluene (25 mL). While stirring, ((3-bromopropoxy)methyl)benzene (1.33 grams, 5.8 mmol) was added dropwise and washed with toluene (25 mL). Solution was refluxed for 2 hours. After cooling to rt and filtering the mixture, the organic mixture was partitioned between 50 mL 1M HCl : 50 mL CHCl₃ and extracted with CHCl₃ (3 x 50 mL). The aqueous phase was adjusted to pH 14 with 2M NaOH, and the resulting organic oil was extracted and combined to the combined organic layers. The basic aqueous layer was extracted with CHCl₃ (3 x 50 mL) and all organics were combined, washed with brine (3 x 50 mL), dried over Na₂SO₄, filtered, and concentrated under reduced pressure. The crude material was purified by silica gel chromatography using CHCl₃ : MeOH : NH₄OH (94.5 : 5.0 : 0.5), resulting in the product as a pale yellow oil in 68% yield. ¹H NMR (500 MHz, CDCl₃) δ 7.38-7.29 (m, 5H), 4.51 (s, 2H), 3.54-3.50 (t, J = 7.8, 2H), 2.93-2.89 (t, J = 7.6, 2H), 2.48-2.41 (m, 6H), 1.89-1.78 (m, 2H).

2-(4-(3-(benzyloxy)propyl)piperazin-1-yl)pyrimidine (10). To a solution of K₃PO₄ (680 mg, 3.2 mmol) in H₂O (10 mL) was added 1-(3-(benzyloxy)propyl)piperazine (351 mg, 1.5 mmol) and 2-chloropyrimidine (172 mg, 1.5 mmol). The mixture was refluxed for 18 hours, cooled to rt, quenched with 0.1M aqueous K₂CO₃ (20 mL), extracted with EtOAc (4 x 30 mL), washed with brine (3 x 25 mL), dried under MgSO₄, and concentrated under reduced pressure. Resulting deep orange oil was purified on silica gel column using 30% EtOAc:Hexanes, yielding the product as a pale orange oil in 32% yield. ¹H NMR (500 MHz, CDCl₃) δ 8.30-8.29 (d, J = 6.6, 2H), 7.35-7.27 (m, 5H), 6.49-6.47 (t, J = 7.4, 1H), 4.51 (s, 2H), 3.85 (br s, 4H), 3.56-3.54 (t, J = 7.2 Hz, 2H), 2.53 (br s, 6H), 1.91-1.85 (m, 2H).

2-(piperazin-1-yl)pyrimidine (13). To a stirring solution of piperazine (3.88 grams, 45 mmol) and K_2CO_3 (3.5 grams, 25.3 mmol) in H_2O (20 mL) at 60 °C was slowly added 2-chloropyrimidine (2.06 grams, 18 mmol). The mixture was stirred for 2 hours and filtered upon cooling to rt. The aqueous layer was extracted with $CHCl_3$ (3 x 25 mL), dried over Na_2SO_4 , and concentrated under reduced pressure, resulting in the product as a pale yellow oil in 81% yield. 1H NMR (500 MHz, $CDCl_3$) δ 8.30-8.29 (d, $J = 6.7$, 2H), 6.48-6.46 (t, $J = 7.2$ Hz, 1H), 3.80-3.78 (t, $J = 6.5$ Hz, 4H), 2.94-2.92 (t, $J = 6.8$ Hz, 4H), 1.97 (s, 1H).

2-(4-(4-bromobutyl)piperazin-1-yl)pyrimidine (15). To a flame-dried round-bottom flask was added 2-(piperazin-1-yl)pyrimidine (750 mg, 4.6 mmol), K_2CO_3 (691 mg, 5.0 mmol), MeCN (20 mL), 1,4-dibromobutane (1.48 grams, 6.9 mmol), and PEG-1000 (100 mg) as a phase-transfer catalyst. The mixture was heated under reflux for 7 hours and upon cooling was filtered, washed with MeCN, and cooled overnight at 0 °C. The crystallized white solid was collected as the product in 18% yield. 1H NMR (500 MHz, $CDCl_3$) δ 8.47-8.46 (d, $J = 5.9$ Hz, 2H), 6.79-6.78 (t, $J = 3.2$, 1H), 4.05 (s, 4H), 3.65-3.63 (m, 4H), 3.53-3.51 (m, 4H), 2.11 (s, 4H).

(4-bromobutyl)triphenylphosphonium bromide (18). To a flame-dried round-bottom flask was added 1,4-dibromobutane (2.16 grams, 10 mmol) and triphenylphosphine (2.63 grams, 10 mmol) in toluene (25 mL). The solution was refluxed for 12 hours and upon cooling to rt was filtered. The white solid was washed multiple times with ether (5 x 25 mL), and air drying of this solid yielded product in 26% yield. 1H NMR (600 MHz, D_2O) δ 7.88-7.70 (m, 15H), 3.51-3.49 (t, $J = 6.7$, 2H), 3.35-3.31 (m, 2H), 2.07-2.03 (m, 2H), 1.90-1.84 (m, 2H).

Triphenyl(4-(4-(pyrimidin-2-yl)piperazin-1-yl)butyl)phosphonium bromide (17). A mixture of (4-bromobutyl)triphenylphosphonium bromide (840 mg, 1.75 mmol) dissolved in MeCN (20 mL) was added slowly to a mixture of 2-(piperazin-1-yl)pyrimidine (860 mg, 5.25 mmol) and K₂CO₃ (490 mg, 3.55 mmol) in MeCN (50 mL). The mixture was heated to reflux for 12 hours. Upon cooling to rt, the mixture was diluted with EtOAc (50 mL), extracted with EtOAc (3 x 50 mL), and washed with brine (3 x 50 mL). The resulting organic layer was dried over MgSO₄, filtered, and concentrated under reduced pressure. The resulting sticky off-white/pale yellow solid was boiled in EtOH for 45 minutes and filtered of all insoluble stick solids. The mother liquor was concentrated under reduced pressure, yielding the product in 5% yield. ¹H NMR (600 MHz, DMSO-d₆) δ 8.35-8.34 (d, J = 6.9, 2H), 7.91-7.76 (m, 15H), 6.62-6.61 (t, J = 3.9, 1H), 3.66 (br s, 4H), 3.61-3.56 (m, 2H), 2.37 (br s, 6H), 1.66-1.58 (dm, J = 31 Hz, 4H).

Triphenyl(3-(4-(pyrimidin-2-yl)piperazin-1-yl)propyl)phosphonium bromide (1). 2-(piperazin-1-yl)pyrimidine (1.0 grams, 6.1 mmol), DIPEA (2.2 grams, 17 mmol), and MeOH (25 mL) were stirred at room temperature for 30 minutes before the addition of (3-bromopropyl)triphenylphosphonium bromide (1.0 grams, 2.2 mmol) slowly portion-wise. The mixture was stirred vigorously at room temperature. After 24 hours, the mixture was concentrated under reduced pressure and the residue was partitioned between DCM (30 mL) and H₂O (30 mL). The aqueous layer was washed with DCM (3 x 30 mL) and the combined organics were dried under Na₂SO₄, filtered, and concentrated under reduced pressure. The resulting sticky oil was dissolved in EtOH and a solid was triturated with EtOAc. The resulting sticky solid was filtered by vacuum filtration, washed with EtOAc, and dried *in vacuo*, resulting in the product in 28% yield. ¹H NMR (600 MHz, DMSO-d₆) δ 8.35-8.34 (d, J = 6.6 Hz, 2H), 7.93-7.77 (m, 15H), 6.63-6.61 (t, J = 6.2, 1H), 3.70 (br s, 4H), 3.61-3.56 (m, 2H), 2.46-2.43 (t, J = 6.9 Hz, 2H), 2.34-2.33 (m, 4H), 1.76-1.72 (m, 2H);

^{13}C NMR (125 MHz, DMSO- d_6) δ 162.4, 158.6, 135.7, 133.1, 130.2, 110.5, 57.4, 52.8, 43.8, 19.9, 18.7; LRMS m/z : 467.6 [M^+]; mp 203-206 °C.

2,2'-((*tert*-butoxycarbonyl)azanediyl)diacetic acid (21). A stirring solution of iminodiacetic acid (2.0 grams, 15 mmol) in dioxane (30 mL) and H_2O (10 mL) was cooled to 0 °C, after which Boc_2O (3.93 grams, 18 mmol) and 2M NaOH (10 mL) were added. The mixture was stirred overnight at rt, concentrated under reduced pressure, and the aqueous layer was acidified with 1M HCl (50 mL) to pH 3.5. The mixture was extracted with EtOAc (3 x 50 mL) and combined organics were dried over Na_2SO_4 , filtered, and concentrated under reduced pressure, yielding an off-white solid as the product in 86% yield. ^1H NMR (600 MHz, DMSO- d_6) δ 12.62 (br s, 2H), 3.91-3.88 (d, J = 14.4 Hz, 4H), 1.36 (s, 9H).

***Tert*-butyl 3,5-dioxo-4-(pyrimidin-2-yl)piperazine-1-carboxylate (23).** 2,2'-((*tert*-butoxycarbonyl)azanediyl)diacetic acid (4.6 grams, 21.4 mmol) was refluxed in Ac_2O (30 mL) for 45 minutes, after which the mixture was concentrated under reduced pressure to dryness. To the residue was added 2-aminopyrimidine (2.04 grams, 21.4 mmol) in toluene (30 mL) which was set to reflux for 48 hours. Upon cooling to rt, the mixture was concentrated under reduced pressure to near-dryness, and the residue was set to reflux in Ac_2O (30 mL) for another 24 hours. Upon cooling to rt, the mixture was concentrated under reduced pressure and purified using silica gel chromatography with 1% MeOH/ CHCl_3 , resulting in the product as an orange oil in 32% yield. ^1H NMR (500 MHz, DMSO- d_6) δ 8.91-8.90 (d, J = 4.8, 2H), 7.46-7.44 (t, J = 5.2 Hz, 1H), 4.52 (s, 4H), 1.51 (s, 9H).

1-(pyrimidin-2-yl)piperazine-2,6-dione (24). To a stirring solution of *tert*-butyl 3,5-dioxo-4-(pyrimidin-2-yl)piperazine-1-carboxylate (500 mg, 1.7 mmol) in DCM (5 mL) was added trifluoroacetic acid (1 mL) dropwise. The mixture was vigorously stirred for 6 hours and concentrated under reduced pressure. The residue was partitioned between DCM (10 mL) and saturated NaHCO₃ (10 mL), extracted with DCM (3 x 10 mL), dried over Na₂SO₄, filtered, and concentrated under reduced pressure, yielding the product as a pale yellow oily solid in 81% yield. ¹H NMR (500 MHz, CDCl₃) δ 8.90-8.89 (d, J = 5.4 Hz, 2H), 7.43-7.42 (t, J = 4.8 Hz, 1H), 3.86 (s, 4H).

5-benzyloxy-2-chloropyrimidine (26). To a stirring solution of 2-chloro-5-hydroxypyrimidine (25 grams, 191.5 mmol) in MeCN (1000 mL) was added K₂CO₃ (29.1 g, 210.7 mmol), followed by dropwise addition of benzyl bromide (36 grams, 210.7 mmol). The reaction was run at room temperature overnight, quenched with H₂O (100 mL), and concentrated under reduced pressure. The residue was dissolved in a 50/50 mixture of CHCl₃ (150 mL) and H₂O (150 mL), extracted with CHCl₃ (3 x 150 mL), washed with brine (3 x 150 mL), dried under Na₂SO₄, filtered, and concentrated under reduced pressure. The resulting crude solid was purified using silica gel chromatography with 2.5% MeOH/CHCl₃, and the product was obtained as a pale yellow solid in 75% yield. ¹H NMR (CDCl₃) δ 8.34 (s, 2H), 7.42-7.39 (m, 5H), 5.15 (s, 2H).

5-(benzyloxy)-2-(piperazin-1-yl)pyrimidine (27). To a stirring solution of piperazine (1.0 grams, 11.6 mmol) in toluene (20 mL) was added Et₃N (1.20 grams, 11.8 mmol) dropwise, and a solution of 5-benzyloxy-2-chloropyrimidine (2.82 grams, 12.8 mmol) in toluene (20 mL) was cannulated into the reaction vessel. The mixture was refluxed overnight, cooled to rt, and concentrated under reduced pressure. The oily residue was partitioned between DCM and H₂O, extracted with DCM (3 x 50 mL), washed with brine (3 x 25 mL), dried over

Na₂SO₄, and concentrated under reduced pressure. The crude product was purified via acid/base extraction, where it was first partitioned between DCM and 1M HCl. The acidic aqueous layer was extracted with DCM (3 x 25 mL, organic I). The acidic aqueous layer was then brought to pH 9 with 1M NaOH, and the aqueous layer was re-extracted with DCM (3 x 25 mL, organic II). Organic II layer was concentrated under reduced pressure, resulting in product as a yellow solid in 23% yield. ¹H NMR (500 MHz, CDCl₃) δ 8.12 (s, 2H), 7.41-7.33 (m, 5H), 5.02 (s, 2H), 3.70-3.68 (t, J = 4.8 Hz, 4H), 2.94-2.92 (t, J = 5.2 Hz, 4H).

(3-(4-(5-(benzyloxy(pyrimidin-2-yl)piperazin-1-yl)propyl)triphenylphosphonium

bromide (28). To a stirring solution of (3-bromopropyl)triphenylphosphonium bromide (86 mg, 184 mmol) in MeOH (3 mL) was added 5-(benzyloxy)-2-(piperazin-1-yl)pyrimidine (100 mg, 369 mmol) in H₂O (3 mL). The mixture was stirred for 1 hour at room temperature, followed by overnight reflux. After cooling to rt, the solution was concentrated under reduced pressure. The residue was partitioned between DCM and H₂O, extracted with DCM (3 x 15 mL), washed with brine (3 x 10 mL), dried over Na₂SO₄, filtered, and concentrated under reduced pressure. The crude material was boiled in EtOAc, filtered, concentrated under reduced pressure. The sticky solid was dissolved in DCM (1 mL) and triturated with hexanes (10 mL) to give the product as a tan solid in 41% yield. ¹H NMR (500 MHz, DMSO-d₆) δ 8.22 (s, 2H), 7.92-7.76 (m, 15H), 7.43-7.33 (m, 5H), 5.09 (s, 2H), 3.60 (br s, 6H), 2.44-2.42 (t, J = 6.2, 2H), 2.33-2.31 (t, J = 5.8, 4H), 1.76-1.68 (m, 2H).

2-(piperazin-1-yl)pyrimidin-5-ol (30). The N₂ atmosphere of a stirring solution containing 5-(benzyloxy)-2-(piperazin-1-yl)pyrimidine (200 mg, 0.73 mmol) in EtOAc/EtOH (27 mL:13 mL) containing 20 wt% Pd(OH)₂/C was purged with H₂ gas. After 24 hours, the H₂

atmosphere was purged, the mixture was filtered through celite, and the filtrate was concentrated under reduced pressure to give the product as an off-white solid in 88% yield. ^1H NMR (500 MHz, DMSO- d_6) δ 8.00 (s, 2H), 3.48-3.46 (t, J = 3.6 Hz, 4H), 2.71-2.70 (t, J = 3.4 Hz, 4H).

2-amino-5-(benzyloxy)-pyrimidine (31). 5-(benzyloxy)-2-chloropyrimidine (20 grams, 90.6 mmol), NH_4OH (200 mL), and EtOH (200 mL) were added to a 600 mL Parr Reactor, sealed, and stirred at 120 °C for 60 hours. Upon cooling, the product was collected and evaporated of organic solvent under reduced pressure. The resulting aqueous layer was basified with 1M NaOH (250 mL) and extracted with EtOAc (4 x 200 mL). The collected organics were extracted vigorously with 1M HCl (4 x 200 mL). The combined acidic layers were adjusted to pH 12 with 1M NaOH and extracted with EtOAc (4 x 250 mL). The combined final organics were dried over Na_2SO_4 , filtered, and concentrated under reduced pressure yielding a yellow-tan solid in 65% yield. ^1H NMR (500 MHz, CDCl_3) δ 8.08 (s, 2H), 7.43-7.33 (m, 5H), 6.21 (s, 2H), 5.05 (s, 2H).

2-amino-5-hydroxypyrimidine (43). The N_2 atmosphere of a stirring solution containing 2-amino-5-(benzyloxy)-pyrimidine (6.0 grams, 29.8 mmol) in EtOAc/EtOH (140 mL:70 mL) with 20 wt% $\text{Pd}(\text{OH})_2/\text{C}$ was purged with H_2 gas. After 24 hours, the H_2 atmosphere was purged, the mixture was filtered through celite, and the filtrate was concentrated under reduced pressure. The product was obtained as a straw-yellow solid in 96% yield. ^1H NMR (600 MHz, DMSO- d_6) δ 9.04 (br s, 1H), 7.85 (s, 2H), 5.90 (s, 2H).

5-((*tert*-butyldiphenylsilyl)oxy)pyrimidin-2-amine (45). To a stirring solution of 2-amino-5-hydroxypyrimidine (3.1 grams, 27.9 mmol) and DIPEA (7.1 grams, 54.9 mmol) in DCM (225 mL) was added *tert*-butyl(chloro)diphenylsilane (6.9 grams, 25.1 mmol)

dropwise and the reaction was stirred overnight. Reaction mixture was concentrated under reduced pressure and diluted in EtOAc/H₂O, extracted with EtOAc (4 x 200 mL), washed with brine, dried over Na₂SO₄, and concentrated under reduced pressure. The crude oil was purified using silica gel chromatography with 0-3% MeOH/CHCl₃ gradient, yielding the product as a pale yellow oil in 55% yield. ¹H NMR (600 MHz, CDCl₃) δ 7.78 (s, 2H), 7.67-7.65 (d, 7.4 Hz, 4H), 7.46-7.37 (m, 6H), 5.40 (br s, 2H), 1.12 (s, 9H).

5-((*tert*-butyldiphenylsilyloxy)-2-chloropyrimidine (46). To a stirring solution of 2-chloro-5-hydroxypyrimidine (5.0 grams, 38.3 mmol) in DCM (250 mL) was added DIPEA (9.90 grams, 76.6 mmol), followed by slow dropwise addition *tert*-butyl(chloro)diphenylsilane (9.48 grams, 34.5 mmol). The mixture was stirred overnight, after which it was partitioned between DCM (250 mL) and H₂O (250 mL), extracted with DCM (3 x 250 mL), washed with brine (2 x 250 mL), dried under Na₂SO₄, filtered, and concentrated under reduced pressure. The crude orange oil was purified using silica gel chromatography with CHCl₃, yielding the product as a deep orange oil in 38% yield. ¹H NMR (500 MHz, CDCl₃) δ 8.05 (s, 2H), 7.66-7.64 (m, 4H), 7.49-4.39 (m, 6H), 1.14 (s, 9H).

***Tert*-butyl 4-(5-(benzyloxy)pyrimidin-2-yl)-3,5-dioxopiperazine-1-carboxylate (32).** 2,2'-((*tert*-butoxycarbonyl)azanediyl)diacetic acid (1.08 grams, 5.0 mmol) was refluxed in Ac₂O (50 mL) for 45 minutes, after which the mixture was concentrated under reduced pressure to dryness. To the residue was added 2-amino-5-(benzyloxy)-pyrimidine (500 mg, 2.5 mmol) in toluene (100 mL) which was set to reflux for 48 hours. Upon cooling to rt, the mixture was concentrated under reduced pressure to near-dryness and the residue was set to reflux in Ac₂O (100 mL) for an additional 24 hours. Upon cooling to rt, the mixture was concentrated under reduced pressure and purified using silica gel chromatography with 1% MeOH/CHCl₃, yielding the product as an orange oil in 46% yield.

^1H NMR (500 MHz, CDCl_3) δ 8.55 (s, 2H), 7.47-7.38 (m, 5H), 5.21 (s, 2H), 4.50 (s, 4H), 1.51 (s, 9H).

1-(5-(benzyloxy)pyrimidin-2-yl)piperazine-2,6-dione (33). To a vigorous stirring solution of *tert*-butyl 4-(5-(benzyloxy)pyrimidin-2-yl)-3,5-dioxopiperazine-1-carboxylate (100 mg, 0.25 mmol) in DCM (5 mL) was added trifluoroacetic acid (1 mL) dropwise. Solution was stirred at room temperature for 3 hours, concentrated under reduced pressure, dissolved in saturated NaHCO_3 (20 mL), and extracted with DCM (4 x 15 mL). Organics were combined, dried under Na_2SO_4 , filtered, and concentrated in vacuo, yielding the product as a clear oil in 55% yield. ^1H NMR (500 MHz, CDCl_3) δ 8.55 (s, 2H), 7.44-7.39 (m, 5H), 5.19 (s, 2H), 3.85 (s, 4H).

3-((*tert*-butyldimethylsilyl)oxy)propan-1-amine (37). To a stirring solution of 3-aminopropan-1-ol (8.25 grams, 109.8 mmol) and *tert*-butyldimethylsilyl chloride (19.04 grams, 126.3 mmol) in DCM (200 mL) was added DIPEA (21.35 grams, 165 mmol). The mixture was vigorously stirred at rt overnight, diluted with H_2O (200 mL), extracted with DCM (3 x 200 mL), dried over MgSO_4 , filtered, and concentrated under reduced pressure. The crude oil was set on hi-vac to remove residual DIPEA before carrying forward to the next step (yield > 90% by NMR).

Diethyl 2,2'-((3-((*tert*-butyldimethylsilyl)oxy)propyl)azanediyl)diacetate (39). To a suspension of K_2CO_3 (7.33 grams, 53 mmol) and KI (7.04 grams, 42.4 mmol) in MeCN (50 mL) was cannulated 3-((*tert*-butyldimethylsilyl)oxy)propan-1-amine (2.00 grams, 10.6 mmol) dissolved in MeCN (150 mL). The mixture was heated to 70 $^\circ\text{C}$, followed by cannulation of ethyl bromoacetate (3.54 grams, 21.2 mmol) portionwise every 30 minutes. After stirring for an additional 2 hours, mixture was cooled to rt, quenched with H_2O (100

mL), and extracted with EtOAc (3 x 150 mL). The combined organics were washed with saturated NH₄Cl (2 x 150 mL) and brine (2 x 150 mL), dried over Na₂SO₄, filtered, and concentrated under reduced pressure. The crude oil was purified using silica gel chromatography with 15% EtOAc/Hexanes, yielding the product as a dark yellow oil in 74% yield. ¹H NMR (500 MHz, CDCl₃) δ 4.15-4.11 (q, J = 7.4 Hz, 4H), 3.63-3.61 (t, 5.8 Hz, 2H), 3.51 (s, 4H), 2.78-2.75 (t, J = 7.6 Hz, 2H), 1.68-1.63 (m, J = 7.2 Hz, 2H), 1.25-1.22 (t, J = 6.8 Hz, 6H), 0.85 (s, 9H), 0.00 (s, 6H).

Diethyl 2,2'-((3-hydroxypropyl)azanediyl)diacetate (42). To a stirring mixture of 3-((*tert*-butyldimethylsilyl)oxy)propan-1-amine (2.0 grams, 5.5 mmol) in EtOH (30 mL) was added conc. HCl (1 mL) dropwise. After 4 hours, the solution was concentrated under reduced pressure, the residue was partitioned between CHCl₃ (30 mL) and H₂O (30 mL), extracted with CHCl₃ (3 x 30 mL), dried over Na₂SO₄, filtered, and concentrated under reduced pressure, yielding the product as a pale yellow oil in 27% yield. ¹H NMR (500 MHz, CDCl₃) δ 4.70 (br s, 1H), 4.16-4.12 (q, J = 7.8 Hz, 4H), 3.75-3.73 (t, J = 5.6 Hz, 2H), 3.48 (s, 4H), 2.84-2.82 (t, J = 6.4 Hz, 2H), 1.66-1.62 (m, 2H), 1.25-1.22 (t, J = 7.4 Hz, 6H).

3-((*tert*-butyldiphenylsilyl)oxy)propan-1-amine (47). To a stirring mixture of 3-aminopropan-1-ol (3.0 grams, 39.9 mmol) in DCM (400 mL) was added DIPEA (10.31 grams, 79.8 mmol) and *tert*-butyl(chloro)diphenylsilane (9.89 grams, 36.0 mmol). The reaction was stirred at rt overnight, quenched with 0.5 M HCl (300 mL), and extracted with DCM (3 x 300 mL). The organics were washed with brine (2 x 250 mL), dried over Na₂SO₄, filtered, and concentrated under reduced pressure. The crude oil was set on hi-vac to remove residual DIPEA before carrying product forward to the next step (yield > 95% by NMR).

Diethyl 2,2'-((3-((*tert*-butyldiphenylsilyl)oxy)propyl)azanediyl)diacetate (48). To a suspension of K_2CO_3 (24.47 grams, 177 mmol) and KI (23.5 grams, 141.6 mmol) in MeCN (200 mL) was cannulated 3-((*tert*-butyldiphenylsilyl)oxy)propan-1-amine (11.1 grams, 35.4 mmol) dissolved in MeCN (600 mL). The mixture was heated to 70 °C, followed by cannulation of ethyl bromoacetate (11.83 grams, 70.8 mmol) portionwise every 30 minutes over a period of 6 hours. After stirring overnight, mixture was cooled to rt, quenched with H_2O (100 mL), and concentrated under reduced pressure. The residue was dissolved in EtOAc (200 mL) and H_2O (200 mL) and extracted with EtOAc (3 x 200 mL). The combined organics were washed with brine (2 x 150 mL), dried over Na_2SO_4 , filtered, and concentrated under reduced pressure. The crude yellow oil was purified using silica gel chromatography with 17% EtOAc/Hexanes, yielding the product as a dark yellow oil in 62% yield. 1H NMR (500 MHz, $CDCl_3$) δ 7.65-7.64 (d, J = 5.6 Hz, 4H), 7.43-7.35 (m, 6H), 4.17-4.12 (q, J = 6.8 Hz, 4H), 3.71-3.69 (t, J = 5.4 Hz, 2H), 3.52 (s, 4H), 2.85-2.82 (t, 7.2 Hz, 2H), 1.75-1.70 (m, 2H), 1.27-1.24 (t, J = 7.2 Hz, 6H), 1.03 (s, 9H).

Ethyl 2-(4-(pyrimidin-2-yl)piperazin-1-yl)acetate (55). Ethyl bromoacetate (1.02 grams, 6.1 mmol) was added dropwise to a stirred mixture of 2-(piperazin-1-yl)pyrimidine (1.0 grams, 6.1 mmol), K_2CO_3 (2.11 grams, 15.3 mmol), and KI (2.03 grams, 12.2 mmol) in MeCN (100 mL). The mixture was heated to 70 °C and ran overnight. After cooling to rt, the mixture was quenched with 50 mL H_2O and MeCN was removed under reduced pressure. The remaining aqueous layer was extracted with EtOAc (3 x 50 mL), washed with brine (3 x 30 mL), dried under Na_2SO_4 , filtered, and concentrated under reduced pressure. The crude oil was purified with silica gel chromatography using 75% EtOAc:Hexanes, and the product was obtained as a deep orange oil in 84% yield. 1H NMR (500 MHz, $CDCl_3$) δ 8.30-8.29 (d, J = 3.8 Hz, 2H), 6.48-6.47 (t, J = 1.6 Hz, 1H), 4.22-4.18

(q, $J = 8.3$, 2H), 3.89-3.87 (t, $J = 6.4$, 4H), 3.25 (s, 2H), 2.65-2.63 (t, $J = 8.2$ Hz, 4H), 1.29-1.26 (t, $J = 7.3$ Hz, 3H).

2-(4-(pyrimidin-2-yl)piperazin-1-yl)acetic acid (56). A solution of ethyl 2-(4-(pyrimidin-2-yl)piperazin-1-yl)acetate (210 mg, 0.84 mmol) was heated in 6M HCl (8 mL) at 75 °C overnight. Upon cooling to rt, the water was removed under reduced pressure and the resulting residue was adjusted to pH ~5.5 with 1M NaOH, resulting in a solid crash out from the oil. This mixture was concentrated to dryness, resulting in a heterogeneous mixture of white and tan solids. The solids were dissolved in EtOH and 50% aqueous MeOH was slowly added dropwise until a granular white solid crashed out of solution. The mixture was filtered through celite, the mother liquor concentrated under reduced pressure, and the product was obtained as a brown solid in 85% yield. $^1\text{H NMR}$ (500 MHz, DMSO- d_6) δ 8.35-8.34 (d, $J = 3.9$, 2H), 6.63-6.61 (t, $J = 6.1$ Hz, 1H), 3.75-3.73 (br t, 4H), 3.15 (s, 2H), 2.59-2.57 (br t, 4H).

Triphenyl(3-(2-(4-(pyrimidin-2-yl)piperazin-1-yl)acetoxy)propyl)phosphonium bromide (51). To a stirring solution of 2-(4-(pyrimidin-2-yl)piperazin-1-yl)acetic acid (50 mg, 0.23 mmol) in DMF (5 mL) was added K_2CO_3 (77 mg, 0.56 mmol 2.5 eq.) and KI (75 mg, 0.45 mmol). After 5 minutes of stirring, (3-bromopropyl)triphenylphosphonium bromide (105 mg, 0.23 mmol) was added and the mixture was set to stir overnight at room temperature. DMF was removed under reduced pressure, and the remaining residue was partitioned between DCM and ice-cold H_2O , extracted with DCM (3 x 15 mL), dried over Na_2SO_4 , filtered, and concentrated under reduced pressure. The crude product was purified using silica gel chromatography with 6% MeOH/DCM. The resulting oil was resuspended in DCM (1 mL) and hexanes (15 mL) were used to triturate the product as a yellow solid in 44% yield. $^1\text{H NMR}$ (500 MHz, DMSO- d_6) δ 8.30-8.29 (2, $J = 3.6$ Hz, 2H),

7.88-7.69 (m, 15H), 6.49-6.47 (t, J = 3.1 Hz, 1H), 4.48-4.46 (t, J = 3.8 Hz, 2H), 4.00-3.94 (m, 2H), 3.85-3.83 (t, J = 3.3 Hz, 4H), 3.29 (s, 2H), 2.61-2.59 (t, J = 3.5 Hz, 4H), 2.08-2.01 (m, 2H); ^{13}C NMR (125 MHz, DMSO- d_6) δ 176.4, 162.4, 158.6, 134.0, 133.9, 130.8, 130.7, 110.8, 62.7, 56.8, 43.7, 20.2, 18.8; LRMS m/z: 525.2 [M^+]; mp = 209-212 °C.

Ethyl 2-(4-(5-(benzyloxy)pyrimidin-2-yl)piperazin-1-yl)acetate (58). A mixture of 5-(benzyloxy)-2-chloropyrimidine (750 mg, 3.4 mmol), ethyl 2-(piperazin-1-yl)acetate (702 mg, 4.1 mmol), Et_3N (1.03 grams, 10.1 mmol), and toluene (40 mL) was refluxed for 16 hours. Upon cooling to rt, toluene was removed under reduced pressure, and the residue was partitioned between CHCl_3 (40 mL) and H_2O (40 mL), extracted with CHCl_3 (3 x 40 mL), dried over Na_2SO_4 , filtered, and concentrated under reduced pressure. The crude oil was purified using silica gel chromatography with 100% EtOAc, yielding the product as a deep orange oil in 18% yield. ^1H NMR (500 MHz, CDCl_3) δ 8.11 (s, 2H), 7.40-7.33 (m, 5H), 5.01 (s, 2H), 4.22-4.19 (q, J = 5.4 Hz, 2H), 3.82-3.80 (t, J = 4.4 Hz, 4H), 3.30 (s, 2H), 2.70-2.68 (t, J = 4.8 Hz, 4H), 1.29-1.27 (t, 5.4 Hz, 3H).

Ethyl 2-(4-(5-hydroxypyrimidin-2-yl)piperazin-1-yl)acetate (59). The N_2 atmosphere of a stirring solution containing ethyl 2-(4-(5-(benzyloxy)pyrimidin-2-yl)piperazin-1-yl)acetate (180 mg, 0.5 mmol) in MeOH (10 mL) containing 20 wt% $\text{Pd}(\text{OH})_2/\text{C}$ was purged with H_2 gas. After 24 hours, the H_2 atmosphere was purged, the mixture was filtered through celite, and the filtrate was concentrated under reduced pressure. The product was obtained as a deep yellow oil in 90% yield. ^1H NMR (500 MHz, CDCl_3) δ 7.94 (s, 2H), 4.16-4.12 (q, J = 6.8 Hz, 2H), 3.63 (s, 4H), 3.20 (s, 2H), 2.59 (s, 4H), 1.24-1.21 (t, J = 7.2 Hz, 3H).

2-(4-(5-(benzyloxy)pyrimidin-2-yl)piperazin-1-yl)acetic acid (60). To a stirring solution of ethyl 2-(4-(5-(benzyloxy)pyrimidin-2-yl)piperazin-1-yl)acetate (500 mg, 1.4 mmol) in THF (17 mL) was added NaOH (168 mg, 4.2 mmol) in H₂O (17 mL), and the reaction was stirred overnight. The reaction was quenched, brought to pH 5 with 1M HCl (10 mL), and extracted with 5% MeOH in EtOAc (5 x 15 mL) to keep product soluble. Organics were dried over Na₂SO₄, filtered, and concentrated under reduced pressure, yielding the product as a white solid in 65% yield. ¹H NMR (500 MHz, DMSO-d₆) δ 8.24 (s, 2H), 7.44-7.32 (m, 5H), 5.10 (s, 2H), 3.65-3.63 (t, J = 5.4 Hz, 4H), 3.17 (s, 2H), 2.60-2.58 (t, J = 5.6 Hz, 4H).

2-(3,5-dioxo-4-(pyrimidin-2-yl)piperazin-1-yl)acetic acid (63). To a reaction vessel was added 1 gram of activated powdered molecular sieves, followed by nitrilotriacetic acid (5.0 grams, 26.16 mmol) and pyridine (80 mL). After 45 minutes of heating at 50 °C, Ac₂O (3.2 grams, 31.39 mmol) was added and the mixture was set to reflux for 2 hours. The mixture was cooled to 50 °C and 2-aminopyrimidine (2.49 grams, 26.16 mmol) dissolved in pyridine (25 mL) was cannulated into the reaction vessel. The reaction was heated to reflux for an additional 2 hours, cooled to rt, filtered through celite, and concentrated under reduced pressure. The crude solid was suspended in DCM (50 mL) and the DCM-insoluble solid was filtered and washed with MeOH (20 mL), yielding the product as an off-white solid in 37% yield. ¹H NMR (600 MHz, DMSO-d₆) δ 12.72 (br s, 1H), 8.99-8.98 (d, J = 4.8 Hz, 2H), 7.67-7.66 (t, J = 4.8 Hz, 1H), 3.82 (s, 4H), 3.50 (s, 2H).

(3-(2-(3,5-dioxo-4-(pyrimidin-2-yl)piperazin-1-yl)acetoxypentyl)triphenylphosphonium bromide (53). To a stirring solution of 2-(3,5-dioxo-4-(pyrimidin-2-yl)piperazin-1-yl)acetic acid (510 mg, 2.04 mmol) in DMF (30 mL) was added K₂CO₃ (704 mg, 5.1 mmol) and KI (677 mg, 5.0 mmol). After stirring for 5 minutes, (3-

bromopropyl)triphenylphosphonium bromide (950 mg, 2.04 mmol) was added and the mixture was stirred overnight at rt. The mixture was concentrated under reduced pressure and partitioned between DCM (15 mL) and H₂O (15 mL), extracted with DCM (4 x 15 mL), dried over Na₂SO₄, filtered, and concentrated under reduced pressure. The crude oil was purified using silica gel chromatography with 5.5% MeOH/DCM. The resulting oil was dissolved in DCM (1 mL) and triturated with heptanes (25 mL) to give the product as a yellow solid in 35% yield. ¹H NMR (600 MHz, DMSO-d₆) δ 8.99-8.98 (d, J = 4.6 Hz, 2H), 7.93-7.77 (m, 15H), 7.68-7.66 (t, J = 4.8 Hz, 1H), 4.23-4.21 (t, J = 6.2 Hz, 2H), 3.84 (s, 4H), 3.69-3.63 (m, 4H), 1.94-1.88 (m, 2H); ¹³C NMR (150 MHz, DMSO-d₆) δ 169.7, 169.4, 159.9, 154.8, 135.1, 135.0, 133.7, 133.6, 130.4, 130.3, 121.8, 118.5, 117.9, 63.5, 54.6, 21.4, 17.4; LRMS m/z: 553.3 [M⁺]; mp 216-218 °C.

2-(4-(5-(benzyloxy)pyrimidin-2-yl)-3,5-dioxopiperazin-1-yl)acetic acid (64). To a reaction vessel was added 1 gram of activated powdered molecular sieves, followed by nitrilotriacetic acid (2.50 grams, 13.08 mmol) and pyridine (80 mL). After 45 minutes of heating at 50 °C, Ac₂O (1.47 grams, 14.4 mmol) was added and the mixture was set to reflux for 2 hours. The mixture was cooled to 50 °C and 2-amino-5-(benzyloxy)-pyrimidine (2.60 grams, 13.08 mmol) dissolved in pyridine (25 mL) was cannulated into the reaction vessel. The reaction was heated to reflux for an additional 2 hours before being cooled to rt, filtered through celite, and concentrated under reduced pressure. The mixture was re-suspended in DCM (30 mL) and the off-white solid that crashed out was filtered, washed with DCM (5 x 30 mL), and dried to give the product in 32% yield. ¹H NMR (600 MHz, DMSO-d₆) δ 12.69 (br s, 1H), 8.75 (s, 2H), 7.51-7.39 (m, 5H), 5.34 (s, 2H), 3.80 (s, 4H), 3.48 (s, 2H).

2-(4-(5-hydroxypyrimidin-2-yl)-3,5-dioxopiperazin-1-yl)acetic acid (65). The N₂ atmosphere of a stirring solution containing 2-(4-(5-(benzyloxy)pyrimidin-2-yl)-3,5-dioxopiperazin-1-yl)acetic acid (1.4 grams, 3.93 mmol) in acetone (100 mL) containing 25 wt% Pd(OH)₂/C was purged with H₂ gas. After 48 hours the H₂ atmosphere was purged, the mixture was filtered through celite, and the filtrate was concentrated under reduced pressure, yielding the product as a pale yellow solid in 93% yield. ¹H NMR (500 MHz, DMSO-d₆) δ 11.87 (br s, 1H), 8.44 (s, 2H), 3.78 (s, 4H), 3.47 (s, 2H).

5.5.2 *In Vitro* Materials and Methods

General. All reagents used were of reagent grade. Compounds **JHX-2** [4-(5-hydroxypyrimidin-2-yl)-*N,N*-dimethylpiperazin-1-sulfonamide], **JHX-3** [*N,N*-dimethyl-3,5-dioxo-4-(pyrimidin-2-yl)piperazine-1-sulfonamide], and **JHX-4** [4-(5-hydroxypyrimidin-2-yl)-*N,N*-dimethyl-3,5-dioxopiperazine-1-sulfonamide] were synthesized according to Jin [1]. **JHX-1-TPP** [Triphenyl(3-(4-(pyrimidin-2-yl)piperazin-1-yl)propyl)phosphonium bromide] was synthesized as shown in **Scheme 4**, and **HK-2-Benzyl-TPP** [(3-(1-(5-(benzyloxy)pyrimidin-2-yl)-2,5-dioxopyrrolidin-3-yl)propyl)triphenylphosphonium bromide] was synthesized by my colleague, Mr. Theodor Woolman (synthesis not published). Cell Titer 96® Aqueous One Solution Cell Proliferation Assay Kit was obtained from Promega (Madison, WI). Rhodamine-123 was purchased from Sigma Aldrich (St. Louis, MO). UV-visible assays were measured on a Molecular Devices SpectraMax Plus³⁸⁴ microplate spectrophotometer (Molecular Devices, Sunnyvale, CA). Fluorescence assays were measured on a FLx800 Microplate Fluorescence Reader (Bio-Tek Instruments, Winooski, VT). All fluorescence images were captured with a Nikon Diaphot 200 inverted microscope equipped with a Hamamatsu Imagem EMCCD camera using the Red

Excitation Filter Block Cy5 (Nikon Instruments Inc, Melville, NY) with 250 ms exposure and gain of 5.

General Incubation Procedure. House Ear Institute-Organ of Corti 1 (HEI-OC1) cells [61] were provided by Dr. Federico Kalinec, David Geffen School of Medicine, University of California, Los Angeles, CA. These cells were grown under permissive conditions (33 °C under a 10% CO₂ atmosphere), which induces expression of an immortalizing gene that triggers de-differentiation and accelerated proliferation, in Dulbecco's Modified Eagle's Medium (DMEM, Mediatech Inc., Manassas, VA) supplemented with 10% fetal bovine serum (FBS, ThermoFisher, Waltham, MA) in 250 mL plastic Cell Culture Flasks as previously described [62]. A uniform population of adhering, growing cells were obtained by performing multiple "slap-and-wash" cycles where the flask was smacked to detach all the non-adhesive, free-floating cells and rinsed with media. For the planned experiments, the cells were seeded onto either 24-well or 96-well clear flat-bottom plastic plates (Nunclon Delta, Round, Thermo Fisher Scientific, Waltham, MA) at a density of ca. 2.0×10^5 cells/mL using 500 μ L or 200 μ L per well, respectively. One day of growth in standard media resulted in around 80% confluence. All studies were conducted, at a minimum, in triplicate.

Non-Conjugated JHX-4 Family Toxicology. 1 mM of JHX-2, JHX-3, or JHX-4 in FBS-free media containing 1.0% DMSO was added to seeded cells in 96-well plates. After 24 hours, the media was removed by aspiration, the cells were washed three times with PBS⁺, and the media was replaced with Cell Titer 96[®] AQueous One Solution Cell Proliferation Assay (MTS, Promega, Madison, WI) solution (20 μ L assay solution in 100 μ L culture media) and incubated for 1 hour according to manufacturer's protocol. Absorbance was

recorded at 490 nm using a plate reader, and results were normalized to blank control cells (100%).

Effects of the Non-Conjugated JHX-4 Family on Mitochondria Fluorescence. The fluorescence staining of mitochondria was conducted according to Chazotte [63]. 1 mM of either JHX-2, JHX-3, or JHX-4 in FBS-free media containing 1.0% DMSO was added to the seeded cells in either 24-well or 96-well plates. Cells were incubated for 2 hours, after which the media was aspirated. The cells were washed 3x with PBS⁺ and stained with 20 µg/mL Rhodamine-123-labeling solution (in PBS⁺) and incubated for another 30 minutes. The stain was aspirated, and the cells were washed 3x with PBS⁺. The cells in the 24-well plates were imaged in PBS⁺ with a fluorescence microscope. The cells in the 96-well plates were analyzed with a fluorescence plate reader, and results were normalized to untreated control cells (100%).

JHX-1-TPP and HK-2-Benzyl-TPP Toxicology. Either 1 nM, 10 nM, 100 nM, 1 µM, or 10 µM of either JHX-1-TPP or HK-2-Benzyl-TPP in FBS-free media containing 1.0% DMSO was added to the seeded cells in 96-well plates. After 24 hours, the media was removed by aspiration, the cells were washed three times with PBS⁺, and the media was replaced with Calcein-AM Staining (Thermo Fisher Scientific, Waltham, MA) solution (2 µM final solution concentration with 100 µL per well) and incubated for 30 minutes according to manufacturer's protocol. Calcein-AM staining was measured with a fluorescence plate reader with results normalized to untreated control cells (100%).

Effects of TPP Compounds on Mitochondria Fluorescence. The fluorescence staining of mitochondria was conducted according to Chazotte [63]. Either 1 nM, 10 nM, 100 nM, 1 µM, or 10 µM of either JHX-1-TPP or HK-2-Benzyl-TPP in FBS-free media containing

1.0% DMSO was added to the seeded cells in either 24-well or 96-well plates. Cells were incubated for 8 hours, after which the media was aspirated. The cells were washed 3x with PBS+ and stained with 20 µg/mL Rhodamine-123-labeling solution (in PBS+) and incubated for another 30 minutes. The stain was aspirated, and the cells were washed 3x with PBS+. The cells in the 24-well plates were imaged in PBS+ with a fluorescence microscope. The cells in the 96-well plates were analyzed with a fluorescence plate reader, and results were normalized to untreated control cells (100%).

5.6 References

1. Jin, H., et al., *Multifunctional antioxidants for the treatment of age-related diseases*. J Med Chem, 2010. **53**(3): p. 1117-27.
2. Kawada, H., et al., *Effects of multifunctional antioxidants on mitochondrial dysfunction and amyloid-beta metal dyshomeostasis*. J Alzheimers Dis, 2015. **44**(1): p. 297-307.
3. Randazzo, J., et al., *Orally active multi-functional antioxidants delay cataract formation in streptozotocin (type 1) diabetic and gamma-irradiated rats*. PLoS One, 2011. **6**(4): p. e18980.
4. Randazzo, J., et al., *Orally active multi-functional antioxidants are neuroprotective in a rat model of light-induced retinal damage*. PLoS One, 2011. **6**(7): p. e21926.
5. Kawada, H., *Multi-Functional Antioxidants Targeting Neurodegenerative Diseases*. 2013.
6. Wang, Y., et al., *Mitochondrial dysfunction in neurodegenerative diseases and the potential countermeasure*. CNS Neuroscience & Therapeutics, 2019. **25**(7): p. 816-824.
7. Frantz, M.-C. and P. Wipf, *Mitochondria as a target in treatment*. Environmental and molecular mutagenesis, 2010. **51**(5): p. 462-475.
8. Madreiter-Sokolowski, C.T., et al., *Targeting Mitochondria to Counteract Age-Related Cellular Dysfunction*. Genes, 2018. **9**(3): p. 165.
9. Balaban, R.S., S. Nemoto, and T. Finkel, *Mitochondria, oxidants, and aging*. Cell, 2005. **120**(4): p. 483-95.
10. Annesley, S.J. and P.R. Fisher, *Mitochondria in Health and Disease*. Cells, 2019. **8**(7).

11. Huang, M.L., et al., *The Role of the Antioxidant Response in Mitochondrial Dysfunction in Degenerative Diseases: Cross-Talk between Antioxidant Defense, Autophagy, and Apoptosis*. Oxid Med Cell Longev, 2019. **2019**: p. 6392763.
12. Sinha, K., et al., *Oxidative stress: the mitochondria-dependent and mitochondria-independent pathways of apoptosis*. Arch Toxicol, 2013. **87**(7): p. 1157-80.
13. Barja, G., *Updating the mitochondrial free radical theory of aging: an integrated view, key aspects, and confounding concepts*. Antioxid Redox Signal, 2013. **19**(12): p. 1420-45.
14. Indo, H.P., et al., *A mitochondrial superoxide theory for oxidative stress diseases and aging*. J Clin Biochem Nutr, 2015. **56**(1): p. 1-7.
15. Hoye, A.T., et al., *Targeting mitochondria*. Acc Chem Res, 2008. **41**(1): p. 87-97.
16. Payne, A.J., et al., *Antioxidant drug therapy approaches for neuroprotection in chronic diseases of the retina*. Int J Mol Sci, 2014. **15**(2): p. 1865-86.
17. Kim, Y.S., et al., *Effects of targeting moiety, linker, bifunctional chelator, and molecular charge on biological properties of ⁶⁴Cu-labeled triphenylphosphonium cations*. J Med Chem, 2008. **51**(10): p. 2971-84.
18. Capuano, B., et al., *Synthesis and Preliminary Pharmacological Evaluation of 4-(2-(2-arylethoxyethyl)ethyl)-1-piperazinecarboxamide Hydrochloride Salts. II. Effect of the Nature and Length of the Linker*. Australian Journal of Chemistry, 2003. **56**(9): p. 875-886.
19. Yakukhnov, S.A. and V.P. Ananikov, *Catalytic Transfer Hydrodebenzylation with Low Palladium Loading*. Advanced Synthesis & Catalysis, 2019. **361**(20): p. 4781-4789.
20. Czech, B.P. and R.A. Bartsch, *Effect of amines on O-benzyl group hydrogenolysis*. The Journal of Organic Chemistry, 1984. **49**(21): p. 4076-4078.

21. Bull, S.D., et al., *Chemoselective debenzoylation of N-benzyl tertiary amines with ceric ammonium nitrate*. Journal of the Chemical Society, Perkin Transactions 1, 2000(22): p. 3765-3774.
22. Sajiki, H. and K. Hirota, *A novel type of PdMC-catalyzed hydrogenation using a catalyst poison: Chemoselective inhibition of the hydrogenolysis for O-benzyl protective group by the addition of a nitrogen-containing base*. Tetrahedron, 1998. **54**(46): p. 13981-13996.
23. Cook, G.R., L.G. Beholz, and J.R. Stille, *Construction of Hydroxylated Alkaloids (.+.-)-Mannonolactam, (.+.-)-Deoxymannojirimycin, and (.+.-)-Prosopinine through Aza-Annulation*. The Journal of Organic Chemistry, 1994. **59**(13): p. 3575-3584.
24. Mills, L.R., L.M. Barrera Arbelaez, and S.A.L. Rousseaux, *Electrophilic Zinc Homo-enolates: Synthesis of Cyclopropylamines from Cyclopropanols and Amines*. Journal of the American Chemical Society, 2017. **139**(33): p. 11357-11360.
25. Mou, J., Z.-M. Zong, and X.-Y. Wei, *FACILE SYNTHESIS OF ANXIOLYTIC BUSPIRONE*. Organic Preparations and Procedures International, 2008. **40**(4): p. 391-394.
26. 田中, 竜., 陽. 小沼, and 正. 大田, *4-ベンジル-2,6-ピペラジンジオンの水素化分解および1-フェニル-2,6-ピペラジンジオンのアミノ基の反応*. 日本化学会誌 (化学と工業化学) , 1978. **1978**(12): p. 1661-1665.
27. Williams, F.L. and K. Baron, *Lead, sulfur and phosphorus interactions with platinum and palladium metal foils*. Journal of Catalysis, 1975. **40**(1): p. 108-116.
28. Argyle MD, B.C., *Heterogeneous Catalyst Deactivation and Regeneration: A Review*. Catalysts, 2015. **5**(1): p. 145-269.

29. Yu, T.-C., *The effect of chlorine, sulfur, and phosphorus compounds on deactivation of palladium catalysts*, in *Chemical Engineering, Chemistry and Environmental Sciences*. 1995, New Jersey Institute of Technology: Digital Commons.
30. Hartung, R., et al., *Selectivity of N- Versus O-Alkylation in Mitsunobu Reactions with Various Quinolinols and Isoquinolinols*. HETEROCYCLES, 2017. **94**: p. 1305.
31. Ito, M., et al., *Biogenetically Inspired Approach to the Strychnos Alkaloids. Concise Syntheses of (±)-Akuammicine and (±)-Strychnine*. Journal of the American Chemical Society, 2001. **123**(33): p. 8003-8010.
32. Green TW, W.P., *Protective Groups in Organic Synthesis*. 1999, New York: Wiley-Interscience.
33. Nicolaou, K.C., et al., *A Mild and Selective Method for the Hydrolysis of Esters with Trimethyltin Hydroxide*. Angewandte Chemie International Edition, 2005. **44**(9): p. 1378-1382.
34. Smith MB, J.M., *Advanced Organic Chemistry: Reactions, Mechanisms, and Structure*. 6th ed. 2007, New York: Wiley-Interscience.
35. Castañeda, F., et al., *Thermal Decomposition of Triphenylphosphonium Alkyl Ester Salts*. Phosphorus, Sulfur, and Silicon and the Related Elements, 2008. **183**(5): p. 1188-1208.
36. Tyurina, Y.Y., et al., *Mitochondria targeting of non-peroxidizable triphenylphosphonium conjugated oleic acid protects mouse embryonic cells against apoptosis: role of cardiolipin remodeling*. FEBS letters, 2012. **586**(3): p. 235-241.

37. Burns, H.D., D.T. Sowa, and L.G. Marzilli, *Improved synthesis of N-(2,-6-dimethylphenylcarbamoylmethyl)iminodiacetic acid and analogs*. Journal of Pharmaceutical Sciences, 1978. **67**(10): p. 1434-1436.
38. 6.6 Silyl Esters, in *Protecting Groups*, P.J. Kociński, Editor. 2005, Georg Thieme Verlag: Stuttgart.
39. Strobrykina, I.Y., et al., *Triphenylphosphonium Cations of the Diterpenoid Isosteviol: Synthesis and Antimitotic Activity in a Sea Urchin Embryo Model*. Journal of Natural Products, 2015. **78**(6): p. 1300-1308.
40. Mondal, D., H. Niu, and K.G. Pinney, *Efficient synthetic methodology for the construction of dihydronaphthalene and benzosuberene molecular frameworks*. Tetrahedron Letters, 2019. **60**(5): p. 397-401.
41. Nam, T.-g., et al., *Pyridine and pyrimidine analogs of acetaminophen as inhibitors of lipid peroxidation and cyclooxygenase and lipoxygenase catalysis*. Organic & Biomolecular Chemistry, 2009. **7**(24): p. 5103-5112.
42. Chen, G.D., et al., *Novel oral multifunctional antioxidant prevents noise-induced hearing loss and hair cell loss*. Hear Res, 2020. **388**: p. 107880.
43. Chen, L.B., *Mitochondrial Membrane Potential in Living Cells*. Annual Review of Cell Biology, 1988. **4**(1): p. 155-181.
44. Huang, M., et al., *Mitochondrial inner membrane electrophysiology assessed by rhodamine-123 transport and fluorescence*. Annals of biomedical engineering, 2007. **35**(7): p. 1276-1285.
45. Teixeira, J., et al., *Development of hydroxybenzoic-based platforms as a solution to deliver dietary antioxidants to mitochondria*. Scientific Reports, 2017. **7**(1): p. 6842.
46. Yuan, C. and D. Acosta, Jr., *Cocaine-induced mitochondrial dysfunction in primary cultures of rat cardiomyocytes*. Toxicology, 1996. **112**(1): p. 1-10.

47. Usta, J., et al., *Linalool decreases HepG2 viability by inhibiting mitochondrial complexes I and II, increasing reactive oxygen species and decreasing ATP and GSH levels*. Chem Biol Interact, 2009. **180**(1): p. 39-46.
48. Baracca, A., et al., *Rhodamine 123 as a probe of mitochondrial membrane potential: evaluation of proton flux through F(0) during ATP synthesis*. Biochim Biophys Acta, 2003. **1606**(1-3): p. 137-46.
49. Ng, L.F., et al., *The mitochondria-targeted antioxidant MitoQ extends lifespan and improves healthspan of a transgenic Caenorhabditis elegans model of Alzheimer disease*. Free Radic Biol Med, 2014. **71**: p. 390-401.
50. Castellani, R.J., et al., *Chapter 18 - Tackling Alzheimer's Disease by Targeting Oxidative Stress and Mitochondria*, in *Developing Therapeutics for Alzheimer's Disease*, M.S. Wolfe, Editor. 2016, Academic Press: Boston. p. 477-502.
51. Gottwald, E.M., et al., *The targeted anti-oxidant MitoQ causes mitochondrial swelling and depolarization in kidney tissue*. Physiological reports, 2018. **6**(7): p. e13667-e13667.
52. Murphy, M.P., *Targeting lipophilic cations to mitochondria*. Biochim Biophys Acta, 2008. **1777**(7-8): p. 1028-31.
53. Zielonka, J., et al., *Mitochondria-Targeted Triphenylphosphonium-Based Compounds: Syntheses, Mechanisms of Action, and Therapeutic and Diagnostic Applications*. Chem Rev, 2017. **117**(15): p. 10043-10120.
54. Akhmadishina, R.A., et al., *Triphenylphosphonium Moiety Modulates Proteolytic Stability and Potentiates Neuroprotective Activity of Antioxidant Tetrapeptides in Vitro*. Front Pharmacol, 2018. **9**: p. 115.
55. Reily, C., et al., *Mitochondrially targeted compounds and their impact on cellular bioenergetics*. Redox Biol, 2013. **1**(1): p. 86-93.

56. Ross, M.F., et al., *Rapid and extensive uptake and activation of hydrophobic triphenylphosphonium cations within cells*. *Biochem J*, 2008. **411**(3): p. 633-45.
57. Millard, M., et al., *Preclinical evaluation of novel triphenylphosphonium salts with broad-spectrum activity*. *PLoS One*, 2010. **5**(10).
58. Asin-Cayuela, J., et al., *Fine-tuning the hydrophobicity of a mitochondria-targeted antioxidant*. *FEBS Lett*, 2004. **571**(1-3): p. 9-16.
59. Rogov, A.G., et al., *New Data on Effects of SkQ1 and SkQT1 on Rat Liver Mitochondria and Yeast Cells*. *Biochemistry (Mosc)*, 2018. **83**(5): p. 552-561.
60. Leo, S., G. Szabadkai, and R. Rizzuto, *The mitochondrial antioxidants MitoE(2) and MitoQ(10) increase mitochondrial Ca(2+) load upon cell stimulation by inhibiting Ca(2+) efflux from the organelle*. *Ann N Y Acad Sci*, 2008. **1147**: p. 264-74.
61. Kalinec, G.M., et al., *A cochlear cell line as an in vitro system for drug ototoxicity screening*. *Audiol Neurootol*, 2003. **8**(4): p. 177-89.
62. Kalinec, G.M., et al., *Working with Auditory HEI-OC1 Cells*. *J Vis Exp*, 2016(115).
63. Chazotte, B., *Labeling mitochondria with rhodamine 123*. *Cold Spring Harb Protoc*, 2011. **2011**(7): p. 892-4.

CHAPTER 6

Conclusions and Future Directions

6.1. Biodistribution Study

To confirm the preliminary distribution studies of the MFAOs conducted in mice, the bioavailability studies presented in Chapter 2 were expanded on Sprague Dawley rats. All compounds were orally-administered to the rats for 7 days with each rat fed chow containing 0.05% of compound. The measured average daily dose based on food weight measurements was 46.2 ± 2.2 mg drug/kg body weight. The levels of unmetabolized compounds were analyzed in ocular, neural, and visceral tissue which included the cornea, iris with ciliary body, lens, neural retina, retinal pigmented epithelium with the choroid, brain, sciatic nerve, kidney, and liver. The distribution values of the compounds ranged from 0 ng drug/mg protein to 3.7 mg drug/mg protein. The parent HK-15 was undetectable in the ocular tissue and the brain, and parents JHX-1 and JHX-5 were undetectable in the sciatic nerve. No clear trends were identified in the distribution profiles of the compounds, suggesting that further investigation is necessary to understand the factors of drug permeation across the various physiological barriers to reach target tissues.

Future work to support the biodistribution study may include *in vitro* and *in vivo* assessments of ADME and PK properties including drug binding to plasma proteins, biological half-life, and toxicity. The bioavailability study has shown that, with the exception of HK-15 in ocular tissues and the brain, and JHX-1, and JHX-5 in the SN, the remainder of the compounds are found in all tissues. It is possible that the metabolites of

the MFAOs and their analogs may also have biological effects. A previous short-term maximum tolerated dose experiment was conducted in mice where the JHX-4 and HK-2 MFAOs were administered up to 1800 mg drug/kg body weight/day without any observed adverse effects. A long-term maximum tolerated dose experiment and/or dose-escalation study will be conducted to confirm these initial results.

6.2. Predictive Modeling Study

The data from the biodistribution study were analyzed with two different data mining algorithms, hierarchical cluster analysis (HCA) and quantitative structure activity relationship analysis (QSAR), to investigate relationships between the calculated physicochemical descriptors of the compounds with their measured tissue levels. The analyses indicated that these two methods were able to identify a myriad of relationships between the compounds, resulting in several physiologically-relevant predictive models of compound distribution to various ocular, neural, and visceral tissues. Many of the models derived from both algorithms were similar, if not identical, and the identified trends agreed with other reported experimental trends of drug passage through various physiological barriers such as the blood-aqueous (BAB), blood-retinal (BRB), blood-brain (BBB), and blood-nerve barriers (BNB).

Future work in this area may include expanding the QSAR models using other physicochemical descriptors as well as multi-variable analysis. The single variable results reported in Chapter 3 identified several physiologically-relevant predictive models. Preliminary investigations using multi-variable correlations have been conducted and suggest that many more models can be developed by expanding these initial approaches.

Analysis with multiple variables may further elucidate the critical relationships between physicochemical descriptors necessary for specific tissue uptake.

6.3. Oxysterol Study

The novel paradigm that oxysterols could restore vision from cataracts was investigated using *in vitro* lens culture studies, solubilization studies, and computational docking studies in Chapter 4. The oxysterols failed to prevent the progression of, or clear, lens opacities. *In silico*, the oxysterols also failed to reach acceptable thresholds for good predictive binding at either the protein dimer interface or the ATP-binding pocket of three model α B-crystallins. Comparatively, the MFAOs were found to bind with higher affinity than the oxysterols to both the dimer interfaces and the ATP-binding pockets of all three model α B-crystallins. These results suggest that the oxysterols most likely do not restore vision through the reported mechanism of action as an α B-crystallin molecular chaperone. The *in silico* docking results support the experimental results of our research group which previously demonstrated that the NF JHX-1 was able to significantly delay the advanced progression of sugar cataract formation *in vivo* without sorbitol dehydrogenase or aldose reductase inhibition, suggesting it may have inherent chaperone activity.

It may be possible that small molecules help prevent the aggregation of the α -crystallins. Computational simulations can help verify these docking results and provide a method to study what happens at the molecular level during the aggregation process. This *in silico* tool may help us understand how the small molecule MFAOs interact with the crystallins and affect the aggregation process.

6.4. Mitochondria-Targeted TPP Synthesis and *In Vitro* Studies

New synthetic approaches were developed towards a new series of triphenylphosphonium-based (TPP) MFAOs. Three non-functional parent compounds and one monofunctional metal chelating compound were successfully synthesized: the C3-linked JHX-1-TPP, the C4-linked JHX-1-TPP, the JHX-1-TPP-Ester, and the JHX-3-TPP-Ester. The results from the *in vitro* studies on HEI-OC1 cells with the non-conjugated JHX-2, JHX-3, and JHX-4 compounds, as well as the novel synthesized JHX-1-TPP and the HK-2-Benzyl-TPP compounds, show that compounds with Fe, Cu, or Zn chelating potential entering the mitochondria may not adversely affect mitochondrial function at sub-micromolar concentrations and provide evidence that development of the TPP-based MFAOs should be further explored. The effects of the TPP compounds confirm our hypothesis that the activity of the MFAOs can be enhanced by directly targeting mitochondrial dysfunction. These findings are summarized in Chapter 5.

Additionally, the progress towards the development of the TPPs have yielded new synthetic strategies for a new series of MFAOs. The initial JHX-series of MFAOs include the *N,N*-dimethyl-3,5-dioxopiperazine-1-sulfonamide or the *N,N*-dimethylpiperazine-1-sulfonamide top ring systems. Using the newly developed synthetic strategies, several novel MFAO series with the piperazine top ring scaffold can be further developed. **Figure 6.1** illustrates the new proposed JHX-based compounds.

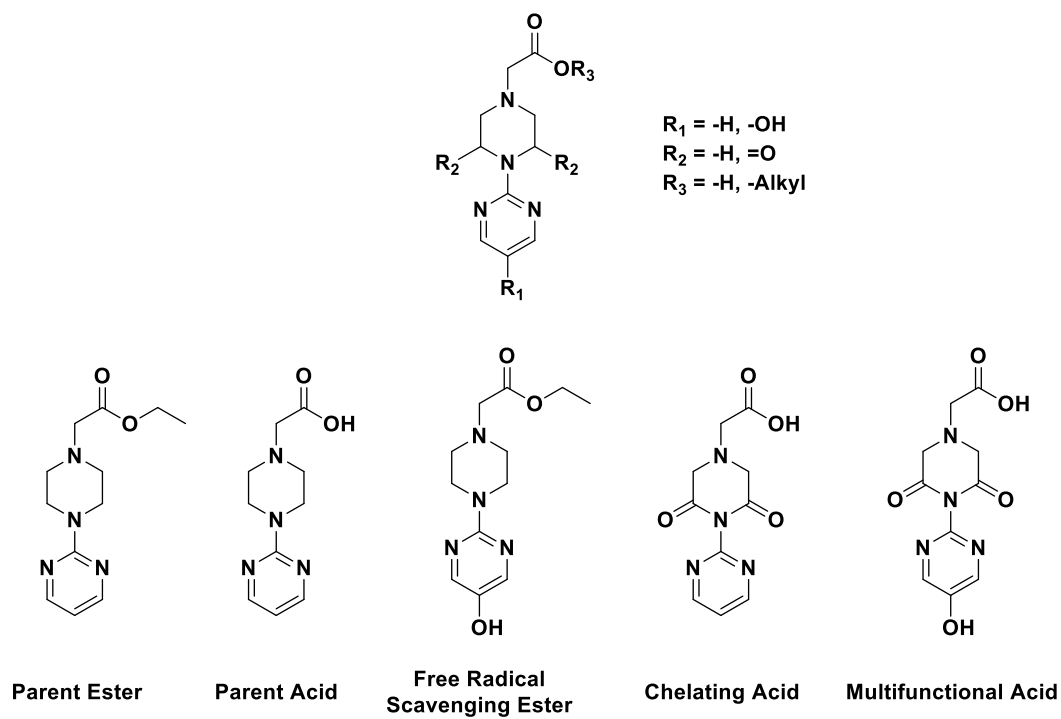


Figure 6.1. The new proposed JHX-based compound series. This series is based on the intermediates developed during the JHX-TPP synthetic approaches which uses an acetic acid or ester group instead of the *N,N*-dimethylsulfamoyl group.